



**HAL**  
open science

# Coupling between transport, mechanical properties and degradation by dissolution of rock reservoir

Kajetan Wojtacki

► **To cite this version:**

Kajetan Wojtacki. Coupling between transport, mechanical properties and degradation by dissolution of rock reservoir. Mechanics [physics.med-ph]. Université Montpellier, 2015. English. NNT : 2015MONTTS153 . tel-01994701

**HAL Id: tel-01994701**

**<https://theses.hal.science/tel-01994701>**

Submitted on 25 Jan 2019

**HAL** is a multi-disciplinary open access archive for the deposit and dissemination of scientific research documents, whether they are published or not. The documents may come from teaching and research institutions in France or abroad, or from public or private research centers.

L'archive ouverte pluridisciplinaire **HAL**, est destinée au dépôt et à la diffusion de documents scientifiques de niveau recherche, publiés ou non, émanant des établissements d'enseignement et de recherche français ou étrangers, des laboratoires publics ou privés.

UNIVERSITÉ DE MONTPELLIER  
— LABORATOIRE DE MÉCANIQUE ET GÉNIE CIVIL —

THÈSE  
pour obtenir le grade de  
DOCTEUR DE L'UNIVERSITÉ DE MONTPELLIER

École Doctorale : INFORMATION, STRUCTURES ET SYSTÈMES  
Spécialité : MÉCANIQUE ET GÉNIE CIVIL

---

Couplage entre transport, comportement  
mécanique et dégradation par dissolution de  
réservoirs de roche

---

par

KAJETAN TOMASZ WOJTACKI

*Soutenue publiquement à Montpellier le 16 Décembre 2015 devant le jury composé de :*

M. El Mostafa Daya	Professeur	LEM3	Président
M. Dariusz Łydźba	Professeur	PWr	Rapporteur
M. Vincent Monchiet	Maître de Conférence	MSME	Rapporteur
M. Pierre Alart	Professeur	LMGC	Examineur
M. Loïc Daridon	Professeur	LMGC	Directeur
M. Yann Monerie	Professeur	LMGC	Co-Directeur
M. Philippe Gouze	Chercheur	CNRS	Membre Invité
Mme. Jolanta Lewandowska	Professeur	LMGC	Membre Invité



UNIVERSITY OF MONTPELLIER  
— LABORATORY OF MECHANICS AND CIVIL ENGINEERING —

THESIS  
to obtain the degree of  
DOCTOR OF PHILOSOPHY OF THE UNIVERSITY OF MONTPELLIER

Doctoral School: INFORMATION, STRUCTURES AND SYSTEMS  
Speciality: MECHANICS AND CIVIL ENGINEERING

---

Coupling between transport, mechanical  
properties and degradation by dissolution of  
rock reservoir

---

by

KAJETAN TOMASZ WOJTACKI

*Publicly defended in Montpellier on 16th December 2015 to the jury:*

Mr. El Mostafa Daya	Professor	LEM3	President
Mr. Dariusz Łydźba	Professor	PWr	Reviewer
Mr. Vincent Monchiet	Associate Professor	MSME	Reviewer
Mr. Pierre Alart	Professor	LMGC	Examiner
Mr. Loïc Daridon	Professor	LMGC	Director
Mr. Yann Monerie	Professor	LMGC	Co-Director
Mr. Philippe Gouze	Researcher	CNRS	Invited Member
Mme Jolanta Lewandowska	Professor	LMGC	Invited Member






*à mes parents,  
à mes grands-parents,  
à mes deux frères*



*L'amitié consiste dans l'oubli de ce que l'on donne, et dans le souvenir de ce que l'on reçoit.*

Alexandre Dumas

## Remerciements

videmment, ce travail n'aurait pas eu lieu sans le soutien et l'opportunité offerts par Jolanta Lewandowska. Je voudrais la remercier de m'avoir ouvert les portes de la recherche en France et de m'avoir guidé durant ma première année de thèse. Je tiens également à remercier Philippe Gouze qui m'a aussi encadré durant cette même période, pour tout ce qu'il m'a appris, pour ses conseils et pour m'avoir aidé dans mes premiers pas de doctorant.

Notamment je tiens à exprimer ma profonde gratitude pour Loïc Daridon et Yann Monerie sans qui ce travail n'aurait pas pu être poursuivi ni accompli. Je voudrais remercier Loïc qui fut pour moi un directeur de thèse attentif, disponible malgré ses nombreuses charges. Ses compétences, sa clairvoyance et son sens de l'humour m'ont beaucoup appris durant mon séjour en France. Un grand merci à Yann pour ses remarques précieuses et son soutien moral dans les moments difficiles de cette aventure surtout à la fin de cette thèse. Je tiens à leur exprimer ma profonde gratitude pour tout ce qu'ils m'ont appris aussi bien scientifiquement qu'humainement. Merci pour votre aide, votre soutien, vos conseils et votre humour.

Je remercie vivement les membres du jury, qui ont accepté d'évaluer mon travail. Je remercie El Mostafa Daya qui a bien voulu présider le jury et examiner mes travaux de thèse. Je remercie mes deux rapporteurs Dariusz Łydźba et Vincent Monchiet pour l'intérêt qu'ils ont porté à mes travaux de recherche, ainsi que pour leurs remarques très constructives. Je remercie Pierre Alart d'avoir accepté le rôle d'examineur.

Je remercie mes collègues doctorants, les nouveaux ainsi que les anciens en espérant n'avoir oublié personne. Je pense notamment à mes collègues de bureau Lhassan, Cecile, Riccardo et Adrien ainsi que la bande des doctorants et post-doctorants : Patrick, Nawfal, Adil, Tarik, Li, Mahmoud, Paul, Lionel, Eric, Nicolas, David, Lo, Mahmoud, Tarik, Maria, Aditi, Capucine, Cecilia, Xavier, Chaoqun, Fatima, Thanh Hai, Benjamin, Lionel, Eric, Maria, Aditi, Daniel et Gilles.

Une dédicace spéciale et un grand merci à Lhassan, Riccardo, Cecile, Paul et David pour leur soutien et leur amitié précieuse. Je voudrai vous remercier pour toutes des moments inoubliables, toutes les conneries qu'on a faites et pour ces soirées qui ont laissées une trace indélébile dans mon foie...

J'adresse ensuite mes remerciements à mes amis de l'UM avec qui j'ai passé beaucoup de temps : Jola, Filip, Vanja et Marko.

Je tiens également à remercier mes monitrices d'équitation : Marine, Charlotte et Mathilde pour ces moments de détente et de convivialité.

Je remercie aussi l'ensemble du personnel du laboratoire LMGC, je pense notamment à Robert, Katya, Reine, Chantal, Roxane, Caroline et Yannick.

Finalement et non le moindre, j'adresse mes plus sincères remerciements à ma famille : mes parents, mes grands-parents, mes deux frères et tous mes proches et amis de Pologne, qui m'ont accompagné, aidé, soutenu et encouragé tout au long de cette thèse.

# Résumé

Le stockage géologique du CO<sub>2</sub> est intensivement étudié comme une des solutions pour réduire les émissions de CO<sub>2</sub> dans l'atmosphère. Ce stockage du dioxyde de carbone (CCS) consiste à capter le CO<sub>2</sub> à la source et à l'injecter, dans un état supercritique, directement dans des lieux de stockage [Fig. 1]. Les aquifères salins, qui sont des formations de grès (ou calcaire) très poreuses et saturées en eau trop salée pour être exploitable, sont de fait de très bons candidats. Dans cette thèse nous allons explorer cette piste en étudiant notamment l'influence du stockage sur ces formations géologiques. La dissolution du dioxyde de carbone s'accompagne d'une acidification de l'eau, engendrant des réactions chimiques et une altération de la roche constituant le réservoir. Les réactions chimiques provoquent des changements importants et irréversibles des propriétés et de la morphologie de la roche [1].

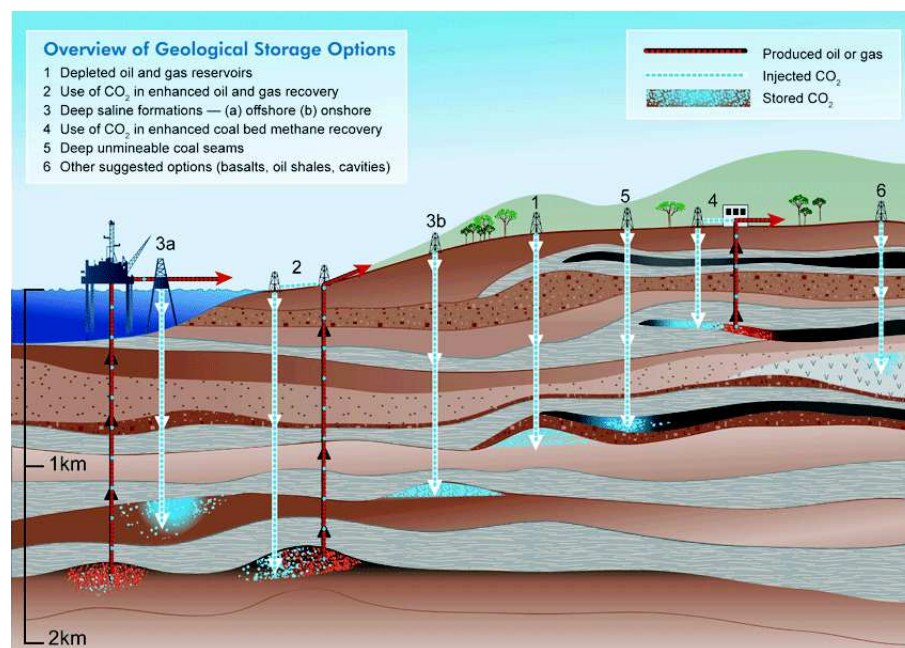


Figure 1: Options différentes de stockage du CO<sub>2</sub> [1].

L'objectif de cette thèse est d'analyser l'évolution des propriétés mécaniques et de transport d'aquifères salins soumis à une dégradation chimique progressive, liée à la dissolution du CO<sub>2</sub> et à l'acidification de l'eau saline. En d'autres termes, l'objectif est de trouver un lien entre l'évolution de la microstructure du matériau, les phénomènes se produisant à l'échelle microscopique, et le comportement macroscopique. Afin de modéliser

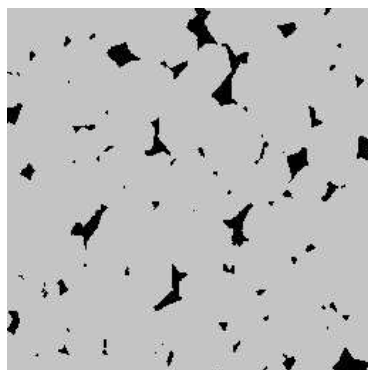
la dégradation chimique, deux hypothèses principales ont été faites: l'hypothèse du long terme et celle de condition de champ lointain. Selon ces hypothèses la dissolution peut être considérée comme uniforme à l'échelle de l'échantillon [2]. La dégradation chimique de la matière est prise en compte d'une façon simplifiée en effectuant une érosion numérique de la microstructure. Pour atteindre cet objectif, la méthodologie suivante a été adoptée :

1. **analyse statistique et morphologique de la microstructure réelle.**
2. **reconstruction de la microstructure et validation morphologique.**
3. **dissolution numérique de l'image réelle et des échantillons générés.**
4. **estimation du comportement effectif**

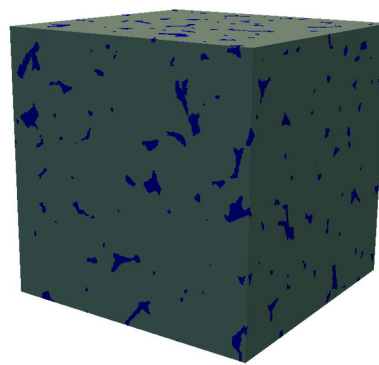
La méthodologie proposée permet de réaliser une analyse détaillée de la relation entre les informations statistiques au niveau micro et les caractéristiques macroscopiques obtenues numériquement.

## Analyse statistique et morphologique de la microstructure réelle

Les formations rocheuses, support des aquifères salins, sont principalement composées de grès. Le grès est une roche sédimentaire composée de grains de sable qui permet généralement la percolation des fluides. La microstructure étudiée est présentée sur la Figure 2 - c'est un échantillon de grès de Fontainebleau, qui a été obtenu par microtomographie aux rayons X. En règle générale, les données sont organisées comme un ensemble d'éléments cubiques (voxels) ayant une valeur unique de niveaux de gris correspondant à une phase matérielle distincte. Dans notre cas, nous considérons un milieu biphasique dans lequel une des valeurs correspond à la phase solide et l'autre aux pores. La taille initiale de la géométrie du grès est de  $256 \times 256 \times 256$  pixels avec une résolution de  $5.01 \mu\text{m}$  par pixel.



(a) couche en 2D



(b) microstructure en 3D

Figure 2: Des visualisations de la géométrie du grès.

## Informations morphologiques

Les propriétés macroscopiques de la roche sont directement liées à la morphologie du réseau de pores et du squelette solide. Pour cette raison la modélisation à l'échelle micro des matériaux hétérogènes aléatoires (type roche ou milieux poreux) doit se baser sur des caractérisations morphologiques et statistiques de la microstructure fiables. Aussi, afin de qualifier morphologiquement le matériau réel, les quatre critères suivants sont utilisés [3] :

- **mesures de base** : porosité, surface spécifique
- **granulométrie** : la granulométrie du squelette solide, estimée en effectuant l'opération de fermeture/ouverture morphologique
- **distribution spatiale** : en utilisant la fonction de covariance, nous sommes capables d'estimer la longueur caractéristique de la phase et de vérifier l'isotropie de la microstructure considérée
- **connectivité** : elle influe fortement sur la perméabilité du milieu et est caractérisable par la tortuosité morphologique.

En effectuant l'analyse morphologique sur la géométrie du grès, nous avons obtenu les informations suivantes<sup>1</sup> :

- **porosité** :  $\varphi = 0.046$
- **rayons moyens**<sup>2</sup> :  $r_{mean}^+ = 23.7 \pm 4.9$  et  $r_{mean}^\circ = 17.4 \pm 3.5$  (Fig. 3)
- **distribution spatiale** : la distribution spatiale des phases est isotrope; la longueur caractéristique de la microstructure est de  $\lambda = 23$  px (Fig. 4)
- **connectivité** : le milieu est percolé dans toutes les directions (Tab. 1) et la fraction volumique du réseau percolé est de  $\varphi_{eff} = 0.029$ .

Table 1: Résumé de la tortuosité morphologique du grès. Pour chaque direction, la valeur moyenne  $\bar{\tau}$ , minimale  $\tau_{min}$ , maximale  $\tau_{max}$  et écart-types sont présentés.

	$\tau_x$	$\tau_y$	$\tau_z$
$\bar{\tau}$	2.21	1.92	2.44
$\tau_{min}$	1.48	1.45	1.25
$\tau_{max}$	3.98	3.58	4.67
$\sigma_\tau$	0.49	0.38	0.70

<sup>1</sup>toutes les valeurs sont présentées en détails dans le Chapitre 2

<sup>2</sup>les signes + et o correspondent aux deux éléments structuraux différents (cross-shaped/diamond et circle binarisée respectivement)



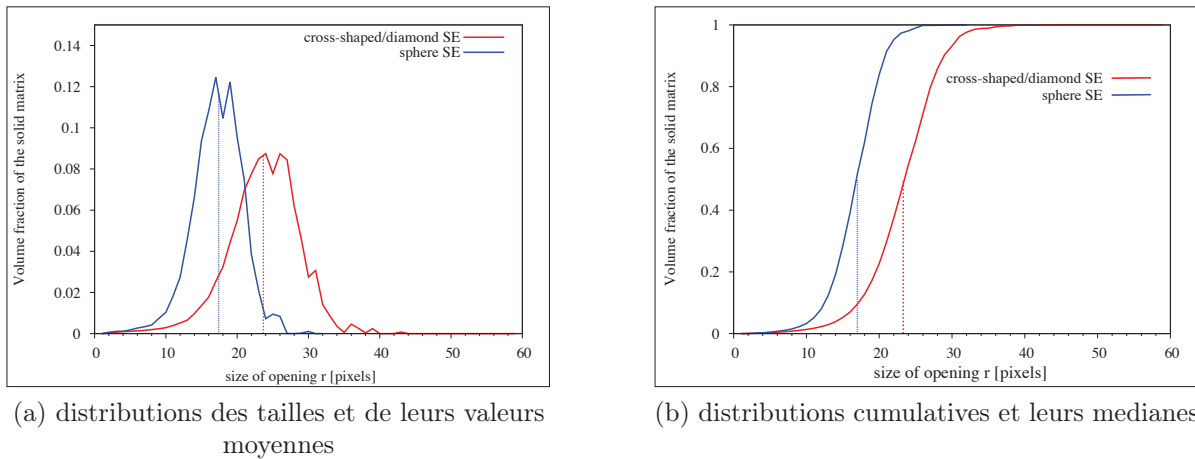


Figure 3: Granulométrie du grès obtenue en utilisant deux éléments structuraux différents.

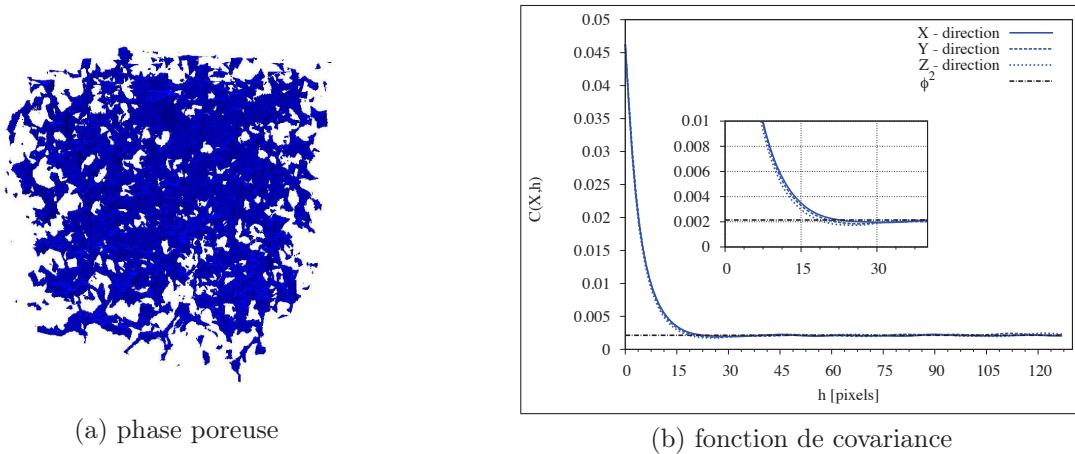


Figure 4: La phase poreuse du grès et sa fonction de covariance ( $\varphi = 4.63\%$ ).

## Reconstruction de la microstructure et validation morphologique

Comme nous l'avons précisé, le processus de formation de grès consiste en série de phénomènes géologiques et hydrodynamiques complexes. L'objectif, ici, est de reconstruire l'échantillon, par un processus aussi simple que possible en mettant en œuvre des étapes de base inspirées par le processus naturel de formation de grès. Pour ce faire nous avons suivi une approche comparable à celle proposée par de Bake et Øren [4, 5], la géométrie 3D modèle du grès est obtenue à l'aide de 3 phases sachant que les informations morphologiques discriminantes sont vérifiées à posteriori :

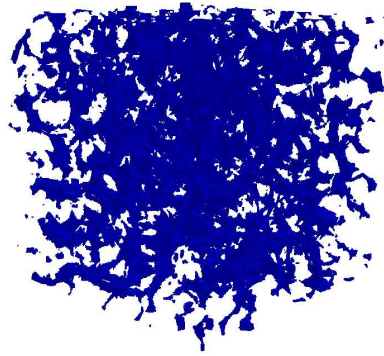
- **la sédimentation:** ou dépôt de grains, nous utilisons des grains monodisperses qui sont déposés initialement dans une boîte 3D selon l'algorithme de minimisation du potentiel gravitationnel (LMGC90 [6, 7])

- **le compactage:** ou réduction de volume en vrac, le compactage est appliqué pour minimiser l'anisotropie et la porosité initiale de l'échantillon
- **la diagenèse:** incrément aléatoire des rayons, ce processus consiste à sélectionner aléatoirement des grains dans l'échantillon puis à en incrémenter le rayon et recommencer ce processus jusqu'à obtenir la valeur de porosité cible. Ici, l'incrément de rayon est constant.

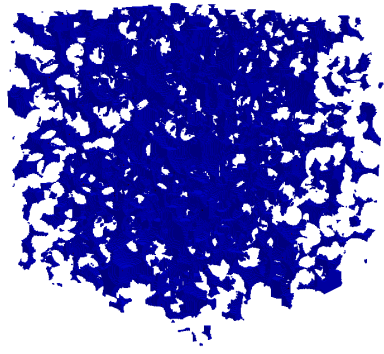
Afin de choisir la meilleure stratégie, nous avons fait une étude paramétrique de ce processus de reconstruction du grès de Fontainebleau. A la suite de cette étude, nous en sommes arrivés à la conclusion qu'il fallait utiliser un rayon initial de 14 px et un compactage triaxial. Chaque réalisation est obtenue à partir du même dépôt géométrique de grains soumis au type de compactage choisi. Ensuite, les échantillons sélectionnés doivent répondre aux deux critères suivants :

1. **percolation** – les réalisations qui ne sont pas percolées dans toutes les directions sont exclues de l'analyse.
2. **porosité effective** – les échantillons qui ne satisfasse pas la condition suivante :  
 $\varphi_{eff} = \varphi_{eff}^{sandstone} \pm 5\%$  ont été exclus.

Le processus de génération a été arrêté lorsque 10 réalisations, satisfaisant les critères évoqués ci-dessus, ont été générées. Les Figures 5 et 6 montrent une très bonne adéquation entre la morphologie du matériau modèle et celui d'un grès de Fontainebleau.

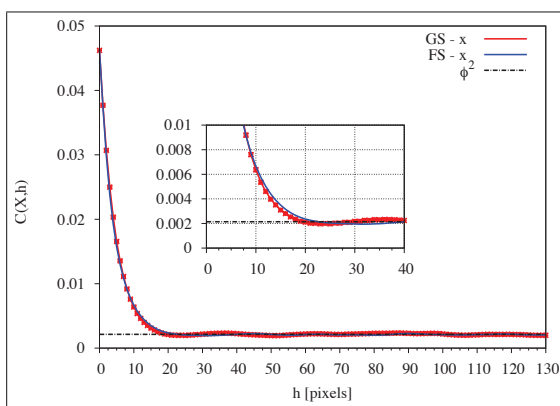
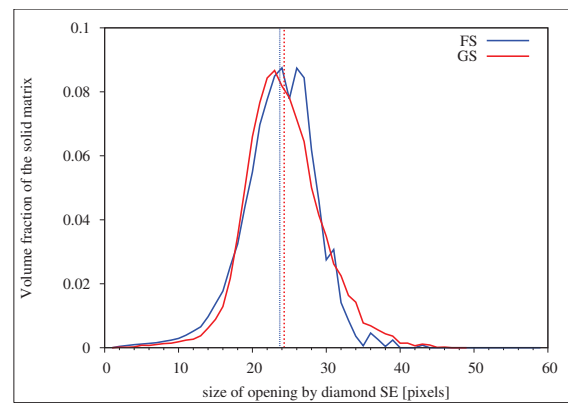


(a) grès



(b) échantillon modèle

Figure 5: Visualisation des microstructures.

(a) covariance - pour direction  $\vec{x}$ 

(b) distributions de tailles

Figure 6: La comparaison de deux descripteurs concernant le grès (FS) et les échantillons générés (GS): la covariance et la granulométrie.

## Dissolution numérique de l'image réelle et des échantillons générés

En ayant une géométrie binarisée de la roche réelle et des géométries reconstruites, nous pouvons proposer maintenant un scénario de dissolution chimique. Nous savons que la microstructure obtenue par microtomographie ne donne qu'une approximation de la connectivité réelle entre les pores. Par conséquent, nous avons examiné deux scénarii différents de dissolution.

Le modèle de la dissolution numérique est basé sur l'opération de base de la morphologie mathématique - la dilatation. La dégradation chimique du squelette solide est prise en compte de façon simplifiée, en effectuant la dilatation de la phase poreuse, en utilisant un élément structurant cubique. Le choix de l'élément structurant isotrope peut être justifié par les hypothèses de champ lointain et les conditions à long terme, lorsque la concentration des réactifs est supposée être distribuée d'une manière homogène dans l'espace des pores à l'échelle de l'échantillon [2,8]. Deux scénarii différents sont envisagés :

- **la dissolution isotrope** : consiste à appliquer la dissolution dans toutes les pores même celles qui ne sont pas connectés [Fig. 7 (a)]
- **la dissolution du réseau** : consiste à appliquer la dissolution uniquement aux pores du réseau percolé [Fig. 7 (b)].

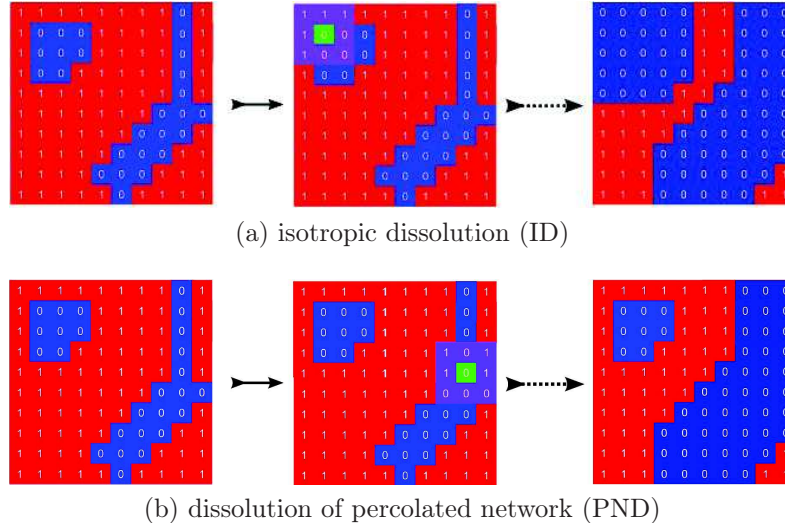
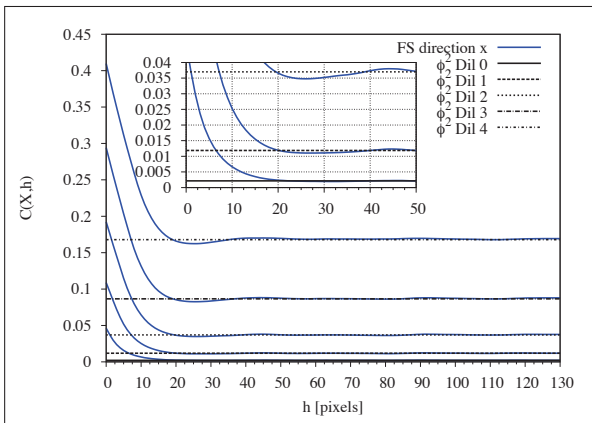


Figure 7: Une visualisation des scénarii de la dissolution numérique en 2D, un cas simplifié.

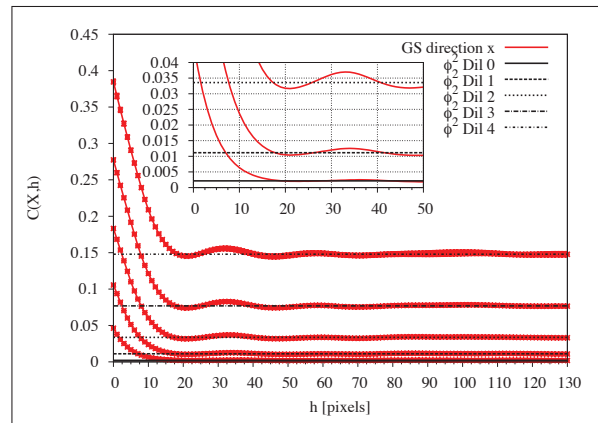
La modélisation proposée est universelle, en ce sens qu'elle utilise une échelle de temps adimensionnelle. Par conséquent, elle peut être adaptée à tout processus dépendant du temps. Le processus de dissolution est effectué en 3D et arrêté lorsque la porosité atteint environ 40%.

Afin de montrer l'influence des scénarii de dissolution sur l'évolution des échantillons, nous présentons sur la Figure 8, l'évolution de la covariance pour le matériau modèle et le grès de Fontainebleau. Dans un souci de clarté, nous présentons uniquement la covariance

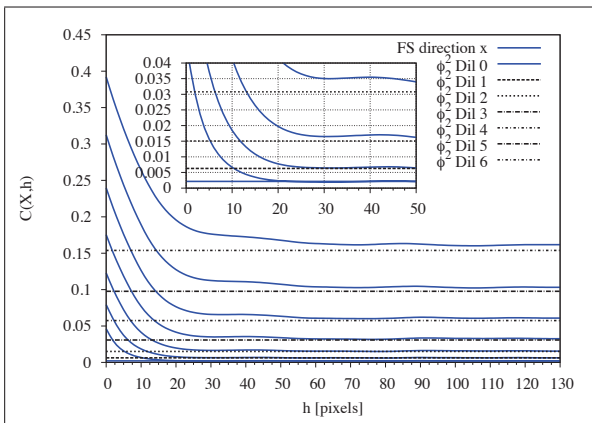
dans la direction  $\vec{x}$ . La Figure 8 montre que chacune des courbes converge vers sa valeur asymptotique. Les deux scénarii induisent une augmentation de la valeur initiale et de fait de la valeur asymptotique. Pour chaque étape de la dissolution, la première valeur,  $Cov(0)$ , de la fonction de covariance se réfère à la porosité initiale de l'échantillon. Nous pouvons voir que la valeur de la porosité varie entre 4.6 et 40%. On observe que les augmentations sont semblables pour le matériau modèle et pour le matériau réel. Ce qui tend à montrer le caractère prédictif de ce matériau modèle. En analysant l'évolution de la covariance, nous pouvons formuler la conclusion suivante, à savoir que, lors de la dissolution isotrope la taille de VER reste constante, tandis que pour la dissolution en réseau, la taille du VER augmente d'une manière significative.



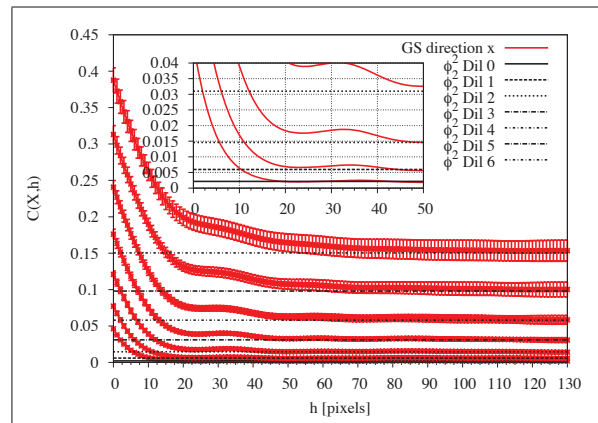
(a) Grès de Fontainebleau - dissolution isotrope



(c) Matériau modèle - dissolution isotrope



(b) Grès de Fontainebleau - dissolution du réseau



(d) Matériau modèle - dissolution du réseau

Figure 8: L'évolution de la covariance pour deux matériaux au cours de deux scénarii de la dissolution.

## Estimation de comportement effectif - homogénéisation linéaire

Lorsque l'on cherche à estimer les propriétés équivalentes d'un milieu élastique hétérogène, on peut résoudre les équations locales d'élasticité en utilisant un code d'éléments finis sur la géométrie d'un VER. L'estimation des propriétés élastiques est alors basée sur la méthode d'homogénéisation périodique [9–11]. Ici, le code d'éléments finis CAST3M est utilisé afin de mettre en œuvre cette méthode. La matrice de rigidité effective, obtenue en résolvant les six problèmes élémentaires correspondants aux six différents cas de chargements généralisés, est donnée par:

$$C_{ijkh} = \left\langle c_{ijpq} \left[ I_{pq}^{kh} + \epsilon_{pq} \left( u'^{kh} \right) \right] \right\rangle, \quad (1)$$

où  $u'^{kh}$  est la solution du problème d'élasticité,  $I_{pq}^{kh}$  le tenseur identité d'ordre quatre qui permet de définir les six chargements généralisés,  $c_{ijpq}$  le tenseur de rigidité microscopique et  $\epsilon_{pq}$  le tenseur de déformations microscopique.

Cependant en extrayant un VER à partir d'une image naturelle de roche ou d'un matériau modèle les hypothèses de périodicité ne sont généralement pas vérifiées. Pour résoudre ce problème, le VER est inclus dans une couche de matériau homogène (Fig. 9) dont le comportement sera in-fine celui recherché. Pour ce faire, la méthode du point fixe est utilisée. Initialement, le tenseur de rigidité de la couche est supposé être égal à celui du squelette du milieu poreux. À chaque itération les propriétés élastiques de la couche sont décrites par le tenseur de rigidité homogénéisé du système à l'itération précédente:

$$\bar{c}_{ijkh}^{layer}[i] = C_{ijkh}^{hom}[i-1], \quad (2)$$

où  $i$  désigne le nombre d'itération et  $\bar{c}_{ijkh}^{layer}$  – le tenseur de rigidité microscopique de la couche.

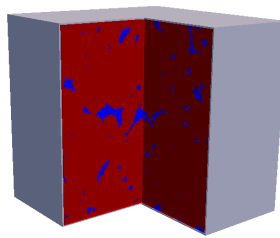


Figure 9: La géométrie du grès de Fontainebleau incluse dans une couche de matériau homogène.

Une microstructure définie par une image numérique est déjà naturellement discrétisée. Lorsque nous utilisons maillage cubique régulier, pour représenter la microstructure, l'influence de la discrétisation est déterminée explicitement [12–14]. Cette relation peut être alors estimée par la formule phénoménologique :

$$P(M) = P_0 + \frac{a}{M}, \quad (3)$$

où  $P(M)$  est le module élastique calculé et  $P_0$  la valeur continue qui correspond au cas  $M \rightarrow \infty$ . Pour estimer cette valeur ( $P_0$ ) nous devons calculer les propriétés élastiques, au moins, pour trois valeurs de  $M$  différentes et ensuite extrapoler les résultats.

### **Méthodologie et résultats**

Afin d'estimer le comportement élastique effectif des échantillons considérés, nous avons utilisé la méthodologie présentée, étape par étape, sur la Figure 10. La Figure 11 montre la comparaison de l'évolution des modules élastiques normalisés en fonction de la porosité. Dans les deux scénarii, l'évolution du comportement est presque identique.

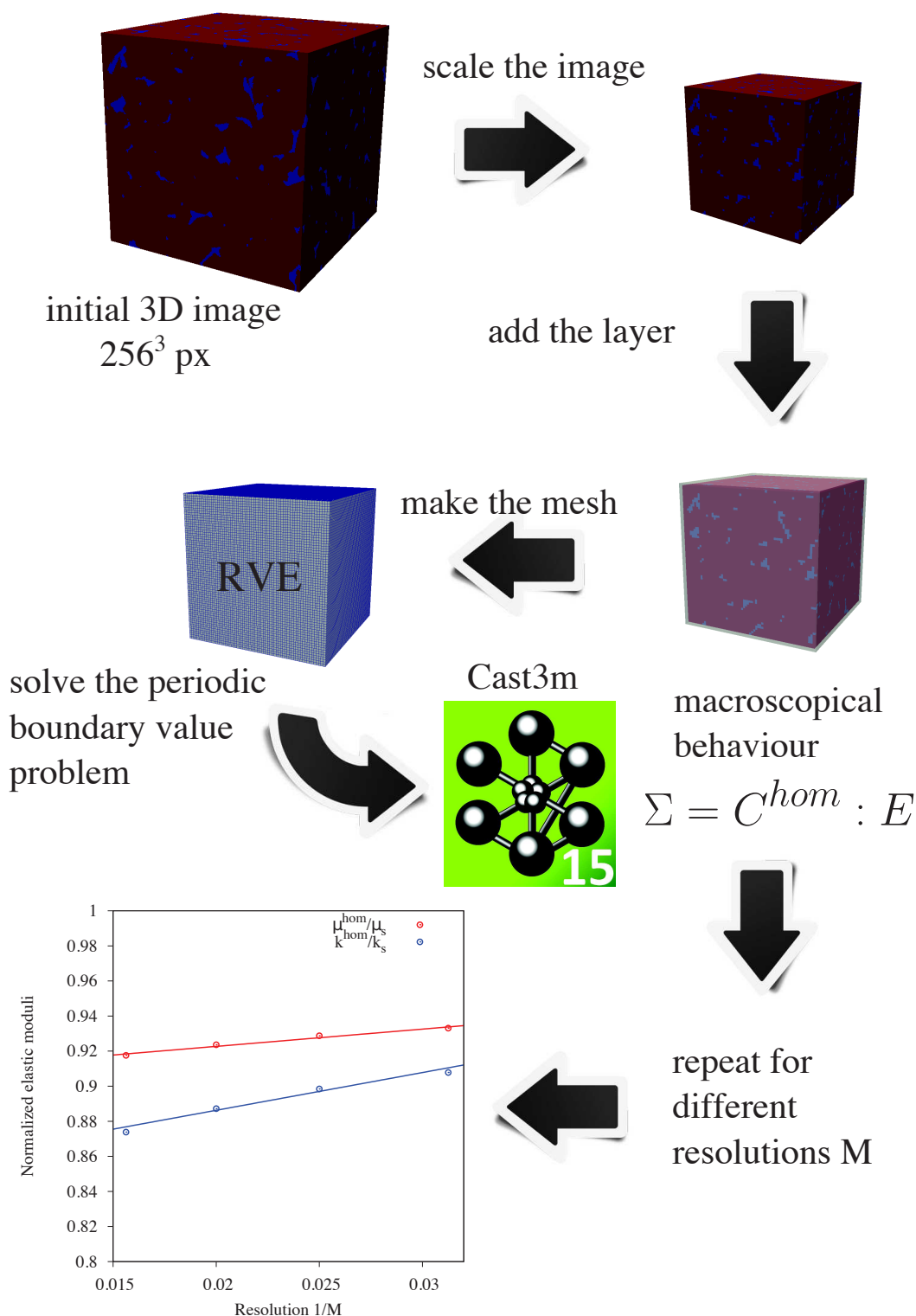
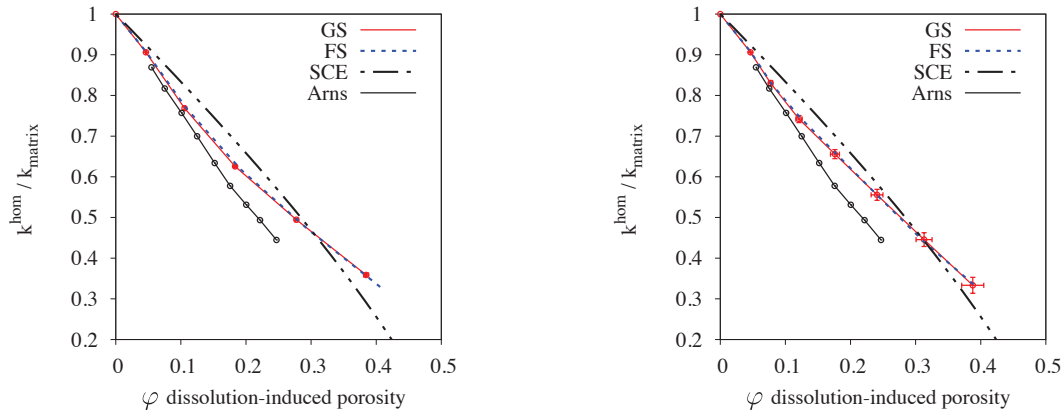
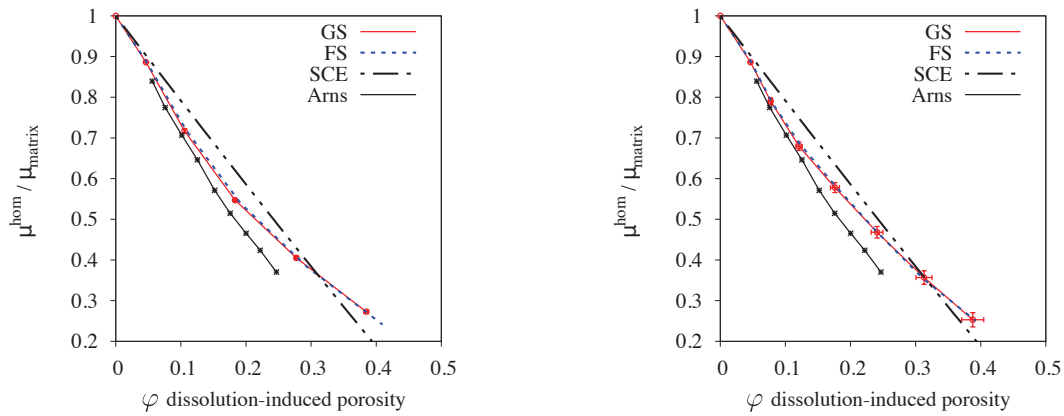


Figure 10: Visualisation de la méthodologie de calcul, de la préparation d'une microstructure jusqu'à l'estimation de son comportement effectif.





(a) normalized bulk modulus - isotropic dissolution (b) normalized bulk modulus - percolated network dissolution



(c) normalized shear modulus - isotropic dissolution (d) normalized shear modulus - percolated network dissolution

Figure 11: Evolution of normalised elastic moduli of sandstone (FS), averaged over all generated samples (GS) (with standard deviations) for both scenarii of numerical dissolution; comparison with self-consistent estimate (SCE) and with results obtained by Arns et al. [15].

## Estimation de comportement effectif - perméabilité

L'évolution de la perméabilité est estimée de manière classique en utilisant la méthode de mise à l'échelle dans la forme de la loi de Darcy. Une approche très courante, dans les simulations d'écoulement de fluide pour les milieux poreux, est utilisée. À savoir, nous utilisons un maillage cubique structuré, dont la résolution est identique à la microstructure considérée. En d'autres termes, chaque voxel est représenté par un élément de maillage (hexaèdre régulier). Afin d'obtenir des champs de vitesse, dans le domaine des pores, les simulations de la mécanique des fluides numérique sont réalisées en utilisant le logiciel OpenFOAM [87]. Dans ce logiciel, les équations de Navier-Stokes sont résolues par la méthode des volumes finis. Nous avons estimé la perméabilité en utilisant la loi de Darcy donnée par l'équation suivante :

$$K = \frac{\mu Q L}{\Delta p A}, \quad (4)$$

où  $\Delta p$  est le gradient macroscopique de pression dans la direction d'écoulement,  $Q$  le flux total,  $L$  désigne la longueur de la géométrie dans la direction d'écoulement,  $A$  la superficie de la section transversale perpendiculaire à la direction d'écoulement et  $\mu$  la viscosité dynamique.

L'augmentation significative de la perméabilité avec la porosité est une observation connue. On remarque que dans le cas de la dissolution du réseau percolé la perméabilité augmente plus rapidement en fonction de la porosité que dans le scenario de la dissolution isotrope.

Nous avons remarqué aussi que l'évolution du comportement élastique normalisé peut être lié à la perméabilité sous la forme suivante :

$$P(K) = 1 - \frac{K^\beta}{\alpha} \quad \text{et} \quad \beta \in (0, 1), \quad (5)$$

Figures 12 et 13 présentent les modules d'élasticité en fonction de la perméabilité pour le scenario de la dissolution isotrope et du réseau percolé respectivement. En général,

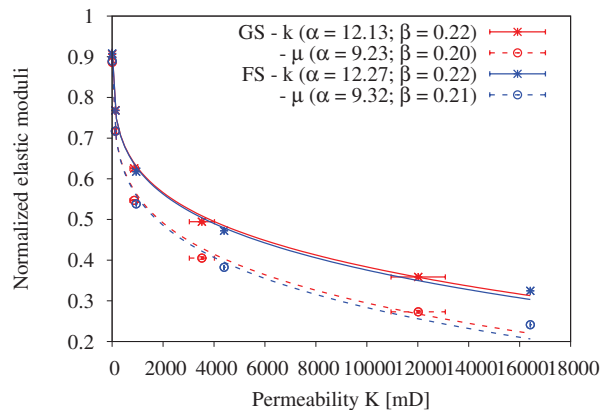


Figure 12: Des moduli élastiques en fonction de perméabilité, pour le grès (FS) et matériaux modèle (GS). Dissolution isotrope.

nous pouvons dire que la méthode de reconstruction proposée, basée sur la reconstruction

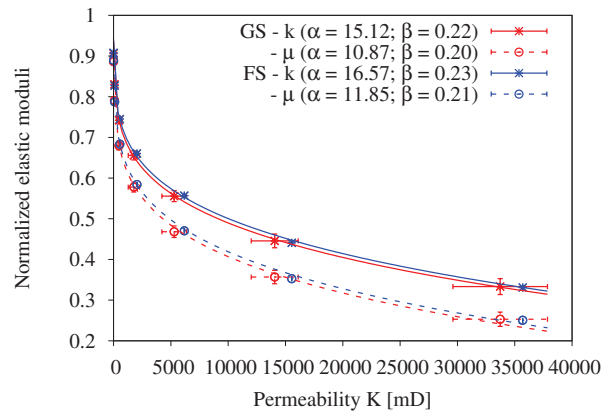


Figure 13: Des moduli élastiques en fonction de perméabilité, pour le grès (FS) et matériaux modèle (GS). Dissolution du réseau.

du squelette solide est efficace aussi pour simuler la perméabilité d'échantillon représentant la microstructure d'une roche.

## Conclusions générales et quelques perspectives

L'objectif de cette thèse est d'analyser l'évolution des propriétés mécaniques et de transport effectives de roches aquifères, qui sont soumises à une dégradation progressive par attaque chimique due à la dissolution du  $\text{CO}_2$ . L'étude proposée s'appuie sur les conditions à long terme et en champ lointain, lorsque la dégradation de la matrice poreuse peut être supposée homogène à l'échelle de l'échantillon. Afin d'effectuer la modélisation les hypothèses suivantes ont été appliquées :

- **characterisation à l'échelle micro** est effectuée directement sur la microtomographie et les équations des phénomènes considérés sont résolues à cette échelle,
- **evolution de microstructure** est représentée par dissolution numérique, au travers deux scenarii différents pour tenir compte résolution finie de microtomographie,
- **modélisation de deux échelles et la périodicité** microstructures obtenues sont supposées être représentatives; les méthodes de techniques de changement d'échelle peuvent être utilisées pour obtenir des comportements effectifs.

### Conclusions

Tout d'abord, une méthode de reconstruction inspirée du processus naturel de formation des grès est développée afin d'obtenir des représentations statistiquement équivalentes à de véritables échantillons. Les échantillons générés sont sélectionnés afin de satisfaire les informations morphologiques extraites de l'analyse des images microtomographiques d'échantillons de roche naturelle. Une méthodologie afin d'estimer les propriétés mécaniques équivalentes des échantillons générés, fondées directement sur des maillages réguliers considérés comme images binaires, est présentée. Le comportement mécanique équivalent est obtenu dans le cadre de l'homogénéisation périodique. Ensuite, l'évolution de la perméabilité est estimée de manière classique en utilisant la méthode de mise à l'échelle dans la forme de la loi de Darcy. Enfin, la dissolution chimique du matériau est abordée par dilatation morphologique de la phase poreuse. De plus, une analyse détaillée de l'évolution des descripteurs morphologiques liée aux modifications de la microstructure lors des étapes de dissolution est présentée. La relation entre les propriétés morphologiques - perméabilité - modules d'élasticité est également fournie. La méthodologie développée dans ce travail pourra être facilement appliquée à d'autres classes de matériaux hétérogènes.

### Perspectives

Une première étude peut être serait de valider expérimentalement les estimations obtenues par ce modèle aussi bien sur le plan mécanique que sur le plan de la perméabilité. Une autre piste d'étude serait d'améliorer les estimations en utilisant des maillages plus fin et ou des stratégies différentes.



# Contents

<b>Résumé</b>	<b>v</b>
<b>1 Introduction</b>	<b>1</b>
<b>2 Literature review</b>	<b>5</b>
2.1 Mathematical morphology and morphological descriptors . . . . .	7
2.1.1 Mathematical morphology . . . . .	7
2.1.2 Morphological descriptors . . . . .	11
2.2 Effective behaviour: elasticity and permeability . . . . .	24
2.2.1 About homogenisation . . . . .	24
2.2.2 Periodic homogenisation method for linear elasticity . . . . .	25
2.2.3 RVE's size estimation . . . . .	26
2.2.4 Influence of the discretization on the effective elastic behaviour es- timation . . . . .	28
2.2.5 Upscaling Stoke's equation - Darcy's law . . . . .	29
2.3 Chemical degradation . . . . .	32
2.4 Structure of the thesis . . . . .	33
<b>3 Limestone - RVE reconstruction by reflectional symmetry</b>	<b>35</b>
3.1 Introduction . . . . .	37
3.2 Microstructure and numerical dissolution . . . . .	38
3.2.1 Limestone - reference geometry . . . . .	38
3.2.2 Sample preparation . . . . .	38
3.2.3 Numerical dissolution . . . . .	40
3.3 Numerical computations of stiffness tensor . . . . .	41
3.3.1 Computations of degradation functions of material parameters . . . . .	41
3.3.2 Results . . . . .	41
3.4 Mechanical parameters versus morphological properties of the rock material	44
3.4.1 Mechanical properties versus diffusive properties . . . . .	44
3.4.2 Mechanical properties versus permeability . . . . .	46

3.5	Conclusions . . . . .	49
<b>4</b>	<b>Fontainebleau sandstone - morphology, reconstruction &amp; validation</b>	<b>51</b>
4.1	Introduction . . . . .	53
4.2	Morphological characterisation of sandstone . . . . .	54
4.2.1	Basic measures . . . . .	54
4.2.2	Number of pores per slice . . . . .	56
4.2.3	Granulometry . . . . .	57
4.2.4	Spatial distribution - covariance function . . . . .	57
4.2.5	Morphological tortuosity . . . . .	59
4.3	Reconstruction methodology . . . . .	61
4.3.1	Grain deposit . . . . .	61
4.3.2	Compaction . . . . .	62
4.3.3	Diagenesis . . . . .	64
4.3.4	Choosing the initial radius . . . . .	64
4.3.5	Choosing the compaction scenario . . . . .	68
4.3.6	Analysis of anisotropy of contacts . . . . .	68
4.4	Morphological validation . . . . .	71
4.4.1	Basic descriptors and tortuosity . . . . .	72
4.4.2	Covariance . . . . .	73
4.4.3	Granulometry . . . . .	73
4.5	Partial conclusions . . . . .	75
<b>5</b>	<b>Numerical dissolution and evolution of morphological descriptors</b>	<b>77</b>
5.1	Methodology . . . . .	79
5.2	Isotropic dissolution – morphological description . . . . .	83
5.3	Dissolution of percolated porous network . . . . .	89
5.4	Conclusions . . . . .	96
<b>6</b>	<b>Elastic behaviour modelling</b>	<b>97</b>
6.1	Introduction . . . . .	99
6.2	Methodology . . . . .	99
6.2.1	Samples preparation . . . . .	99
6.2.2	Periodisation - fixed point method . . . . .	101
6.2.3	Effective properties . . . . .	101
6.2.4	Influence of discretization on elastic moduli . . . . .	102
6.2.5	Precision of the simulations . . . . .	103
6.3	First results . . . . .	105

---

6.4	Influence of RVE size . . . . .	107
6.5	Final results . . . . .	108
6.6	Conclusions . . . . .	109
<b>7</b>	<b>Hydraulic conductivity modelling</b>	<b>111</b>
7.1	Methodology . . . . .	113
7.1.1	Samples preparation . . . . .	113
7.1.2	Solving algorithm . . . . .	113
7.1.3	Characteristic length and Reynolds number . . . . .	115
7.1.4	RVE size estimation . . . . .	116
7.2	Results . . . . .	117
7.2.1	Porosity - permeability relationships . . . . .	117
7.2.2	Tortuosity - permeability relationships . . . . .	119
7.3	Mechanical properties versus permeability . . . . .	123
7.4	Conclusions . . . . .	124
<b>8</b>	<b>General conclusions &amp; perspectives</b>	<b>125</b>
<b>A</b>	<b>Algorithms and pseudocodes</b>	<b>129</b>
A.1	Morphological operations . . . . .	129
A.2	Morphological descriptors . . . . .	130
<b>B</b>	<b>Macroscopic problem</b>	<b>133</b>
B.0.1	Solution of the macroscopic boundary problem . . . . .	135
<b>C</b>	<b>Connected component labelling</b>	<b>137</b>
	<b>Bibliography</b>	<b>141</b>






*One never notices what has been done;  
one can only see what remains to be  
done.*

Marie Skłodowska-Curie

# 1

## Introduction

he geological storage of CO<sub>2</sub>, a.k.a. Carbon Capture and Storage (CCS), is intensively investigated as a solution to reduce emission of CO<sub>2</sub> to the atmosphere. It consists in capturing carbon dioxide at source and then its injection into suitable geological formations [1]. European Union climate and energy package [16] contains directives whose purpose is to create a legal framework for CO<sub>2</sub> injection into deep geological formations and to define procedures for a safe storage that minimizes negative influence to the environment. During geological storage, certain physical and chemical mechanisms trigger irreversible changes of rock microstructure, which lead to modifications of its effective properties. In order to avoid catastrophic damages, it is essential to define geological formations behaviour. In literature, several options of underground storage [Fig. 1.1] are considered:

- depleted oil and gas reservoirs – this method is considered to be one of the most practical and advantageous. In particular, the geology of these locations is well known through an exploration process. In these formations gases and liquids have been held for million of years and due to this fact, the available capacity is considered to be very substantial and relatively reliable.
- enhanced oil recovery – by using standard extraction methods only a part of oil can be recovered from the fields. Injection of CO<sub>2</sub> can enhance oil recovery. In supercritical form carbon dioxide can easily penetrate voids of the reservoir. In contact with crude oil a part of CO<sub>2</sub> is absorbed and reduce its initial viscosity. Thereupon, the oil starts to swell and can be brought out easier by the wells.
- unmineable coal seams – the coal matrix possess a huge amount of micropores into which gas molecules of methane could be adsorbed. Due to this fact, CO<sub>2</sub> injection can enhance coal bed methane recovery (ECBM). However, permeability of coal strongly decreases with depth, what may hinder injection of carbon dioxide.

- saline aquifers – deep underground porous reservoirs located several kilometres below surface. Those formations are saturated with saline brine which is unsuitable for consumption. In general, saline aquifers are considered to possess the largest storage capacity, in comparison to the other underground locations, what makes them a well promising option for CO<sub>2</sub> storage.

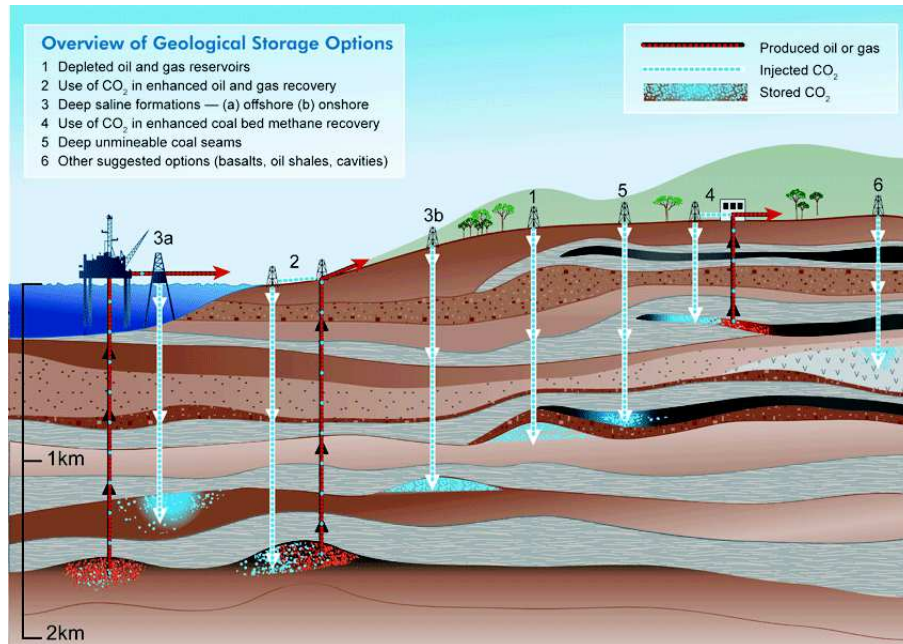


Figure 1.1: Options of geological storage of CO<sub>2</sub> <sup>1</sup>.

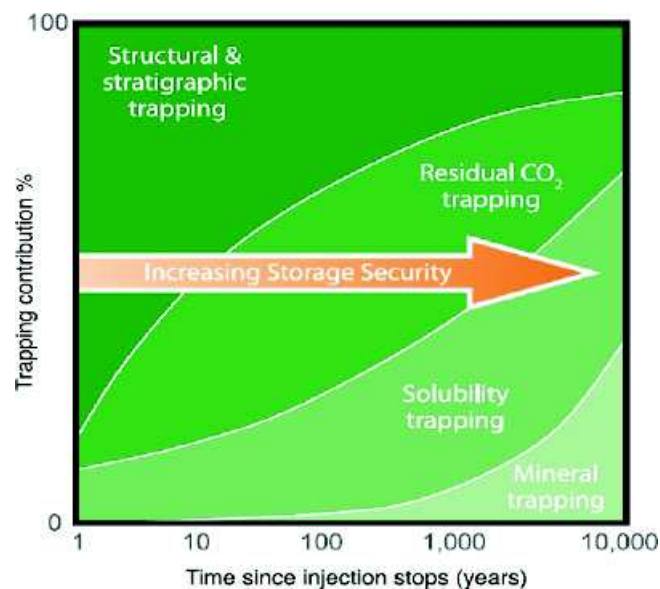


Figure 1.2: Contribution of trapping mechanisms as a function of time [1].

<sup>1</sup>source: <http://www.co2crc.com.au/aboutccs/storage.html>.

---

Effectiveness of geological storage depends on a combination of physical and geochemical trapping phenomena [Fig. 1.2]. Carbon dioxide can remain trapped underground by virtue of a number of mechanisms, such as [1]:

- structural and stratigraphic – existence of caprocks (a low-permeability rock layer), is the cardinal means to store carbon dioxide in any geological formations. Just after injection into a formation, CO<sub>2</sub> begins to move upwards, until it meets a blockade in the form of the caprock.
- residual – this mechanism comes into play very quickly after the injection. The skeleton of porous medium acts like a sponge. In supercritical state carbon dioxide is relatively non-wetting in comparison with saline brine, exists as a separate phase. During migration through the pores some part of CO<sub>2</sub> can be spontaneously disconnected and trapped by acting capillary forces.
- solubility (dissolution) - in the longer term, significant quantities of CO<sub>2</sub> dissolve in saline brine. Water containing carbon dioxide becomes heavier and then starts to migrate downward to the bottom of geological formation where it rests trapped.
- mineral – carbon dioxide can induce chemical interactions with the rock and saline water. Solubility triggers formations of ionic species, associated by a rise in the pH, what causes a chemical reaction with substances formatting the porous skeleton. The rate of reactions of the dissolved CO<sub>2</sub> highly depends on the chemical compositions of porous rock. In case of carbonate minerals, reactions proceed very quick (days), but if skeleton is composed of silicate minerals their rate is rather slow (thousands of years).

The aim of this thesis is to analyse evolution of mechanical and transport properties of saline aquifer, which is subjected to progressive chemical degradation due to CO<sub>2</sub> dissolution and acidification of the saline water. The objective is to find a link between evolving microstructure of the material, phenomena occurring at microscopic scale, and observed macroscopic behaviour. The proposed study focuses on the long-term and the far field conditions, when dissolution of porous matrix can be assumed to be homogeneous at sample scale [2, 8]. Chemical degradation of material is taken into account in a simplified way by performing numerical erosion of the microstructure. To achieve the objective, the following methodology has been proposed:

1. **statistical and morphological analysis** of real microstructure. To describe a heterogeneous material, following main morphological criteria have been used [17]: basic measures, connectivity, sizing and spatial distributions (Chapter 4).
2. **reconstruction of microstructure and morphological validation.** In this work a simple method to reconstruct a model material of sandstone is proposed and implemented. The reconstruction is inspired by nature (formation process of sandstone) and consists in two steps: deposit of grains and diagenesis process (Chapter 4).

3. **numerical dissolution** of the real image and generated samples. All the microstructures have been subjected to two different scenarii of dissolution. Evolution of chosen morphological descriptors is analysed and presented in the Chapter 5.
4. **numerical estimations** of various mechanical properties. Periodic homogenization method for linear elasticity [9] is chosen to estimate the mechanical behaviour and Darcy's law to calculate permeability [18] (Chapters 6 & 7).

The proposed methodology enables to carry out a detailed analysis about the relation between obtained morphological, statistical informations and numerical results.


*Gentleman, jokes ended, the staircase  
begins.*

Bolesław Wieniawa-Długoszowski

# 2

## Literature review

---

his chapter explores the literature that is helpful to understand the development of the methodology and to interpret the results. First of all, mathematical morphology and statistical tools, used to characterise microstructure of fontainebleau sandstone, are featured. The next subsection presents short theoretical introduction of homogenization method for linear elasticity, fluid flow in porous media and RVE estimation problem. The last subsection contains the state of art of chemical degradation problem. Finally, a short structure of the thesis is presented.

---

## Contents

---

<b>2.1</b>	<b>Mathematical morphology and morphological descriptors . . .</b>	<b>7</b>
2.1.1	Mathematical morphology . . . . .	7
2.1.2	Morphological descriptors . . . . .	11
<b>2.2</b>	<b>Effective behaviour: elasticity and permeability . . . . .</b>	<b>24</b>
2.2.1	About homogenisation . . . . .	24
2.2.2	Periodic homogenisation method for linear elasticity . . . . .	25
2.2.3	RVE's size estimation . . . . .	26
2.2.4	Influence of the discretization on the effective elastic behaviour estimation . . . . .	28
2.2.5	Upscaling Stoke's equation - Darcy's law . . . . .	29
<b>2.3</b>	<b>Chemical degradation . . . . .</b>	<b>32</b>
<b>2.4</b>	<b>Structure of the thesis . . . . .</b>	<b>33</b>

---

## 2.1 Mathematical morphology and morphological descriptors

Mathematical morphology provides clear and essential description of images by studying them in the framework of set theory. Using appropriate sets, called structuring elements, mathematical morphology can simplify image data by presenting their essential shape characteristic and eliminating irrelevances. Foundations of the theory are attributed to George Matheron [19] and Jean Serra [20] of École des Mines de Paris. Mathematical morphology has become very popular in recent years in the field of digital image processing, it is important to highlight that both of them have made a big advance in many areas of engineering, material science, medicine etc. In this study we propose to use basic concepts of mathematical morphology and statistical analysis, as a very useful tools to characterise the properties and to provide an efficient method to generate equivalent heterogeneous material. This section is written as a basic foundation course that introduces apparatus used in the thesis.

### 2.1.1 Mathematical morphology

There is a lot of possible ways to introduce the basics of the theory, for readers who would like to know more, may see [19–28]. For the purpose of this study we introduce basic concepts by using binary images. Moreover, this framework poses several advantages, it is intuitive and relatively simple. Historically, mathematical morphology has been defined for Euclidean spaces. The transformation from  $d$ -dimensional continuous space  $\mathbb{R}^d$  to discrete space  $\mathbb{Z}^d$  is called discretization or quantisation. Discrete space can be sampled by means of different kinds of grids shown in Figure 2.1. In our case, the regular square (in 2D) or cubic (in 3D) grid were used. Each point of the grid (pixel in 2D or voxel in 3D) possesses a scalar value and is referenced by its coordinates  $x, y$  and  $z$ .

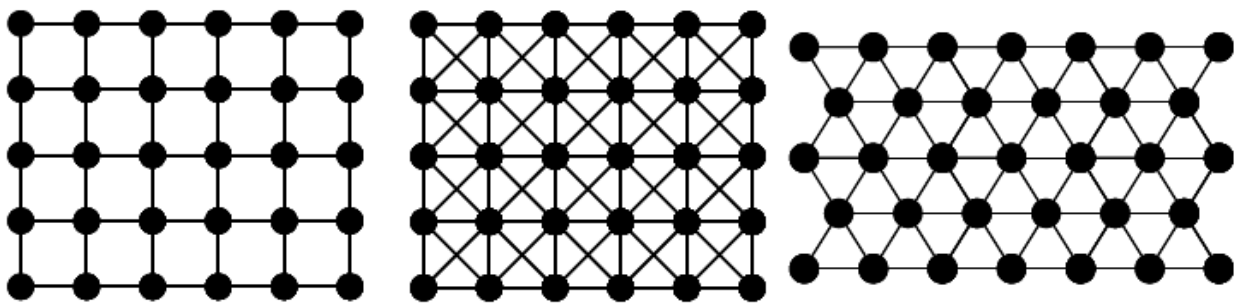


Figure 2.1: Illustration of grids and connectivities [23].

Firstly, we have to recall a definition of a binary image [22]:

**Definition 2.1** Let  $\mathbb{Z}^d$  be the  $d$ -dimensional discrete space and  $D_A \subset \mathbb{Z}^d$  is the definition domain (grid). Binary image  $A$  is a mapping

$$A : D_A \subset \mathbb{Z}^d \rightarrow \{0, 1\}. \quad (2.1)$$



In that case, to each pixel of the grid one of two possible values, 0 or 1 is assigned. Generally speaking, a binary image consist in two disjoint sets which represent two phases: 1-valued foreground, usually visualised by white colour, and 0-valued background, represented by black colour.

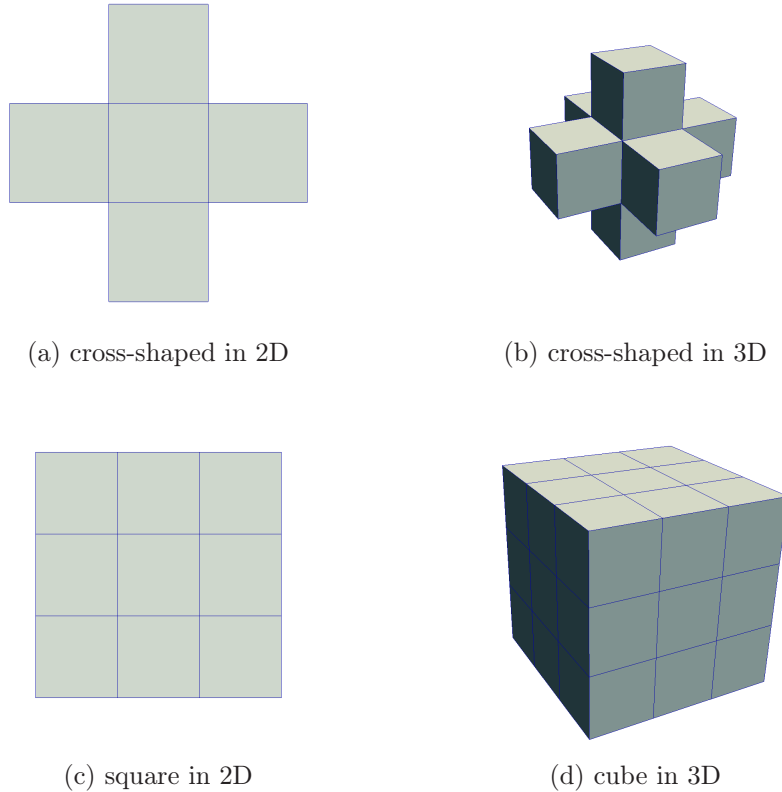


Figure 2.2: Examples of isotropic, symmetric structuring elements on regular grids.

In general, morphological operations describe interactions between an image and a structuring element hence provide useful tools to measure the size of objects and to describe their shapes. The two most basics operations, of mathematical morphology, are dilation and erosion [19]. They have a wide array of uses, for example: removing noise, isolation or joining elements in an image.

The structuring element is itself a binary image, subset of the grid [Fig. 2.2]. Its shape, size and orientation can be adapted to our needs. Structuring element can also define the connectivity of the grid and plays a important role in the theory. Figure 2.2 (a) and (c) present structuring elements which are symmetric, they can be described in following way:

- cross-shaped:  $B = \{(-1, 0), (0, -1), (0, 0), (0, 1), (1, 0)\}$ ,
- square:  $B = \{(-1, -1), (-1, 0), (-1, 1), (0, -1), (0, 0), (0, 1), (1, -1), (1, 0), (1, 1)\}$ .

Pixel localised in point  $(0, 0)$  is the origin of the structuring element and the rest is called neighbourhood. Of course structuring element does not have to be symmetric, we can use, for example,  $B = \{(0, 0), (1, 0)\}$ .

Before we go further, we introduce a notation that is helpful to explain and understand the effects of basic operations. Let  $X$  be an arbitrary set,  $X_p$  is its translation by a vector  $p \in \mathbb{Z}^d$ , we can write:

$$X_p = \{x + p \mid x \in X\}. \quad (2.2)$$

A complement of  $X$ , denoted by  $X^c$ , is given as follows:

$$X^c = \{x \in \mathbb{Z}^d \mid x \notin X\}. \quad (2.3)$$

A symmetrical set to  $X$ , with respect to the origin, is denoted by  $\check{X}$  and can be given in following form:

$$\check{X} = \{x \mid b \in X, x = -b\}. \quad (2.4)$$

Let us recall definitions of dilation and erosion.

**Definition 2.2** *The dilation of  $X$  by structuring element  $B$  is given by:*

$$\delta_B(X) = X \oplus B = \{x \in \mathbb{Z}^d \mid \check{B}_x \cap X \neq \emptyset\} = \{x + b \mid x \in X, b \in B\}. \quad (2.5)$$

**Definition 2.3** *The erosion of  $X$  by structuring element  $B$  is given by:*

$$\epsilon_B(X) = X \ominus B = \{x \in X \mid B_x \subseteq X\} = \{x \in X \mid x + b \in X, b \in B\}. \quad (2.6)$$

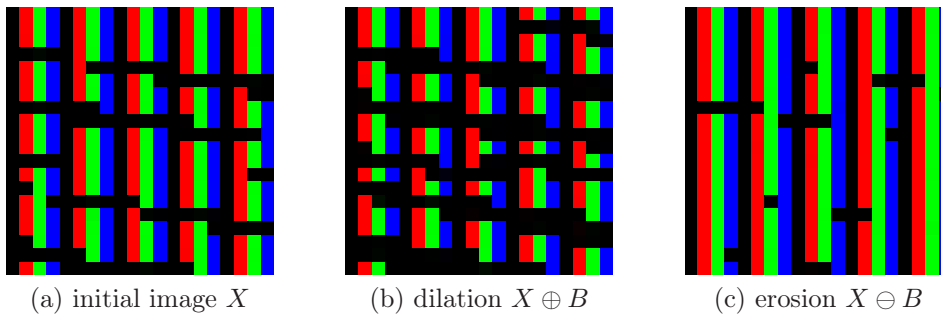


Figure 2.3: Effects of erosion and dilation, by using the  $3 \times 3$  square structuring elements.

We can remark that dilation enlarges white phase of binary image while erosion has the opposite effect [Fig. 2.3 & 2.5]. We can notice that dilation is the dual operation to the erosion, what can be written as follows:

$$(X \ominus B)^c = X^c \oplus \check{B}. \quad (2.7)$$

If the structuring element is symmetric, equation 2.7 can be written in following way:

$$(X \ominus B)^c = X^c \oplus B. \quad (2.8)$$

In other words, to obtain the eroded set  $X$  we can apply dilation on the complement of  $X$  and, after all, we take the complement of  $X^c \oplus B$ . This procedure is illustrated in Figure 2.4. An implementation of dilation and erosion, used in the thesis and applied on 3D binary image, is presented by Pseudocodes A.2 and A.3 in Annexe A.

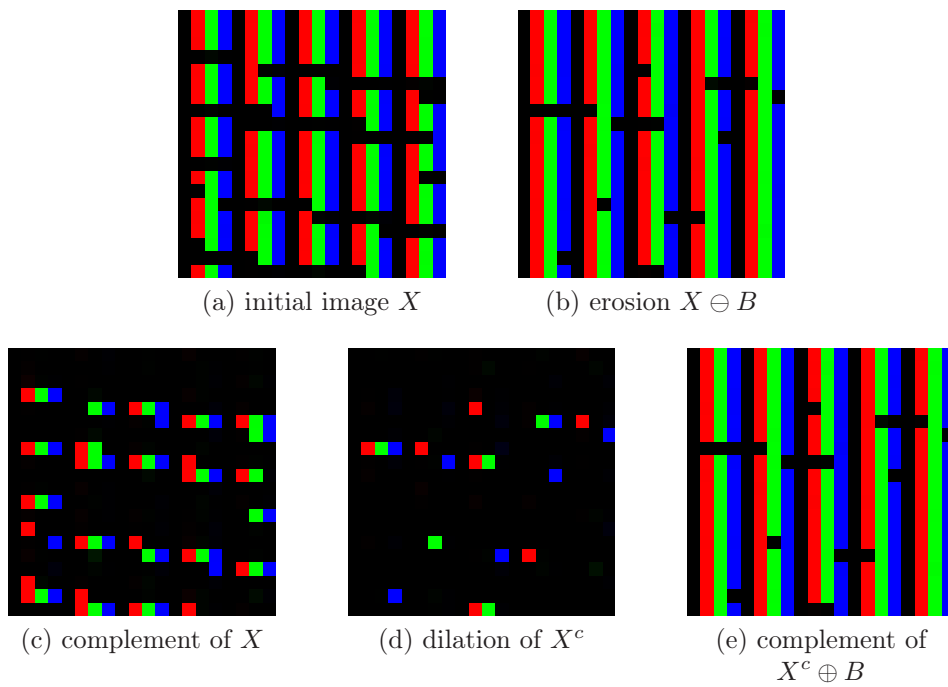


Figure 2.4: Visualisation of duality between erosion and dilation.

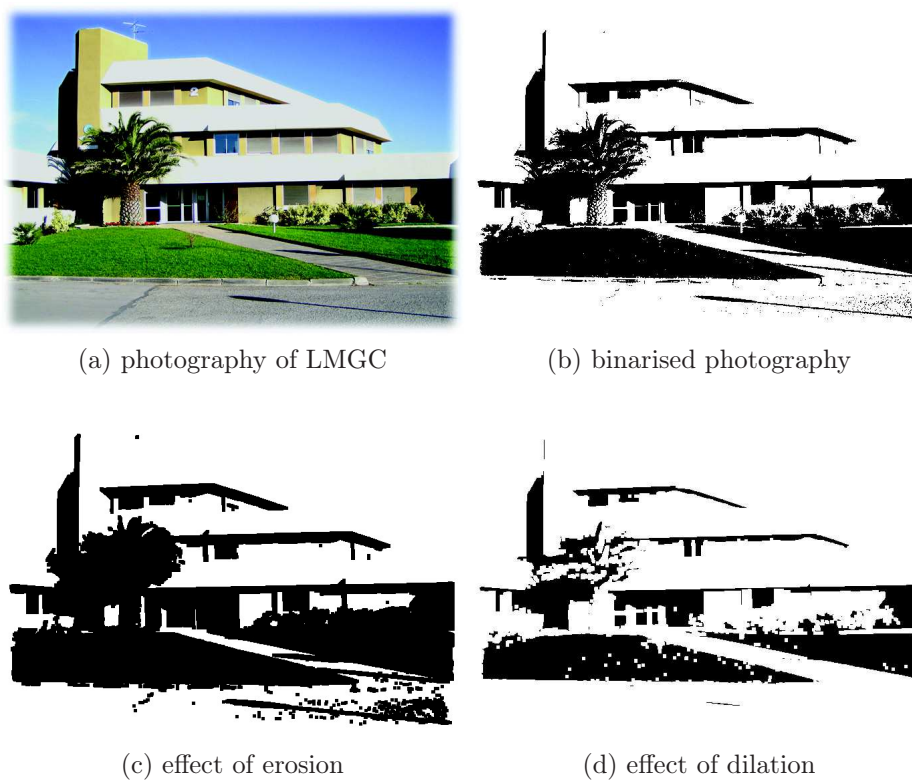


Figure 2.5: Effects of erosion and dilation, by using the  $5 \times 5$  square structuring elements.

Other operations, that play important role in the theory, are opening and closing. In digital image analysis, those two operations, are the workhorse of morphological noise removal and filtering. We start with the definition of opening.

**Definition 2.4** *The set  $X$  opened by structuring element  $B$  is given by:*

$$X \circ B = (X \ominus B) \oplus B. \quad (2.9)$$

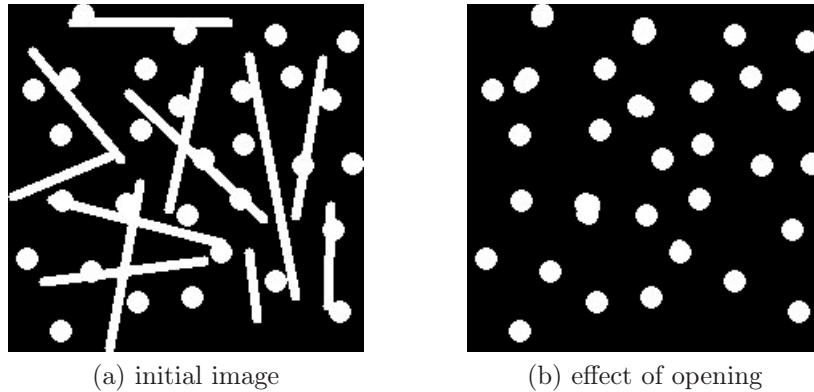


Figure 2.6: Effects of opening, by using disk shaped structuring element of 11 pixels in diameter.<sup>1</sup> Size of images is  $222 \times 217$  px. Sticks possess thickens of 6 pixels, while diameter of circles is 14 px.

Generally speaking, opening consist of dilation that is followed by erosion. It removes certain objects of the foreground and places them in the background. In other words, opening acts like a filter, result of this operation depends strictly on the shape and size of structuring elements [Fig. 2.6]. Closing is defined in following way:

**Definition 2.5** *The set  $X$  closed by structuring element  $B$  is given by:*

$$X \bullet B = (X \oplus B) \ominus B. \quad (2.10)$$

After performing closing on image, small objects from background are moved to foreground [Fig. 2.7]. Like in case of opening, result depends on the structuring element, that was used to perform the operation. Closing and opening are satisfying duality, what can be written in following form:

$$X \bullet B = (X^c \circ \check{B})^c. \quad (2.11)$$

### 2.1.2 Morphological descriptors

**Porosity**  $\varphi$  is one of the most basic global descriptor of porous media. It is defined as a ratio of the volume of the pore space  $V_p$  to the total volume of a sample  $V_{total}$ , what can be written as follows:

$$\varphi = \frac{V_p}{V_{total}} = \frac{V_p}{V_p + V_s} = 1 - \frac{V_s}{V_p + V_s}, \quad (2.12)$$

<sup>1</sup>source: <http://homepages.inf.ed.ac.uk/rbf/HIPR2/open.htm>

<sup>2</sup>source: <http://homepages.inf.ed.ac.uk/rbf/HIPR2/close.htm>

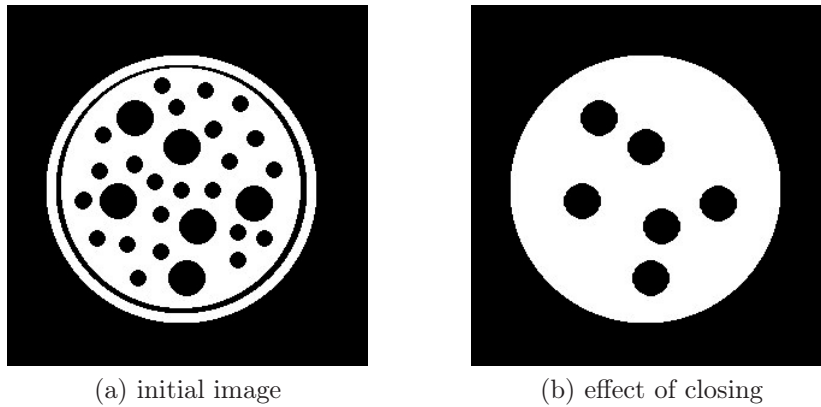


Figure 2.7: Effects of closing, by using disk shaped structuring element of diameter equal to 22 px. Diameter of larger inclusions is 31 px while smaller ones is 14 px.<sup>2</sup> Size of the image is 300×300 px.

where  $V_s$  denotes the volume of the solid phase. Measurement of porosity, adapted to binarized media and used in the thesis, is presented by Pseudocode A.4 in Annexe A. In the field of porous media theory we have to distinguish between two main types of porosities [18, 29]. The first kind is a so-called interconnected or effective porosity which forms percolated/percolating pore network. The second one is the isolated or non-interconnected porosity. Let  $\varphi_{eff}$  and  $\varphi_{iso}$  denote effective and isolated porosity respectively. We can write, that:

$$\varphi_{eff} = \varphi - \varphi_{iso}. \quad (2.13)$$

From the point of view of transport properties like diffusion or fluid conductivity isolated pores are irrelevant (they can not be penetrated) hence, it is important to consider only the effective porous space to estimate their values. In the literature we can find also 'dead-end' and 'blind' pores [Fig. 2.8], which are interconnected from one side. However, their impact on the mass transport properties is relatively small. In this work all pores of type  $d$  will be treated as the isolated ones [Fig. 2.8]. To extract the interconnected pores (percolated porous network) Connected Components Labelling algorithm was implemented [25, 30]. The program scans an image and groups its pixels into components shearing the same value (label) if they are connected. The central role is played by definition of pixels connectivity, which can be represented by an arbitrary structuring element. To illustrate the method, geometry presented in Figure 2.8 is subjected to Connected Components Labelling algorithm. In Figure 2.9 we can see 6 separated pores having different labels, which were visualised by different colours. For the purpose of this study, the cross-shaped element [Fig. 2.2 (b)] has been chosen to analyse connectivity of 3D structures. Figure 2.10 shows the result of the algorithm, which was applied to the microtomography of Fontainebleau sandstone.

**Specific surface** [18, 29] has an important influence to a variety of physico-chemical properties of the medium like, for example, adsorption capacity, heat transfer and fluid conductivity. Specific surface can be defined as ratio of the measure of interstitial surface of pores to the total volume of the investigated sample. Let us denote the specific surface

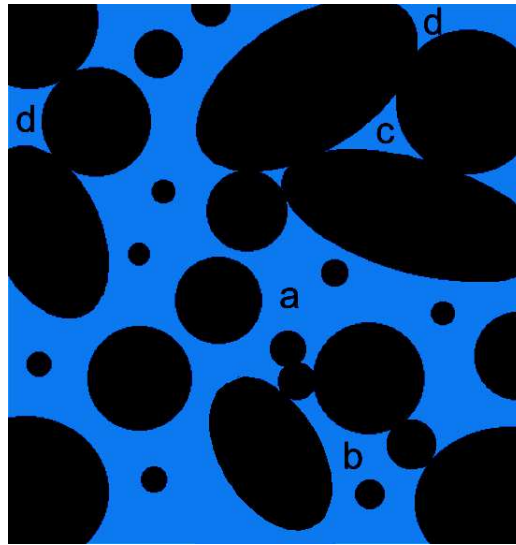


Figure 2.8: Different types of pores: a – interconnected; b - blind; c – isolated; d - open.

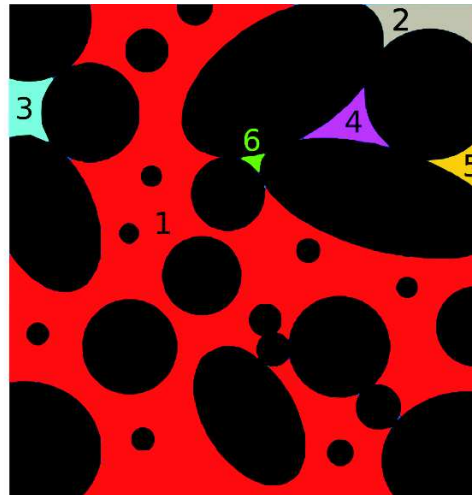


Figure 2.9: Visualisation of CCL algorithm effect.

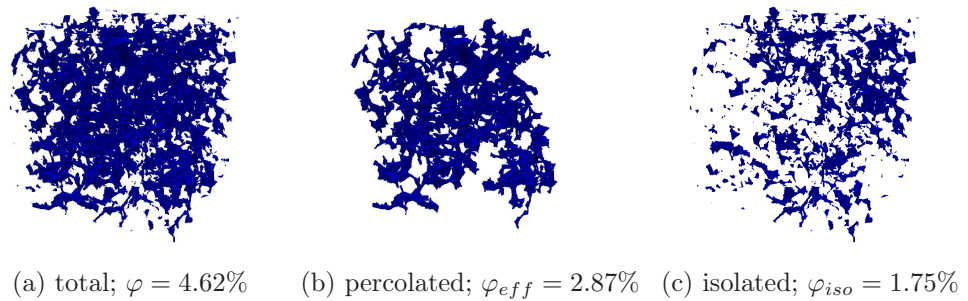


Figure 2.10: Visualisation of Fontainebleau sandstone (FS) microstructure.

as  $S_t$ , we can write:

$$S_t = \frac{S(\varphi)}{V_{total}}, \quad (2.14)$$

where  $V_{total}$  is a volume of the sample and  $S(\varphi)$  is the interstitial surface of the pores. Making the direct link with main types of porosity, we can define effective specific surface  $S_{eff}$  and the isolated one  $S_{iso}$ . It can be written as follows:

$$S_{eff} = \frac{S(\varphi_{eff})}{V_{total}}, \quad (2.15)$$

$$S_{iso} = \frac{S(\varphi_{iso})}{V_{total}} = S_t - S_{eff}, \quad (2.16)$$

where  $S(\varphi_{eff})$  and  $S(\varphi_{iso})$  is the interstitial surface of the interconnected and isolated pores respectively.

Specific surface can be estimated directly by analysing binary image of the medium, pixel by pixel. For this purpose for each pixel of porous phase its neighbourhood is scanned by using cross-shaped structuring element [Fig. 2.2 (b)]. If any component of structuring element is located in opposite (solid) phase the value of specific surface counter  $\tilde{S}_t$  increase by 1, after all counter is divided by the total volume (in 3D). The method is presented by Pseudocode A.5 Annexe A. It is very well known that discretization of the image induce an overestimated value for the measure of the specific surface. However, in our study the relative changes of the parameter are much more important than the value itself. Figure

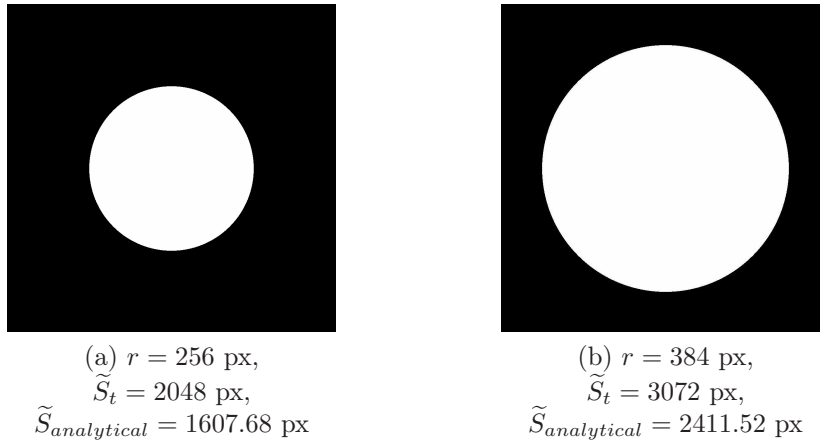


Figure 2.11: Estimation of specific surface counters of circle in relation to radii increase.

2.11 presents an estimation of specific surface counters  $\tilde{S}_t$  of a circle for two different values of radius. In case presented in Figure 2.11, we can notice, that relative change of specific surface is the same for both examples – calculated  $\tilde{S}_t$  and analytical one  $\tilde{S}_{analytical}$  – and is equal to 0.5. Value of  $\tilde{S}_{analytical}$  is given by equation:

$$\tilde{S}_{analytical} = 2\pi r. \quad (2.17)$$

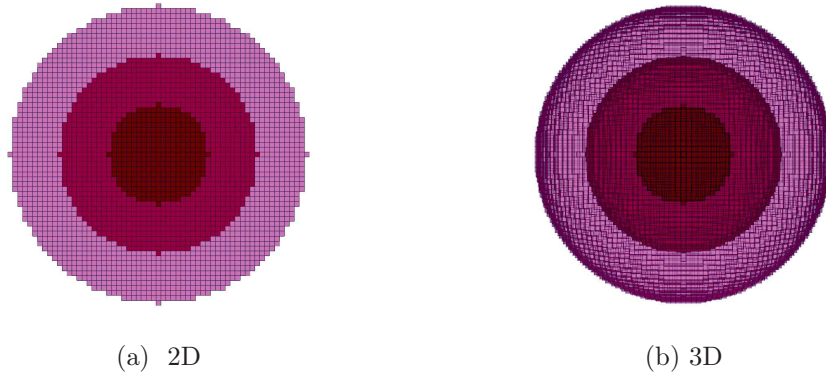


Figure 2.12: Structuring elements of radii  $r \in \{10, 20, 30\}$  px, representing binarized spheres.

**Granulometric curve** describe well investigated media and give an idea of the characteristic size of the underlying granular structure. Polydispersity is characterised by the proportions of particles having different sizes - radii or diameters. Depending on a method of estimation, polydispersity can be presented by the number  $n(r)$  or the volume  $g(r)$  of particles as a function of their size  $r$ . Mathematical morphology allows us to measure particle size, with respect to their volume, by morphological opening [20, 22, 23, 31]. The principle of the method consists in performing morphological openings on the investigated phase of a microstructure and in successive increasing the structuring element's size. After each operation, the change of solid volume fraction is calculated. It is obvious that the central role in this methodology is played by the shape of used structuring element. Let  $B$  be a structuring element, and  $B_r$ ,  $r = 0, 1, \dots$ , is a family of structuring elements where,  $r$  has a notion of characteristic length. Let  $X$  be a set (binary image), the granulometric function  $G_r(X)$  is given by:

$$G_r(X) = 1 - \frac{|X \circ B_r|}{|X|}, \quad (2.18)$$

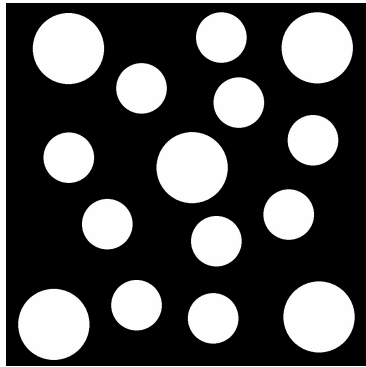
where symbol  $|\cdot|$  denotes the measure (cardinality) of a set. By using such defined granulometric function we have to notice that we estimate cumulative particle size distribution with respect to the volume. Volumetric size distribution is defined in following way:

$$g_r(X) = G_{r+1}(X) - G_r(X), \quad (2.19)$$

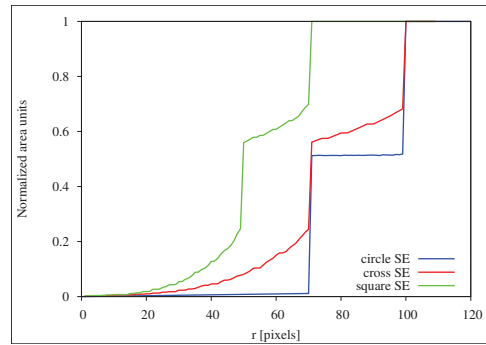
Figures 2.13 and 2.14 present granulometric function obtained for different shapes of structuring elements. It is important to notice that the shape has a direct influence on the results. If the shape of the structuring element does not corresponds to the geometry of investigated set the results could be encumbered with significant error. Missing of shape may change main characteristics of grain size distribution - its mean, median, extremities and standard deviation.

Therefore, for the purpose of the thesis binarized sphere and cross - shaped element are used to characterise granulometry of solid matrix.



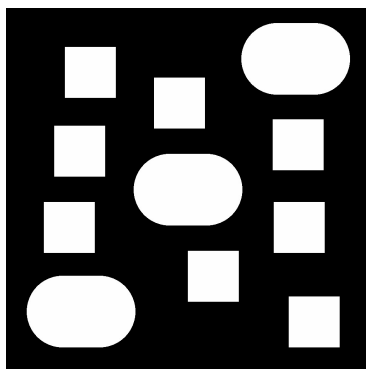


(a)

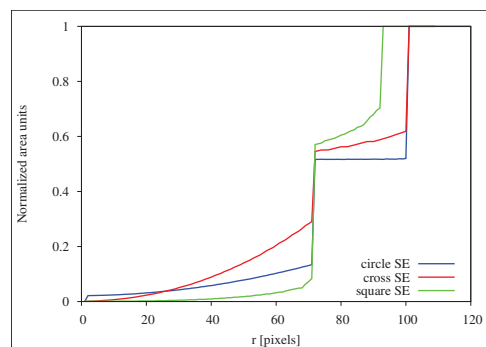


(b)

Figure 2.13: Granulometric function of two population of discs of diameters  $d_1 = 143$  px and  $d_2 = 201$ . Both populations poses the same volume fraction.



(a)



(b)

Figure 2.14: Granulometric function of two populations: squares of edge length  $a = 143$  px and overlapping circles of diameter  $d = 201$ . Both populations possess the same volume fraction.

**Covariance function and covariogram** [3, 24, 32] are used to describe spatial distribution of phase of microstructure and other useful characteristics of investigated structure. In the framework of set theory, binary image consist in two sets (phases). We can assume that a binary image representing heterogeneous medium is one of the possible realisations generated by a specific stochastic process [24, 32]. The domain of the porous medium consist of two disjoint sets (phases), solid  $X_s$  and porous one  $X_p$ . We can write as follows:

$$X_s \cap X_p = \emptyset. \quad (2.20)$$

For example, porous phase can be described by the characteristic or indicator function. It is defined by the following equation:

$$k_p(x) = \begin{cases} 1 & \text{if } x \in X_p \\ 0 & \text{if } x \notin X_p \end{cases}, \quad (2.21)$$

analogically we can define  $k_s$ . Each phase, solid and porous, possesses its volume fraction  $\varphi_s$  and  $\varphi$  respectively. What can be written as:

$$\varphi = \langle k_p(x) \rangle, \quad (2.22)$$

$$\varphi_s = \langle k_s(x) \rangle, \quad (2.23)$$

where  $\langle \cdot \rangle$  denotes volume average, given by:

$$\langle \cdot \rangle = \frac{1}{|V|} \int_V \cdot \, dV \quad (2.24)$$

It is easy to note, that:

$$k_p(x) + k_s(x) = 1. \quad (2.25)$$

Among statistical descriptors, the covariogram is a convenient tool to investigate stationary and ergodic media<sup>3</sup>. It characterises geometrical dispersion of the set representing a phase of a binary image. To simplify notation, let  $X$  denotes porous or solid phase. The covariogram  $K(X, \vec{h})$  is a measure of the intersection of set  $X$  and its translation by vector  $\vec{h}$  [Fig. 2.15], we may write (where  $k = k_p$  for the covariogram of porous phase and  $k = k_s$  for the covariogram of solid phase):

$$K(X, \vec{h}) = K(\vec{h}) = \mu(X \cap X_{-\vec{h}}) = \int_{\mathbb{R}^d} k(x)k(x + \vec{h})dx \quad \vec{h} \in \mathbb{R}^d, \quad (2.26)$$

where  $\mu(\cdot)$  denotes a measure. Covariogram possesses following properties:

$$\left\{ \begin{array}{l} K(\vec{0}) = \int_{\mathbb{R}^d} k(x)^2 dx = \mu(X), \\ K(\vec{h}) = K(-\vec{h}), \\ \int_{\mathbb{R}^d} K(\vec{h}) d\vec{h} = \left[ \int_{\mathbb{R}^d} k(x) dx \right]^2 = [\mu(X)]^2, \\ \lim_{\|\vec{h}\| \rightarrow \infty} K(\vec{h}) = 0. \end{array} \right. \quad (2.27)$$

---

<sup>3</sup>ergodic system possesses the same behaviour averaged over time as averaged over the space for each state of the system

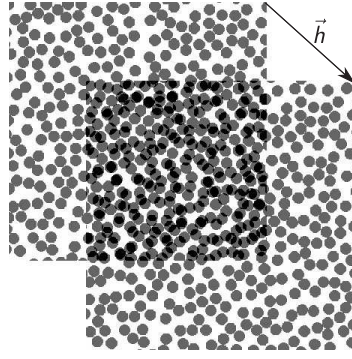


Figure 2.15: Surface area of black region is the graphical representation of  $K(X, \vec{h})$  for a given vector  $\vec{h}$ .

Probabilistic interpretation of covariogram is covariance function denoted by  $C(X, \vec{h})$ . It is a two-point probability function, which returns the value of probability that two points  $x$  and  $x + \vec{h}$  belong to the set  $X$ . We may define this function as follows:

$$C(X, \vec{h}) = P \left\{ x \in X, x + \vec{h} \in X \right\}. \quad (2.28)$$

In order to link covariance function with covariogram, we can write:

$$C(X, \vec{h}) = E \left\{ K(X, \vec{h}) \right\} = E \left\{ \int_{\mathbb{R}^d} k(x)k(x + \vec{h})dx \right\}, \quad (2.29)$$

where  $E \{ \cdot \}$  means the expected value. In case of isotropic media, values of covariogram and covariance are invariant to the direction of the translation vector  $\vec{h}$ . It can be easily examined by plotting covariance function for different directions. From this point of view, covariance is an interesting tool to investigate anisotropy of the medium. Covariance function provides a number of interesting information, concerning geometrical structure of investigated medium:

- the value of  $\|\vec{h}\|$  at which  $C(X, \vec{h}) = \varphi^2(X)$  is the covariance range (which is denoted in this work as  $A_3$  and  $\varphi(X)$  denotes volume fraction of considered phase), this distance gives an information about points correlations, over this distance two points can be considered as non-correlated (independent)
- the first local minimum of  $C(X, \vec{h})$ , if exists, has a notion of characteristic length between inclusions, it is so-called repulsion distance (denoted as  $\delta$ ),
- if  $C(X, \vec{h})$ , does not converge to its theoretical asymptotic value  $\varphi^2(X)$  we can assume that the chosen scale is too small, does not contain sufficiently enough statistical information of the medium, or that the medium has a long-distance interactions and does not verify the hypothesis of stationarity assumption,
- the periodicity of  $C(X, \vec{h})$  implies the periodicity of the microstructure and vice versa,

- the slope for all orientations of vector  $\vec{h}$  is proportional to the specific surface of the phase  $S_t \propto \int_0^{4\pi} \left[ \frac{\partial C(h, \theta)}{\partial h} \right]_{h=0} d\theta$ .

As we said before, covariance function should be calculated for all possible directions of vector  $\vec{h}$ . One of the solution is to use discrete Fourier transform (DFT). This choice seems to be natural, since eq. 2.29 presents convolution of characteristic function with itself. In practice, we apply a series of DFT operations on a binary image X, according to the equation:

$$\tilde{C}(X) = F^{-1} (|F(X)|^2), \tag{2.30}$$

where  $|\cdot|$  stands for absolute value, we obtain the map in grey level values -  $\tilde{C}(X)$ . Therefore, the  $\tilde{C}(X)$  should be correlated to satisfy following properties:

$$\begin{cases} C(\vec{0}) = \varphi(X), \\ C(\vec{h}) = C(-\vec{h}) \leq C(\vec{0}), \\ \lim_{\|\vec{h}\| \rightarrow \infty} C(\vec{h}) = [\varphi(X)]^2. \end{cases} \tag{2.31}$$

In order to achieve the goal, we measure the maximum of grey level value in region  $\Omega_1$  and

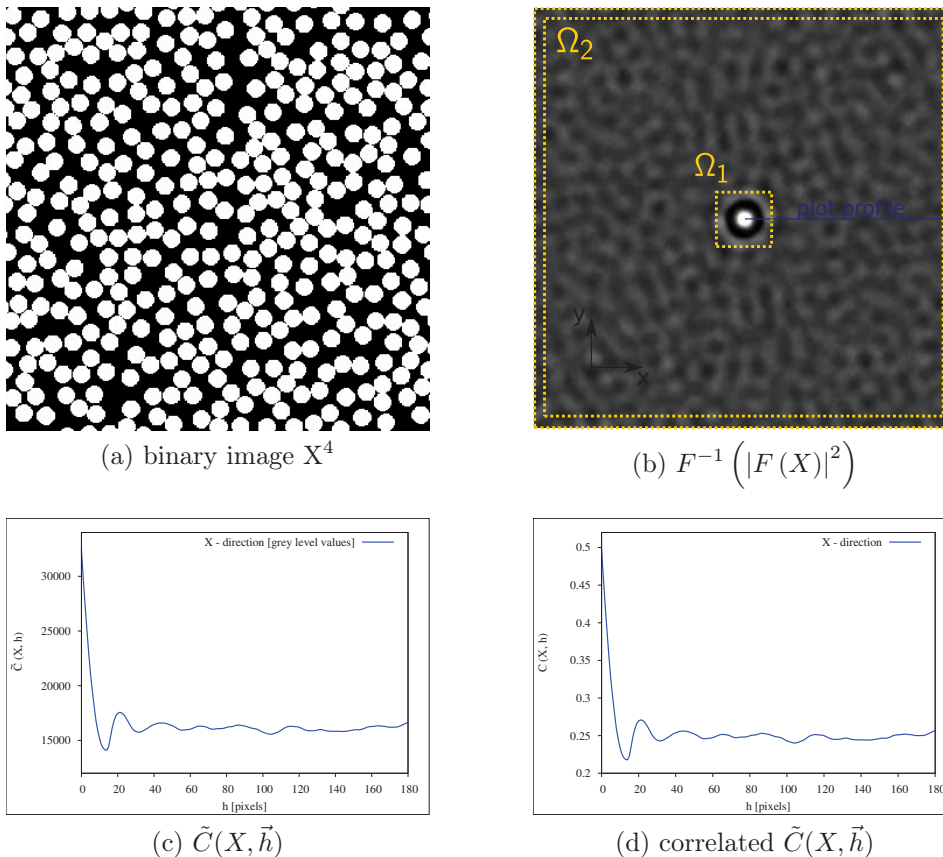


Figure 2.16: Microstructure and its covariance functions

the mean value of the domain  $\Omega_2$  which correspond to  $\varphi(X)$  and to  $\varphi^2(X)$  respectively.

<sup>4</sup>source: <http://ciks.cbt.nist.gov/garbocz/paper19/node2.html>.

Finally, by using this linear correlation, each point of the domain possess a value in range  $[0, \varphi(X)]$ . This method is summarised in Algorithm A.7 and illustrated in the Figure 2.16.

**Morphological tortuosity** is one of the measurements which characterises complexity of porous network. Like covariance function it is an inartistically three-dimensional function and can not be obtained from slices. This parameter has a significant influence to transport properties.

In order to define tortuosity, let us begin with a definition of the geodesic distance [22, 33, 34]. We consider two points  $x, y$  which belong to a set  $X$ . The length of the shortest curve, which connects this two points and remains in the set  $X$ , is called the geodesic distance. Let  $L(c)$  be the length of the curve  $c = (c_1, c_2, \dots, c_n)$ , where  $c_i$  is the  $i^{th}$  element of the curve, a pixel in our case. Thus, by recalling the definition proposed by [22, 33], we can write:

$$D_{geo}(x, y) = \min \{L(c) | c_1 = x, c_n = y\}, \quad (2.32)$$

In the next step of the methodology we have to consider two disjoint sets  $A$  and  $B$  that will play a role of a source of propagation. The geodesic distance between a point  $x \in X$  and a subset  $A$  is defined by following equation [Soille (2003)]:

$$D_{geo}(x, A) = \min \{D_{geo}(x, y) | x \in X, y \in A\}, \quad (2.33)$$

In order to define tortuosity of a medium we have to consider that sources  $A$  and  $B$  are placed in the opposite boundaries of the investigated geometry [Fig. 2.19]. Let  $D_{AB}$  denotes the euclidean distance between the sources. Morphological tortuosity for each point  $x \in X$  is defined as follows:

$$\tau_{AB}(x) = \frac{D_{geo}(x, A) + D_{geo}(x, B)}{D_{AB}}, \quad (2.34)$$

In order to obtain a spatial distribution of morphological tortuosity we used the method proposed by Decker et al. [35]:

1. determination of geodesic distance map to the set  $A - D_{geo}(x, A)$
2. determination of geodesic distance map to the set  $B - D_{geo}(x, B)$
3. conditional sum of two maps -  $\forall_{x \in X} \tau'_{AB}(x) = D_{geo}(x, A) + D_{geo}(x, B)$   
if  $D_{geo}(x, A) \wedge D_{geo}(x, B) \neq 0$ , else  $\tau'_{AB}(x) = 0$
4. normalisation by the euclidean distance -  $\tau_{AB}(x) = \tau'_{AB}(x)/D_{AB}$ .

Since we are analysing digitised images of a real material, we can compute tortuosity by using geodesic dilations. In this method the shape of the structuring element, used to estimate the geodesic distance maps, has a direct influence on the morphological tortuosity. It was showed by Peyrega et al. [36], that the structuring elements like squares (2D) or cubes (3D) are irrelevant to estimate the morphological tortuosity. The solution is to use discretised disc and spheres in 2D and 3D respectively. The fast marching method as a numerical, iterative method to solve eikonal equation, was proposed by Sethian [37].

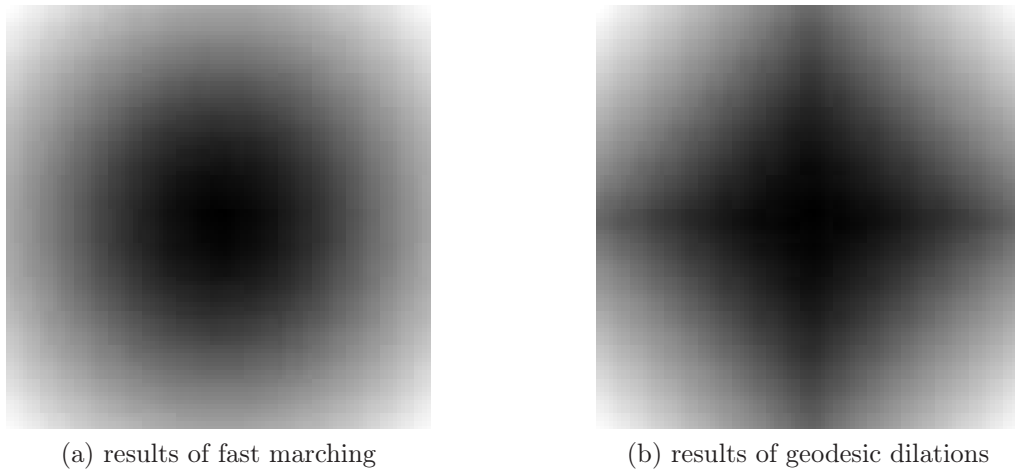


Figure 2.17: Map of distances calculated by two methods: solving eikonal equation by fast marching and geodesic dilation (cross-shaped structuring element). For both cases the source is located in the centre of the image. Grey scale colours represent arrival times (distance) from the centre of the image to each pixel. Brightness increase with the distance.

Figure 2.17 shows the differences between geodesic distance maps calculated by two methods (fast marching and geodesic dilation). Generally speaking, the equation describes a wavefront propagation and is given as follows:

$$\|\nabla T(x)\| = \frac{1}{f(x)}, \quad (2.35)$$

where  $T(x)$  is the arrival time of a wavefront propagating with speed  $f(x)$  at point  $x \in X$ . The method and algorithm are explained and presented by Sethian [37]. In our case the speed will be equal to 1 (propagation of one pixel per iteration), it means that arrival time  $T(x)$  returns the value corresponding to a distance. The result of the method is a maps of pixels possessing a values corresponding to the length of the shortest path containing  $x$  and connecting two disjoint sets  $A$  and  $B$ .

To illustrate the method we will use the contour map of France, for the purpose of the explanation the localisation of Corsica was changed [Fig. 2.18 (a)]. At the first step we placed the set  $A$  on the upper boundary and started to solve eikonal equation by fast marching method. For the sake of clarity, part of images, where the wave is not propagating, is coloured in green. Figure 2.19 shows the evolution of arrival times calculated for the image (in the image dark colour corresponds to short arrival times and red one area where the wave has not arrived yet). As a result we obtained the map of arrival times (geodesic distance map) from the source [Fig. 2.21 (a)]. We can clearly see how the wavefront is propagating and that the wavefront has not arrived to Corsica, which is unconnected. The next step is analogical, the only difference is localisation of the set  $B$  [Fig. 2.21 (b)]. Figure 2.20 presents propagation of the wavefront in this case. Since we have two maps of distances we perform the conditional addition, described in the algorithm. After all, we have to divide obtained values by the euclidean distance between sources. Figure 2.22 shows the results of the methodology. It is easy to notice that the results are

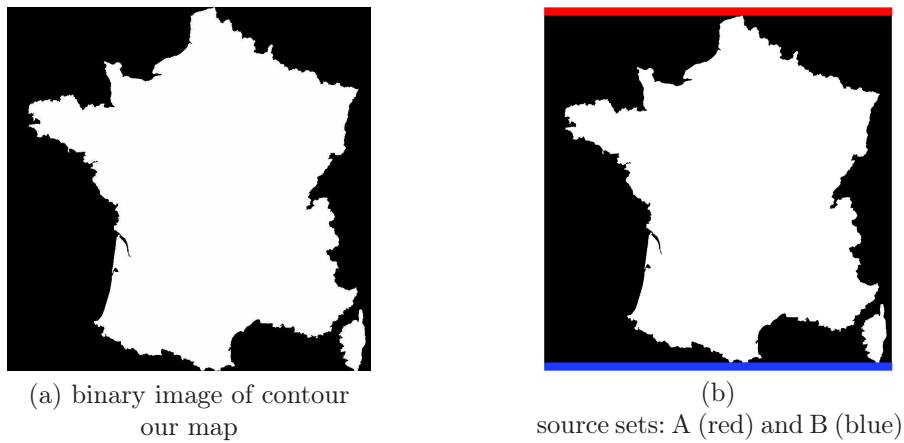


Figure 2.18: Initial binary image and localisation of sources; white phase is the medium in which the wave is propagating.

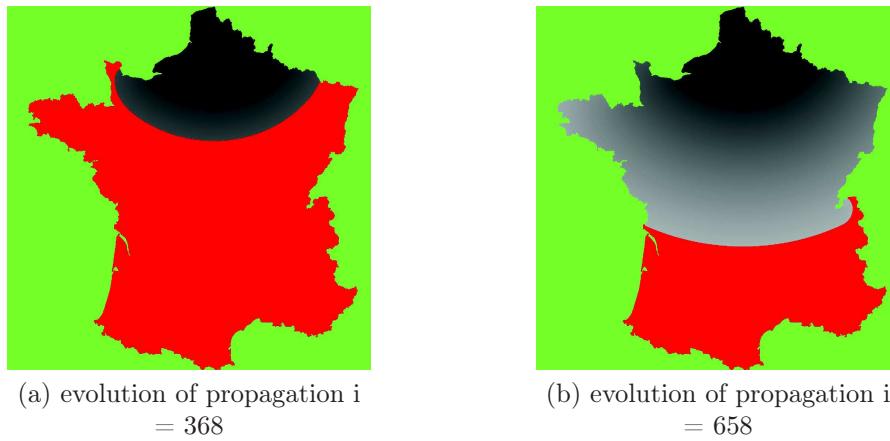


Figure 2.19: Map of arrival time of a wavefront calculated at two different iterations, in case when the set A plays the role of the source. Red colour demotes the area where the wave has not arrived yet.

not affected by non-interconnected subsets. As a results of the conditional addition, at the final step Corsica possess 0-valued tortuosity.

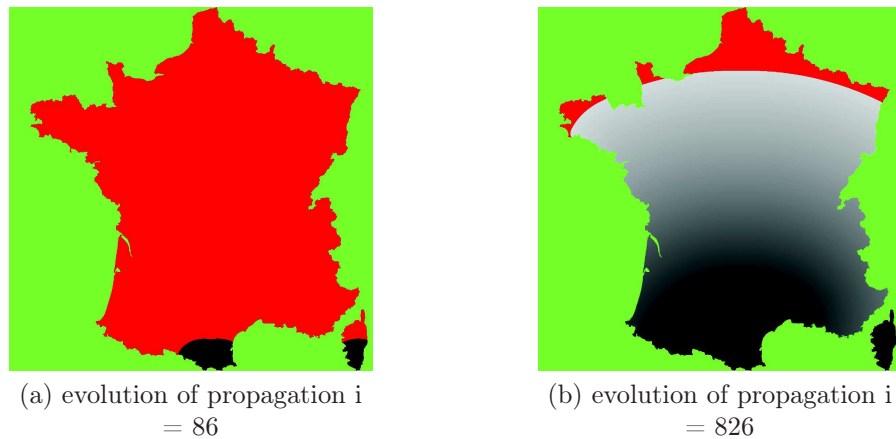


Figure 2.20: Map of arrival time of a wavefront calculated at two different iterations, in case when the set B plays the role of the source. Red colour denotes the area where the wave has not arrived yet.

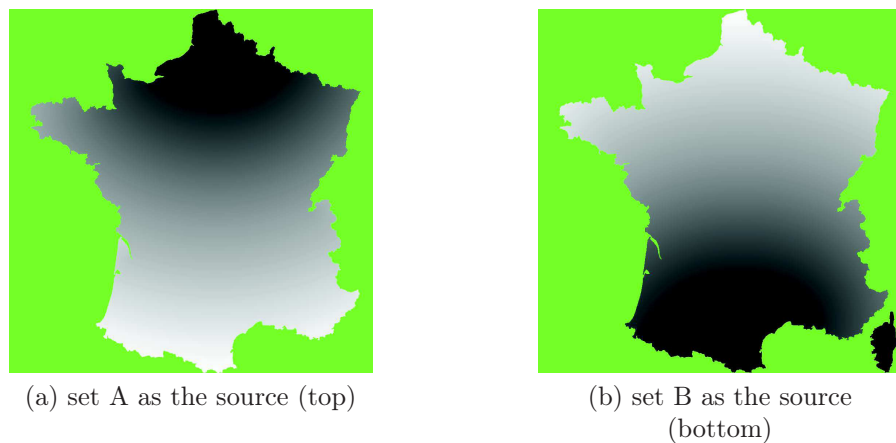


Figure 2.21: Map of arrival time of a wavefront calculated for two different localisations of the source.

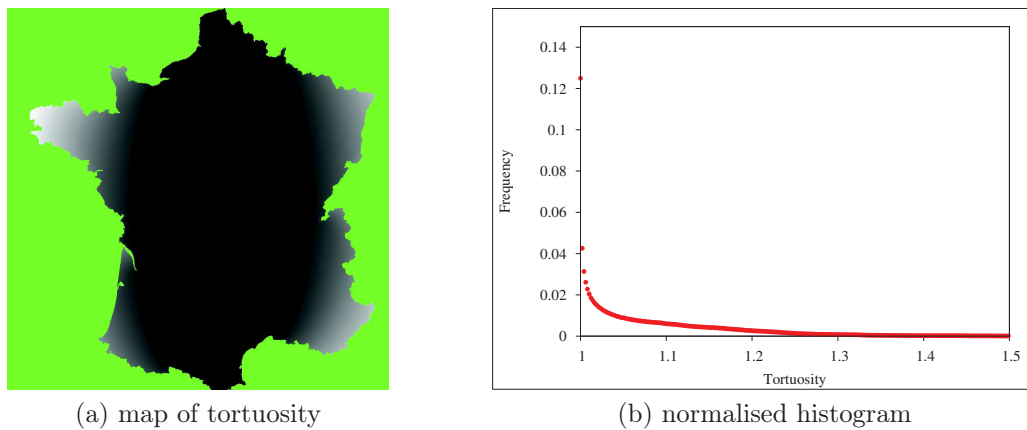


Figure 2.22: Map of tortuosity and its distribution.



## 2.2 Effective behaviour: elasticity and permeability

One of the main, classical idea of continuum mechanics is the assumption that a considered medium is 'averagely' homogeneous in its volume. A lot of materials, like composites, porous media etc., seem to satisfy this idea at certain scale. However, analysing the microstructure of any material we may conclude that each of them poses its scale, at which inhomogeneities (heterogeneities) appear. In this section a brief introduction to periodic homogenization and RVE's estimation are presented. Next, influence of discretization on elastic properties is featured. Finally, a method of permeability estimation by solving Stoke's equation and upscaling method in the framework of Darcy's law are presented.

### 2.2.1 About homogenisation

The upscaling method consist in two main issues: separation of scales and structure–property relation. Role of the homogenisation may be interpreted as a bridge which links effective behaviour of the medium with its microstructure. Or, we can say that homogenisation provides quantitative description of microstructure–property relation, which enables to determine bounds of the effective behaviour. Due to this fact, we can briefly say that the method of homogenisation is 'correctly' used if exists, between considered micro and macro scales, a finite number of separable scales. Once we are handled with the separation of scales, we can take up the structure–property estimation. Generally speaking, it consists in a determination of the representative volume element (RVE). All definitions reveal that the RVE should contain enough microstructural informations of the studied medium to determine its effective behaviour. Covariance function, presented before, is

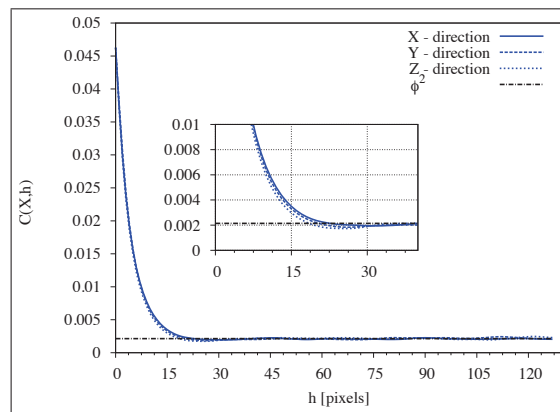


Figure 2.23: Covariance function of sandstone.

an efficient tool, that gives informations of lower bound of RVE size [Fig. 2.23]. The covariance range is the distance (length) over which two points in the microstructure are uncorrelated (independent), hence the RVE size can not be smaller than the covariance range. The method of RVE estimation is presented further in the subsection.

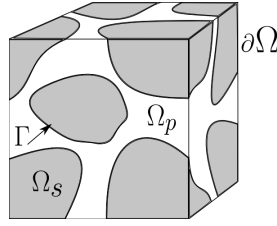


Figure 2.24: The periodic cell  $\Omega$ . The symbol  $\partial\Omega$  represents the outer boundary.  $\Omega_s$  and  $\Omega_p$  denote solid and porous phase respectively.

### 2.2.2 Periodic homogenisation method for linear elasticity

In this work, periodic boundary conditions, prescribed on the RVE cell, are considered. Within the strain approach framework, the method of periodic homogenization can be briefly summarised as follows [9–11].

For a periodic geometry of a RVE  $\Omega$  [Fig. 2.24], submitted to an overall prescribed strain  $E$ , the local fields of stress  $\sigma$  and strain  $\epsilon(u)$  are also  $\Omega$ -periodic ( $u$  denotes displacement field). Let  $u'$  stands for periodic displacement field, therefore we can write that the strain field can be decomposed in following way  $\epsilon(u) = E + \epsilon(u')$ , where  $E$  is the constant part and  $\epsilon(u')$  denotes fluctuating one. What is more, in particular, this decomposition implies that  $\langle \epsilon(u') \rangle = 0$  and  $\langle \epsilon(u) \rangle = E$ , where the brackets  $\langle \cdot \rangle$  denotes the average of a field on the RVE, in the sense:

$$\langle \cdot \rangle = \frac{1}{|\Omega|} \int_{\Omega} \cdot \, d\Omega \quad (2.36)$$

Let the property of solid phase is defined by microscopic stiffness tensor  $c$  and  $\vec{n}$  is the outer unit vector of outer boundary  $\partial\Omega$ . Therefore, the local problem can be written in following way:

$$\begin{cases} \operatorname{div}(\sigma) = 0 & \text{in } \Omega_s, \\ \sigma = c : (E + \epsilon(u')) & \text{in } \Omega_s, \\ u' \text{ is periodic, } \sigma \cdot \vec{n} \text{ is antiperiodic} & \text{on } \partial\Omega, \end{cases} \quad (2.37)$$

The effective (homogenized) stiffness tensor  $C$  satisfies following equation:

$$C : E = \Sigma = \langle \sigma \rangle = \left\langle c : (E + \epsilon(u')) \right\rangle, \quad (2.38)$$

where  $\Sigma$  stands for the overall stress field. A classical way in order to compute the effective stiffness tensor  $C$  is to solve three tractions and three shearing tests. Let  $u'_{kh}$  stands for the solution of the mechanical test, given by  $E = I^{kh}$ , where:

$$I^{kh} = \frac{1}{2} (\delta_{ik}\delta_{jh} + \delta_{ih}\delta_{jk}), \quad (2.39)$$

where  $I^{kh}$  is the fourth order identity tensor, and  $\delta$  denotes the Kronecker delta symbol. Finally, the macroscopic stiffness tensor  $C_{ijkh}$  element is given by:

$$C_{ijkh} = \left\langle c_{ijpq} \left[ I_{pq}^{kh} + \epsilon_{pq}(u'^{kh}) \right] \right\rangle. \quad (2.40)$$

To obtain full effective, macroscopic stiffness tensor, six tests have to be performed over a cell of RVE.

When RVE geometry presents three planes of symmetry, periodic boundary conditions can be replaced by **symmetry boundary conditions** [9] imposed on the external boundary  $\partial\Omega$ . Therefore, local boundary value problem can be solved in the 1/8 of the whole periodic cell (in 3D). The type of the symmetry boundary conditions depends on the mechanical test that is being performed:

- for traction test

$$\begin{aligned}\vec{u}_N &= \vec{0} \quad \text{on} \quad \partial\Omega \\ \vec{\sigma}_T &= \vec{0} \quad \text{on} \quad \partial\Omega\end{aligned}\tag{2.41}$$

- for shearing test in the plane  $(\vec{i}, \vec{j})$

- on the external planes orthogonal to the axis  $\vec{i}$  and  $\vec{j}$

$$\begin{aligned}\vec{u}_T &= \vec{0} \\ \vec{\sigma}_N &= \vec{0}\end{aligned}\tag{2.42}$$

- on the external planes orthogonal to the axis  $\vec{k}$

$$\begin{aligned}\vec{u}_N &= \vec{0} \\ \vec{\sigma}_T &= \vec{0}\end{aligned}\tag{2.43}$$

where  $\vec{u}_N$ ,  $\vec{u}_T$  are displacements in normal and tangential directions respectively, given by:

$$\vec{u}_N = (\vec{u} \cdot \vec{n})\vec{n} \quad \text{and} \quad \vec{u}_T = \vec{u} - \vec{u}_N.$$

Analogically  $\vec{\sigma}_N$  and  $\vec{\sigma}_T$  represent normal and tangential stress vectors what can be written in following way:

$$\vec{\sigma}_N = ((\sigma \cdot \vec{n}) \cdot \vec{n})\vec{n} \quad \text{and} \quad \vec{\sigma}_T = \sigma \cdot \vec{n} - \vec{\sigma}_N.$$

The set  $(\vec{i}, \vec{j}, \vec{k})$  represents unit vectors of the standard basis.

### 2.2.3 RVE's size estimation

As we said before, within a general multi-scale method, it is necessary to determine the RVE over which the measured physical properties (e.g. aforementioned effective linear elastic properties) become representative for the entire material [32, 38–41]. We evoke two main, classical approaches of RVE determination, and later a statistical one:

- geometrical RVE - consist in dividing the entire investigated geometry into cubic subsamples, the size effect of searched descriptor (e.g. porosity, specific surface) can be determined by changing the cube size, localisation and orientation. It is assumed that the 'geometrical RVEs' are independent of the investigated physical property. Finally, RVE is defined when the searched descriptor begins to converge to its global value [Fig. 2.25 (a)]

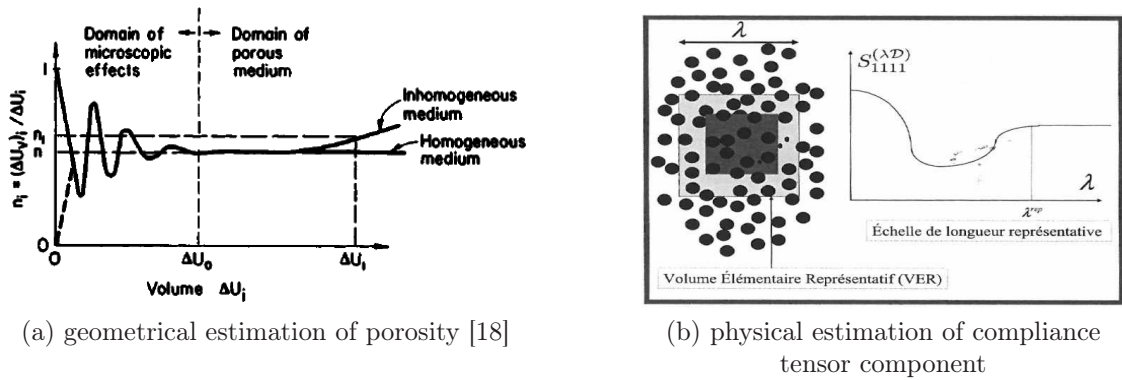


Figure 2.25: Different methods of RVE size determination.

- physical RVE - consist in dividing the entire investigated geometry into cubic sub-samples and based on the requirement that the overall responses with respect to some given physical behavior do not depend on the actual position. The size of such 'physical RVEs' depends on the physical property considered and on the microstructure. Finally, RVE is defined when the searched effective property begins to stabilise [Fig. 2.25 (b)].

Statistical approach presents other kind of RVE estimation proposed by Kanit et al [42]. Which can be briefly introduced as physico – statistical approach. Generally speaking, the method consist in extraction of sub-samples of investigated material and analysis of standard deviation's fluctuations of searched physical property, as a functions of size and number of realisations. What is more, the methodology describes quantitatively the relation between number of realisations, precision (error) and size of the RVE. The results of the study can also be interpreted as a determination of the minimal number of statistically equivalent realisations of the microstructure that have to be investigated for a fixed size of RVE and wanted precision in order to predict the effective behaviour of the medium.

Previously mentioned covariance function allows us to introduce a tool that gives an information on the domain size of considered microstructure for which measured effective properties can be considered as representative. This tool is so-called integral range which is given by equation [9, 19, 42]:

$$\tilde{A}_d = \frac{1}{C(X, 0) - C(X, 0)^2} \int_{\mathbb{R}^n} [C(X, \vec{h}) - C(X, 0)^2] d\vec{h}. \quad (2.44)$$

Let  $\langle Z(V) \rangle$  denotes the spatial average of a scalar random field  $Z(\vec{x})$  over a volume  $V$ . Kanit et al. [42] introduced the integral range  $\tilde{A}_d$  of  $Z(\vec{x})$  to any random function. The statistical fluctuations of  $\langle Z(V) \rangle$ , are related to the integral range  $\tilde{A}_d$  by equation:

$$D_Z^2(V) = D_Z^2 \times \left( \frac{\tilde{A}_d}{V} \right)^\alpha, \quad (2.45)$$

where  $\alpha = 1$  in geostatistic,  $D_Z^2$  is point variance of the random process  $Z$ . In case of biphasic media with property  $Z_1$  for first phase and  $Z_2$  for the second one, point variance

is defined as:

$$D_Z^2 = V_f (1 - V_f) (Z_1 - Z_2)^2, \quad (2.46)$$

where  $V_f$  denotes volume fraction of the first phase. Merging (2.45) and (2.46) we obtain:

$$D_Z^2(V) = V_f (1 - V_f) (Z_1 - Z_2)^2 \left( \frac{\tilde{A}_d}{V} \right)^\alpha. \quad (2.47)$$

Knowing that in classical sample theory the absolute error  $\varepsilon_{abs}$  and relative error  $\varepsilon_{rel}$  are connected with exact mean value  $M$  of the random process  $\langle Z(V) \rangle$  obtained from  $N$  statistically independent realisations, we can write:

$$\varepsilon_{abs} = \frac{2D_Z(V)}{\sqrt{N}}, \quad \varepsilon_{rel} = \frac{\varepsilon_{abs}}{M} = \frac{2D_Z(V)}{\sqrt{NM}}. \quad (2.48)$$

By combining (2.45) and (2.48) we obtain:

$$N = \frac{4}{M^2 \varepsilon_{rel}^2} V_f (1 - V_f) (Z_1 - Z_2)^2 \left( \frac{\tilde{A}_d}{V} \right)^\alpha. \quad (2.49)$$

And finally the size of RVE may be obtained by transforming eq. (2.49):

$$V_{RVE} = \left( \frac{4}{N \varepsilon_{abs}^2} V_f (1 - V_f) (Z_1 - Z_2)^2 \right)^{1/\alpha} \tilde{A}_d. \quad (2.50)$$

For the determination of RVE size, the methodology of Kanit et al. [2003] can be briefly summarised in following way:

- generating different realisations (which are assumed to be statistically equivalent) of the reference microstructure for 4-5 different sizes of the edge length
- performing the mechanical tests to obtain effective elastic properties
- obtaining mean value and variances of effective properties for chosen volume sizes
- identifying the integral range  $A_d$  and power  $\alpha$  in the eq. 2.45
- setting wanted precision for estimation and number of realisations - using eq. 2.50 to estimate RVE size

#### 2.2.4 Influence of the discretization on the effective elastic behaviour estimation

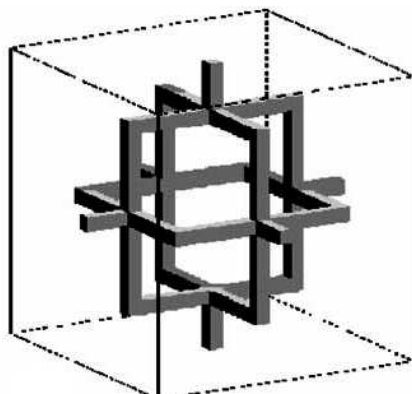
Since the RVE is defined we can predict the effective elastic behaviour using the rule described by equation 2.40. However, results of finite element method are sensitive to the discretization (meshing). In the case of heterogenous materials the amount of publication dealing with influence of mesh, mesh density, size etc. is not significant.

Since we are dealing with digitised heterogeneous media a natural way is to represent each voxel by a cubic mesh element. In literature we can find publications which are essential to deal with discretisation problem for such a kind of mesh. Papers that presents quantitative description of a relation between number of mesh elements (resolution) and effective stiffness of the system were published by Garboczi and Day [12] and Roberts and Garboczi [13, 14]. Their results were confirmed by Gatt et al. [43] in the case of porous ceramics with ellipsoidal inclusions, randomly distributed in space. Relations between computed elastic moduli and resolution is presented in Figure 2.26 and 2.27. This overestimation of stiffness may be interpreted as a consequence of lack of precision in the representation of contours of the interfaces between phases.

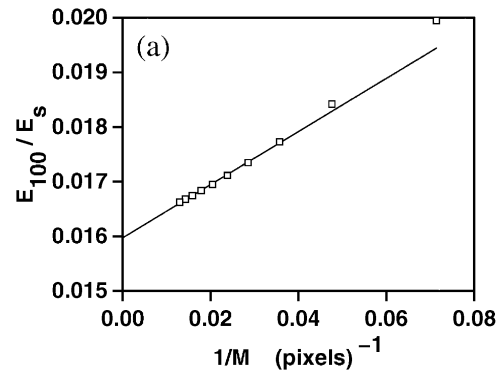
Let  $M$  denotes the number of voxels (elements of regular mesh) along the cubic edge of the cell. It is shown that discretization error for FE methods can be estimated according to following phenomenological formula:

$$P_{FEM} \approx P_0 + \frac{a}{M}, \quad (2.51)$$

where  $P_{FEM}$  is the computed elastic modulus and  $P_0$  is so-called continuum value, which corresponds to the case when  $M \rightarrow \infty$ . To deal with this error we have to compute elastic properties at least for three different values of  $M$  and then extrapolate the results, by fitting linear function according to the least squares method.



(a) model of open-cell solid



(b) Young's modulus of the cell

Figure 2.26: Results of Roberts and Garboczi [14]. The Young's modulus evolution as a function of the resolution  $M$ .

### 2.2.5 Upscaling Stoke's equation - Darcy's law

Permeability is a measure of the ability of a porous media to transmit fluids. It is a critical property in defining the flow capacity of a rock sample. The true absolute permeability of porous rock is an intrinsic property of the rock, reflecting its internal structure. The permeability of a rock is a constant value, unchanged by different types of fluids that have different viscosities or other physical properties. This rule is followed by all liquids at laminar flow rates that are nonreactive with the rock. Understanding interactions between micro-structural geometry and macroscopic effective properties of porous media is an issue

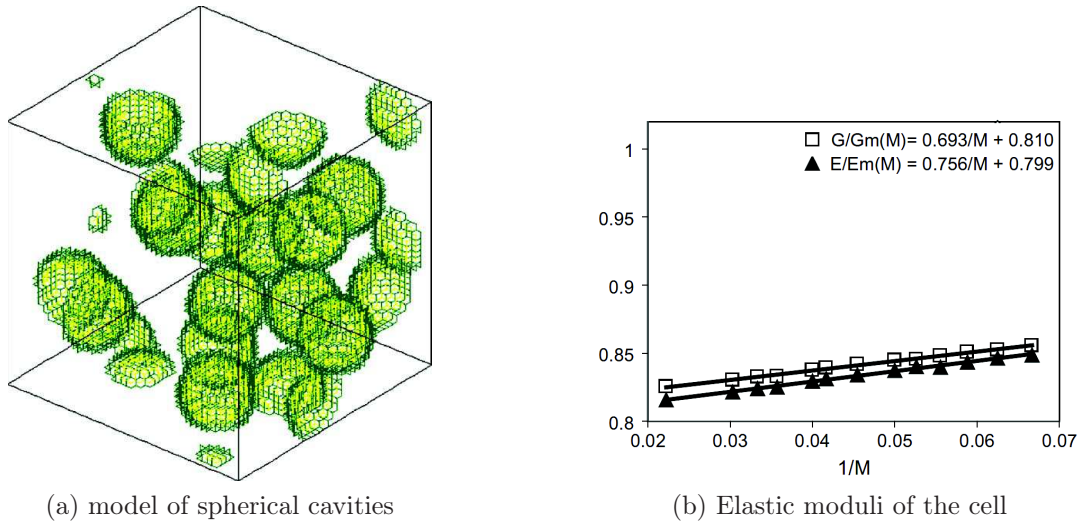


Figure 2.27: Results of Gatt et al. [43]. Influence of the resolution  $M$  on the Young's and shear moduli values.

in a wide range of industrial fields as hydrology, petrology etc. A huge effort has been spent to theoretically estimate or to numerically establish a relation between geometric microstructure and macroscopic physical properties. For porous media, permeability is the macroscopic parameter of significant interest, and its measurement is essential to predict macro-scale behaviour of flows.

In order to estimate effective permeability, we considered two scales: the microscale, where structure of the material of the porous phase is determined [Fig. 2.28] and the macro-scale, where the computed effective properties are assumed to be representative. For the purpose of the study we consider incompressible single phase flow characterised by low Reynolds numbers. Above assumptions lead us to solve the Stokes' equations. By neglecting gravity, the conservation equation in the porous space can be written as follows:

$$\nabla \vec{v} = 0 \quad (2.52)$$

and the momentum equation:

$$\tilde{\mu} \nabla (\nabla \vec{v}) = \nabla p, \quad (2.53)$$

where  $\vec{v}$  denotes the velocity field,  $p$  is the pressure and  $\tilde{\mu}$  stands for dynamic viscosity of the investigated fluid. The Stoke's equation at macroscale is transformed into Darcy's law, which can be written as follows:

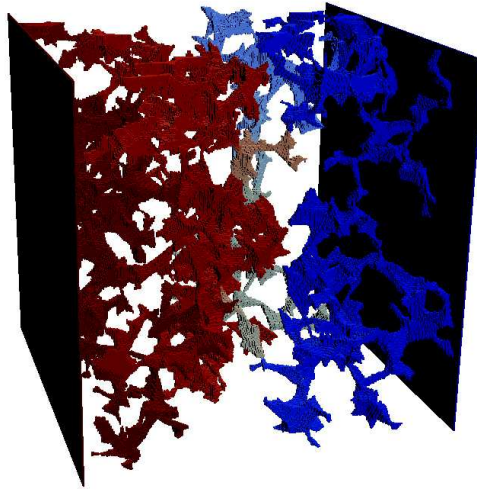
$$\langle \vec{v} \rangle = -\frac{K}{\tilde{\mu}} \nabla P, \quad (2.54)$$

where  $\langle \vec{v} \rangle$  is the average velocity of the fluid,  $K$  denotes the permeability tensor and  $\nabla P$  is the macroscopic gradient of pressure. Since  $\vec{v}$  is defined only in the porous domain  $\Omega_p$  we have:

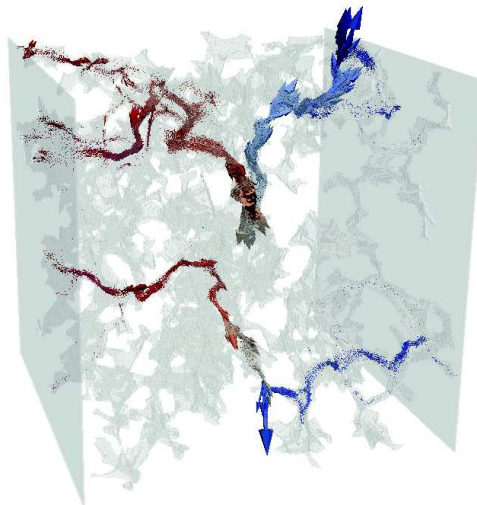
$$\langle \vec{v} \rangle = \frac{1}{|\Omega|} \int_{\Omega_p} \vec{v} \, d\Omega, \quad (2.55)$$

Finally, the permeability of porous rock can be calculated by solving a local boundary value problem of water flow in the pore domain eq. 2.52 and eq. 2.53. As the boundary





(a) pression distribution in a porous network



(b) velocity field (pression distribution colours)

Figure 2.28: Visualisation of pressure distribution and streams.

conditions, at the pore geometry of the microstructure, we will apply the *non - slip conditions*. We can determine e.g. the permeability tensor component  $K_{xx}$  as follows:

$$K_{xx} = -\frac{\langle v_x \rangle \tilde{\mu}}{\Delta P_x}, \quad (2.56)$$

where  $\Delta P_x$  denotes macroscopic gradient of pressure in the  $\vec{x}$  direction,  $\langle v_x \rangle$  is the average velocity of the fluid in the  $\vec{x}$  direction ( $\langle v_x \rangle = \langle \vec{v} \cdot \vec{x} \rangle$ ) and  $\tilde{\mu}$  is the dynamic



viscosity.

## 2.3 Chemical degradation

Chemical dissolution is the main phenomenon which increases porosity of materials and affects their properties. The chemo-mechanical coupling problem has been intensively studied in recent years. Historically, first publications dealing with chemo-mechanical coupling concerned concrete, mortar or cement paste. There is also a wide range of recently published papers concerning experiments of chemical degradation of these materials tested in different conditions (see for example Nguyen *et al.* [44], Yurtdas *et al.* [45], Huang *et al.* [46]). The results obtained confirm a general weakening of the material during chemical degradation (loss of strength and stiffness). Significant part of numerical models focus on leaching of calcium from cementitious structures. For example, a model based on scalar continuum damage was presented by Le Bellego *et al.* [47]. Ulm *et al.* [48] introduced an analytical model linked to the theory of Biot-Coussy. From the other hand, discrete model is shown in paper of Chatzigeorgiou *et al.* [49]. Finally, homogenization approach was applied in works by Nguyen *et al.* [50] and Stora *et al.* [51].

The experimental studies considering CO<sub>2</sub> injection into the rock reservoirs performed in the laboratory conditions, relatively close to the injection point, show different behaviours depending on physical parameters of injected fluid (temperature, pressure), chemical composition of injected fluid and initial rock parameters (see Luquot *et al.* [52], Gouze *et al.* [53], Eggermann *et al.* [54], Eggermann *et al.* 2006 [8], Izgec *et al.* 2008 [55] among others). For example, Eggermann *et al.* [54] performed an experimental study of chemical degradation of hydrocarbon rock reservoirs (which are considered by them as potentially the best candidates for CO<sub>2</sub> geological storage) in the far field region. They analysed three different scenarios of dissolution: uniform, compact and wormholing. Xie *et al.* [56] performed hydrostatic and triaxial compression tests on samples of limestone, chemically degraded by dissolved CO<sub>2</sub>. The significant influence of chemical degradation, in immersion condition, on the mechanical behaviour of material have been shown. They also showed that chemical degradation intensifies deformation of material with time. The CO<sub>2</sub> injection to non-carbohydrate rock sample has been studied by Canal *et al.* [57]. They focused on the siliceous sandstone reservoirs. Their results suggest that mineral dissolution and cracking processes act in a synergetic way during the acidic injection. At the same time, they emphasize that increase of permeability noticed after a long time can be explained mainly by dissolution process of a solid phase. On the other hand some investigations showed the decrease of permeability at the beginning of injection of fluid into rock samples (Qajar *et al.* [58], Izgec *et al.* [55]). The authors relate this phenomenon with closing of pores throats by solid particles disconnected from the solid skeleton near to the inlet of injection. Later, increase and stabilization of permeability were noticed. In the experimental research of behaviour of soil at long time scale after CO<sub>2</sub> injection (Bemer *et al.* [2], Nguyen *et al.* [59]) it is assumed that porous aquifer is saturated by saline water and concentration of the dissolved CO<sub>2</sub> is uniformly distributed in the pore space. The authors showed that chemical degradation can be considered as homogenous in the sample scale. Moreover, their results show that porosity increases uniformly in time over the whole length of the sample. Because of increasing porosity material weakening occurs.

Decrease of both, stiffness and shear strength, and increase of permeability have been also noticed. The comparison of measured petrophysical properties of limestone and bioclastic grainstone samples under no flow conditions in two different environment (exposition to wet supercritical CO<sub>2</sub> and CO<sub>2</sub> saturated water) has been shown in the paper of Rimmelé *et al.* [60]. The significant homogeneous porosity increase over whole sample, for both fluid compositions, has been noticed. Under no flow conditions (for both compositions) the fluid reaction with the rocks occurred, but CO<sub>2</sub> saturated water was more reactive than supercritical CO<sub>2</sub>. The experiments of permeability of cap rocks have been carried out by Bachaud *et al.* [61]. Diffusion and permeability coefficients have been measured under reservoir thermodynamic conditions and compared before and after the alternation. Despite of increase of porosity, the initial low-value transport parameters were conserved. This was called by the authors a non-catastrophic weakening of the material. Moreover, for few samples a decrease of diffusion coefficients was noticed.

The modelling of chemo-mechanical coupling is a subject of a large number of papers published in the recent years. The proposed approaches are very different. Several models were obtained by periodic homogenization method [62]– [63]. For example, Peter [62], [64], Peter and Böhm [65] proposed a homogenisation analysis of elasticity problem with time evolving microstructure. In this model the equations are transformed to a fixed periodic reference geometry. This operation was necessary because during the evolution of the geometry the periodicity was not conserved. The obtained model seems to be difficult to perform numerical simulations. In Lewandowska [66] a macroscopic incremental model of chemo-mechanical coupling by using the periodic homogenization was proposed. In this study it was assumed that the chemical dissolution of solid at the microscopic scale is governed by diffusion equation. Coussy [67] proposed a phenomenological model in which variations of poroelastic parameters are described as a function of irreversible porosity caused by chemical degradation. Numerical and computational aspects of chemo-mechanical modelling related to flow and transport phenomena during the injection process are presented in the papers by Doughty *et al.* [68], Kumar *et al.* [69], Hovorka *et al.* [70], analytical models of the same phenomena are presented by Saripalli *et al.* [71] and Nordbotten *et al.* [72]. In conclusion, the state of the art shows that although there is a lot of publications dealing with the problem of chemo-mechanical coupling, the appropriate model of anisotropic rock dissolution with geomechanical effects in the context of CO<sub>2</sub> geological storage, is still lacking. The difficulty resides in the fact that, by its nature, the problem is site specific in the sense the chemical composition of both the rock and saline water determine the behaviour of the system. The experiments are difficult to perform because of the involved time-scale. For all these reasons, a universal model which would be able to link the macroscopic behaviour with the microscopic scale (evolving microstructure), is still searched.

## 2.4 Structure of the thesis

Chapter 3 presents work that has been done during the first year of my thesis, under the supervision of Jolanta Lewandowska and Philippe Gouze. One of the points of the work was to reconstruct periodic RVE by using reflectional symmetry. The first approach concerned evolution of effective parameters (tortuosity, stiffness and permeability ten-

sors) trigger by dissolution process of oolitic limestone [73]. The sequel concerns the work done during the two last years under the supervision of Loïc Daridon and Yann Monerie. Chapter 4 contains a morphological description of the microstructure of Fontainebleau sandstone. It also shows the reconstruction method that has been used to generate statistically equivalent realisations of sandstone, and morphological validation of the samples. Chapter 5 presents two different scenarii of numerical dissolution. Natural microstructure and generated samples were subjected to the method. Evolution of morphological descriptors is compared and analysed. Chapters 6 & 7 present numerical results concerning estimations of effective properties. Finally, Chapter 8 contains general conclusions and perspectives.


*We are not to tell nature what she's gotta be.  
... She's always got better imagination than  
we have.*

Richard Feynman

# 3

## Limestone - RVE reconstruction by reflectional symmetry

---

his first approach is based on reconstruction method of RVE by using reflectional symmetry (periodisation process). In the chapter, estimation of effective behaviour of limestone is presented. Periodic homogenization method for linear elasticity, with symmetric boundary conditions, is used to estimate effective behaviour of the medium. Then, chemical degradation of porous matrix is taken into account by performing morphological erosion by cross - shaped structuring element. Numerical computations show progressive degradation of all components of the stiffness (orthotropic) tensor. Moreover, evolution of associated mass transfer properties (as tortuosity and conductivity tensors), is discussed.

---

## Contents

---

<b>3.1</b>	<b>Introduction</b>	<b>37</b>
<b>3.2</b>	<b>Microstructure and numerical dissolution</b>	<b>38</b>
3.2.1	Limestone - reference geometry	38
3.2.2	Sample preparation	38
3.2.3	Numerical dissolution	40
<b>3.3</b>	<b>Numerical computations of stiffness tensor</b>	<b>41</b>
3.3.1	Computations of degradation functions of material parameters	41
3.3.2	Results	41
<b>3.4</b>	<b>Mechanical parameters versus morphological properties of the rock material</b>	<b>44</b>
3.4.1	Mechanical properties versus diffusive properties	44
3.4.2	Mechanical properties versus permeability	46
<b>3.5</b>	<b>Conclusions</b>	<b>49</b>

---

### 3.1 Introduction

A first methodology (Fig. 3.1), provides in a simple way how to take into account the chemo-mechanical coupling in multi-scale modelling of porous media, represented by limestone microstructure. In the proposed method, chemical degradation is performed as a numerical dissolution (dilation/erosion) of REV's geometry. The link between evolving microstructure and macroscopic scale is found by periodic homogenization, which assumes periodicity of material. The problem of periodicity of RVE, which is a digitised image of a rock, is tackled by assumption of symmetry – orthotropy (see 3.2.2). The numerical computations are performed on a set of samples presenting different degraded states. By solving particular boundary value problems, given by homogenization theory, the evolution of macroscopic parameters is obtained. In the modelling, that is performed during the first year of PhD, the X-ray tomography of oolitic limestone (from Paris Basin) is used. Samples preparation and numerical dissolution are carried out by ImageJ [74]. Numerical calculations were performed by Comsol Multiphysics. As an example of an application of the study, a simple model of a one-dimensional settlement of the rock formation is presented in Annexe B.

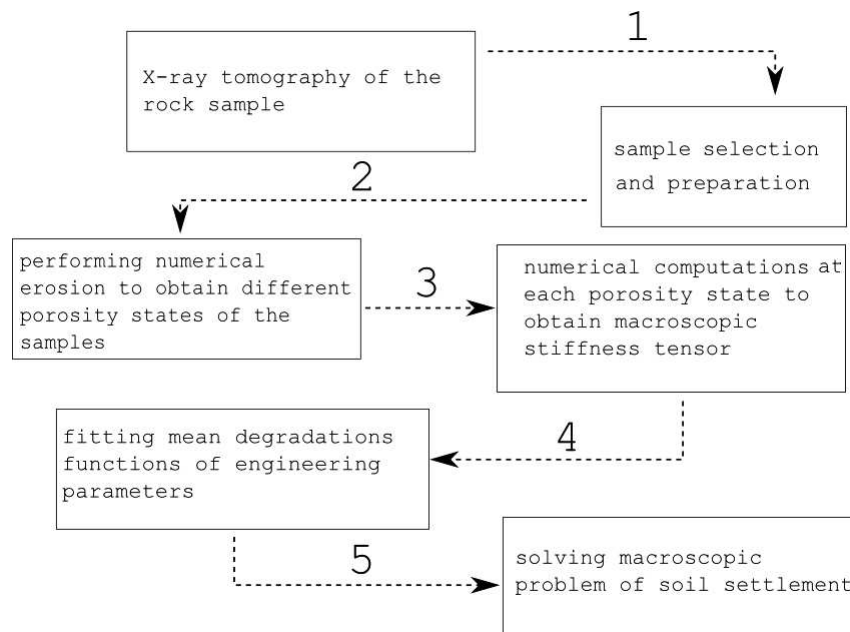


Figure 3.1: Illustration of the proposed methodology.

Methodology we propose can take into account the geometry evolution effects of real anisotropic rock sample on mechanical properties and estimate the subsidence due to chemical degradation. (problem of settlement, formulated in Annexe B, is an iterative process for which continuous functions of material parameters dependent of porosity variations have to be known). To predict deformation due to time dependent changes of rock microstructure we propose a general methodology presented in Figure 3.1. The first step is to prepare the digital image of the microstructure of the rock which will be investigated. The second step consists in preparation of samples to perform mechanical tests at different degraded states. The next step is to perform, for each state, appropriate numerical com-

putations by solving local boundary value problem and calculating the full macroscopic stiffness tensor. Afterward, the data should be processed and the degradation functions have to be fitted. The last step is to use obtained functions to compute the subsidence.

## 3.2 Microstructure and numerical dissolution

### 3.2.1 Limestone - reference geometry

We investigated a geometry of a natural rock. It is a sample of an oolitic limestone from Mondeville formation of the Middle Jurassic age (Paris Basin) [53]. The chemical composition of the rock corresponds to a magnesium-calcite formula  $\text{Ca}_\alpha\text{Mg}_\beta\text{CO}_3$  with  $\alpha = 0.99$  and  $\beta = 0.01$ . The digital image of the microstructure has been obtained by X-ray tomography. The size of the image is  $1067 \times 1067 \times 2000$  pixels, where 1 pixel =  $5.06 \mu\text{m}$ , so the physical dimensions are  $5.4 \times 5.4 \times 10.12 \text{ mm}^3$ . The raw images were processed (see for example [75]) in order to obtain a binary image displaying the solid fraction and the void fraction (or porosity). The initial porosity of the sample calculated by ImageJ software is  $\varphi = 9.3\%$ .

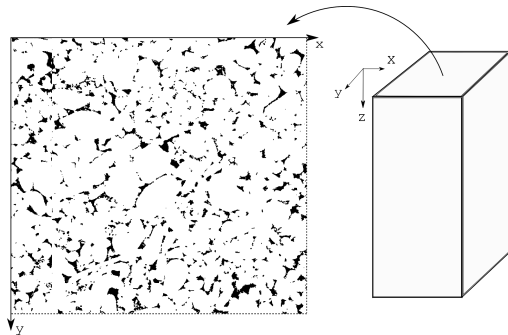


Figure 3.2: Front view of the microstructure in  $XY$  plane of size  $1067 \times 1067$  pixels. White part corresponds to the solid phase, black to pore space.

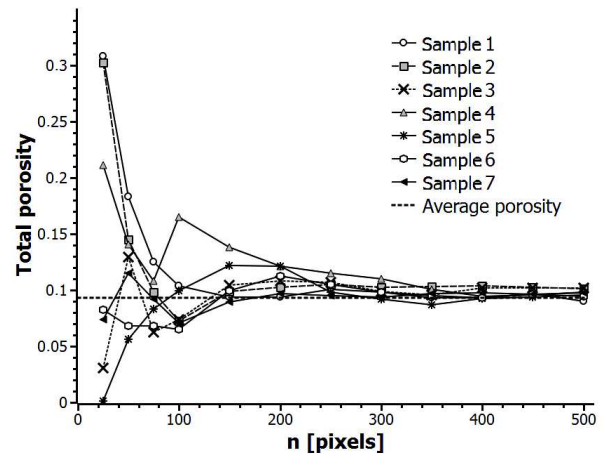


Figure 3.3: Porosity as a function of edge length of the REV  $n$ .

### 3.2.2 Sample preparation

By using ImageJ application image of microstructure has been imported, as shown in Figure 3.2. In order to know the size of the REV for the particular material, the porosity as function of the dimension of the REV, taken from seven different regions in the sample, was analysed (Figure 3.3). From Figures 3.3 and 3.4 it can be clearly seen that all lines converge toward the average value of porosity  $\varphi = 9.3\%$  when the dimension of the REV approaches 200 pixels. However, the microstructure of the size  $200 \times 200 \times 200$  pixels appeared to be too large for numerical computations. Therefore, in what follows we adopted a particular strategy. We assumed that the rock microstructure is periodic, and

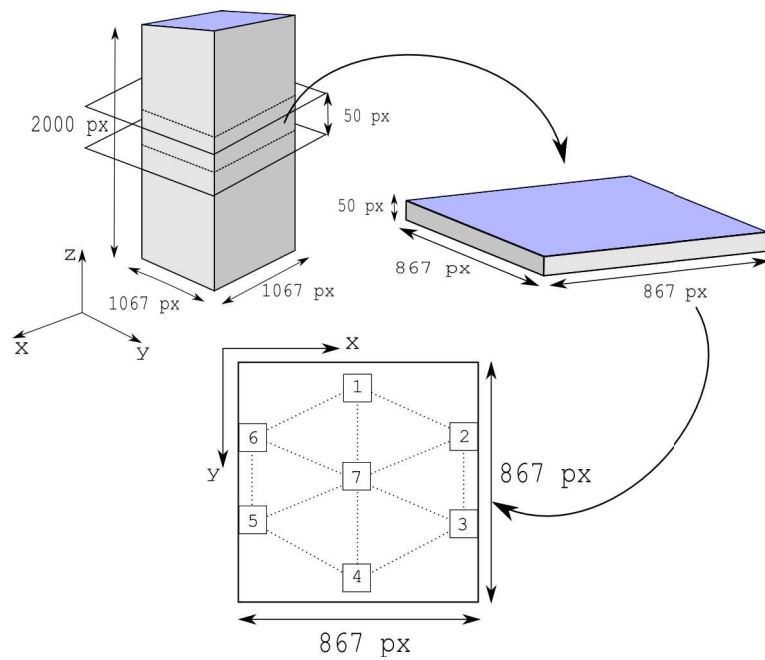


Figure 3.4: Samples preparation - cross section of the microstructure.

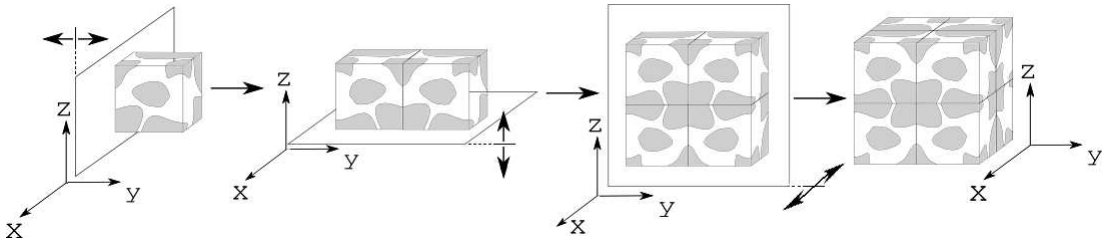


Figure 3.5: Periodization process.

that the period presents three reflectional planes of symmetry. Then, seven cubic sub-samples of the size  $50 \times 50 \times 50$  pixels, each representing  $1/8$  of the complete period, were selected for further analysis. So, the real size of the analysed microstructure was  $100 \times 100 \times 100$  pixels. These samples are located in the central part of the microstructure as shown in Figure 3.4. The samples localization are the vertices of a symmetrical hexagon and the centre point. Each sample was further processed (see section 3.2.3). Finally, on seven cubic sub-samples computations were performed at different dissolution states and all results of numerical computations were interpreted together (see section 3.3 for further discussion).

In the numerical computations, each sample is considered as a  $1/8$  of the period. That means that if we want to reconstruct the period we have to perform the so called 'periodization process' by using symmetries, as shown in Figure 3.5. We can see three reflection symmetries by using three perpendicular planes. Note that  $X, Y, Z$  are assumed to be the axes of natural anisotropy.



### 3.2.3 Numerical dissolution

The aim is to perform parametric study to present dependence of mechanical properties in the whole range the theoretical porosity changes. We assume that dissolution of porous matrix is the only process responsible for chemo-mechanical coupling. Chemical degradation has been performed as a numerical dissolution (dilation/erosion) of the solid phase by ImageJ [74]. For three selected samples (sample 1, sample 4, sample 7) numerical dissolution is performed. The main assumption is that solid part of each microstructure dissolves uniformly in all directions. It consist in removing one pixel in 6-directional neighbourhood in single non-dimensional time step. This assumption was appropriate due to the uniformity of the chemical composition and long time scale (long term behaviour) in which the distribution of pressure and  $\text{CO}_2$  concentration in saline water is approximately uniform at the sample scale [2, 59].

For each of seven samples we performe numerical dissolution. As an example in Figures 3.6-3.7, the dissolution process of sample 4 is shown. We can see the evolving pores and the solid skeleton volumes. The total porosity varies between 16.3% to 37.8%. Note that  $\varphi_{eff}$  corresponds to effective porosity of samples in which unconnected pores and unconnected solid parts have been deleted. In Figure 3.6 percolation in  $\vec{z}$  direction appears. At the last state of dissolution the percolation in all directions exists, as shown in Figure 3.7. As to the solid part, it is connected in each direction at each solid state.

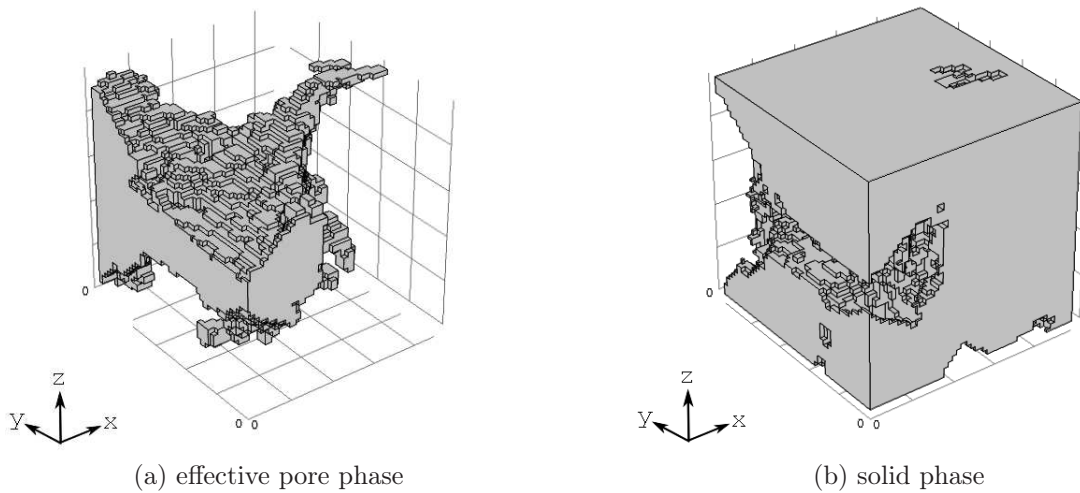


Figure 3.6: Microstructure of sample 4;  $\varphi = 16.3\%$ ,  $\varphi_{eff} = 14.9\%$ .

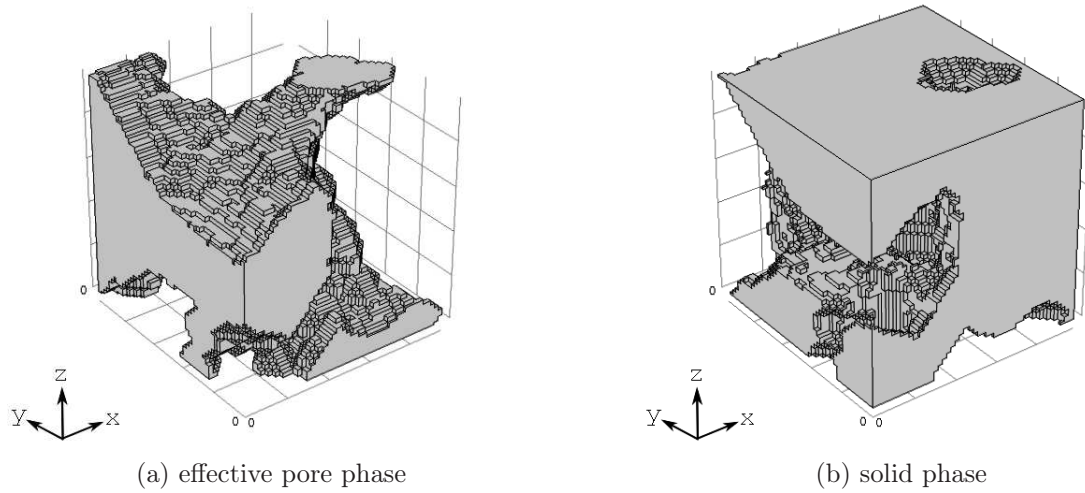


Figure 3.7: Microstructure of sample 4;  $\varphi = 37.8\%$ ,  $\varphi_{\text{eff}} = 37.8\%$ .

### 3.3 Numerical computations of stiffness tensor

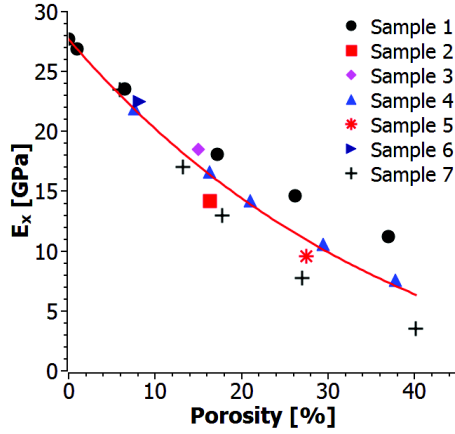
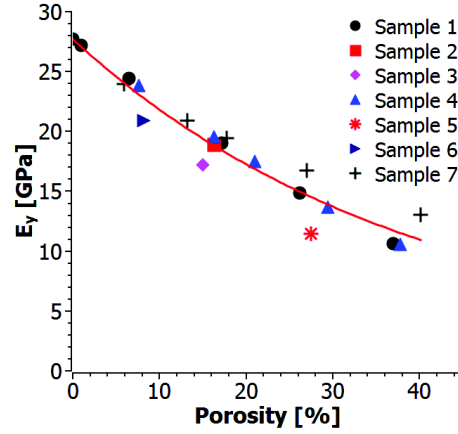
#### 3.3.1 Computations of degradation functions of material parameters

In order to compute degradation functions of mechanical parameters the numerical computations using homogenization approach are performed. We adopte the following strategy. The computations are carried out for all seven samples at the initial state of the rock and three selected samples at different states of chemical degradation. Than, all results were interpreted together to define the degradation functions. The choice of such approach can be justified by the experimental results [2], [59]. Indeed, the experiments showed that the spatial variations of measured porosity within the rock material were of the same order that porosity variations of a sample due to the dissolution.

The computations are carried out for all seven samples at the initial state of the rock and three selected samples (sample 1, sample 4, sample 7) at different degraded states. We assumed that the solid material (at microscopic scale) is isotropic with following values of Young modulus and Poisson ratio:  $E_{\text{micro}} = 27.7 \text{ GPa}$ ,  $\nu_{\text{micro}} = 0.27$ . These values correspond to the average material parameters of Euville limestone from the basin of Paris, measured by Nguyen *et al.* [63]. The computations has been performed by using FEM code with a number of mesh elements varying from 100000 to 250000.

#### 3.3.2 Results

All results (for initial and degraded samples) were interpreted together as functions of porosity. The mean degradation functions were fitted to all samples data. The character of variations for each parameter can be described by exponential decay function in the form  $A \exp(-x/B) + C$ , where constants  $A$ ,  $B$ ,  $C$  were fitted by least square method. The correlation coefficient varies between 0.94 and 0.99.

Figure 3.8: Degradation function of  $E_x$ .Figure 3.9: Degradation function of  $E_y$ .

In Figures 3.8 - 3.16 the variation of engineering parameters ( $E_x$ ,  $E_y$ ,  $E_z$ ,  $G_{yz}$ ,  $G_{zx}$ ,  $G_{xy}$ ,  $\nu_{xy}$ ,  $\nu_{yz}$ ,  $\nu_{zx}$ ) with porosity are shown. Nine of them are independent, since material is orthotropic [76]. This property was systematically checked by verifying the relations between Poisson ratios and Young's moduli

$$\frac{\nu_{ij}}{E_i} = \frac{\nu_{ji}}{E_j} \quad i \neq j \quad \text{and} \quad i, j \in (x, y, z). \quad (3.1)$$

The relative error for each test is less than 0.1%. Also the zero-elements of the matrix were confirmed by computations. Figures 3.8-3.10 show Young's modulus for each direction as function of porosity. The drop of  $E_x$  is the most significant. Figures 3.11-3.13 present three shear moduli. As we can see, the most significant decrease concerns  $G_{zx}$ . For Poisson ratios  $\nu_{xy}$ ,  $\nu_{yz}$ ,  $\nu_{zx}$ , no general trends appear (Figures 3.14-3.16). Finally, the analysis of the results presented in Figures 3.8-3.13 show that degradation data for sample 4 is very close to the plot of mean degradation function. For this reason sample 4 was chosen to further computations (see section 3.4).

The numerical results could be compared with experimental data. Unfortunately, no experiments on orthotropic material are available in the literature. The comparison with experimental results of degradation of isotropic material provided in [2] and [59] shows a similar trend of dependence of mechanical parameters on porosity.

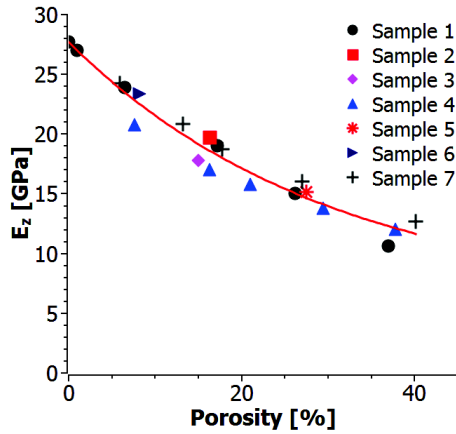


Figure 3.10: Degradation function of  $E_z$ .

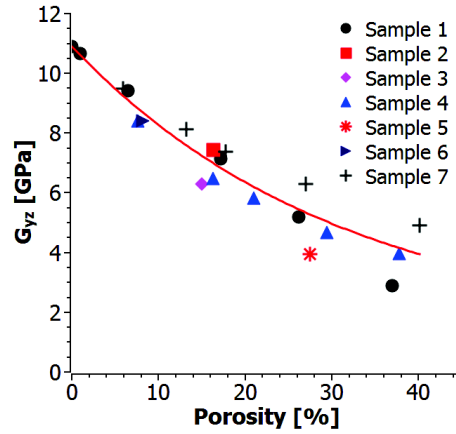


Figure 3.11: Degradation function of shear modulus  $G_{yz}$ .

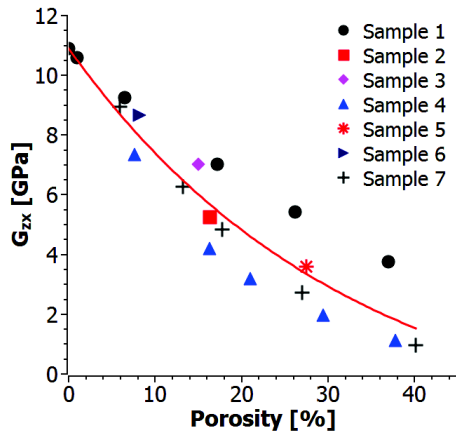


Figure 3.12: Degradation function of shear modulus  $G_{zx}$ .

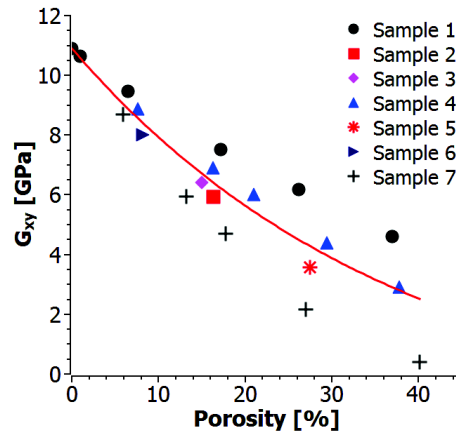


Figure 3.13: Degradation function of shear modulus  $G_{xy}$ .

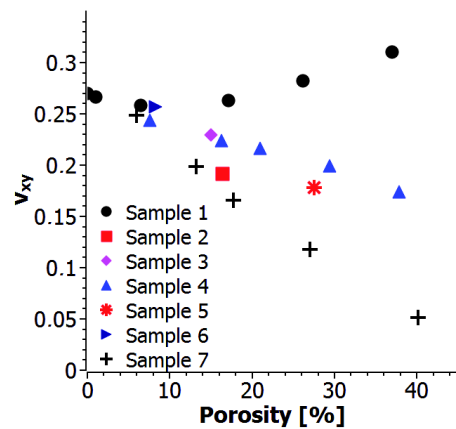


Figure 3.14: Poisson ratio  $\nu_{xy}$  as a function of porosity.

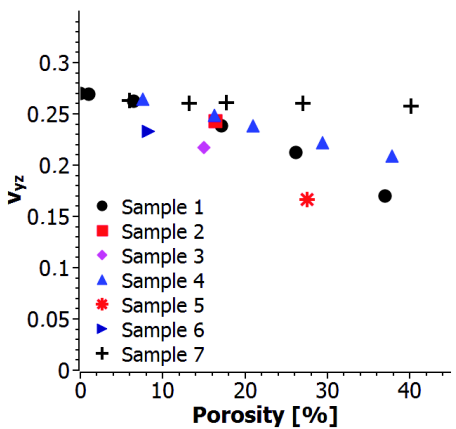


Figure 3.15: Poisson ratio  $\nu_{yz}$  as a function of porosity.

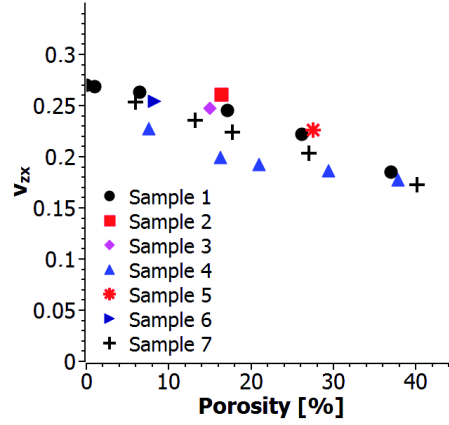


Figure 3.16: Poisson ratio  $\nu_{zx}$  as a function of porosity.

### 3.4 Mechanical parameters versus morphological properties of the rock material

The upscaling method by periodic homogenization provides the link between the microscopic and macroscopic scales. Therefore, the variations of mechanical parameters of the rock can be analysed in relation with microstructure and its morphological properties. In this section permeability, diffusion and tortuosity tensors for selected rock sample (sample nr 4) at initial and degraded states are calculated. In view of previous assumption of existence of three planes of symmetry,  $X$ ,  $Y$ ,  $Z$  are the principal axes of these tensors. This situation does not change during the one-dimensional settlement due to the material degradation process. The aim is to analyse the correlation between those parameters and the mechanical properties when microstructure is subjected to evolution.

#### 3.4.1 Mechanical properties versus diffusive properties

In order to calculate effective diffusion tensor for a particular periodic microstructure following local boundary value problem for the vector  $\vec{\chi}$  is solved [77–79]

$$\frac{\partial}{\partial y_i} \left[ D \left( \mathbb{I}_{ij} + \frac{\partial \chi_j}{\partial y_i} \right) \right] = 0 \quad \text{in } \Omega_p \quad \text{and} \quad i, j \in (1, 2, 3), \quad (3.2)$$

$$N_i \left[ D \left( \mathbb{I}_{ij} + \frac{\partial \chi_j}{\partial y_i} \right) \right] = 0 \quad \text{on } \Gamma \quad \text{and} \quad i, j \in (1, 2, 3), \quad (3.3)$$

where  $\vec{\chi}$  is  $y$ -periodic and its volumetric average is equal to zero.  $D$  is the diffusion coefficient at the microscopic scale.  $\vec{N}$  is the external normal unit vector to the  $\Omega_p$  (pore domain). In the computations periodic boundary conditions are replaced by the symmetry conditions, as proposed in [80]. The effective diffusion tensor is given by

$$D_{ij}^{eff} = \frac{1}{|\Omega|} \int_{\Omega_p} D \left( \mathbb{I}_{ij} + \frac{\partial \chi_j}{\partial y_i} \right) d\Omega \quad (3.4)$$

and the tortuosity tensor by

$$\tau_{ij} = \frac{1}{|\Omega|} \int_{\Omega_p} \left( \mathbb{I}_{ij} + \frac{\partial \chi_j}{\partial y_i} \right) d\Omega. \quad (3.5)$$

Note that tortuosity is usually defined in phenomenological approaches, see for example [18], as the ratio

$$\tau = \frac{\Lambda}{\Lambda'}, \quad (3.6)$$

where  $\Lambda$  is the straight distance between two positions of a particle,  $\Lambda'$  is length of trajectory connecting these two positions. According to this definition, tortuosity varies between 0 and 1. In Figure 3.17 the tortuosity of the sample 4 as a function of the increasing porosity, occurring during chemical degradation, is presented. We can observe the increase of the tortuosity in the direction  $\vec{y}$  and  $\vec{z}$ , and constant (almost zero value) in the  $\vec{x}$  direction. In general, the increase of tortuosity is related to the decrease of the particles trajectory in the pores [18]. Therefore, it can be interpreted as "straightening" of pores (pores become less tortuous). In the  $\vec{x}$  direction there is no percolation until the effective porosity reaches about 38%. Figure 3.18 presents tortuosity tensor components divided by the effective porosity. It can be said, that kinetics of changes of tortuosity in relation to increase of the effective porosity is different for  $\tau_z$ , than  $\tau_y$ . It can be seen that the rate of "straightening" of trajectories for  $\tau_y$  is almost constant during dissolution.

In Figures 3.19–3.22 relations between tortuosity tensor components and mechanical parameters are shown. For all parameters the increase of tortuosity ( $\tau_y$  and  $\tau_z$ ) is associated with the decrease of Young and shear moduli.

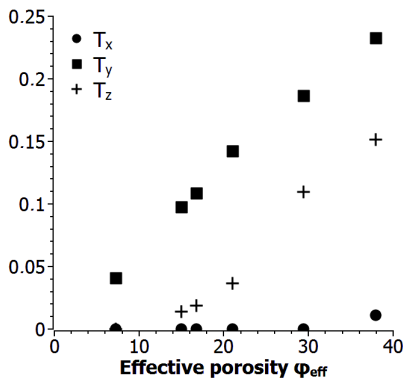


Figure 3.17: Tortuosity parameters for each direction as a function of effective porosity.

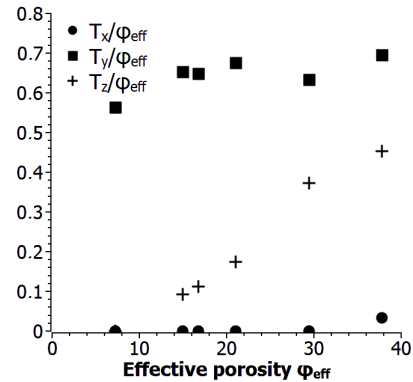


Figure 3.18: Tortuosity parameters for each direction divided by corresponding effective porosity.

Finally, specific surface of the microstructure for sample 4 (in evolution), is calculated. In Figure 3.23 the specific surface as a function of the effective porosity, is drawn. We can see a general trend of increase of specific surface with porosity. For porosity equal to 21% a local decrease appears, that can be explained by fusion of pores forced by chemical dissolution.

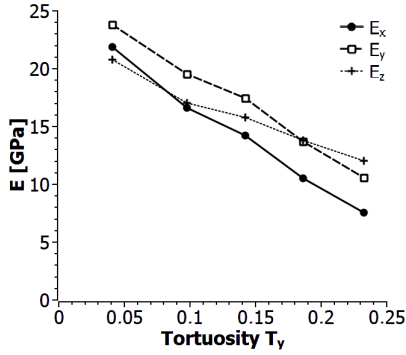


Figure 3.19: Young modulus as function of tortuosity  $\tau_y$ .

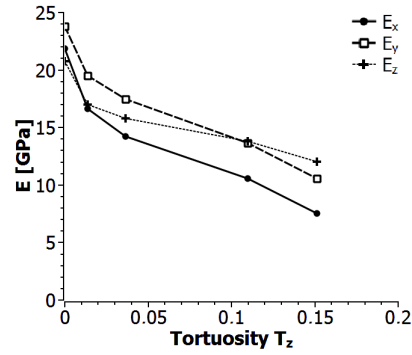


Figure 3.20: Young modulus as function of tortuosity  $\tau_z$ .

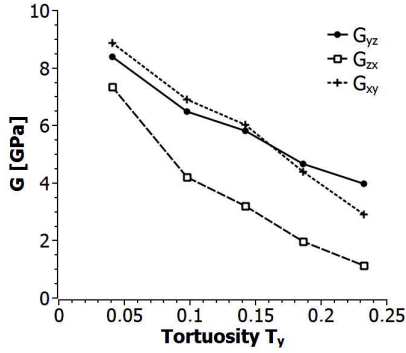


Figure 3.21: Shear modulus as function of tortuosity  $\tau_y$ .

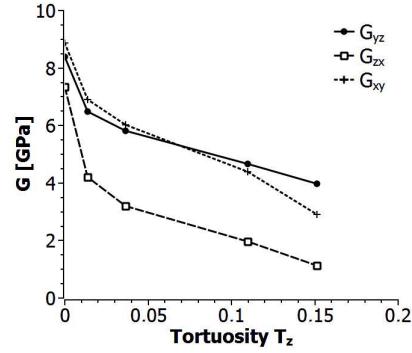


Figure 3.22: Shear modulus as function of tortuosity  $\tau_z$ .

### 3.4.2 Mechanical properties versus permeability

Permeability of porous rock can be calculated by solving a local boundary value problem of water flow in pore domain. Since microstructure presents symmetries, problem to be solved in order to compute permeability in  $\vec{z}$  direction (for example), is as follows:

1. Stokes equation

$$\eta \Delta \vec{v} - \nabla p = 0 \quad \text{in } \Omega_p, \quad (3.7)$$

2. Incompressibility condition

$$\nabla \cdot \vec{v} = 0 \quad \text{in } \Omega_p, \quad (3.8)$$

with following boundary conditions (Figure 3.24)

- on the surface 1: pressure  $p_1 = 1$
- on the surface 2: pressure  $p_2 = 0$
- on all other external surfaces: slip condition
- on all internal solid surfaces: non-slip condition

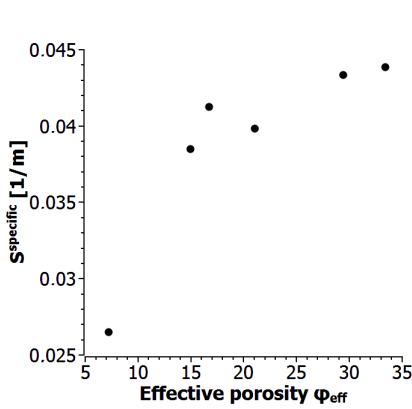


Figure 3.23: Specific surface as function of effective porosity.

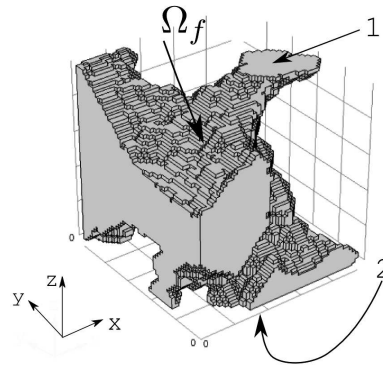


Figure 3.24: Pore volume of sample 4 in degraded state, with indicated notation for boundary conditions.

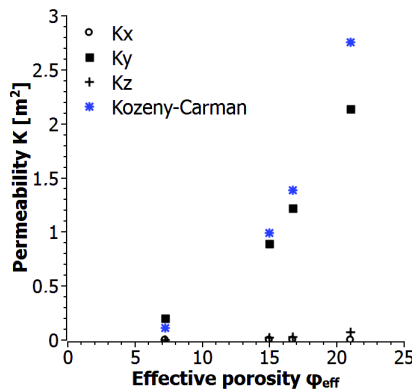


Figure 3.25: Comparison of permeability tensor elements and Kozeny-Carman permeability.

The permeability  $K_z$  can be calculated from the Darcy law that is valid at the macroscopic scale [81]

$$K_z = -\frac{\langle v_z \rangle \eta}{\frac{\partial}{\partial z} p}, \quad (3.9)$$

where  $\partial p / \partial z$  means macroscopic gradient of pressure in the  $\vec{z}$  direction,  $\langle v_z \rangle = \langle \vec{v} \cdot \vec{z} \rangle$  is the average fluid velocity component in the  $\vec{z}$  direction and  $\eta$  is the dynamic viscosity. In the problem formulation we use result of theoretical analysis, concerning the scale separation, for the case of symmetry of the period, as in [80]. The computations are performed for sample 4 in its initial and degraded states. The results of computations of three components ( $K_x$ ,  $K_y$ ,  $K_z$ ) as functions of the effective porosity are presented in Figure 3.25. We can observe a significant increase of  $K_y$  while  $K_z$  increases only slightly and  $K_x$  remains zero (no percolation in  $X$  direction in this range of porosity). In the same figure, the Kozeny-Carman classical solution for isotropic media is shown for comparison. Similar study was performed by Narsilio et al. [82].

In Figures 3.26-3.29 the relations between Young and shear moduli, and non-zero elements of permeability tensor, are presented. A general trend of decrease of the mechanical parameters as function of increasing permeability is confirmed.



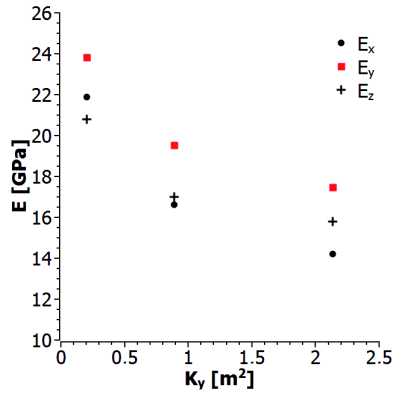


Figure 3.26: Young moduli as a function of  $K_y$ .

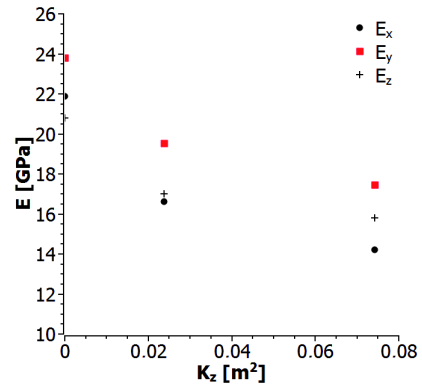


Figure 3.27: Young moduli as a function of  $K_z$ .

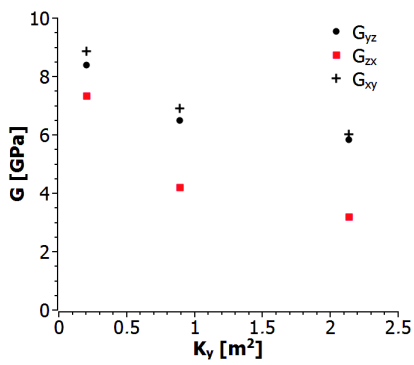


Figure 3.28: Shear moduli as a function of  $K_y$ .

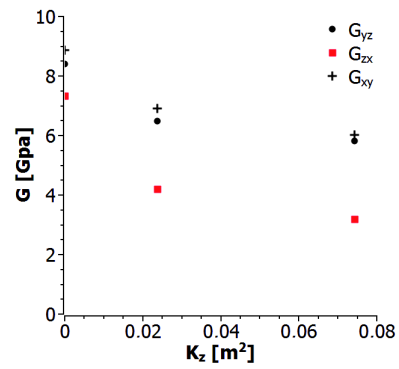


Figure 3.29: Shear moduli as a function of  $K_z$ .

Numerical computations confirm that the loss of mass of solid (increase of porosity) is linked with weakening of the material. Although, porosity systematically increases, the hydraulic conductivity increases significantly only in the direction  $\vec{y}$ . On the other hand, the Young's modulus in the direction  $\vec{y}$  ( $E_y$ ) is not the most affected by the degradation. It seems that in the direction  $\vec{y}$  a preferential path appeared within which a lot of contacts in the directions  $\vec{x}$  and  $\vec{z}$  had been lost. Since the most significant decrease of Young modulus occurred in the direction  $\vec{x}$ , we can suppose that the preferential path cut the maximum number of contacts in the  $\vec{x}$  direction with respect to others ( $\vec{y}$  and  $\vec{z}$ ). It is also confirmed by the decrease of two shear moduli linked to the direction  $\vec{x}$ , namely ( $G_{xy}$  and  $G_{zx}$ ). The modulus  $G_{xy}$  decreases less rapidly than  $G_{zx}$  that can be explained by the fact that the number of lost contacts in the direction  $\vec{y}$  is less than in the direction  $\vec{z}$ . Similarly, we can expect that the drop of modulus  $G_{yz}$  is less than the two others since the lost of contacts in the direction  $\vec{y}$  and  $\vec{z}$  is less important than in the direction  $\vec{x}$ . The latter is confirmed in Figures 3.11-3.13.

Interestingly, the highest decrease of Young modulus  $E_x$  (and associated shear moduli  $G_{xy}$  and  $G_{zx}$ ) is not related with the important variations of the transfer parameters (tortuosity, conductivity). Therefore, we can say more generally, that the decrease of mechanical parameters is not necessarily related with percolation.

As far as tortuosity is concerned, we observed that the rate of increase of the tortuosity is constant in the direction  $\vec{y}$ , but is subjected to significant changes in the direction  $\vec{z}$ . Nevertheless, the change of kinetics of tortuosity is not reflected in the kinetics of changes of mechanical parameters in the respective directions.

These conclusions have to be verified by performing more numerical computations and experiments.

## 3.5 Conclusions

A methodology linking dissolution of rock at the microscopic scale during the geological storage of CO<sub>2</sub>, and the geomechanical behaviour of the saline aquifer, is proposed. The performed numerical computations for an orthotropic microstructure showed progressive degradation of all components of the stiffness tensor that follow an exponential decay function. The relation between the mechanical parameters and the transfer properties (tortuosity and conductivity tensors) during the dissolution process are also studied. It was found that the high increase of conductivity (in the direction  $\vec{y}$ ) does not correspond (as could be expected) to the highest weakening of the Young modulus in this direction. Moreover, the highest decrease of Young modulus (in the direction  $\vec{x}$ ) is not associated with percolation in this direction. This first results clearly show that morphological information about microstructure can be very useful in qualitative explanation of chemical degradation process.

Regarding first approach, in order to understand better the mechanism of numerical dissolution and its influence to microstructure we propose to develop much more detailed morphological analysis. Particularly we focus on much bigger RVE size and we suggest to modify periodisation process.




*There is no branch of mathematics, however abstract, which may not some day be applied to phenomena of the real world.*

Nikolai Lobachevsky

# 4

## Fontainebleau sandstone - morphology, reconstruction & validation

---

 In this chapter, a new approach based on equivalent media more than on real sample is proposed. The morphological tools, introduced in Chapter 2 are used to perform quantitative description of microstructure of Fontainebleau sandstone. The extracted informations help us to adapt the reconstruction methodology and to choose suitable generated microstructures, which are in good agreement with the studied rock sample.

---

## Contents

---

<b>4.1</b>	<b>Introduction</b>	<b>53</b>
<b>4.2</b>	<b>Morphological characterisation of sandstone</b>	<b>54</b>
4.2.1	Basic measures	54
4.2.2	Number of pores per slice	56
4.2.3	Granulometry	57
4.2.4	Spatial distribution - covariance function	57
4.2.5	Morphological tortuosity	59
<b>4.3</b>	<b>Reconstruction methodology</b>	<b>61</b>
4.3.1	Grain deposit	61
4.3.2	Compaction	62
4.3.3	Diagenesis	64
4.3.4	Choosing the initial radius	64
4.3.5	Choosing the compaction scenario	68
4.3.6	Analysis of anisotropy of contacts	68
<b>4.4</b>	<b>Morphological validation</b>	<b>71</b>
4.4.1	Basic descriptors and tortuosity	72
4.4.2	Covariance	73
4.4.3	Granulometry	73
<b>4.5</b>	<b>Partial conclusions</b>	<b>75</b>

---

## 4.1 Introduction

Sandstone is a type of sedimentary rock composed of sand-sized grains of minerals. Rock formations that are primarily composed of sandstone usually allow percolation of water or other fluids and are enough porous to store large quantities of fluid, making them valuable aquifers and petroleum reservoirs.

Sandstones are clastic in origin and are formed from cemented grains that may either be fragments of pre-existing rock or mono-mineralic crystals. Grain sizes in sands are defined (in geology) within the range from 0.0625 mm to 2 mm. Formation of sandstone involves two principal stages illustrated in Figure 4.1. Firstly, layers of sand accumulate as the result of sedimentation. Finally, once it has accumulated, the sand becomes sandstone when it is compacted by pressure of overlying deposits and cemented by precipitation of minerals within the pore spaces between sand grains.

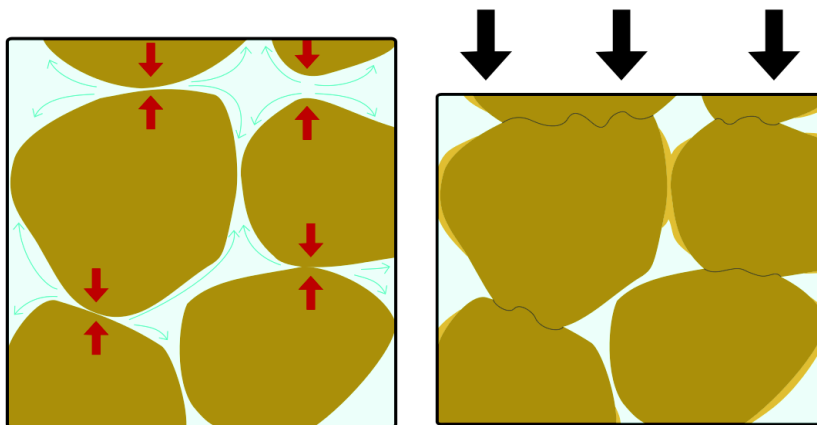
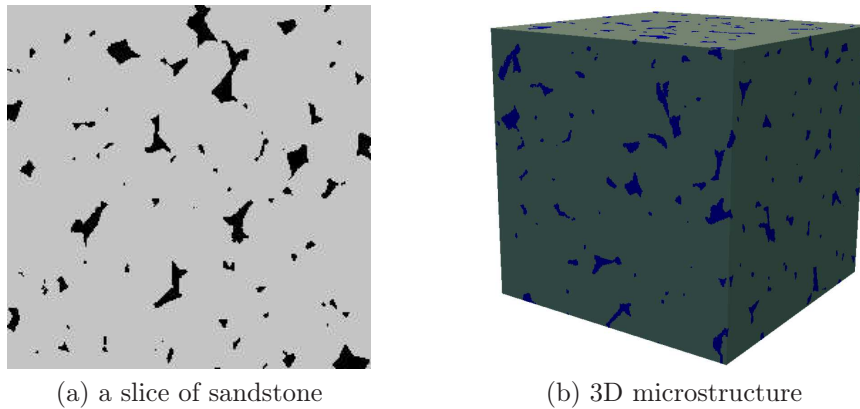


Figure 4.1: Simplified visualisation of formation process of sandstone. We can see two phases: the first one is the deposit of subsequent layers of sand grains (deposit); consequently during sedimentation the upper layers press the grains localised on the bottom (compaction); in the meantime, the precipitation of minerals, cementation occurs (diagenesis)<sup>1</sup>.

The investigated microstructure is presented in Figure 4.2. Standard X-ray microtomography images comprise grayscale maps with values proportional to the linear attenuation coefficient at each material point. Typically, data is organized as a collection of cubic volume elements (voxels), each of which is assigned a unique grayscale value. Next, the data are segmented into a number of distinct categories corresponding to distinct material phases. In our case we consider biphasic (binary) media in which one of values correspond to solid or pore phase. The initial size of the sandstone geometry is  $256 \times 256 \times 256$  voxels with resolution  $5.01 \mu\text{m}$  per voxel.

<sup>1</sup>source: [https://en.wikipedia.org/wiki/Sedimentary\\_rock#/media/File:Pressure\\_solution\\_sandstone.svg](https://en.wikipedia.org/wiki/Sedimentary_rock#/media/File:Pressure_solution_sandstone.svg).



(a) a slice of sandstone

(b) 3D microstructure

Figure 4.2: Visualisation of sandstone geometry.

## 4.2 Morphological characterisation of sandstone

Modelling of microstructure of random heterogeneous materials (porous media) can be based on morphological and statistical characterisation. In this part, basic morphological tools that are available to quantitatively characterise a structure of heterogeneous media are presented. They can be easily obtained from analysis of binary images of the microstructure. To describe a random media, we can use the following main morphological criteria [17]:

- **basic measures** are global measures e.g. porosity, specific surface. To describe a heterogeneous material (sandstone) we also investigate distribution of global descriptors, e.g. porosity, number of pores, by analysing slices of the geometry in different planes.
- **sizing of objects** consist in quantitative description of particular characteristics like length, surface or volume. To characterise sandstone, which is composed by sand grains, we use granulometric function, obtained by morphological openings/closings.
- **spatial distribution** is a very important descriptor to investigate characteristic length and presence of scales. Scales, characteristic lengths, clustering of object and isotropy can be described by so called, second order statistics. In the thesis, for this purpose we use covariance function.
- **connectivity** has a significant influence on physical properties of media consist of different phases. Fluid flow in porous media involve the existence of percolated network across its domain. For the purpose of this work, the connectivity of the porous phase is quantitatively described by morphological tortuosity.

### 4.2.1 Basic measures

**Porosity** is calculated in two steps: by counting the number of voxel representing the pore space ( $V_p$ ) and then by dividing the value by number of all voxels representing the entire

microstructure ( $V_{total} = 256 \times 256 \times 256 = 16777216$  voxels). The method of estimation of porosity is presented by Pseudocode A.4 in Annexe A. Finally, global value of **porosity** obtained for the studied specimen is:

$$\varphi = \frac{V_p}{V_{total}} = 0.046. \quad (4.1)$$

To perform more detailed analysis of porosity distribution, the 3D microstructure of sandstone is decomposed into individual slices, like presented in Figure 4.2 (a). For each projection ( $XY$ ,  $XZ$  and  $YZ$  planes) the value of porosity of each image is measured. In Figure 4.3 (a) we can see fluctuations around the mean value of porosity from about 2.7% to 7.5%. The slice number equal to 0 corresponds to the top of the specimen and the slice number 255 to the bottom of the specimen in the considered plane. The porosity is quite homogeneously distributed in the specimen. In Figure 4.3 (b), results are presented by normalised histograms, distributions possess similar character. Average value for each plane is of course the same ( $\bar{\varphi} = 4.63\%$ ), standard deviations are equal 0.74, 0.63 and 0.82 for plane  $XY$ ,  $XZ$  and  $YZ$  respectively.

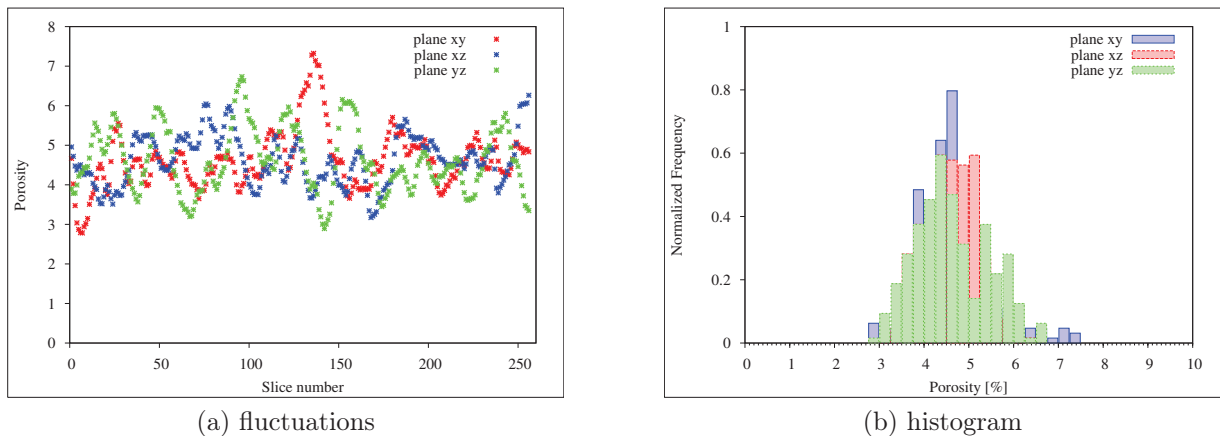


Figure 4.3: Porosity of each slice estimated for all planes of the microstructure.

In order to obtain **effective porosity**, we extract percolated porous network of sandstone, using CCL [Annexe C]. A visualisation of the network is presented in Figure 4.6 (a). The estimated effective porosity of the specimen is:

$$\varphi_{eff} = \frac{V_{eff}}{V_{total}} = 0.029. \quad (4.2)$$

In order to estimate **specific surface** for each pixel of porous phase its neighbourhood is scanned by cross-shaped SE. If any component of structuring element is located in opposite (solid) phase the value of surface increase by  $1 \text{ px}^2$ . After all, obtained value is divided by total volume  $V_{total}$ . The method is presented by Pseudocode A.5 contained in the Annex A. Specific surface of the microstructure of sandstone is equal to:

$$S_t = \frac{S(\varphi)}{V_{total}} = \frac{853054}{V_{total}} = 0.051 \text{ px}^{-1}. \quad (4.3)$$



Table 4.1: Mean number of pores  $\bar{n}$  per slice and standard deviations  $\sigma$  for each plane (FS).

	$XY$	$XZ$	$YZ$
$\bar{n}$	66	68	72
$\sigma$	7	6	7

**Effective specific surface**  $S_{eff}$  is calculated in analogical way for the extracted percolated network, its value is:

$$S_{eff} = \frac{S(\varphi_{eff})}{V_{total}} = \frac{484604}{V_{total}} = 0.029 \text{ px}^{-1}. \quad (4.4)$$

### 4.2.2 Number of pores per slice

This descriptor is obtained by analysing the microstructure of sandstone in 2D images. In order to compute number of disjoint pores, connectivity is defined by 4-neighbourhood cross - shaped structuring element (SE) In Figure 4.4 (a) we can see the fluctuations of number of pore per slice around a mean value [Tab. 4.1]. Normalised histograms are presented in Figure 4.4 (b).

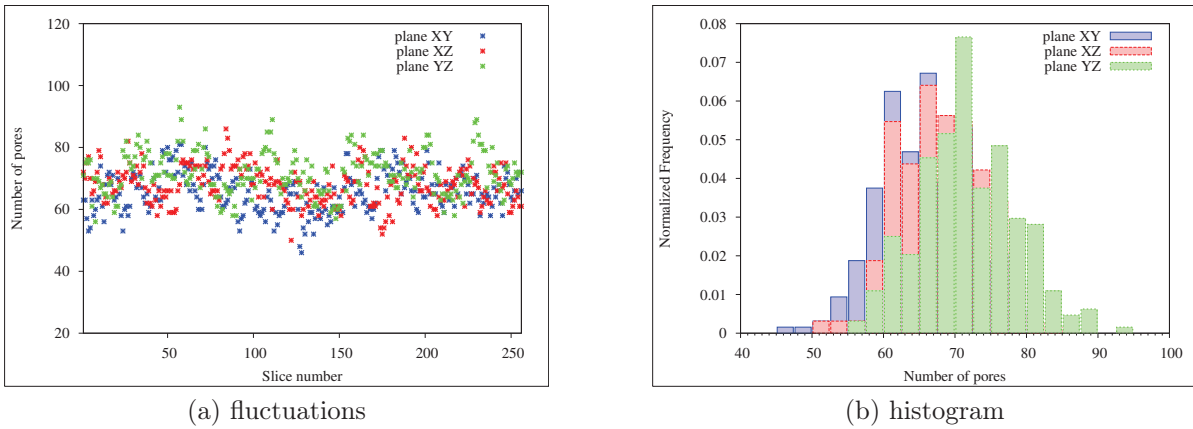


Figure 4.4: Number of pores per slice computed for each plane of the microstructure.

Finally, the mean number of pores per slice and their standard deviations [Fig. 4.4 (b)], for each plane, are summarised in Table 4.1.

The both distributions of global descriptors [Fig. 4.3 and Fig. 4.4] give the first impression that microstructure of sandstone possess geometrical isotropy.

### 4.2.3 Granulometry

Granulometry is an approach to compute a volumetric size distribution of objects in binary images, using a series of morphological opening operations with progressively increasing size of structuring element. In order to estimate granulometry of sandstone we use two different structuring elements: binarized sphere and cross - shaped. Aforementioned method is presented in Section 2.1.

Figure 4.5 (a) shows normalised radii distribution by volume, corresponding to cumulative distribution, presented on the right side [Fig. 4.5 (b)]. Analysis of the figures is summarised in Table 4.2, where mean, median, maximal value of the distributions and standard deviations are presented. As we can see, both distribution are translated with respect to each other, and their values should be tread only as a rough approximation of real granulometry and as a tool to validate reconstructed equivalent samples.

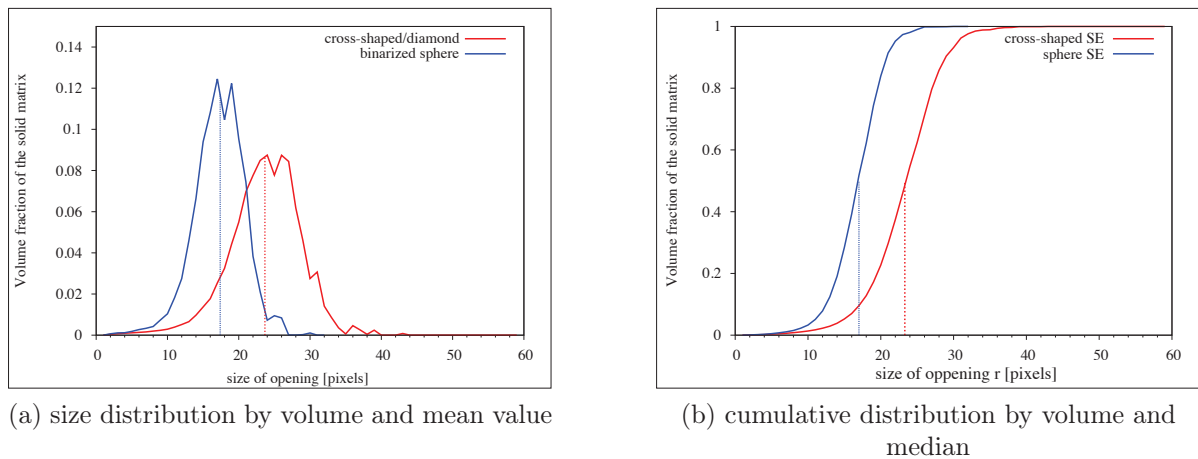


Figure 4.5: Granulometry of sandstone obtained using two different SE.

Table 4.2: Summary of morphological granulometry of sandstone (FS). Notation is following: sign  $\circ$  denote results obtained using binarized spheres, while  $+$  denotes cross-shaped SE and  $\sigma_r$  stands for standard deviation of distribution.

	$r_{max}^{\circ}$	$r_{mean}^{\circ}$	$r_{median}^{\circ}$	$\sigma_r^{\circ}$	$r_{max}^{+}$	$r_{mean}^{+}$	$r_{median}^{+}$	$\sigma_r^{+}$
FS	30	17.4	17	3.5	43	23.7	23.5	4.9

Both mean values,  $r_{mean}^{+} = 23.7 \pm 4.9$  and  $r_{mean}^{\circ} = 17.4 \pm 3.5$ , gives an approximation of the radii that should be used in the reconstruction process, which is discussed and presented in the next section [Section 4.3].

### 4.2.4 Spatial distribution - covariance function

In order to compute covariance of the microstructure we follow the method featured in Section 2.1. Pseudocode A.7 presents this method step by step. Figure 4.6 (b) shows covariance function calculated for three different orientations, along  $\vec{x}$ ,  $\vec{y}$  and  $\vec{z}$  axes.

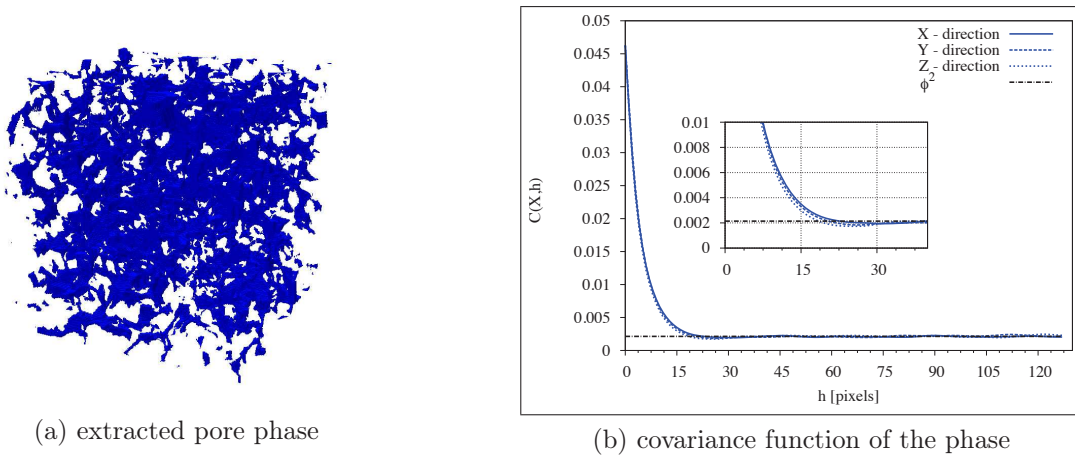


Figure 4.6: Covariance function calculated for entire microstructure of sandstone ( $\varphi = 4.63\%$ ).

The analysis of Figure 4.6 (b) gives us following informations about sandstone's microstructure :

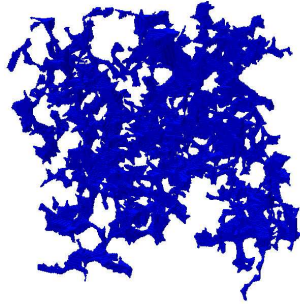
- **geometrical isotropy** - we can see that for each investigated orientations, all plots reach the asymptotic value almost at the same point, what is more, the curves are almost perfectly overlapping
- **covariance range** is about  $A_3 = 23$  pixels - the point when the plot reach the asymptotic value
- **repulsion distance** of structure varies from about  $\delta = 24$  to 31 pixels - the first local minima

The same method was applied to the binary image representing percolated porous network [Fig. 4.7 (a)]. Figure 4.7 (b) presents following informations

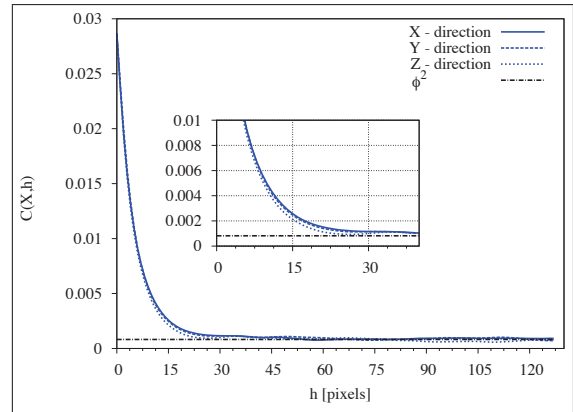
- **geometrical isotropy** - we can see that for all investigated orientations each plot presents similar trend
- **covariance range** depends significantly on the orientation e.g.  $A_3^x = 55$  pixels,  $A_3^y = 70$  pixels, while  $A_3^z = 79$  pixels

What means that from morphological point of view, the RVE size should be bigger if we consider transport phenomena. In this case isolated pores are irrelevant and it is necessary to consider only the percolated network.

In conclusion, microstructure of the studied sandstone presents spatial isotropy of the phases distribution. Hence, we can expect isotropic behaviour in the sense of linear elasticity, where all pores play a role. However, spatial isotropy of the percolated porous phase distribution does not have to imply directly isotropic behaviour in the case of transport properties e.g. tortuosity or permeability.



(a) extracted percolated pore phase



(b) covariance function of the phase

Figure 4.7: Covariance function calculated for percolated porous network of sandstone ( $\varphi_{eff} = 2.86\%$ ).

### 4.2.5 Morphological tortuosity

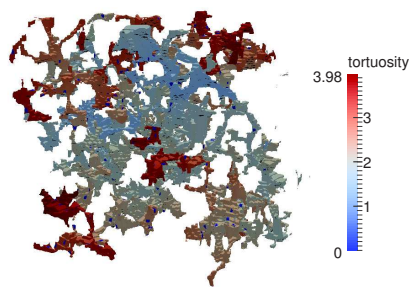
Tortuosity of sandstone is estimated according to the method presented in section 2.1, using Fast Marching algorithm. In order to compute tortuosity we performed 6 tests, two tests for  $\vec{x}$ ,  $\vec{y}$  and  $\vec{z}$  directions. The histograms in Figures 4.8 – 4.10 present the distribution of tortuosity, which were computed for the investigated microstructure. The mean value of tortuosity components  $\tau_i$  is obtained according to following equation:

$$\bar{\tau}_i = \frac{1}{\varphi_{eff}} \langle \tau_i \rangle. \quad (4.5)$$

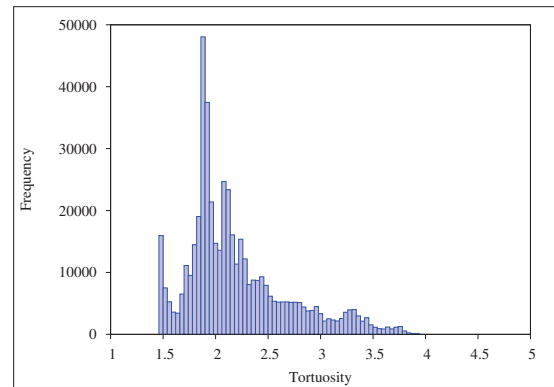
Table 4.3: Summary of morphological tortuosity of sandstone. For each direction the average value  $\bar{\tau}$ , minimal  $\tau_{min}$ , maximal one  $\tau_{max}$  and standard deviation are presented.

	$\tau_x$	$\tau_y$	$\tau_z$
$\bar{\tau}$	2.21	1.92	2.44
$\tau_{min}$	1.48	1.45	1.25
$\tau_{max}$	3.98	3.58	4.67
$\sigma_\tau$	0.49	0.38	0.70

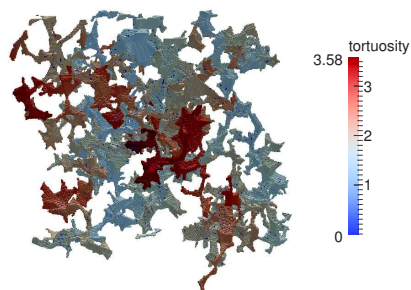
Table 4.3 gives more details about the extremities and average values of tortuosities. Analysing Figures 4.8 – 4.10, we can say that the tortuosity distributions presents different trends. What is more, we can see differences in both between the values of diagonal components as in the character of the distributions. However, for all distributions significant part is included in common range of tortuosities values ( $\bar{\tau}_i \pm \sigma_i$ ). Tortuosity in direction  $\vec{z}$ , which is parallel to gravitational acceleration vector, represent the most tortuous structure. What can be explained by formation process of sandstone, in which gravitational compression induce significant changes of the microstructure.



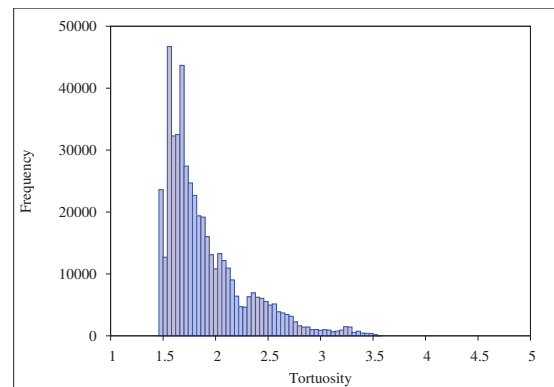
(a) visualisation of distribution



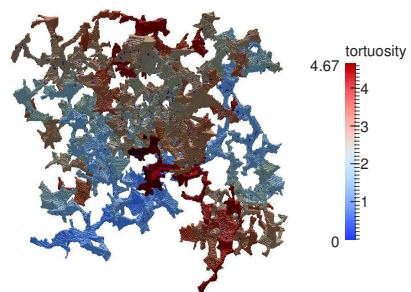
(b) histogram

Figure 4.8: Tortuosity of sandstone; component  $\tau_x$ .

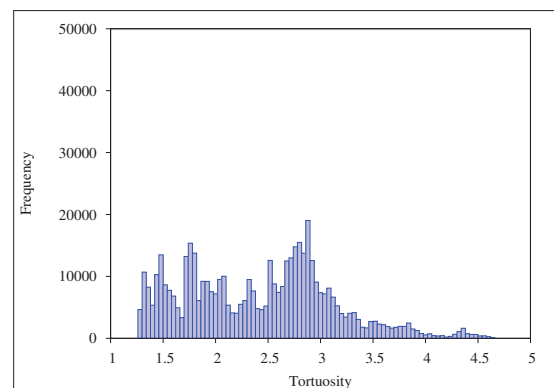
(a) visualisation of distribution



(b) histogram

Figure 4.9: Tortuosity of sandstone; component  $\tau_y$ .

(a) visualisation of distribution



(b) histogram

Figure 4.10: Tortuosity of sandstone; component  $\tau_z$ .

## 4.3 Reconstruction methodology

As we said before, formation process of sandstone consists in series of complex geological and hydrodynamical phenomena. For the purpose of this work, we did not attempt to numerically imitate the natural process of formation of sandstone. The aim is to reconstruct the specimen, in a simplest possible way, by implementing some basic stages inspired by natural process of sandstone formation. In our approach we followed the works of Bake and Øren [4,5], in which the reconstruction is undertaken by following processes:

- **grain deposit** - grain assembly. This stage can be seen as sandgrains transport and deposition.
- **compaction** - bulk volume reduction. This step mimics the natural compression caused by sedimentation.
- **diagenesis** - radii increment. This stage is imitating the cementation and mineralization process.

### 4.3.1 Grain deposit

From the previous analysis we know that the microstructure of sandstone is fully percolated and possess geometrical isotropy. Due to this fact, we used monodisperse spheres, whose deposit is initially isotropic [Figure 4.13]. Besides, in 3D this kind of deposit is initially percolated in all directions. The grains were placed one by one into a three-dimensional box according to the algorithm of gravitational potential minimization [83]. The position of each new grain is chosen to minimise the gravitational potential and no overlapping is allowed. Hence, the grain is placed along line  $L$  such that the  $z$  coordinate of its centre is minimum in the space [Fig. 4.11].

The grains deposit was performed by using LMGC90<sup>2</sup>, which was developed in Mechanics and Civil Engineering Laboratory of the University of Montpellier (LMGC) by F. Dubois and M. Jean [6, 7]. The software allows to model a collections of deformable or rigid particles of various shapes. The size of the three-dimensional box is  $400 \times 400 \times 500$  pixels. To reconstruct the microstructure of sandstone we used three different values of initial radii:

- 10 pixels (8813 grains in the box)
- 15 pixels (2718 grains in the box)
- 20 pixels (1127 grains in the box).

All the initial values of radii were smaller than the mean radius identified by morphological granulometry [Fig. 4.5]. Even if the initial deposit is composed of monodisperse grains, the diagenesis process induces polydispersity and heterogeneity in the sample. For the sake of simplicity, each geometrical deposit is named R10, R15 and R20, where the number denotes the value of initial radius of considered grains assembly.

---

<sup>2</sup>[https://git-xen.lmgc.univ-montp2.fr/lmgc90/lmgc90\\_user/wikis/home](https://git-xen.lmgc.univ-montp2.fr/lmgc90/lmgc90_user/wikis/home)

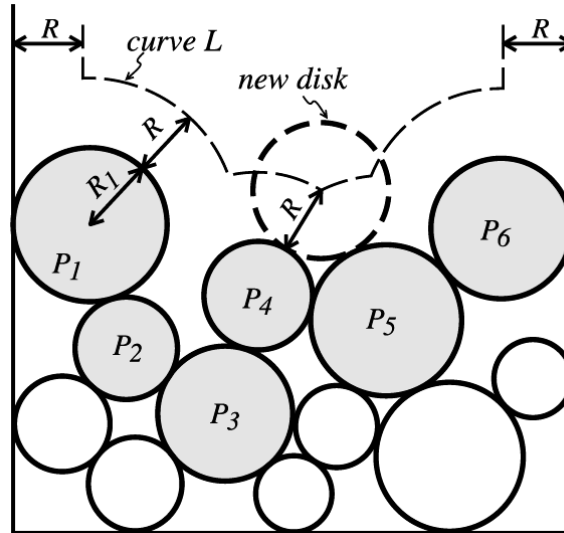


Figure 4.11: Construction of a geometrical deposit. Centre of deposited sphere is located along the curve L and at a point where the gravitational potential is minimum [84].

### 4.3.2 Compaction

Samples, generated according to geometrical rules (potential minimisation), present loose packing of spheres, to increase compacity a compaction step is applied. During compaction, friction coefficient is set to zero, to facilitate rearrangements of the grains. For each geometrical deposit, two different scenarii of compaction are proposed:

- gravitational sedimentation, illustrated in Figure 4.12 (b)
- triaxial compaction, presented in Figure 4.12 (c)

For the sedimentation scenario, a gravity force  $F = mg$  is acting for each grain. The sedimentation is characterised by relative displacement  $\epsilon_z = z_1/h$ , where  $h$  is the initial height of a grain assembly and  $z_1$  is the total change of this height during the sedimentation [Table 4.4].

In case of triaxial compaction, a force is applied on the three walls (right, back, top), while other walls were fixed [Fig. 4.12 (c)]. The triaxial compaction is characterised by relative volume reduction  $\epsilon_V = V_1/V_0$ , where  $V_0$  is the initial volume of the box and  $V_1$  is the volume after the compaction [Table 4.4]. Moreover, for the triaxial compaction the relative displacements  $\epsilon_x$ ,  $\epsilon_y$  and  $\epsilon_z$  are also presented.

After this stage of reconstruction we export the positions of grains centres to perform the next step of the method - diagenesis. Finally, nine different cases are analysed, and for the sake of clarity a new notation is introduced:

- triaxial compactions: C10, C15 and C20
- gravitational sedimentation: S10, S15 and S20
- geometrical deposit: G10, G15 and G20



Table 4.4: Summary of compactions characteristics. For each geometrical deposit: R10, R15 and R20 the values of maximal sedimentation (grey) and relative volume reduction, in case of triaxial compaction, are presented.

	<i>R10</i>	<i>R15</i>	<i>R20</i>
$\epsilon_z$ [%]	19.82	18.97	16.35
$\epsilon_V$ [%]	24.95	20.66	19.88
$\epsilon_x$ [%]	4.56	3.98	2.98
$\epsilon_y$ [%]	4.01	3.01	3.40
$\epsilon_z$ [%]	17.69	15.22	14.52

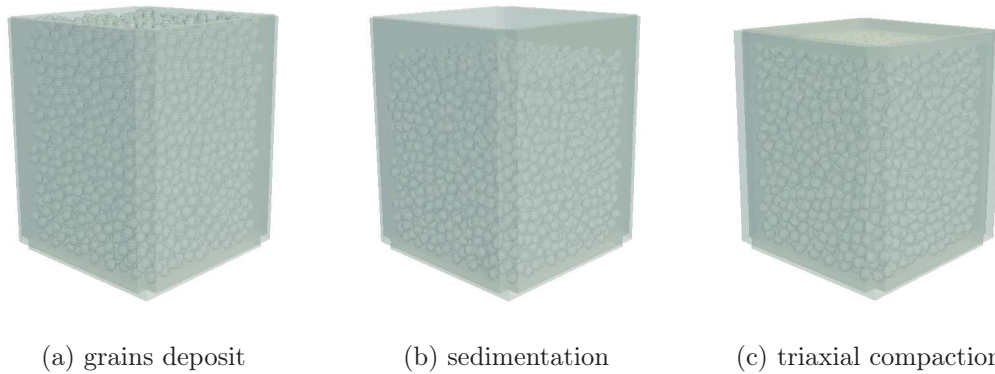


Figure 4.12: Visualisation of the grain deposit stages.

where numbers denote initial radii of the grains assembly.

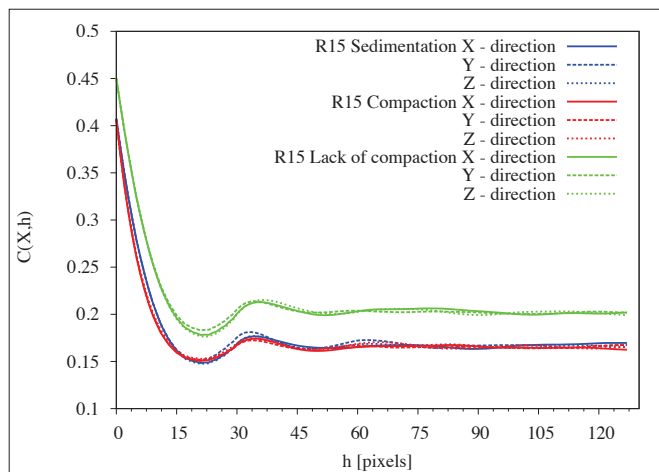


Figure 4.13: Covariance function of the loose grains packing.



### 4.3.3 Diagenesis

In general, aim of diagenesis is to control porosity of a specimen by increasing radii of grains. In order to avoid border effects and regular packing of spheres, porosity is measured in a window ( $256 \times 256 \times 256$  pixels), placed inside the box. The localisation of the window is showed in Figure 4.14. After compaction step, positions of each grain and radii values are exported and treated in code written in c++ to perform the next step of the methodology.

In this thesis, diagenesis process consists of two steps. First step is uniform radii increment by the value of 1 px at the time, until the following criterion is satisfied:

$$\frac{\varphi^{window} - \varphi^{sandstone}}{\varphi^{sandstone}} \geq 0.8, \quad (4.6)$$

where  $\varphi^{window}$  denotes the porosity measured in the window and  $\varphi^{sandstone}$  is the porosity of the reference sample.

The second one, consist in radii increment by 1 px of randomly chosen grains. This step took a place until porosity is adjusted to the desired one with a relative error lower than  $10^{-2}$ .

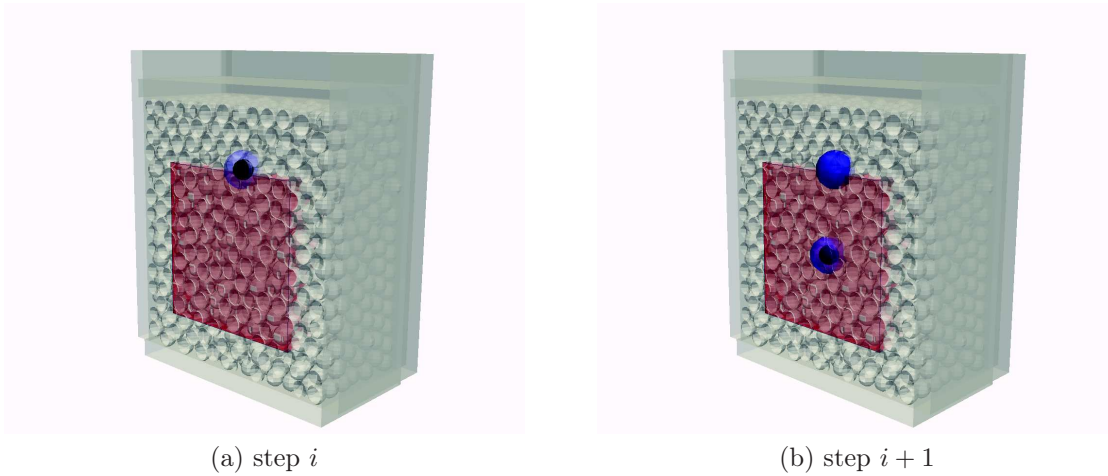


Figure 4.14: Simplified visualisation of the diagenesis process and localisation of the window.

### 4.3.4 Choosing the initial radius

In order to choose the appropriate initial radius of the grain deposit, all the realisations are analysed using following descriptors: specific surface, number of pores per slice, morphological granulometry and covariance function. Aforementioned descriptors are summarised in Table 4.5. We can clearly see that in all cases, except covariance ranges for G15, S15 and G15, the generated samples are missing the reference values - sandstone characteristics. Analysing specific surface  $S_t$ , number of pores per slice  $\bar{n}$  and mean radii  $\bar{r}^+$ , we

can deduce that the searched radii lays between 10 and 15 px. From the point of view of compaction scenarii, no significant difference between generated samples is noticed. However, some characteristics of geometrical deposit G10 ( $S_t$  and  $\bar{n}$ ) are substantially different in comparison with each scenario of compaction (S10 and C10). It seems that it is triggered by fact that geometrical deposit possess significant initial porosity. Therefore, relatively more iterations of radii increment are performed, what can provoke vanishing of small pores. Due to this fact, we can notice low value of specific surface  $S_t$  and number of inclusion in comparison with other deposits with initial radius 10 px.

Table 4.5: Summary of morphological descriptors of each scenario: geometrical deposit (G10, G15, G20); triaxial compaction (C10, C15, C20) and sedimentation (S10, S15, S20)

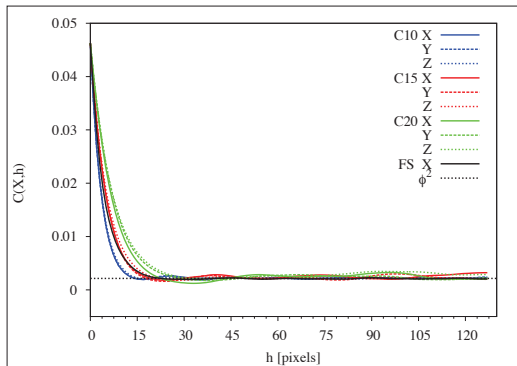
	G10	G15	G20	C10	C15	C20	S10	S15	S20	FS
$S_t$	0.059	0.045	0.033	0.066	0.047	0.034	0.065	0.047	0.034	0.051
$\bar{n}_{xy}$	87	48	30	108	52	29	106	56	28	66
$\bar{n}_{xz}$	88	50	28	107	52	29	104	54	27	68
$\bar{n}_{yz}$	87	48	29	107	53	30	104	54	29	72
$\bar{r}^+$	20.5	26.9	35.4	18.4	25.4	34.1	18.4	25.1	34.8	23.7
$A_3^x$	17	19	28	15	20	23	14	19	29	23
$A_3^y$	34	20	31	15	19	30	15	20	30	21
$A_3^z$	33	23	32	16	22	35	32	23	28	19

Figure 4.15 presents covariance functions computed, for each realisation and for sandstone, in directions  $\vec{x}$ ,  $\vec{y}$  and  $\vec{z}$ . Figures 4.16 and 4.17 show granulometric function and number of pores for plane  $XZ$  respectively. Analysing those plots we can see that deposits composed of grains having the initial radius value  $r_{initial} = 15$  px are in better correlation with sandstone, than the other initial granulometries.

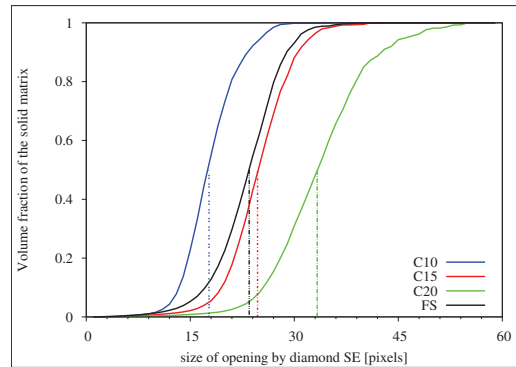
In general, the process of diagenesis can introduce more heterogeneities to the system what can entail differences between plots of covariance function, plotted for different orientations. However, in our case, it is negligible and to justify above, we presented in Figure 4.13 the covariance of generated realisations (R15) before subjecting them to the diagenesis process. We can see that for all scenarios initial isotropy is present and covariance ranges have almost the same value.

Figure 4.18 presents variations of porosity for plane  $XY$ , we can clearly see that fluctuations in the case of triaxial compaction are significantly smaller than in other scenarii and are in better correlations with the reference geometry [Fig. 4.3]. This fact can be explained by more homogenous compaction due to grain rearrangements induced by triaxial compression.

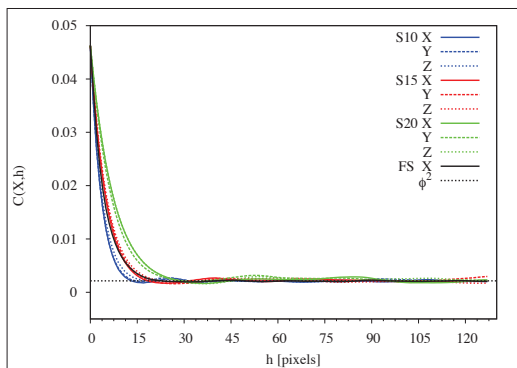
Summarising all, the searched initial radius is in the range from 10 up to 15 px.



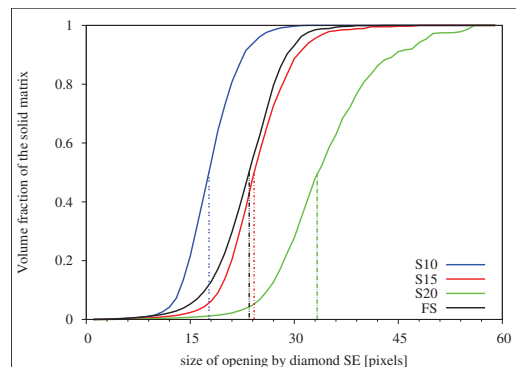
(a) triaxial compaction



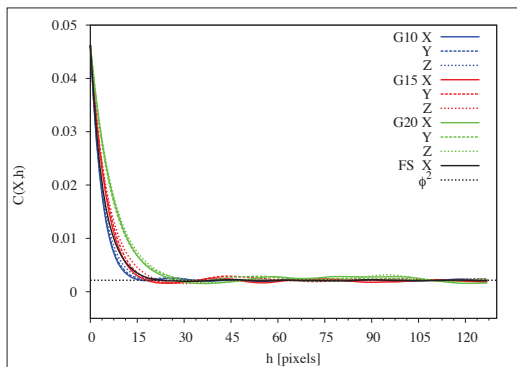
(a) triaxial compaction



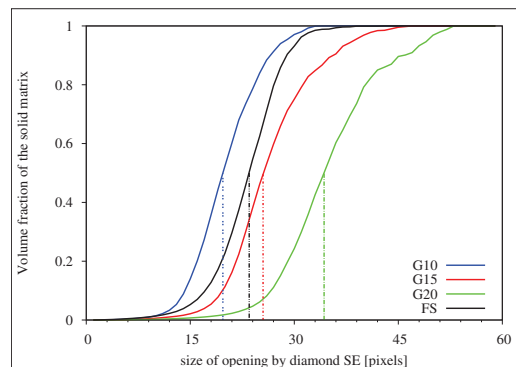
(b) sedimentation



(b) sedimentation



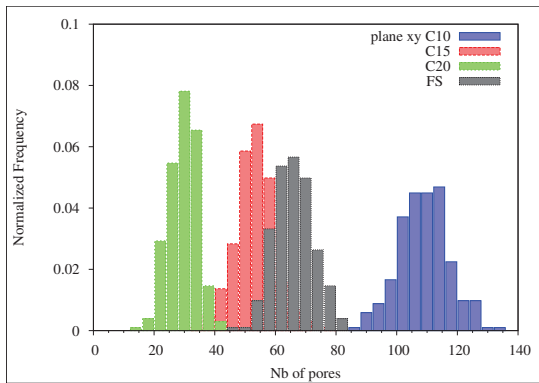
(c) geometrical deposit



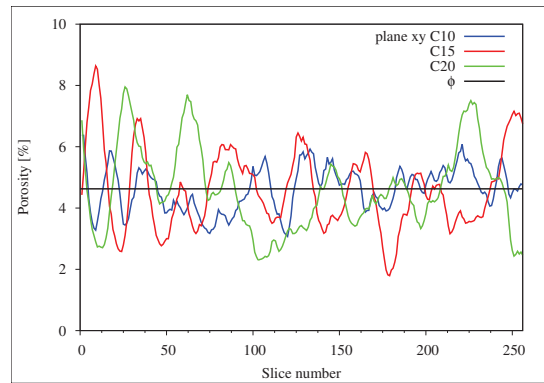
(c) geometrical deposit

Figure 4.15: Covariance function obtained for sandstone and for each deposit. For clarity, only covariance in direction  $\vec{x}$  of the reference geometry (sandstone) is presented.

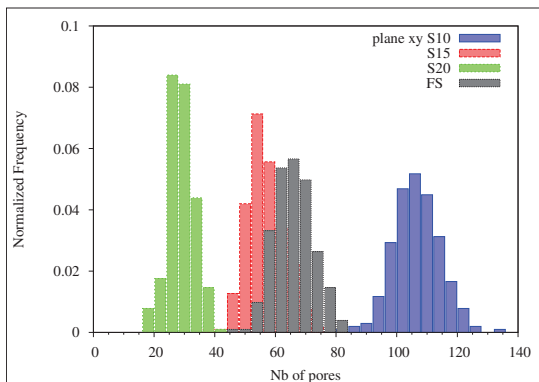
Figure 4.16: Cumulative granulometric curve by volume obtained for sandstone and for each deposit. For each granulometry median value is presented by dashed vertical lines.



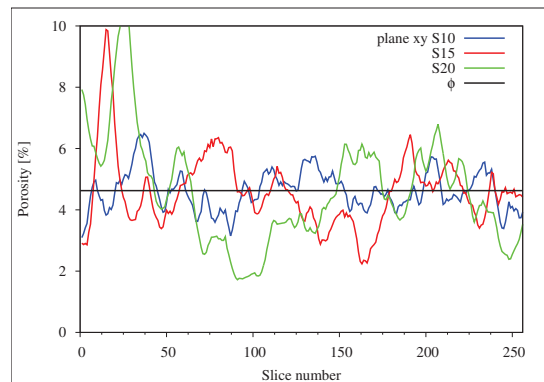
(a) triaxial compaction



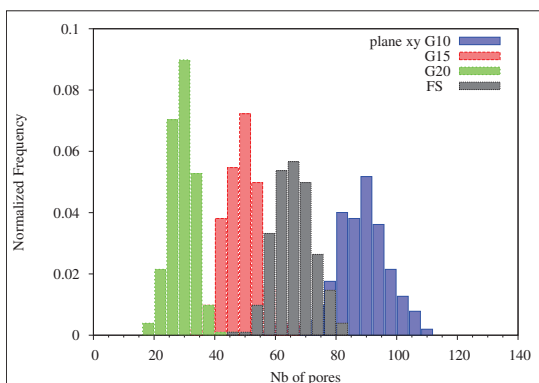
(a) triaxial compaction



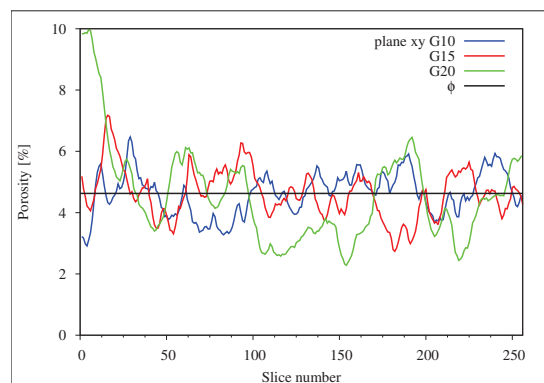
(b) sedimentation



(b) sedimentation



(c) geometrical deposit



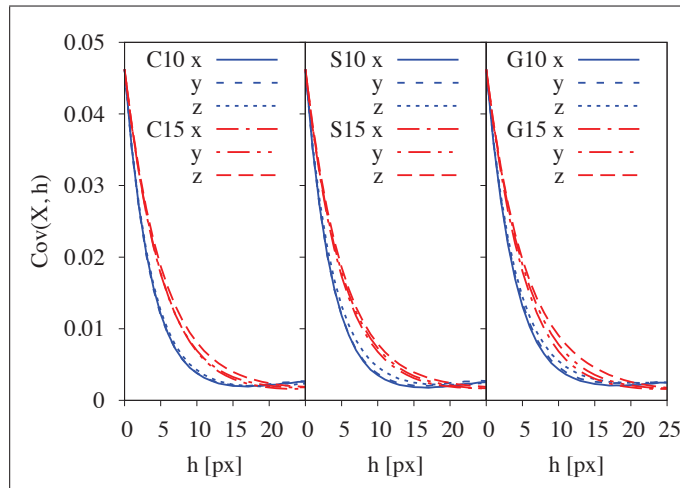
(c) geometrical deposit

Figure 4.17: Histograms presenting number of pores per slice (plane  $XZ$ ) obtained for sandstone and for each deposit.

Figure 4.18: Histograms presenting porosity variations per slice (plane  $XY$ ) obtained for sandstone and for each deposit.

### 4.3.5 Choosing the compaction scenario

Since we know that searched value of initial radius is in the range from 10 up to 15 px, in order to chose the scenario of compaction, we analyse covariance functions presented in Figure 4.19. Each figure presents covariances plotted for each scenario of compaction. The letters C, S, G denote triaxial compaction, sedimentation and geometrical (no compaction) deposit respectively. The numbers 10 [blue] and 15 [red] correspond to different initial radii of grain deposit. Regarding Figure 4.19 and approaching to initial radii of 10 px we can see that the most isotropic geometry is obtained by applying triaxial compaction.



(a)

Figure 4.19: Covariance function of deposits as a descriptor used to compaction scenario. Covariances are plotted for initial values of radii: 10 and 15 px, for each scenario of compaction

### 4.3.6 Analysis of anisotropy of contacts

To dispel any doubts concerning the choice of the scenario of compaction, we present inhere a brief analysis of anisotropy of contacts. Within the framework of contact dynamic, it is convenient to use fabric tensor  $F$  [85] to characterize the distribution of normal directions  $n^c$  at contacts. Fabric tensor is given by:

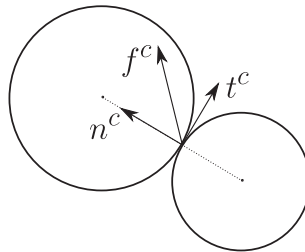


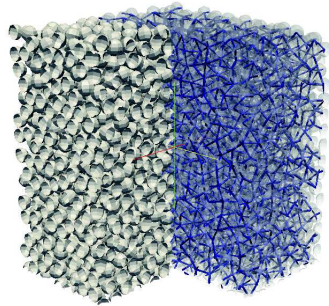
Figure 4.20: Contact force  $f^c$  between two grains and its decomposition on normal  $n^c$  and tangential component  $t^c$ .

$$F = \frac{1}{N_c} \sum_{c=1}^{N_c} n^c \otimes n^c, \quad (4.7)$$

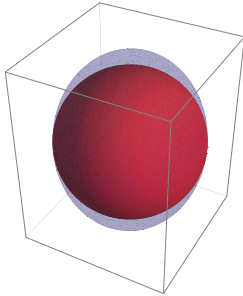
where  $n^c$  is unit vector representing the normal direction of the force at contact,  $\otimes$  is the dyadic product [Fig. 4.20] and  $N_c$  is the number of contacts. The anisotropy parameter  $a_c$  of fabric tensor is characterized by:

$$a_c(F) = 1 - \frac{\|F : I - F\|}{\|F\|}, \quad (4.8)$$

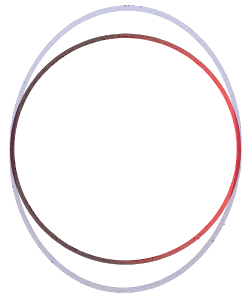
where  $I_{ij} = \delta_{ij}$ , with  $\delta$  the Kronecker delta and  $\|F\| = \sqrt{F : F} = \sqrt{F_{ij}F_{ij}}$  for any second order tensor. We investigate distributions of contacts for sedimentation scenario S15 [Fig. 4.21] and triaxial compaction C15 [Fig. 4.22] in both cases  $r_{initial} = 15$  px. The anisotropy parameter  $a_c(F)$  are equal 0.982 and 0.999 for S15 and C15 respectively. The analysis of contacts anisotropy confirms that the scenario of triaxial compaction with initial radius  $r_{initial} = 15$  px gives the most isotropic results.



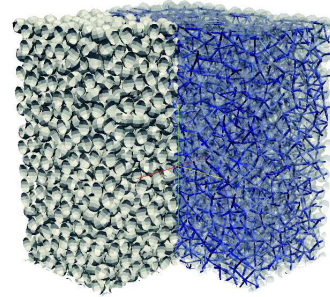
(a) sedimentation scenario and normal forces distribution;  
 $r_{initial} = 15$  px



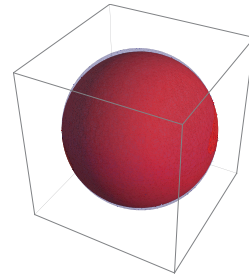
(b) transformation of the unit sphere (red) by the fabric tensor (blue)



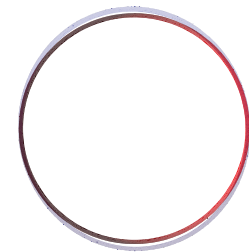
(c) transformation of the unit sphere in plane  $ZY$  for  $x = 0$



(a) triaxial compaction scenario and normal forces distribution;  
 $r_{initial} = 15$  px



(b) transformation of the unit sphere (red) by the fabric tensor (blue)



(c) transformation of the unit sphere in plane  $ZY$  for  $x = 0$

Figure 4.21: Visualisation of normal forces distribution of sedimentation scenario and of associated fabric tensor; the anisotropy parameter  $a_c = 0.982$ .

Figure 4.22: Visualisation of normal forces distribution of triaxial compaction and of associated fabric tensor; the anisotropy parameter  $a_c = 0.999$ .

## 4.4 Morphological validation

Finally, to reconstruct the microstructure of Fontainebleau sandstone, we have chosen  $r_{initial} = 14$  px and triaxial compaction scenario. Each sample is obtained from the same geometrical grain deposit subjected to chosen type of compaction. Nevertheless, the diagenesis process, consisting of random radii increment, allows us to obtain morphologically different microstructures. After all, generated realisations are subjected to rough sorting process, which consists of two filters:

1. **percolation** – samples which were not percolated in all directions were excluded from the further analysis.
2. **effective porosity** – samples which were not satisfying the following condition were excluded:  $\varphi_{eff} = \varphi_{eff}^{sandstone} \pm 5\%$ .

The generation process is stopped when 10 realisations, satisfying above conditions, are constructed. According to the aforementioned conditions, 70 realisations are generated. CPU time necessary to generate those realisations is equal to 21h 7min, what gives 18min 6s per one realisation [2.6 GHz Intel Core i7].

In Figures 4.23, 4.24 and 4.25 we can see comparison of the real microstructure and one of the generated samples. At first sight, we can see that the 3D visualisations of porous network are very similar, therefore, two-dimensional slice as well.

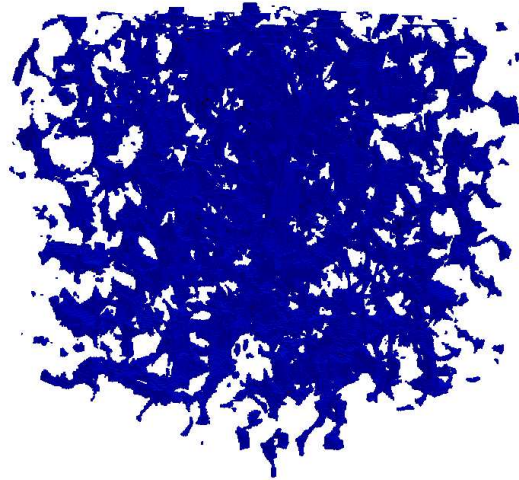


Figure 4.23: 3D visualisation of porous phases of sandstone.



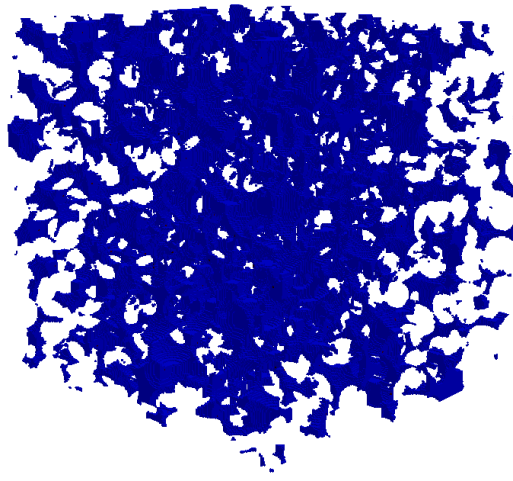
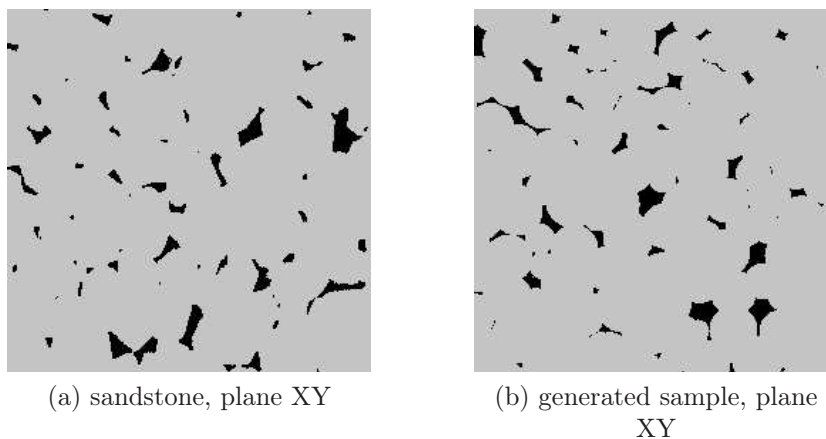


Figure 4.24: 3D visualisation of one selected generated sample porous network.



(a) sandstone, plane XY

(b) generated sample, plane XY

Figure 4.25: Example of 2D images of microstructures: sandstone and generated one.

#### 4.4.1 Basic descriptors and tortuosity

Selected 10 samples are subjected to morphological analysis. Table 4.6 presents basic descriptors like porosity, effective porosity, specific surface, effective specific surface and diagonal components of tortuosity tensor. First row of the table presents the results obtained for the reference geometry - sandstone (FS). The two last ones show average values of the descriptors and standard deviation calculated for the generated specimens. The results present good convergence of global descriptors. The tortuosity, as a descriptor is very sensitive to both, connectivity and spatial distribution of pore phase. However, the values of sandstone's tortuosity are contained in the range of average tortuosities of generated samples and their standard deviations.

Table 4.6: Morphological validation of generated microstructures vs. sandstone.

Name	$\varphi_{eff}[\%]$	$S_t[1/px]$	$S_t^{eff}[1/px]$	$\bar{\tau}_x$	$\bar{\tau}_y$	$\bar{\tau}_z$
<b>FS</b>	2.87	0.0508	0.0289	2.22	1.92	2.44
G1	2.87	0.0497	0.0284	2.41	2.39	2.50
G2	2.86	0.0500	0.0287	2.46	2.59	3.12
G3	2.85	0.0502	0.0289	2.44	2.10	1.99
G4	2.89	0.0499	0.0283	2.40	2.49	1.98
G5	2.72	0.0491	0.0273	1.93	1.85	1.92
G6	2.96	0.0493	0.0292	2.44	2.01	1.91
G7	2.74	0.0500	0.0278	2.64	2.66	2.49
G8	2.96	0.0494	0.0268	2.12	1.96	2.34
G9	2.78	0.0500	0.0275	2.16	2.18	2.89
G10	2.84	0.0502	0.0280	2.09	2.11	1.88
mean	2.80	0.0498	0.0281	2.31	2.23	2.30
st. dev.	0.12	0.0005	0.0007	0.39	0.37	0.41

#### 4.4.2 Covariance

Figure 4.26 presents a spatial descriptor - covariance function. For clarity, results for each direction are presented separately. The figure shows comparison between sandstone and averaged covariance of generated samples for directions:  $\vec{x}$ ,  $\vec{y}$ ,  $\vec{z}$ , and  $\vec{d}$ . We can see a very good spatial correlation between reconstructed specimens and the real microstructure. Table 4.7 presents covariance ranges and their standard deviations obtained for generated samples. For comparison the same characteristics of sandstone are also showed.

Table 4.7: Summary of averaged covariance ranges of the generated samples (GS) and comparison with sandstone (FS).

	$A_3^x$	$A_3^y$	$A_3^z$	$A_3^d$
<b>FS</b>	23	21	19	18
GS	20	19	19	21

What is interesting, mean repulsion distance  $\delta$  of generated samples [Fig. 4.26], does not depend on the orientation. What can be induced by regular shape of solid skeleton components, binarized spheres, and homogeneous distribution of pores.

#### 4.4.3 Granulometry

Figures 4.27–4.28 presents comparison of grain size distribution and cumulative granulometric function by volume of sandstone and averaged ones obtained for generated samples. Although, the methodology of reconstruction is not strictly based on the granulometry of sandstone nevertheless, the results are in good correlation. Table 4.8 presents the most important characteristics e.g. maximal, mean, median values and standard deviations obtained for both structuring elements: binarized sphere and diamond/cross-shaped.

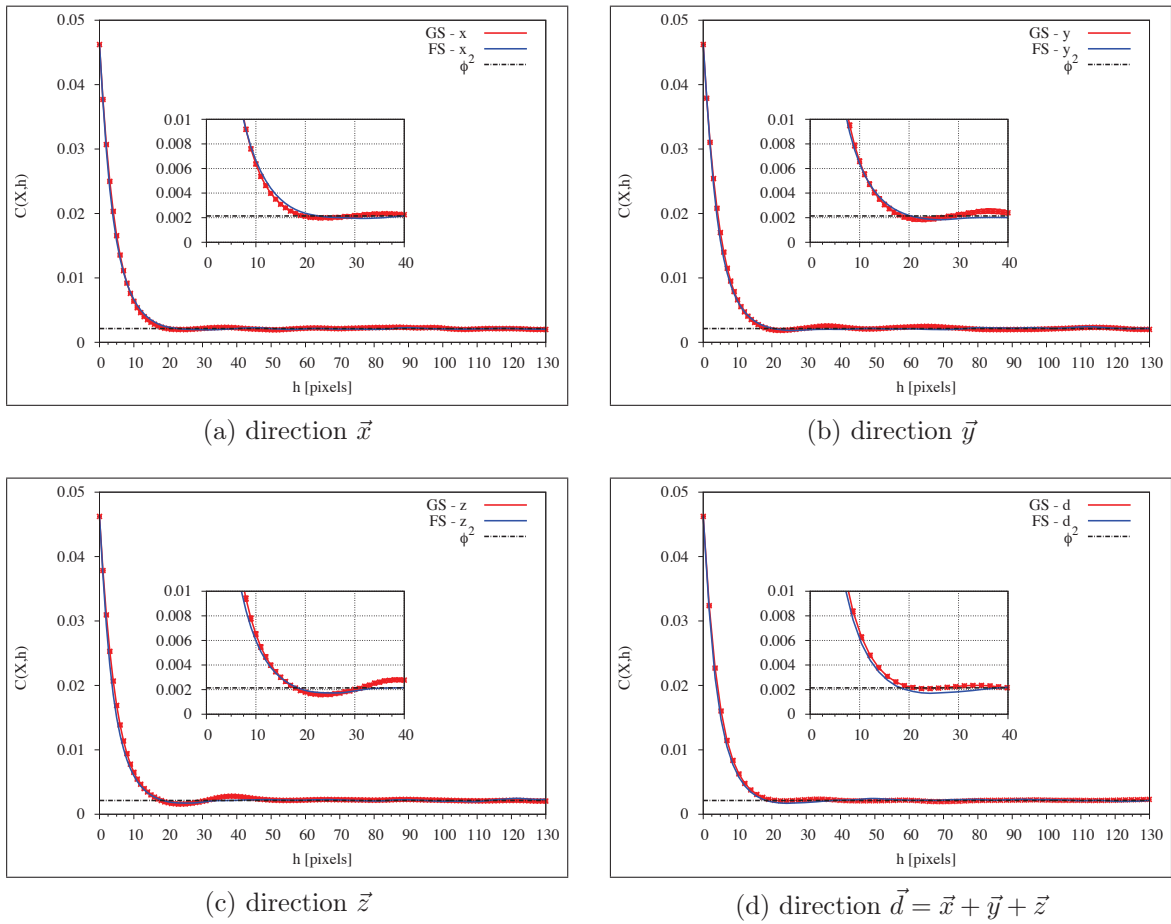


Figure 4.26: Comparison of covariance function of sandstone (FS) and averaged covariance of generated samples (GS); plotted for different directions.

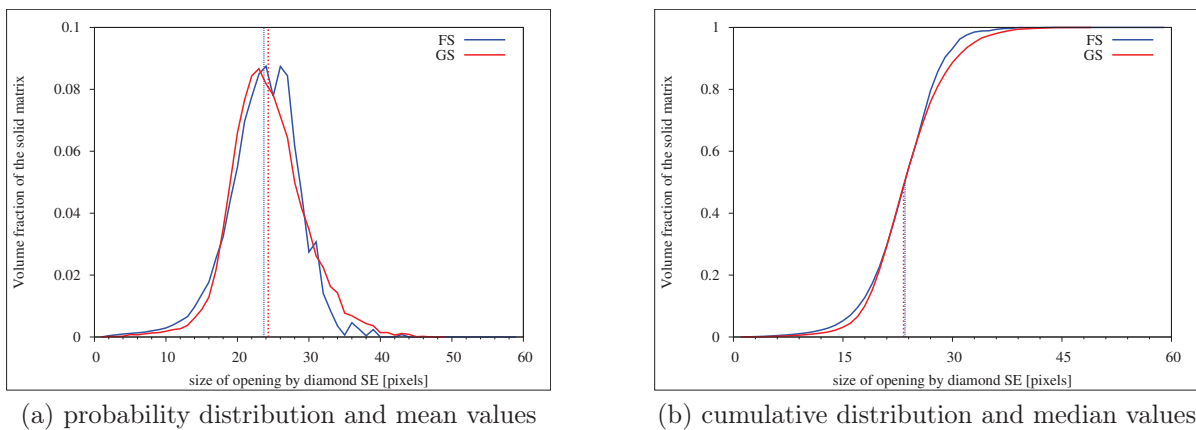


Figure 4.27: Comparison of granulometry (by volume) of sandstone (FS) and averaged obtained for generated samples (GS) using diamond (cross-shaped) SE.

Analysis of covariance function and granulometry, obtained by binarized circle, presents consistency between the repulsion distances  $\delta$  and average solid particle size. We have

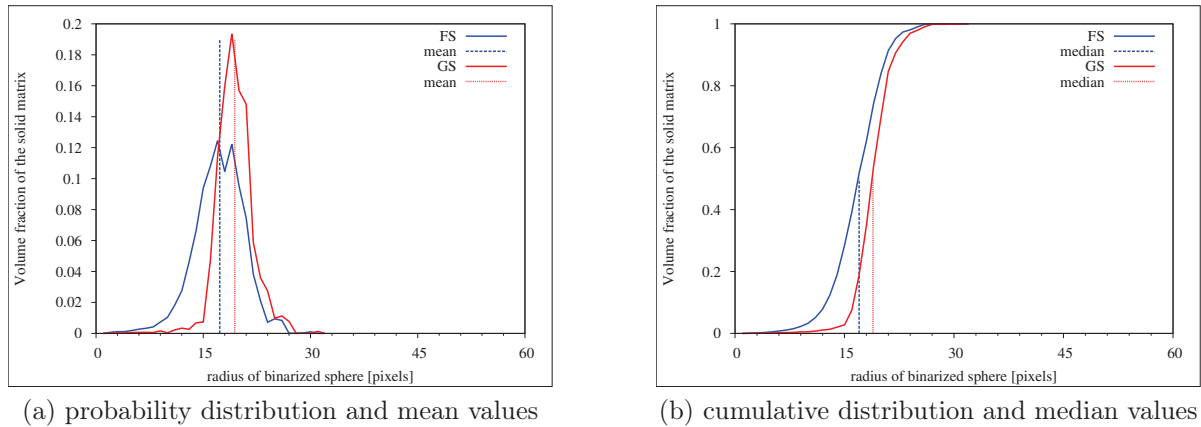


Figure 4.28: Comparison of granulometry (by volume) of sandstone (FS) and averaged obtained for generated samples (GS) using diamond binarized spheres.

Table 4.8: Summary of averaged morphological granulometry of generated samples (GS) and comparison with sandstone (FS).

	$r_{max}^{\circ}$	$r_{mean}^{\circ}$	$r_{median}^{\circ}$	$\sigma_r^{\circ}$	$r_{max}^{+}$	$r_{mean}^{+}$	$r_{median}^{+}$	$\sigma_r^{+}$	$\delta$
FS	30	17.4	17	3.5	43	23.7	23.5	4.9	24-31
GS	31	19.4	18.9	2.5	48	24.3	23.7	5.2	23

to note that repulsion distance is a half of a measure of characteristic length between inclusions, therefore the average value of radius of solid particles should satisfy following condition:

$$r \leq \delta. \quad (4.9)$$

Hence, we can say that granulometry obtained using cross-shaped SE is slightly overestimated. However, taking into account a numerical bias (1 px), we may conclude that granulometry obtained by cross-shaped structuring element is passable.

## 4.5 Partial conclusions

In this chapter, firstly, a detailed characterisation of the real microstructure is provided. Performed morphological description is based on binary image analysis and mathematical morphology, that can quantitatively describe the geometrical properties of the microstructure. In the analysis, four types of descriptors are: global, sizing of objects, spatial distribution and connectivity. Porosity and specific surface are introduced as a basic global descriptors. Morphological openings operations are used to extract granulometry of specimen. Spatial distribution of phases is characterised by covariance function. Morphological tortuosity, used to describe connectivity, confirms the fact that the investigated microstructure is percolated in each direction.

Secondly, an efficient method to generated equivalent microstructure, inspired by natural process, is proposed. The method consist in three steps: grain deposit, compaction and diagenesis process. Grain deposit, a step that imitates the transport of sand grains, is

composed of monodisperse spheres which are deposited in 3D box.

During the compaction step, that can be seen as a sandgrains bulk volume reduction, a triaxial compression is used. The diagenesis process, that imitates mineralization, is composed of two phases, first is a uniform radii increment and second, composed of random radii increment. The diagenesis process - induces heterogeneity of grains collection and polydispersity.

Finally, the morphological description of the generated samples confirms that they can be treated as statistically equivalent realisations of investigated Fontainebleau sandstone's microstructure. To select 10 representative realisations a rough sorting process, consists of two filters concerning effective porosity and connectivity, is used. Using the reconstruction methodology we can easily obtain samples which are percolated in all directions.


*—When shall we three meet again in  
thunder, lightning, or in rain? —When  
the hurlyburly's done, when the battle's  
lost and won.*

Shakespeare, Macbeth

# 5

## Numerical dissolution and evolution of morphological descriptors

---

 In this chapter two models of chemical dissolution are presented. Microstructure of Fontainebleau sandstone and all generated samples are subjected to two different scenarios of numerical dissolution. Chemical dissolution triggers microstructure modifications which induce evolution of the macroscopic behaviour of the media. Therefore, evolution of certain morphological descriptors is presented and discussed.

---

**Contents**

---

5.1	Methodology . . . . .	79
5.2	Isotropic dissolution – morphological description . . . . .	83
5.3	Dissolution of percolated porous network . . . . .	89
5.4	Conclusions . . . . .	96

---

## 5.1 Methodology

Analysis of binarized geometry of natural rock gives only approximation of real connectivity. Therefore, we investigate two different scenarii of dissolution - firstly, dissolution of the entire pore space and than of the percolated network. Model of numerical dissolution is based on basic operation of mathematical morphology - dilation. Chemical degradation of the solid skeleton is taken into account in a simplified way, by performing dilation of the porous phase using cubic structuring element. The choice of an 3D isotropic SE can be justified by far field and long term conditions, when concentration of reactants is assumed to be homogeneously distributed in the pores space at the sample scale [2, 8]. Hence, at each iteration (dissolution step) all solid voxels from 26-neighbourhood of the pores are removed. Two different scenarii are considered:

- isotropic dissolution – consist in dissolving all void space even if pores are isolated [Fig. 5.1 (a)]
- dissolution of percolated network – consist in dissolving only percolated porous network [Fig. 5.1 (b)].

The proposed modelling is universal, in the sense that it uses non-dimensional time scale. Therefore, it can be adjusted to any time-dependent process. Moreover, the precipitation of minerals could also be easily introduced by this method.

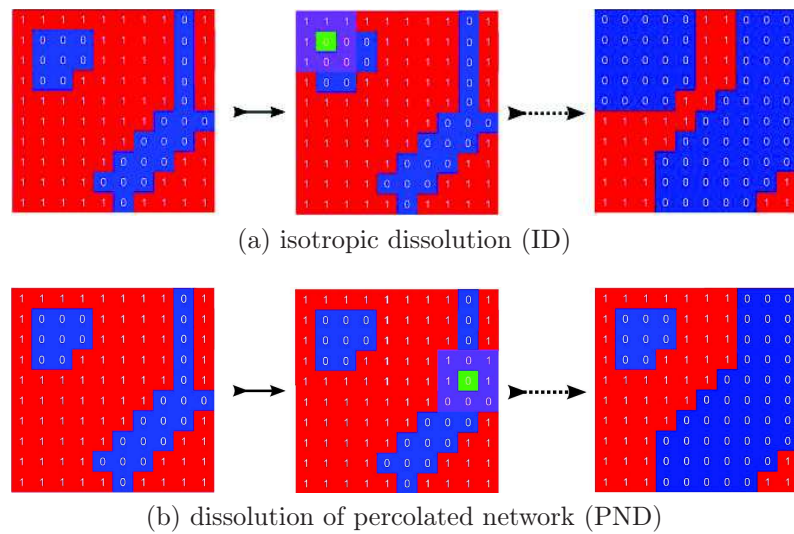


Figure 5.1: Visualisation of two scenarii of numerical dissolution in 2D, simplified case.

Let set  $X$  represents binary image of porous medium. The results of  $i$ -th step of isotropic dissolution is defined by dilation of porous phase, by structuring element  $B$ . We can write, in recursive form:

$$X_i^{iso} = X_{i-1}^{iso} \oplus B, \quad i \in \{1, 2, 3 \dots\}, \quad (5.1)$$

where  $X_0^{iso} = X_0$  is the initial image and exponent  $iso$  stands for isotropic dissolution. Figure 5.2 presents effect of this scenario on 3D microstructures.



Let us denote by  $\Xi(\cdot)$  an operator acting on binary image, which returns percolated porous network. The results of  $i$ -th step of percolated network dissolution is defined by dilation of the extracted percolated porous phase, by structuring element  $B$ . It can be written in following way:

$$X_i^{pnd} = \left[ \Xi \left( X_{i-1}^{pnd} \right) \oplus B \right] + X_0, \quad i \in \{1, 2, 3 \dots\}, \quad (5.2)$$

where  $X_0^{pnd} = X_0$  is the initial image, sign '+' is the addition of binary images and exponent *pnd* stands for percolated network dissolution.

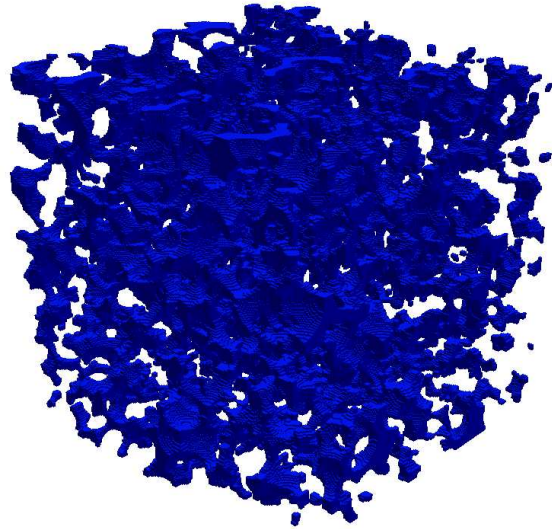
The following equation:

$$\Xi \left( X_i^{pnd} \right) = \Xi \left( X_i^{iso} \right), \quad i \in \{1, 2, 3 \dots\}, \quad (5.3)$$

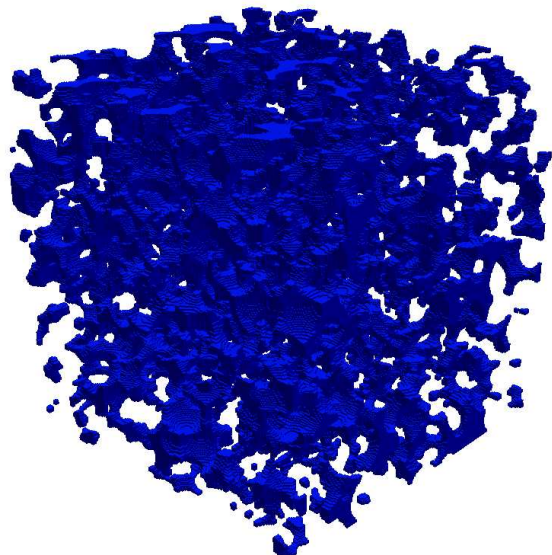
is satisfied only when percolated network never connects with isolated pores in both cases or isolated pores do not exist.

Dissolution processes, described by equations 5.1 – 5.2 are performed in 3D and are stopped when porosity reach about 40%. What means that in both cases, of isotropic dissolution and percolated porous network, we perform respectively, 4 and 6 iterations. Aforementioned method is illustrated in Figures 5.3 and 5.4. Both figures present evolving microstructure of Fontainebleau sandstone (2D slices) during isotropic and percolated network dissolution scenario respectively. In Figure 5.4 two pores are included in a circle, pore in blue circle connects and get dissolved [Fig. 5.4 (d) - (e)], while the pore in red circle remains isolated.

Methodology of estimating morphological descriptors is the same like in previous chapter. Analysis is performed for each geometry representing different stage of dissolution. In this chapter main global parameters, like porosity, specific surface and their effective equivalents, are presented and analysed. To describe modifications of solid skeleton, evolution of granulometric function is showed. Evolution of spatial distribution of porous phase is presented using covariance functions. Finally, morphological tortuosity is discussed. Aforementioned analysis is provided for both scenarii of numerical dissolution. All the figures present comparison between behaviour of real geometry (blue) and averaged trend of generated realisations (red).



(a) FS



(b) G4

Figure 5.2: Visualisation of pores space at 2nd dissolution step of isotropic dissolution. Fontainebleau sandstone (FS) and one of the generated samples (G4).

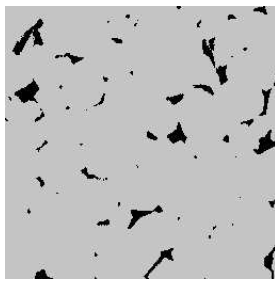
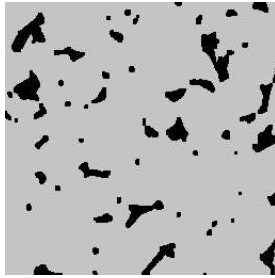
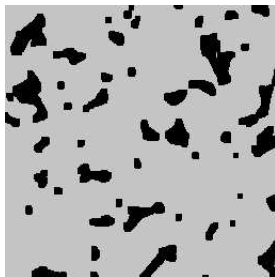
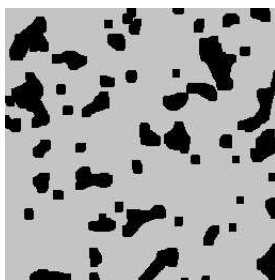
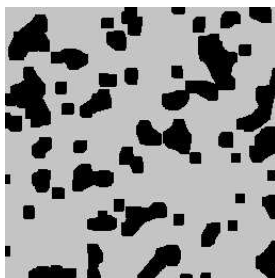
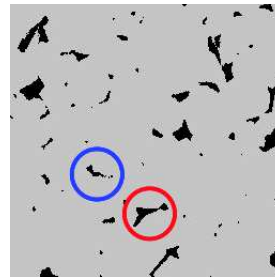
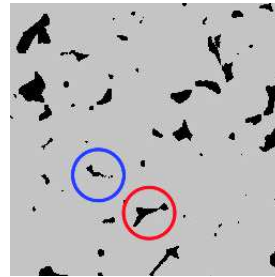
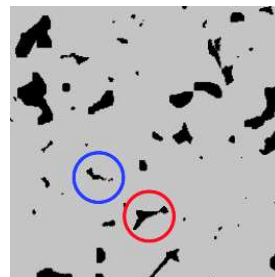
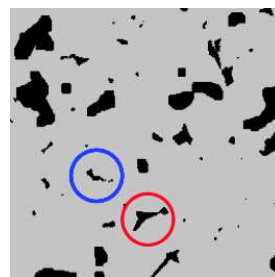
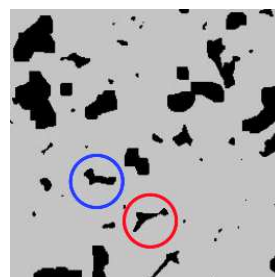
(a) initial image  $X_0$ (b) first step  $X_1^{iso}$ (c) second step  $X_2^{iso}$ (d) third step  $X_3^{iso}$ (e) fourth step  $X_4^{iso}$ (a) initial image  $X_0$ (b) first step  $X_1^{pnd}$ (c) second step  $X_2^{pnd}$ (d) third step  $X_3^{pnd}$ (e) fourth step  $X_4^{pnd}$ 

Figure 5.3: Four steps of isotropic dissolution scenario. Example of sandstone, plane  $XY$ ,  $z = 1$ .

Figure 5.4: Four steps of dissolution of percolated network. Example of sandstone, plane  $XY$ ,  $z = 1$ .

## 5.2 Isotropic dissolution – morphological description

Analysis begins with the evolution of global descriptors like porosity and effective porosity, which are presented in Figure 5.5 (a) and Figure 5.5 (b) respectively. We can see a comparison of sandstone behaviour and average trend obtained for generated samples. Porosity and effective porosity of sandstone increase faster in function of dissolution step. This can be triggered by fusions of pores whose are distributed initially in slightly different way. Moreover, during isotropic dissolution connections with isolated pores are easily achieved and can change significantly evolution of mentioned descriptors.

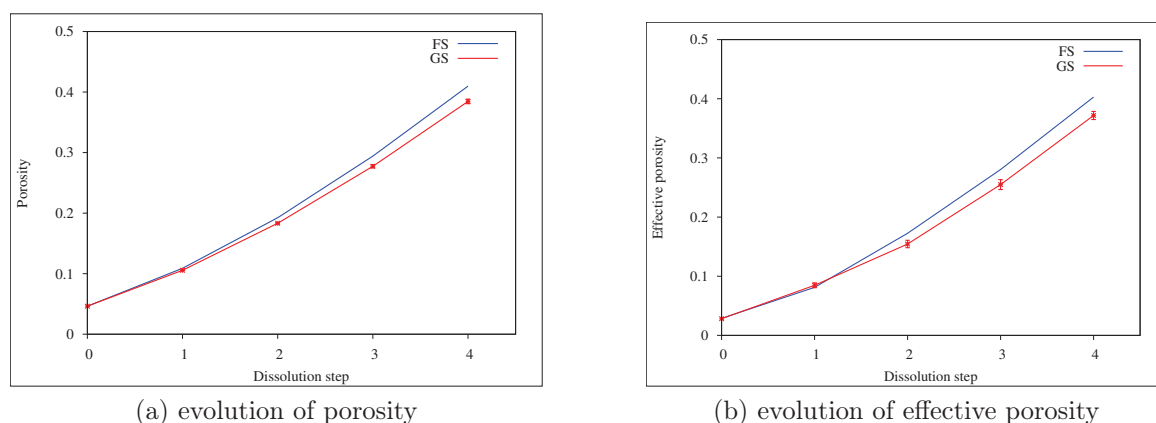


Figure 5.5: Evolution of porosity and effective porosity as a function of dissolution step.

Figure 5.6 (a) and Figure 5.6 (b) present evolution of specific surface and effective specific surface respectively. In general, specific surface and effective specific surface of sandstone increase faster. Moreover, the significant increase of effective specific surface value, between step 1 and 2, presented in Figure 5.6 (b), with respect to quite uniform increase of specific surface [Fig. 5.6 (a)], may be explained by fusion of isolated pores with percolated network.

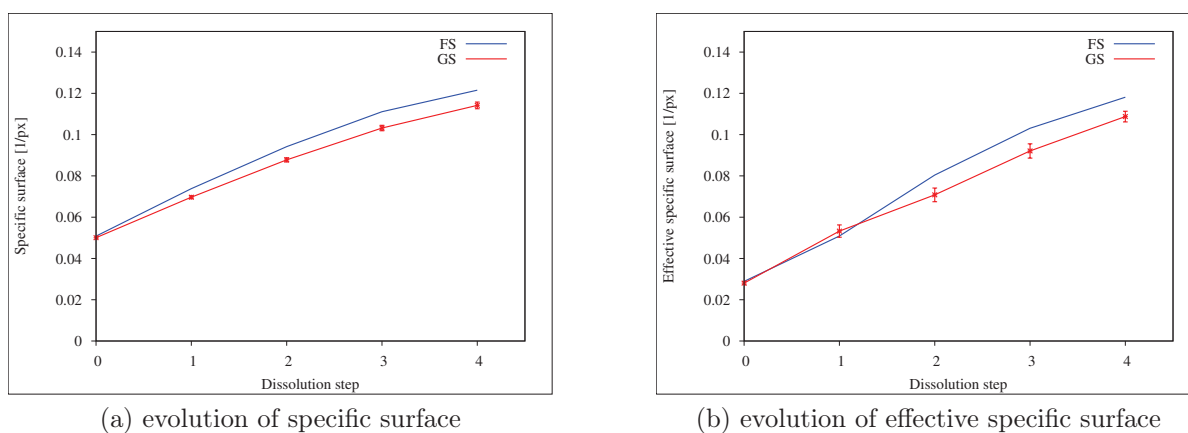


Figure 5.6: Evolution of specific surface and effective specific surface as a function of dissolution step.

The next descriptor is covariance function. Figures 5.7 and 5.8 present averaged covariance evolution of generated samples and covariance of sandstone. For the sake of simplicity the functions are plotted for three chosen directions:  $\vec{x}$ ,  $\vec{y}$  and  $\vec{z}$ . Values of covariance ranges and repulsion distances of generated samples and sandstone are summarised in Table 5.1 and 5.2 respectively.

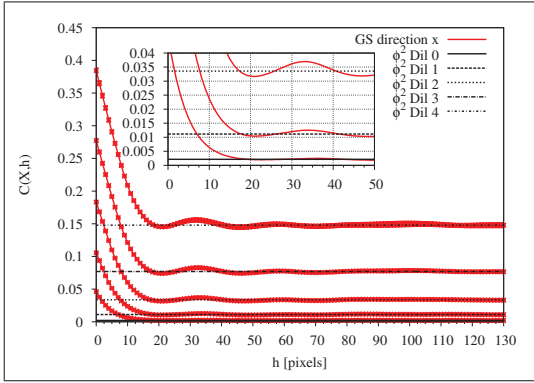
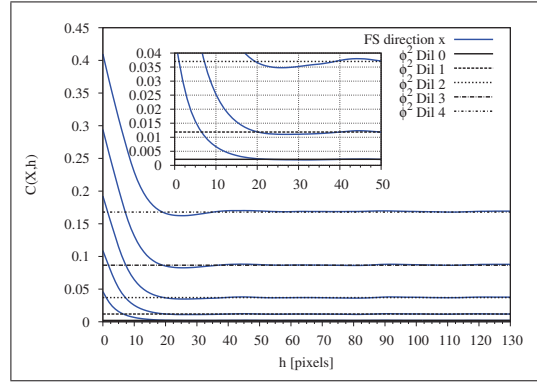
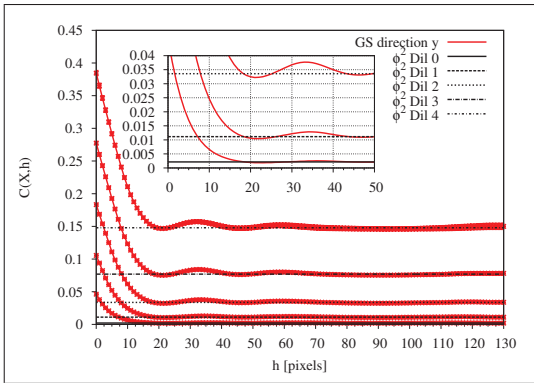
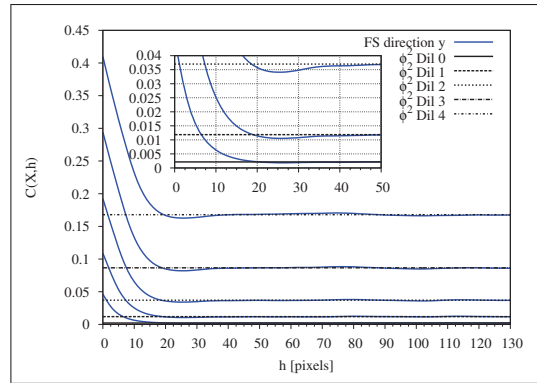
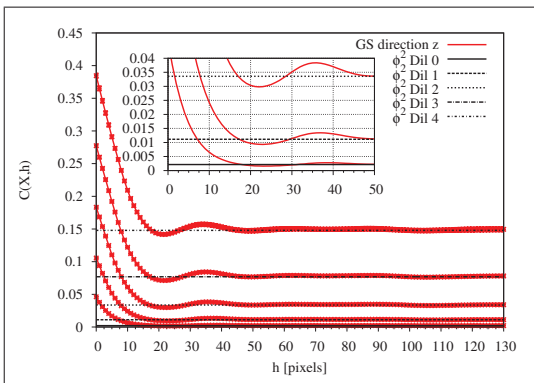
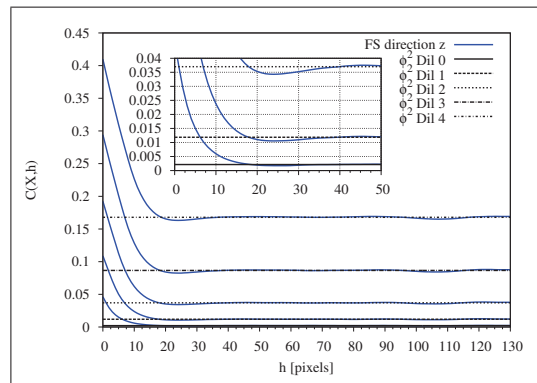
(a) covariance function for direction  $\vec{x}$ (a) covariance function for direction  $\vec{x}$ (b) covariance function for direction  $\vec{y}$ (b) covariance function for direction  $\vec{y}$ (c) covariance function for direction  $\vec{z}$ (c) covariance function for direction  $\vec{z}$ 

Figure 5.7: Evolution of averaged covariance of generated samples.

Figure 5.8: Evolution of covariance function of Fontainebleau sandstone.

At first sight we can see that in both figures evolution of generated samples and sandstone is almost the same. Moreover, for both specimen, covariance range remains quasi-constant for all dissolution steps and geometrical isotropy is conserved. Small fluctuations of covariance range may be explained by a numerical bias linked to the method of estimation. In general, a fact that characteristic length of microstructure is almost constant during isotropic dissolution scenario implies that the RVE size can remain constant. The method of dissolution by cubic SE does not perturb initial isotropy of the system. General decrease of repulsion distance is present. However, the change is expected to be more significant (1 px for each dissolution step).

Figures 5.9 and 5.10 present evolutions of covariance functions of generated samples and sandstone calculated for extracted percolated network (isotropic dissolution). At first sight we can see that both function present similar behaviour. However, for generated samples, covariance range increases almost twice in comparison to the covariance range of entire pore network. This implies that the RVE size should be bigger in the case when only the percolated network is taken into account. Nonetheless, the geometrical isotropy is conserved.

Table 5.1: Evolution of covariance ranges and repulsion distances obtained from averaged covariance function of generated samples. Isotropic dissolution scenario.

	$A_3^x$	$A_3^y$	$A_3^z$	$\delta_x$	$\delta_y$	$\delta_z$
Initial	20	19	19	23	23	23
Step 1	18	18	18	21	21	23
Step 2	18	19	18	21	22	22
Step 3	18	19	18	21	21	22
Step 4	19	20	18	21	21	21

In case of sandstone, evolution of covariance of entire [Fig. 5.8] and percolated network [Fig. 5.10] are almost identical, what is caused by the fact that since 2nd dissolution step more than 90% of the pore space is represented by percolated network. Interesting conclusion is the fact that for initial state and 1st dissolution state the covariance ranges are significantly greater than for other further stages. Hence, it is possible, that the RVE size of percolated network can decrease during the isotropic dissolution process.

Table 5.2: Evolution of covariance ranges and repulsion distances obtained for sandstone. Isotropic dissolution scenario.

	$A_3^x$	$A_3^y$	$A_3^z$	$\delta_x$	$\delta_y$	$\delta_z$
Initial	23	21	19	31	26	24
Step 1	24	19	18	27	26	24
Step 2	20	19	18	26	25	24
Step 3	20	19	19	26	25	24
Step 4	19	20	19	25	26	24

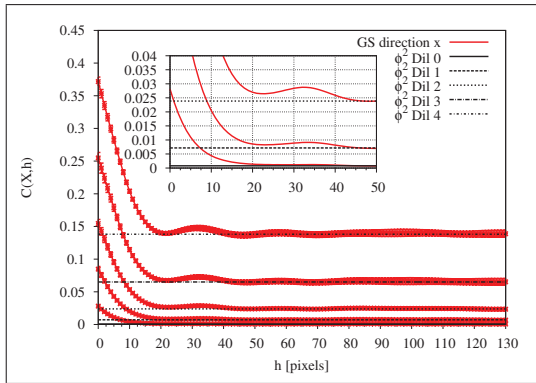
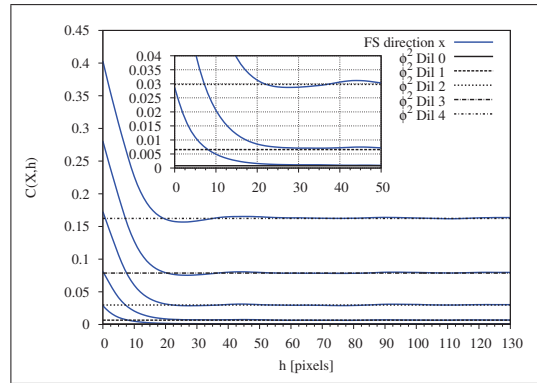
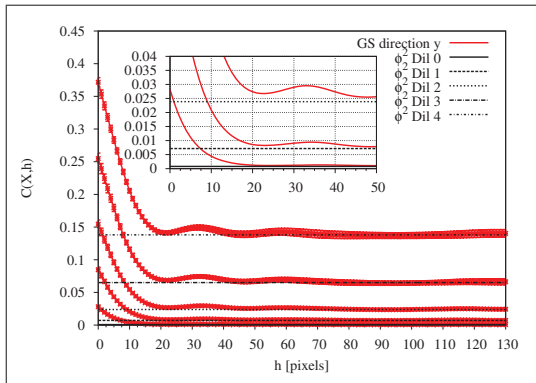
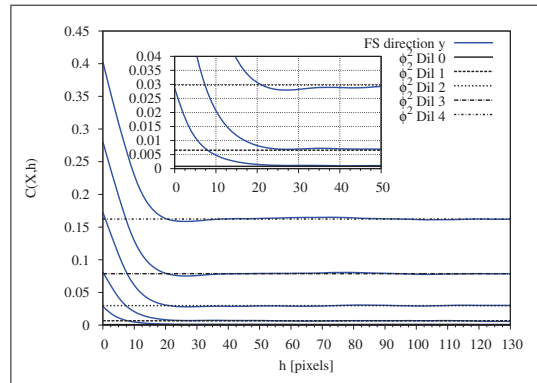
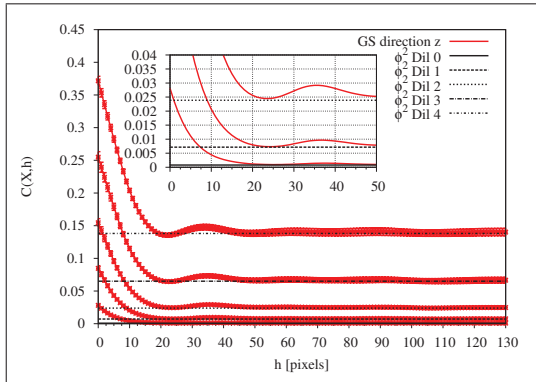
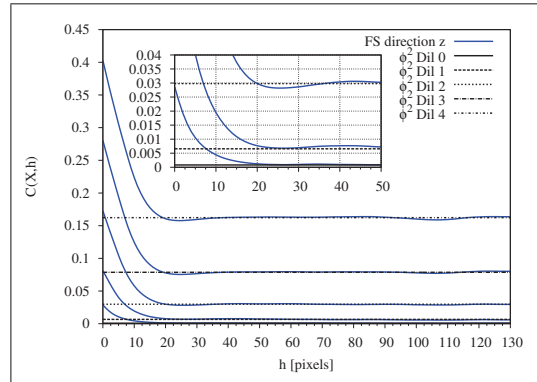
(a) covariance function for direction  $\vec{x}$ (a) covariance function for direction  $\vec{x}$ (b) covariance function for direction  $\vec{y}$ (b) covariance function for direction  $\vec{y}$ (c) covariance function for direction  $\vec{z}$ (c) covariance function for direction  $\vec{z}$ 

Figure 5.9: Evolution of averaged covariance function of generated samples. Case of extracted percolated network during isotropic dissolution.

Figure 5.10: Evolution of covariance function of Fontainebleau sandstone. Case of extracted percolated network during isotropic dissolution.



Figure 5.11 presents evolution of tortuosity components during isotropic dissolution. Results are summarised in Table 5.3, general decreasing trend versus asymptotic value equal to 1 is observed. At first sight we can notice that with progressive dissolution both evolutions of tortuosities (sandstone and generated samples) get more convergent. Similar behaviour concerns values of all components what is triggered by fusions of isotropically distributed pores and straightening of paths due to the dilation. Moreover, standard deviations decrease progressively what can be explained by translation of distributions towards the limit value equal to 1. Similar behaviour is observed for all directions. For the sake of simplicity, the fact is justified by Figure 5.11 (d) presenting distributions of tortuosity component  $\tau_z$ , of one of generated samples, at initial state, 2nd and final one.

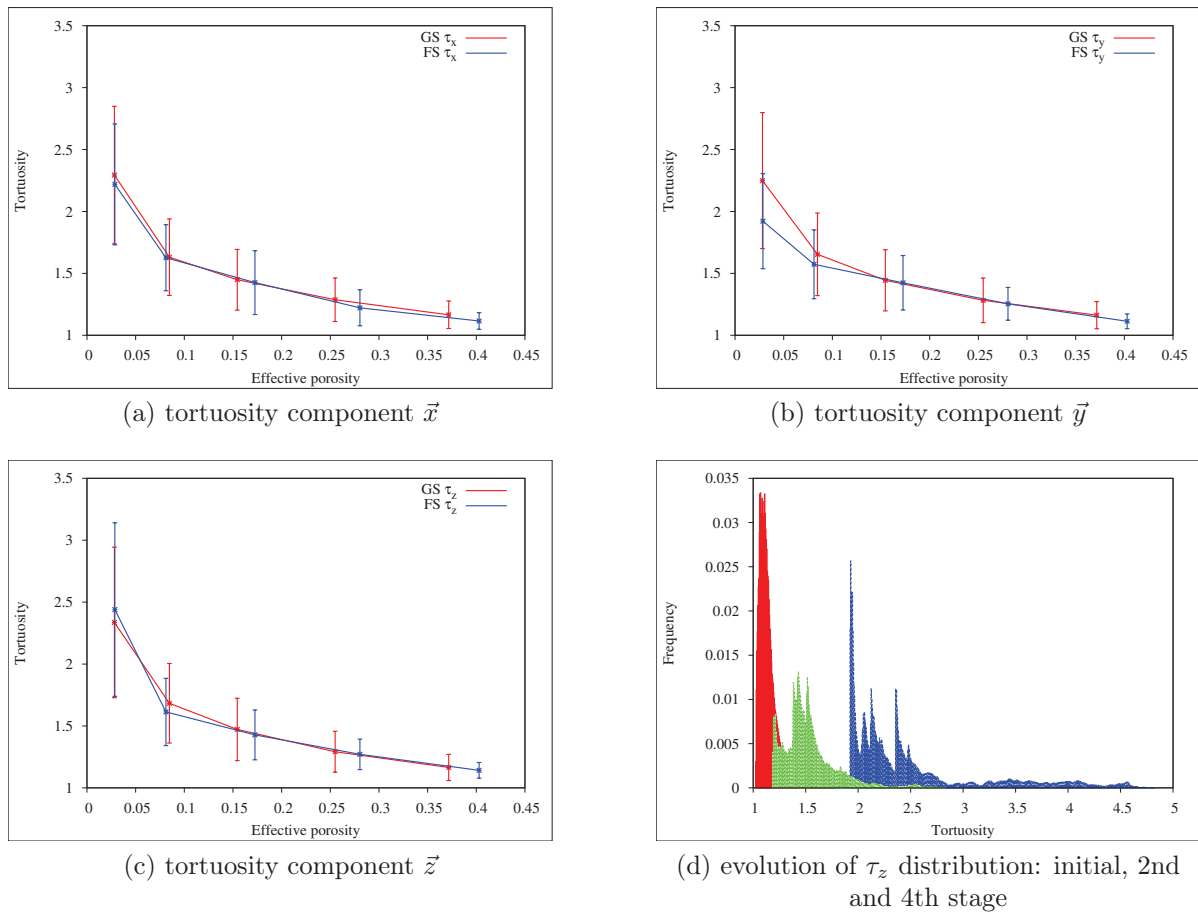


Figure 5.11: Evolution of tortuosity components  $\bar{\tau}_x$ ,  $\bar{\tau}_y$  and  $\bar{\tau}_z$  as a function of effective porosity – isotropic dissolution scenario. Subfigure (d) presents evolution of distribution for one of the generated samples.



Table 5.3: Evolution of tortuosity components and standard deviations of mean distributions. Isotropic dissolution scenario.

FS	$\bar{\tau}_x$	$\bar{\tau}_y$	$\bar{\tau}_z$	$\sigma_{\tau_x}$	$\sigma_{\tau_y}$	$\sigma_{\tau_z}$
Initial	2.22	1.92	2.44	0.49	0.38	0.70
Step 1	1.63	1.57	1.61	0.27	0.28	0.27
Step 2	1.43	1.42	1.43	0.26	0.22	0.20
Step 3	1.22	1.25	1.27	0.15	0.13	0.12
Step 4	1.12	1.11	1.14	0.07	0.06	0.06
GS	$\bar{\tau}_x$	$\bar{\tau}_y$	$\bar{\tau}_z$	$\sigma_{\tau_x}$	$\sigma_{\tau_y}$	$\sigma_{\tau_z}$
Initial	2.31	2.23	2.30	0.50	0.49	0.55
Step 1	1.63	1.65	1.68	0.31	0.33	0.32
Step 2	1.45	1.44	1.47	0.24	0.25	0.25
Step 3	1.29	1.28	1.29	0.18	0.18	0.17
Step 4	1.16	1.16	1.16	0.11	0.11	0.11

The next descriptor, which is presented in Figure 5.12, is morphological granulometry. In order to estimate the grain size distribution we use two structuring elements: cross-shaped and binarized sphere. Obtained data is summarised in Table 5.4. At the first sight we can notice two important things, remarked for both SE. The first one is a progressive decrease of mean and maximal radii, for both specimens, what is triggered by the erosion of solid matrix. The second, is the fact that standard deviations, calculated using cross-shaped SE, are bigger than those for binarized spheres. It can be explained by more significant mismatching of shape of cross-shaped SE with the shape of solid skeleton subjected to progressive dissolution. What reveals also in overestimating of extremities of  $r$ .

Table 5.4: Evolution of granulometry of generated samples and sandstone using two SE: + cross-shaped and  $\circ$  binarized spheres.

FS	$\bar{r}^+$	$r_{max}^+$	$\sigma_r^+$	$\bar{r}^\circ$	$r_{max}^\circ$	$\sigma_r^\circ$
Initial	24	43	4.9	17	30	3.5
Step 1	20	40	5.2	15	29	3.7
Step 2	18	36	5.3	14	27	3.7
Step 3	15	34	5.3	12	26	3.8
Step 4	13	31	5.1	11	24	3.8
GS	$\bar{r}^+$	$r_{max}^+$	$\sigma_r^+$	$\bar{r}^\circ$	$r_{max}^\circ$	$\sigma_r^\circ$
Initial	24	48	5.2	19	31	2.5
Step 1	21	47	5.3	17	30	2.7
Step 2	19	45	5.0	15	28	3.0
Step 3	16	42	4.9	13	27	3.3
Step 4	14	40	4.8	12	26	3.4

Numerical dissolution by cubic SE changes shape of the solid skeleton what can be noticed by missing the shape of both, cross-shaped and spherical structuring element. This can be seen in the distributions plots [Fig. 5.12 (a) and (c)]. The situation recalls data presented

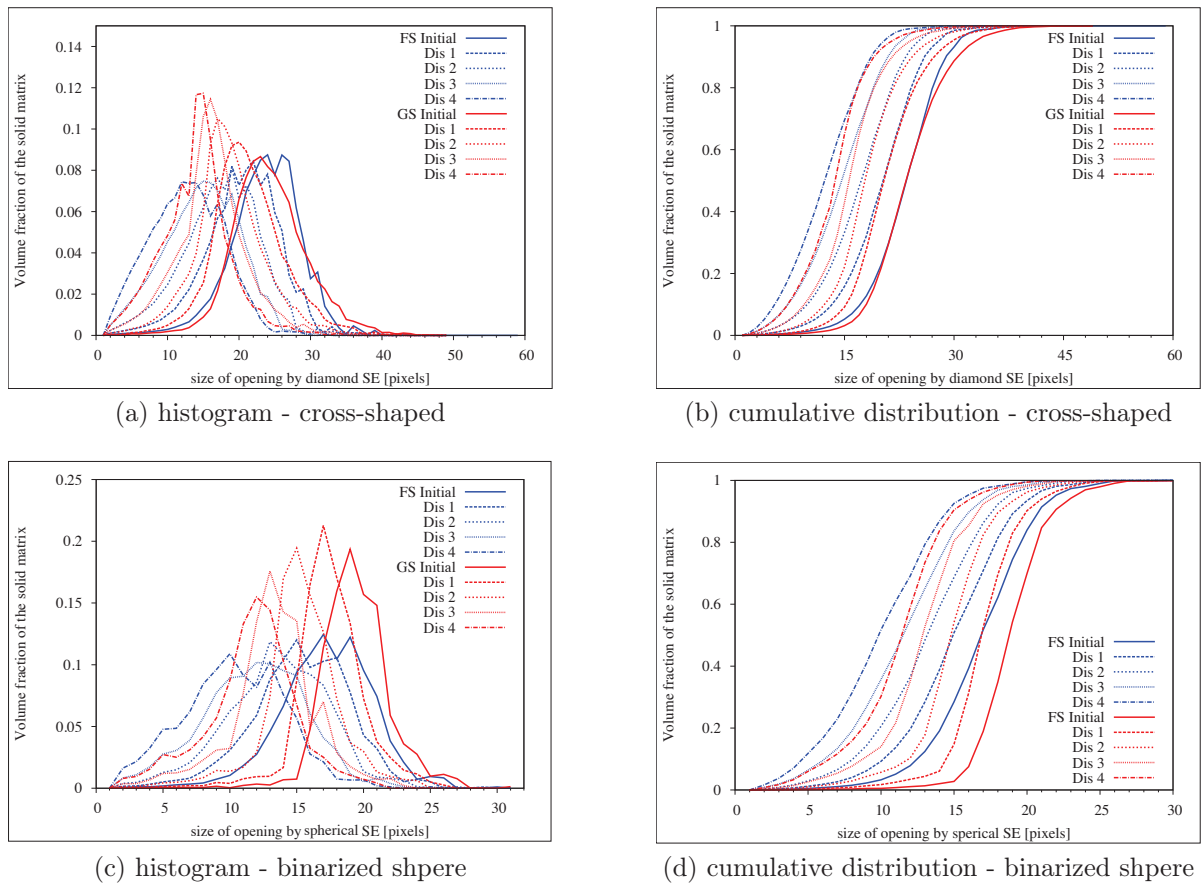


Figure 5.12: Evolution of morphological granulometry during isotropic dissolution.

in Figure 2.14 (b).

Comparing the evolution of mean radii, obtained by morphological granulometry using both SE, with evolution of repulsion distance we can say that the results are satisfying eq. 4.9. This condition is crucial to eventually prove irrelevancy of using certain SE.

### 5.3 Dissolution of percolated porous network

Like before, we begin analysis with evolution of global descriptors namely porosity and effective porosity, which are presented in Figure 5.13 (a) and Figure 5.13 (b) respectively. In those figures, a comparison between sandstone behaviour and average trend obtained for generated samples is shown. Both evolutions are almost perfectly overlapping, this fact may be explained by very similar initial values of effective porosity. Moreover, during percolated dissolution scenario fusions of isolated pores does not induce significant changes of porosity. Since they are not dissolved their contribution is rather irrelevant in comparison with increase of porosity of percolated network. Figure 5.14 presents evolution of specific surface and effective specific surface as a function of dissolution step respectively. We can see that both behaviours are almost the same. What can be explained by the same reasons as for the previous descriptors.

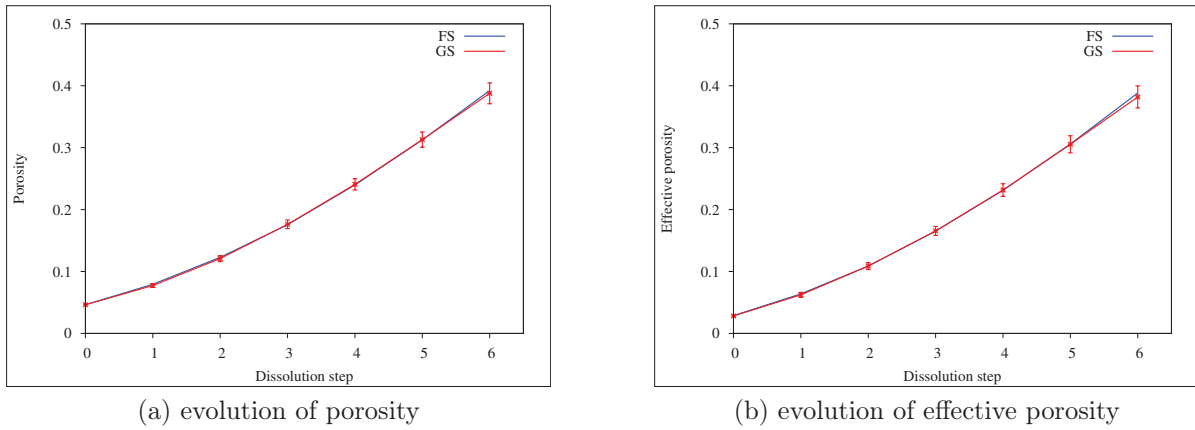


Figure 5.13: Evolution of porosity and effective porosity as a function of dissolution step.

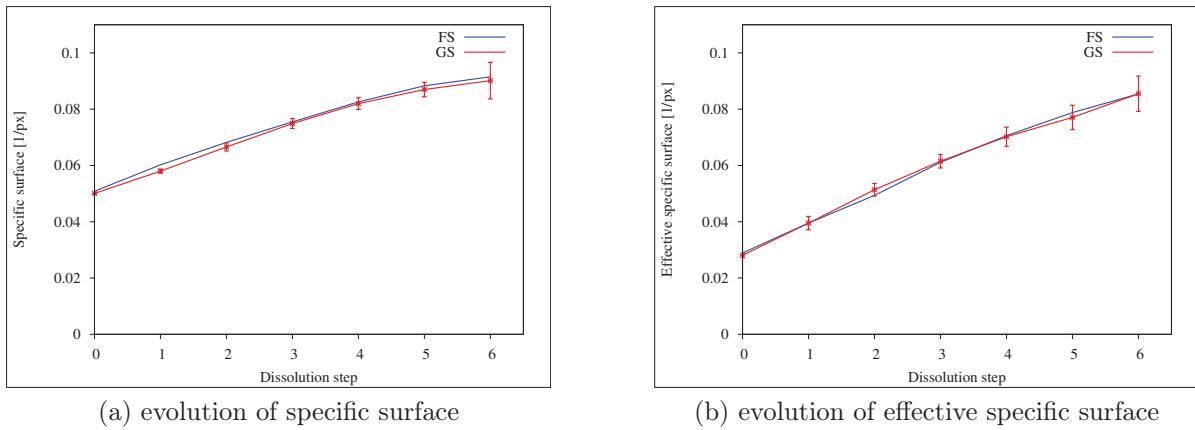


Figure 5.14: Evolution of specific surface and effective specific surface as a function of dissolution step.

Spatial distributions of porous phase, obtained by covariance function, are presented in Figure 5.15 and Figure 5.16. For the sake of clarity, three chosen directions are presented separately. For real and reconstructed samples we can notice similar behaviour. In the first sight we can see that covariance do not cross the sill for all considered directions. In this case, that covariance range can be defined as a value of  $h$  over which the plot is 'sufficiently' close to the theoretical asymptote. Due to the ambiguity of the 'definition' data is not presented in any table. However, we can see that progressive dissolution of percolated network increase consistently value of covariance ranges. This implies that RVE size increases in comparison to the initial state. Analysing Figure 5.15 (b) and 5.16 (b), and the plot representing last dissolution state, we can notice that covariance range is about 100 px. What means that at the RVE size increases significantly during percolated network dissolution. For investigated geometries, real and generated, we can see that covariance losses clearly marked repulsion distances with progressive dissolution. This can be explained by existence of of an agglomeration of pores. However geometrical isotropy is conserved but not at the same extent as for isotropic dissolution scenario.

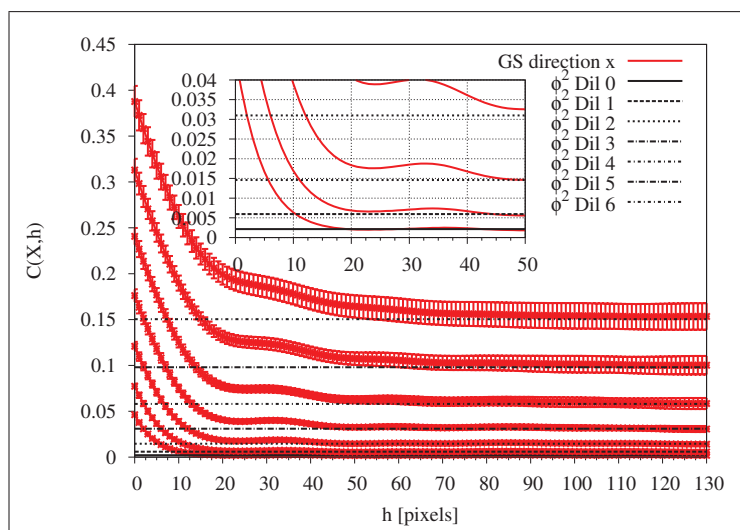
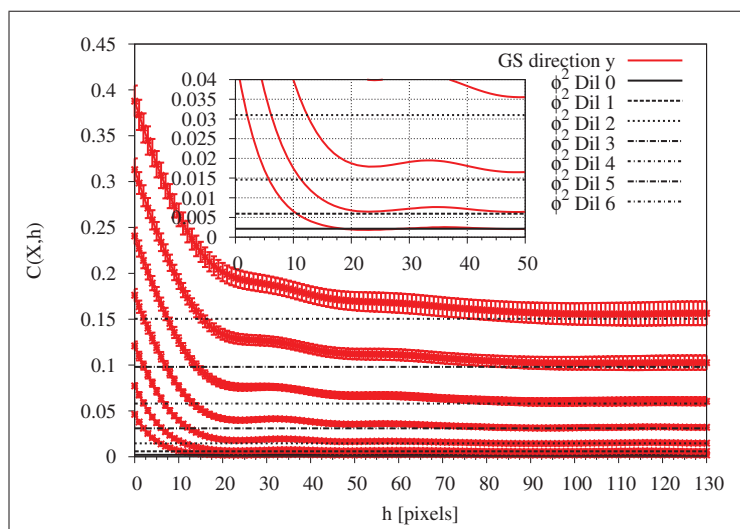
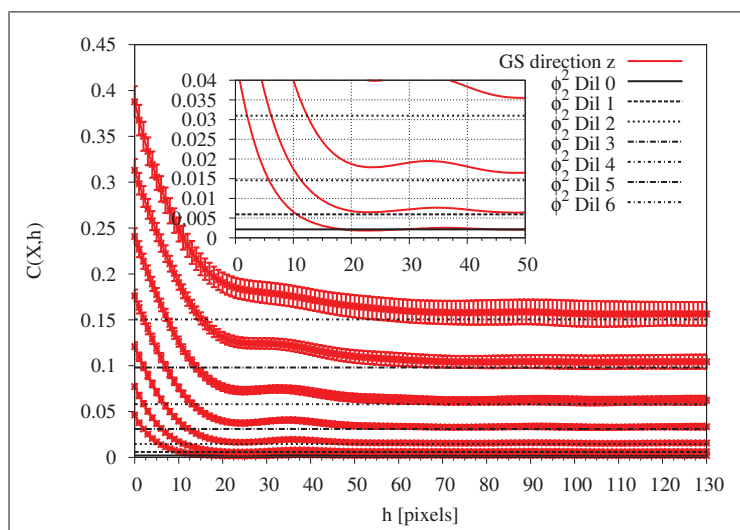
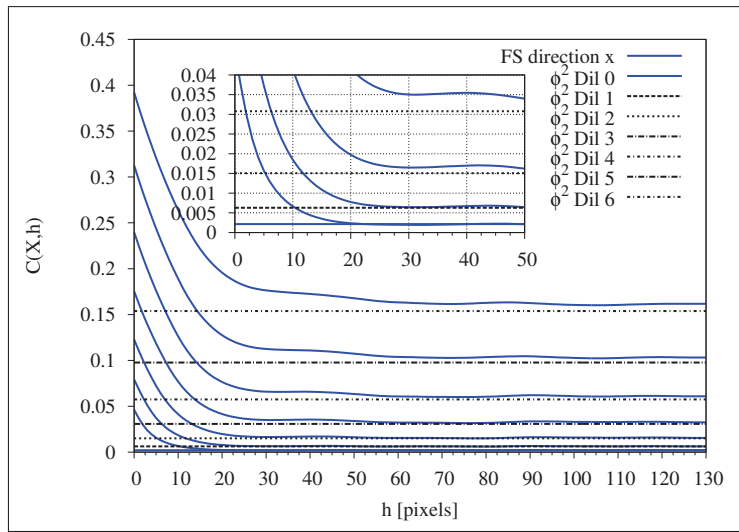
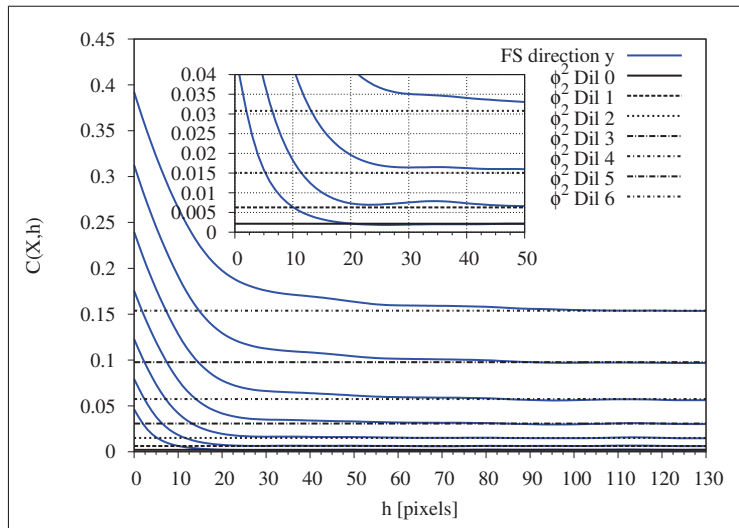
(a) covariance function for direction  $\vec{x}$ (b) covariance function for direction  $\vec{y}$ (c) covariance function for direction  $\vec{z}$ 

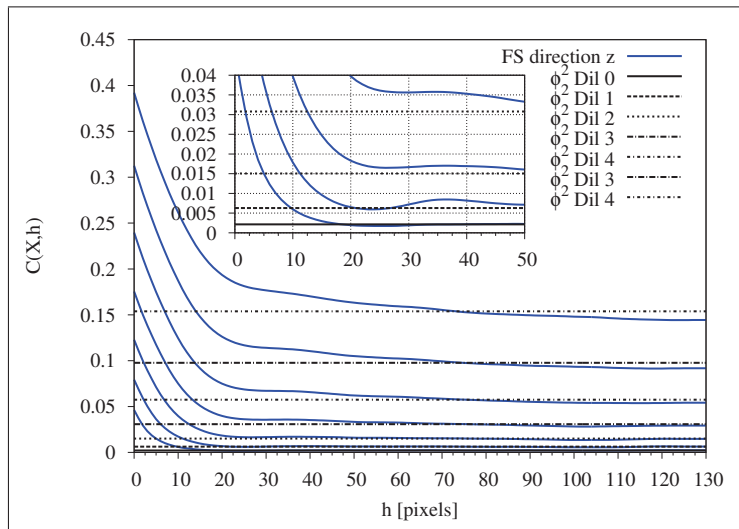
Figure 5.15: Evolution of averaged covariance function  $C(X, \|\vec{h}\|)$  of generated samples during dissolution of percolated porous network.



(a) covariance function for direction  $\vec{x}$



(b) covariance function for direction  $\vec{y}$



(c) covariance function for direction  $\vec{z}$

Figure 5.16: Evolution of covariance function  $C(X, \|\vec{h}\|)$  of sandstone during dissolution of percolated porous network.

Figure 5.17 presents evolution of tortuosity components caused by dissolution of percolated porous matrix. Results are summarised in Table 5.5. Like in case of isotropic dissolution a general decreasing trend versus value 1 is observed. We can see, that results representing tortuosity evolution of sandstone are less convergent with those obtained for generated samples. Standard deviations values became smaller what can be explained by translation of distributions towards 1 triggered by straightening of paths due to the dilation. Similar behaviour is observed for all tortuosity components and both specimens. Figure 5.17 (d) presenting distributions of tortuosity component  $\tau_z$ , of one of generated samples, at initial state, 2nd and final one, to visualise the fact that distribution becomes more regular during dissolution and to justify decrease of standard deviations.

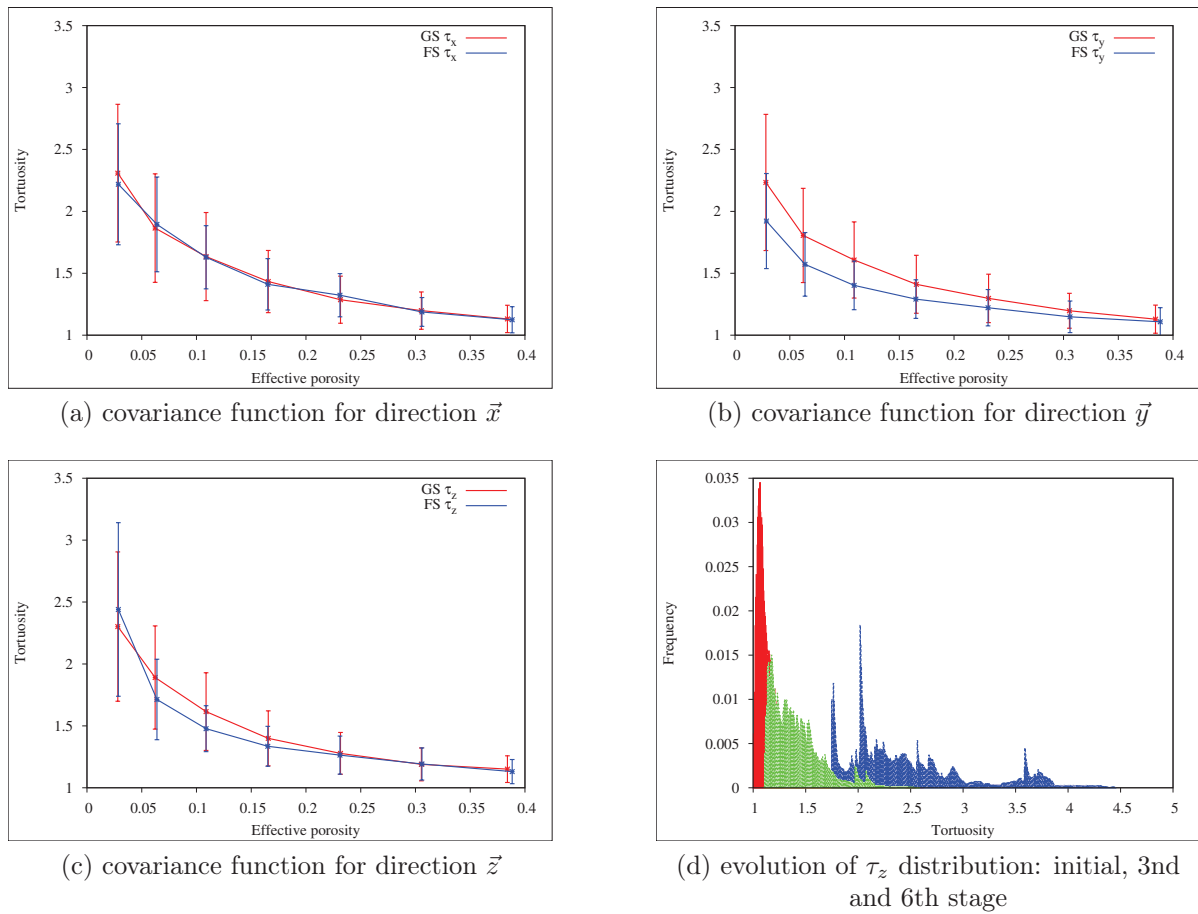


Figure 5.17: Comparison of tortuosity components evolution  $\tau_x$ ,  $\tau_y$  and  $\tau_z$  as a function of effective porosity – dissolution of percolated network.

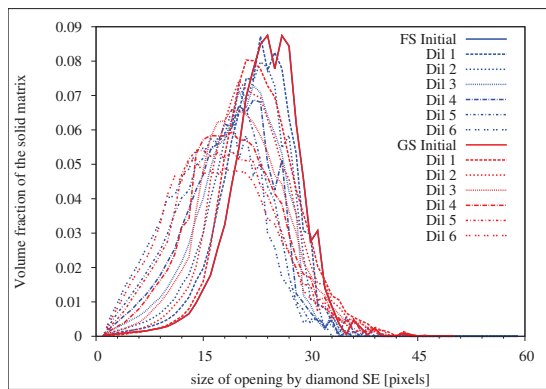
The next descriptor is granulometry, which is presented in Figure 5.18 and summarised in Table 5.6. At the first sight we can notice two important things, remarked for both structuring elements. The first one is a progressive decrease of mean and maximal radii, for both specimens, sandstone and reconstructed, what is triggered by the erosion of solid matrix. The next is the fact that standard deviations increase significantly during progressive dissolution [Tab. 5.6]. The overestimation for smaller values of  $r$  is caused by mismatching the shape of solid skeleton by both SE. From the right sight distribution

Table 5.5: Evolution of tortuosity components and standard deviations of mean distributions. Percolated network dissolution.

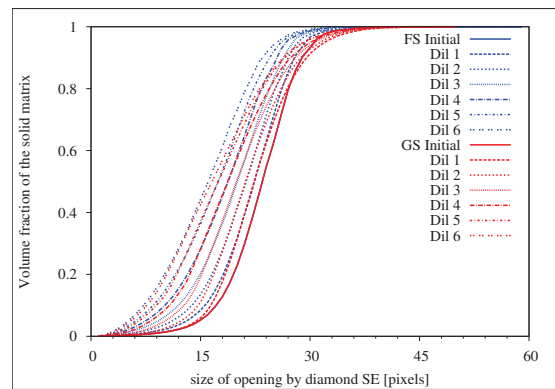
FS	$\bar{\tau}_x$	$\bar{\tau}_y$	$\bar{\tau}_z$	$\sigma_{\tau_x}$	$\sigma_{\tau_y}$	$\sigma_{\tau_z}$
Initial	2.22	1.92	2.44	0.49	0.38	0.70
Step 1	1.89	1.57	1.71	0.38	0.26	0.33
Step 2	1.63	1.40	1.48	0.25	0.20	0.19
Step 3	1.41	1.29	1.34	0.21	0.16	0.16
Step 4	1.32	1.22	1.26	0.17	0.15	0.15
Step 5	1.19	1.15	1.19	0.12	0.13	0.13
Step 6	1.12	1.11	1.13	0.11	0.11	0.10
GS	$\bar{\tau}_x$	$\bar{\tau}_y$	$\bar{\tau}_z$	$\sigma_{\tau_x}$	$\sigma_{\tau_y}$	$\sigma_{\tau_z}$
Initial	2.31	2.23	2.30	0.50	0.49	0.55
Step 1	1.87	1.81	1.89	0.44	0.38	0.42
Step 2	1.63	1.61	1.62	0.36	0.31	0.31
Step 3	1.43	1.41	1.40	0.25	0.23	0.22
Step 4	1.29	1.30	1.28	0.19	0.20	0.17
Step 5	1.20	1.20	1.19	0.15	0.14	0.13
Step 6	1.13	1.13	1.15	0.11	0.11	0.11

is moved only slightly what is an effect of less homogenous spatial dissolution what also causes significant increase of standard deviations for both SE.

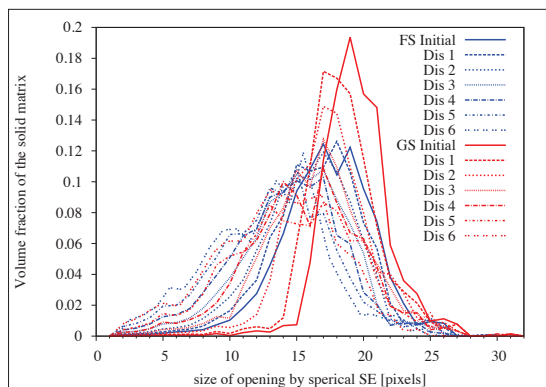
Like in the case of isotropic dissolution, dilation of effective porous phase by cubic SE changes shape of the solid skeleton what can be notice by missing the shape of both, cross-shaped and spherical structuring element. This can be seen in the distributions plots [Fig. 5.18].



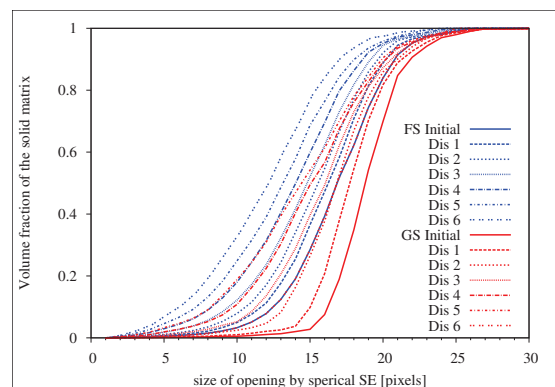
(a) histogram - cross-shaped



(b) cumulative distribution - cross-shaped



(c) histogram - binarized sphere



(d) cumulative distribution - binarized sphere

Figure 5.18: Evolution of morphological granulometry during dissolution of percolated network.



Table 5.6: Evolution of granulometry of generated samples and sandstone using two SE: + cross-shaped and  $\circ$  binarized spheres.

FS	$\bar{r}^+$	$r_{max}^+$	$\sigma_r^+$	$\bar{r}^\circ$	$r_{max}^\circ$	$\sigma_r^\circ$
Initial	24	43	5.0	17	30	3.5
Step 1	23	40	5.1	16.5	29	3.6
Step 2	21	38	5.4	16	28	3.7
Step 3	20	36	5.7	15	27	3.9
Step 4	18	35	5.9	14	25	4.1
Step 5	17	33	6.1	13	24	4.3
Step 6	16	32	6.2	12	24	4.5
GS	$\bar{r}^+$	$r_{max}^+$	$\sigma_r^+$	$\bar{r}^\circ$	$r_{max}^\circ$	$\sigma_r^\circ$
Initial	24	48	5.1	19	31	2.5
Step 1	22	47	5.5	18	30	3.0
Step 2	21	45	5.8	17	29	3.5
Step 3	20	44	6.2	16	28	4.0
Step 4	19	43	6.0	16	27	4.4
Step 5	18	41	6.9	15	27	4.7
Step 6	17	39	7.3	13	25	4.8

## 5.4 Conclusions

In the chapter two methods of numerical dissolution are clearly featured: isotropic scenario and dissolution of percolated porous network. The numerical erosion of solid skeleton is being performed till the value of total porosity reaches 40%.

Microstructural changes triggered by both scenarii are quantified using morphological descriptors like: porosity, specific surface, morphological granulometry, covariance function and morphological tortuosity.

Despite of different behaviour of evolution of global descriptors the spatial distribution of phases and morphological tortuosity present good convergence between real geometry and reconstructed samples. While for percolated network dissolution the situation is opposite. For both scenarii of microstructure evolution, morphological granulometry, obtained by using two different SE (cross-shaped and binarized sphere), demonstrate that the grains size estimation is encumbered with significant errors due to the overestimation of extremal values of radii. What is caused by mismatching the evolving solid skeleton's shape, by used structuring elements.

Analysing covariance ranges, two important conclusions are noticed. Namely, that during isotropic dissolution of entire network, RVE's size remains constant, while for the second scenario the size increases significantly.

*All models are wrong, but some are useful.*

George E. P. Box

# 6

## Elastic behaviour modelling

---

**A** methodology to estimate effective mechanical properties of investigated material is presented in this chapter. The method is based directly on binary images. To estimate the effective behaviour periodic homogenisation is used. Due to lack of geometrical periodicity a fixed point method, using additional layer spread over the considered image, is adapted. This method is used to estimate effective mechanical properties in case of two scenarii of numerical dissolution. Therefore, comparison of this two scenarii is presented and discussed.

---

---

**Contents**

---

<b>6.1</b>	<b>Introduction</b>	<b>99</b>
<b>6.2</b>	<b>Methodology</b>	<b>99</b>
6.2.1	Samples preparation	99
6.2.2	Periodisation - fixed point method	101
6.2.3	Effective properties	101
6.2.4	Influence of discretization on elastic moduli	102
6.2.5	Precision of the simulations	103
<b>6.3</b>	<b>First results</b>	<b>105</b>
<b>6.4</b>	<b>Influence of RVE size</b>	<b>107</b>
<b>6.5</b>	<b>Final results</b>	<b>108</b>
<b>6.6</b>	<b>Conclusions</b>	<b>109</b>

---

## 6.1 Introduction

One of the tools that allows us to obtain effective properties is so-called periodic homogenization. It is a classic and common methodology enabling to obtain effective elastic properties. This classical approach treats heterogeneous media as materials possessing hierarchical structure which can be described by a finite number of separable scales. For the purpose of this study, two levels are used: micro and macro-scale. Effective properties (macro-scale) are assumed to be homogeneous and can be estimated through averaging process. This approach takes into account all interactions between phases forming heterogeneous structure at micro-scale. Aforementioned method is implemented using computer code for the analysis of structures by the finite element method - Cast3M. This code was developed in the Service of Mechanical and Thermal Studies (SEMT) of the French Atomic Energy Commission (CEA). Cast3M is a powerful software designed for mechanical linear elastic, thermal and heat transfer problems as well as nonlinear problems (elastic, plastic, creep materials). CT image is in fact a sub-sample of investigated heterogeneous structure, therefore important questions, concerning the validity of estimated properties, arrives: what is the influence of the RVE size representing random microstructure and what are the errors of carried out numerical estimations?

In this chapter we are going to answer to those questions step by step. Firstly, the preparation of samples in order to obtain different discretizations is presented. Secondly, the problem of geometrical periodicity of considered microstructure is illustrated and certain solution is proposed. Nextly, the influence of discretization by using structured mesh is clearly featured [12–14]. After this a parametrical study concerning used methodology is presented. The next section presents influence of RVE size according to methodology proposed by Kanit et al. [42]. Finally, the evolutions of effective properties, triggered by two different scenarii of dissolution are showed and discussed.

## 6.2 Methodology

In order to estimate effective behaviour of considered samples and elastic moduli - porosity relationships we used a methodology [Fig. 6.1], which is explained, step by step, in the following section.

### 6.2.1 Samples preparation

The first step to estimate effective behaviour of considered samples via 3D binary image is to prepare geometries representing studied microstructures at different resolutions. A convenient way is perform scaling of binary image using ImageJ. Each considered geometry is imported to the software and rescaled by desired factor. For such obtained samples structured meshes (hexahedron), are used to create discretised grid. Each voxel of 3D binary image is represented by one cubic mesh element. Aforementioned steps are necessary to obtain different resolutions which are required to estimate influence of the discretization. The explicit estimation is presented later [Subsection 6.2.4]. The structured grid is created by code which was developed for this purpose. Mesh is described

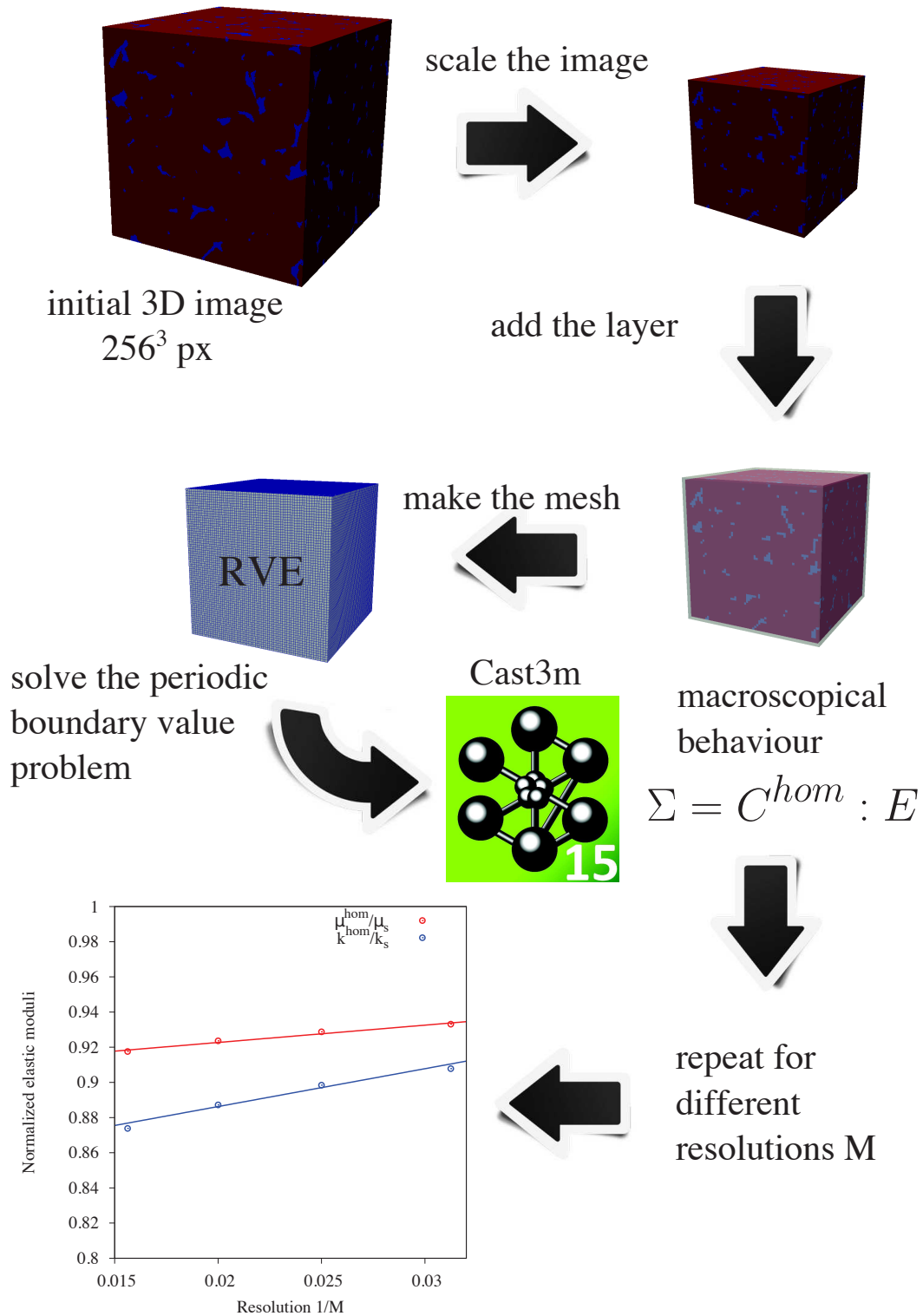


Figure 6.1: Visualisation of computational methodology. From sample preparation to effective behaviour estimation.

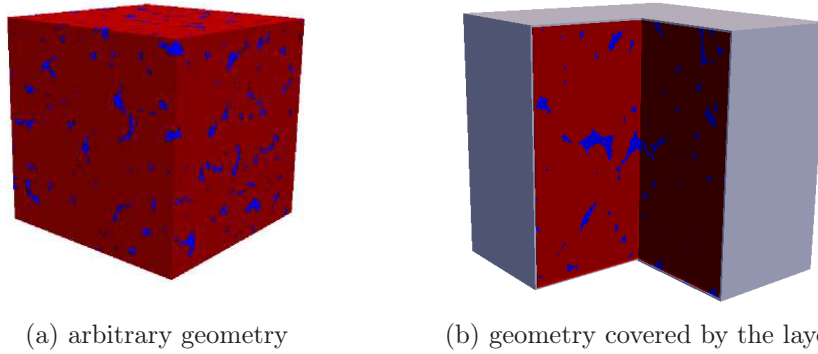


Figure 6.2: Visualisation of the periodisation method by using homogeneous layer.

in a way that is compatible with GMSH, a open source three-dimensional finite element mesh generator [86]. Nextly, using the script written by Laurent Champaney<sup>1</sup> the grid is transformed into code readable for Cast3m. The mesh is represented by two volumes: solid and porous phase.

### 6.2.2 Periodisation - fixed point method

However, since we are dealing with images of rocks or generated equivalent samples, geometrical periodicity is not achieved in a direct way. To solved this problem we use *fixed point method*. First step is to spread a layer over the extracted cubic cell [Fig. 6.2]. Initially, stiffness tensor of the layer is assumed to be equal to the stiffness tenor of solid phase. This choice is as good as any other initial values prescribed to the tensor components. However, the choice affects the number of iteration which are necessary to obtain convergence defined below. By treating the layer as an other phase, at each iteration its elastic properties are described by the calculated homogenised stiffness tensor of system from the previous step:

$$C_{klmn}^{layer}[i] = C_{klmn}^{hom}[i - 1], \quad (6.1)$$

where  $i$  denotes iteration number. The stopping criterion for this method is defined by following equation:

$$\frac{\|C^{layer}[i] - C^{hom}[i]\|}{\|C^{hom}[i]\|} \leq 10^{-4}, \quad (6.2)$$

where symbol  $\|\cdot\|$  stands for a quadratic norm. Therefore, to the grid an additional volume, representing layer is adjoined.

### 6.2.3 Effective properties

In order to calculate the effective stiffness matrix of considered geometry technique of periodic homogenization is used, which is presented in Chapter 2. Effective stiffness

<sup>1</sup><http://laurent.champaney.free.fr/perso/conversion.html>

tensor  $C$  is obtained by using following relation:

$$\Sigma = C : E, \quad (6.3)$$

where  $\Sigma$  is the macroscopic stress tensor and  $E$  denotes macroscopic deformation tensor. A typical way, in order to obtain the homogenised stiffness tensor  $C$  is to solve six elementary problems, three tractions and three shear tests. Finally,  $C$  is given by following rule:

$$C_{ijkl} = \langle c_{ijkl} + c_{ijlm} \epsilon_{lm}(u^{kh}) \rangle, \quad (6.4)$$

where  $\epsilon_{lm}$  is the microscopic strain tensor. And  $u^{kh}$  is a local displacement periodic vector, the solution of the problem given by the unit macroscopic strain  $E^{kh} = (e_k \otimes e_h + e_h \otimes e_k) / 2$ , where symbol  $\otimes$  means the tensorial product.

Obtained effective stiffness tensors are projected on the classical isotropy basis, defined by matrix  $J = 1/3 e_i \otimes e_i$  and  $K = I - J$ . The measure of the isotropy of an arbitrary tensors  $C$  is given by following equation:

$$\zeta(C) = \frac{\|C - \text{proj}_{J,K}(C)\|}{\|C\|}, \quad (6.5)$$

where the operator of projection  $\text{proj}_{J,K}(\cdot)$  is defined in following way:

$$\text{proj}_{J,K}(C) = \left[ \frac{C :: J}{J :: J} J + \frac{C :: K}{K :: K} K \right]. \quad (6.6)$$

Aforementioned method of periodic homogenisation is using code CAST3M, which is a software designed for the analysis of structures using finite element method.

#### 6.2.4 Influence of discretization on elastic moduli

Discretization error comes out always when the real continuous model is assembled by a grid. When we are using regular cubic mesh to represent continuum media the influence can be explicitly determined [12–14], as mentioned in Section 2.2.4.

Let  $M$  denotes the number of hexahedrons along the edge of the discretised geometry, it is shown that discretization error for FE methods of any elastic moduli can be estimated according to following formula:

$$P(M) = P_0 + \frac{a}{M}, \quad (6.7)$$

where  $P(M)$  is the computed elastic modulus and  $P_0$  is so-called continuum value, which corresponds to the case when  $M \rightarrow \infty$ . To estimate this searched value, we have to compute elastic properties at least for three different values of  $M$  and then extrapolate the results, by fitting linear function according to the least squares method.

### 6.2.5 Precision of the simulations

Concerning the aforementioned method, important questions arise:

- what should be the contrast between Young moduli of solid matrix and pores?
- what is the influence of the layer and its thickness  $d$ ?

The elastic properties of the solid phase are taken from Mavko et al. [87]: bulk modulus is equal  $k = 37.0$  GPa and the shear modulus  $\mu = 44.0$  GPa. Using the relation between the elastic moduli of homogeneous isotropic materials it means that Young modulus  $E$  and Poisson ratio  $\nu$  are equal 94.53 GPa and 0.0742 respectively. Firstly, we answer to the question concerning contrast of properties, Poisson ratios of phases are set to be equal. Let contrast between Young moduli of the solid and porous phase be denoted by  $\kappa$  and defined in following way:

$$\kappa = \frac{E_{solid}}{E_{pores}}. \quad (6.8)$$

The influence of  $\kappa$  arises from the potentially ill-conditioned finite element stiffness matrix. Since the property of a cubic mesh corresponds to the phase associated to the voxel, the boundaries of the porous phase are not explicitly meshed. A small value of Young modulus  $E_{pores}$  is affected to the meshes associated to the porous phase, small compared to the value of the Young modulus of the solid phase  $E_{matrix}$ . The contrast  $\kappa$  has thus to tend to infinity and in practice to a huge value. However, when  $\kappa$  increases, the porous phase is better represented, but the finite element stiffness matrix is worse conditioned. Since the Poisson ratios of phases are set to be equal, the influence of  $\kappa$  is studied. Numerical results are obtained for entire sample of size  $256 \times 256 \times 256$  pixels scaled by factor four. What means that size of the geometry is  $64 \times 64 \times 64$  pixels. In this study we investigate 10 different contrast values varying from 1 to 10. Figure 6.3 presents bulk and shear moduli normalised by their values obtained for maximal considered contrast  $\kappa = 10^{10}$ . We can see that convergence is obtained for  $\kappa = 10^8$ .

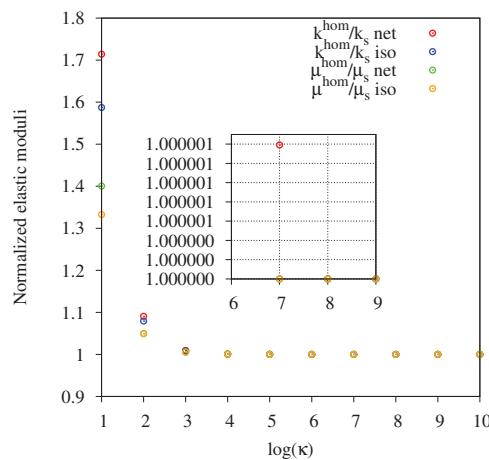


Figure 6.3: Influence of contrast  $\kappa$  (net - percolated network dissolution; iso - isotropic dissolution).



In order to evaluate the influence of added layer associated to fixed point method to determine bulk and shear moduli we perform estimation using geometrically periodic sample at three different dissolved states. To obtain periodic image we scale sandstone geometry and then by symmetrical reflections the desired sample is reconstructed. Properties of phases are same as those mentioned in previous section. Over the three same samples a layer is added and aforementioned methodology is applied. Figures 6.4 presents obtained results. As we can see, estimated bulk and shear moduli are slightly overestimated. The

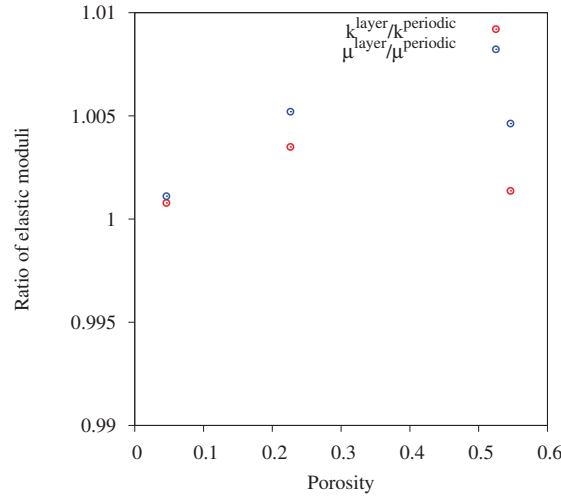


Figure 6.4: Influence of the methodology

relative error is less than 0.6% in considered range of porosity. Therefore, we can assume that the results are not encumbered by error related to used methodology.

The last question is the influence of layer thickness. Inhere we investigate the last degraded state of sandstone in case of percolated network dissolution and resolution  $M = 50$ . Figure 6.5 presents normalised bulk and shear moduli as function of layer thickness. The normalisation factor is the value of the moduli obtained for layer thickness  $d = 1$  px. The small fluctuations ( $\epsilon_{\text{relative}} \ll 0.1\%$ ) are observed rather due to the different values obtained by stopping criterion (eq. 6.2) then due to the real influence of the thickness. Therefore for all further computations layer thickness is set to be equal to 1.

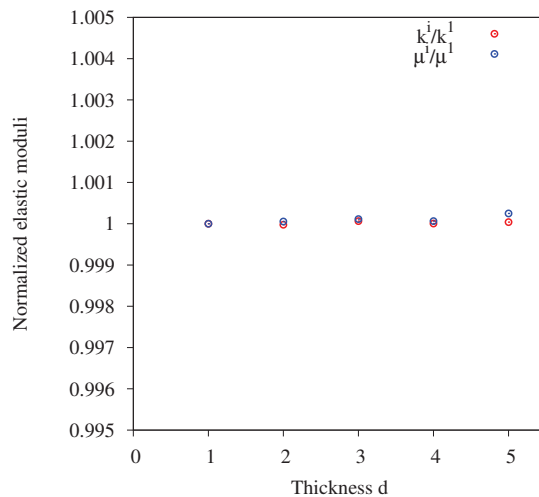


Figure 6.5: Parametrical study - layer thickness  $d$ .

### 6.3 First results

Aforementioned methodology is applied for each considered sample at different dissolved state. For the purpose of the thesis we investigate entire geometry of sandstone and degraded samples, however due to the limitations of memory in used computers, we use smaller resolutions:  $M = 64$  px,  $M = 50$  px,  $M = 40$  px and  $M = 32$  px. Finally, 484 computations are performed, 121 for each resolution: 11 different degraded states of each sample: real sandstone and 10 realisations.

For each sample having different resolution the computations are performed. Next, the obtained effective stiffness tensors are projected on the isotropy basis (eq. 6.5) and corresponding bulk and shear moduli are extracted. Figure 6.6 presents evolution of isotropy factor  $\zeta(C)$  of sandstone and averaged value for 10 realisations in function of dissolution step ( $M = 64$ ). We can see that in case of isotropic dissolution obtained factor

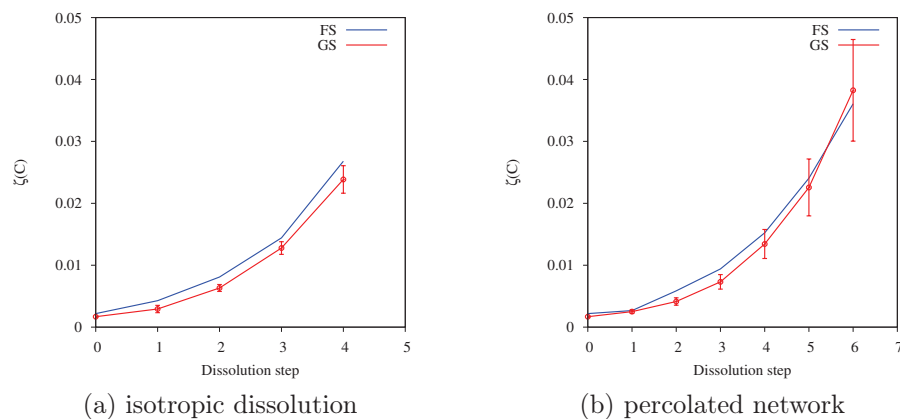


Figure 6.6: Evolutions of samples effective stiffness tensor isotropy factor  $\zeta(C)$ .

is smaller, what stands for closer isotropy of stiffness effective tensor. The results are in

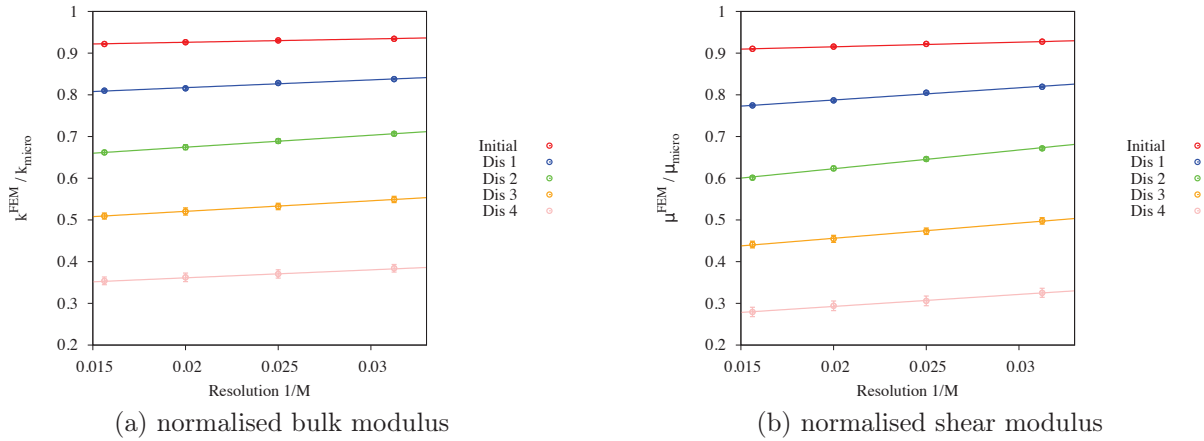


Figure 6.7: Influence of discretization - isotropic dissolution. For both plots the correlation factor  $r^2 > 0.99$ .

good agreement with covariance function evolution, which was presented in Section 5.2 and 5.3. We could see, that during dissolution of percolated network, obtained covariance functions were overlapping with less consistency than in the other scenario.

Figures 6.7 and 6.8 presents the linear fit to obtained data, according to the equation 6.7. For all functions the correlation factor  $r^2 > 0.99$ . The y-intercept of each function stands for the continuum value of searched moduli. Figure 6.7 presents results obtained for normalised averaged values of bulk and shear moduli over 10 realisations for isotropic scenario dissolution and initial states. At first sight a decreasing trend for all curves is noticed what is confirmed in the literature. A general non monotonic trend of standard deviations is viewed, however following relation is always satisfied for both moduli:

$$\sigma_{P(M=64)} < \sigma_{P(M=32)}, \quad (6.9)$$

where  $\sigma_{P(M)}$  stands for standard deviations obtained for given resolution  $M$  over generated samples. Hence, we assume that  $\sigma_{P(M=64)}$  stands as a standard deviation for continuum values of elastic moduli  $k$  and  $\mu$ . The same analysis concerns Figure 6.8, where results obtained for percolated network dissolution are presented.

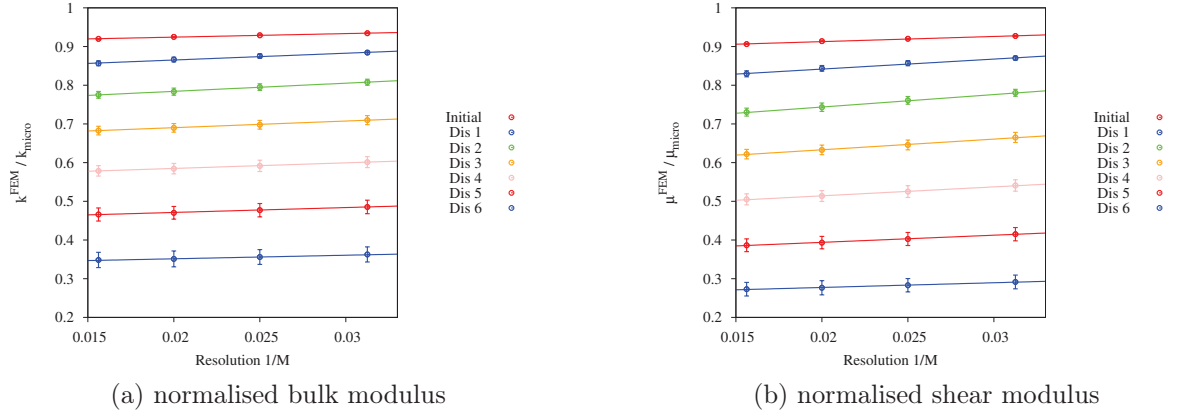


Figure 6.8: Influence of discretization - percolated network dissolution. For both plots the correlation factor  $r^2 > 0.99$ .

## 6.4 Influence of RVE size

Inhere, the methodology of RVE size estimation, presented in Section 2.2.3 is evoked. As it is said before for the purpose of this thesis we use maximal possible size of investigated microstructure,  $V = 256 \times 256 \times 256$  pixel. Therefore, according to the methodology of Kanit [42], relative errors  $\epsilon_{rel}$  are estimated by following equation:

$$\epsilon_{rel} = \frac{2D_Z(V)}{\bar{Z}\sqrt{N}}, \quad (6.10)$$

where  $\bar{Z}$  denotes the mean of searched property (effective bulk modulus  $k$  or shear modulus  $\mu$ ),  $D_Z(V)$  is standard deviation and  $N$  stands for number of realisations. In our case number of equivalent independent realisations  $N = 11$ . Relative errors obtained using this method are presented in Tables 6.1 and 6.2. General increasing trend with increasing dissolution is noticed. Estimated errors are significantly bigger for percolated network dissolution. What confirms a fact that a bigger RVE size is needed in order to obtain similar accuracy in comparison with isotropic dissolution scenario. However, due to scaling it seems that errors are slightly overestimated (eq. 6.9).

Table 6.1: Relative errors of apparent moduli estimation;  $V = 256 \times 256 \times 256$  pixel,  $N = 11$ . Isotropic dissolution scenario.

	$\epsilon_{rel}^k$ [%]	$\epsilon_{rel}^\mu$ [%]
Initial	0.04	0.05
Dil 1	0.15	0.18
Dil 2	0.36	0.42
Dil 3	0.88	1.04
Dil 4	1.18	2.06

Table 6.2: Relative errors of apparent moduli estimation;  $V = 256 \times 256 \times 256$  pixel,  $N = 11$ . Percolated network dissolution scenario.

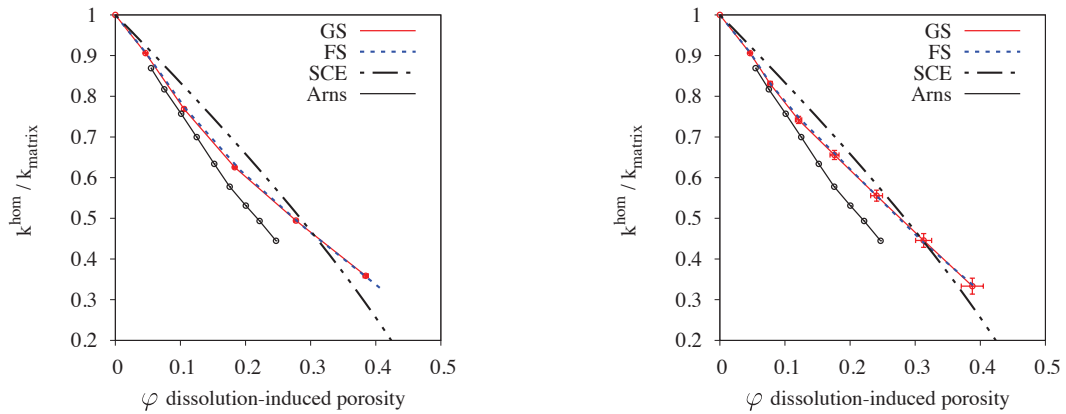
	$\epsilon_{rel}^k$ [%]	$\epsilon_{rel}^\mu$ [%]
Initial	0.04	0.05
Dil 1	0.45	0.57
Dil 2	0.70	0.87
Dil 3	0.98	1.20
Dil 4	1.41	1.70
Dil 5	2.19	2.57
Dil 6	3.41	3.88

## 6.5 Final results

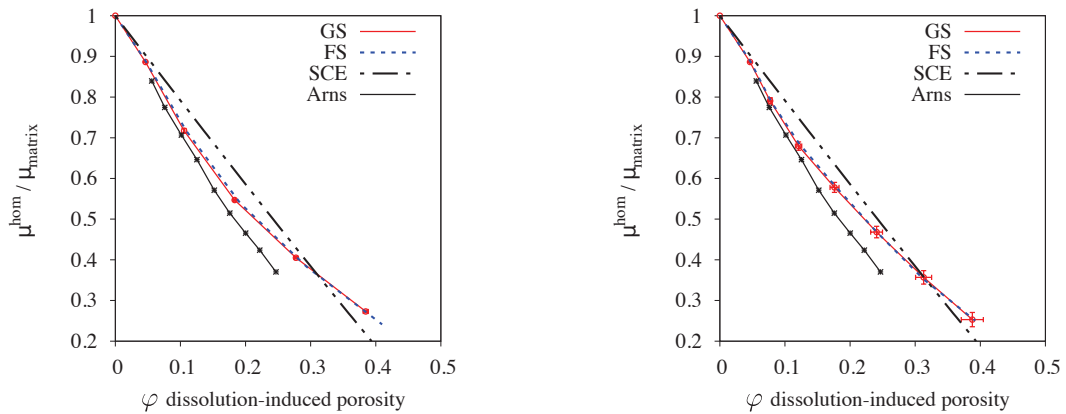
Extracted continuum values of bulk and shear moduli ( $M \rightarrow \infty$ ), for both scenarii of dissolution, are presented in Figure 6.9. Previously mentioned figures present also results obtained by Arns et al. [15] who was using methodology, based directly via microtomography of sandstone. In this paper, different realisations of sandstone microstructure were extracted from 4 images representing real core samples. In their study porosity is varying from 0.055 to 0.24.

At the first sight, evolution of elastic properties as a function of porosity [Fig.6.9] for sandstone and the generated samples are in excellent consistency (for each scenario). In general, for both scenarii, shear modulus decreases more significantly than bulk modulus. Although different mechanism responsible for porosity variation, our results and those presented in [15] show very similar trend.

In Figure 6.9, the comparison of (a) and (b), (c) and (d) shows that results obtained for both scenarii of dissolution are very similar. The obtained results as well as those of Arns *et al.* [15] are in coherence with the self-consistent estimate [88] which often represents media with total disorder.



(a) normalized bulk modulus - isotropic dissolution (b) normalized bulk modulus - percolated network dissolution



(c) normalized shear modulus - isotropic dissolution (d) normalized shear modulus - percolated network dissolution

Figure 6.9: Evolution of normalised elastic moduli of sandstone (FS), averaged over all generated samples (GS) (with standard deviations) for both scenarii of numerical dissolution; comparison with self-consistent estimate (SCE) and with results obtained by Arns et al. [15].

## 6.6 Conclusions

In this chapter a methodology to predict effect of dissolution on elastic behaviour is presented. The relation between elastic properties and porosity is derived directly using microtomographic images. Due to the lack of geometrical periodicity a new method of periodisation is proposed. It consist in spreading a layer over the 3D image, which mechanical properties change during the calculations and are adjusted by the estimated effective stiffness tensor of the investigated system. In order to decrease an influence of finite resolution a method proposed by Roberts, Day and Garboczi et al. [12–14] is applied.

In comparison with Arns et al. [15] obtained results are overestimated, probably due to the limit of image resolution or due to different mechanism responsible for increase

of porosity. In order to dispel any doubts we should use higher resolution to perform numerical computations.

However, the fixed point method works well with the methodology of Roberts and Garboczi and induces negligible errors in comparison analysing geometrically periodic case. The relations of average elastic behaviour - porosity of reconstructed samples are in very good agreement with evolution of the properties calculated for sandstone.

A complete methodology to estimate evolution of mechanical behaviour from generated samples morphologically equivalent to microtomographies was presented. Modelling of dissolution phenomenon and the final results shows that a sophisticated modelling of the dissolution process will not affect significantly the results.

*Water is the driving force of all nature.*

Leonardo da Vinci

# 7

## Hydraulic conductivity modelling

---

**A** classical way in order to estimate permeability, based on the binary image, is presented in this chapter. To estimate the effective behaviour Darcy's law is used as upscaling technique of governing Navier-Stokes equations solved at micro-scale. Analysis of permeability evolution triggered by two scenarii of numerical dissolution, provided on real rock image as well as on the generated samples, is featured. Relationships of elastic moduli - permeability is proposed.

---



---

**Contents**

---

<b>7.1</b>	<b>Methodology . . . . .</b>	<b>113</b>
7.1.1	Samples preparation . . . . .	113
7.1.2	Solving algorithm . . . . .	113
7.1.3	Characteristic length and Reynolds number . . . . .	115
7.1.4	RVE size estimation . . . . .	116
<b>7.2</b>	<b>Results . . . . .</b>	<b>117</b>
7.2.1	Porosity - permeability relationships . . . . .	117
7.2.2	Tortuosity - permeability relationships . . . . .	119
<b>7.3</b>	<b>Mechanical properties versus permeability . . . . .</b>	<b>123</b>
<b>7.4</b>	<b>Conclusions . . . . .</b>	<b>124</b>

---

## 7.1 Methodology

Recent development of pore-scale imaging techniques and computer science have notably simplified studies of transport phenomena in heterogeneous media. Nowadays, a common approach to estimate permeability is to process X-ray microtomography images, extract effective porous phase and then to calculate numerically the steady-state flow for incompressible fluid. We apply the same way of calculations on binary images representing different dissolved states of sandstone and generated samples. In the method two-scales are considered. Firstly, a micro-scale where the governing equations are discretised and numerically solved. Secondly, a macro-scale where the estimated effective properties, obtained by using averaging techniques, are assumed to be representative.

### 7.1.1 Samples preparation

Sample preparation is made by means of an extraction of the percolated porous network. As we said before, isolated pores are irrelevant in order to investigate transport phenomena in porous media. A very common approach in fluid flow simulations, based on X-ray microtomography image, is to use structured cubic mesh whose resolution is the same as the resolution of the image of the considered geometry. It means that each voxel is represented by one cubic mesh element (regular hexahedra). However, the recent studies of Guibert et al. [89] have shown that mesh resolution can affect significantly on the results. They observed that the obtained permeability decreases with increasing mesh refinement level. This suggests that numerical error related to permeability determination is linked with the number of cells discretising the smallest pore throats of a sample. Moreover, even the finest mesh refinement used in their work highlights the fact that the permeability obtained numerically must be taken with caution. Nevertheless, for the purpose of this work, structured meshes, are used to create discretised grid, with the same resolution as the resolution of the image. In regard of work of Guibert et al., it can be explained by a fact that since first step of isotropic dissolution the smallest pores are represented minimum by 3 voxels.

### 7.1.2 Solving algorithm

In order to obtain velocity field in pore domain, a computational fluid dynamics simulations are run using free open source software OpenFOAM [90]. In this software the governing equations of Navier-Stokes, for single phase flow, are solved using finite volume method. Pressure and velocity are calculated iteratively by a steady-state solver based on Semi- Implicit Method for Pressure-Linked Equations (SIMPLE) algorithm [91]. This algorithm is a type of Pressure-Based Method techniques which deal with pressure-velocity coupling in numerical simulations of the fluid flow [92, 93].

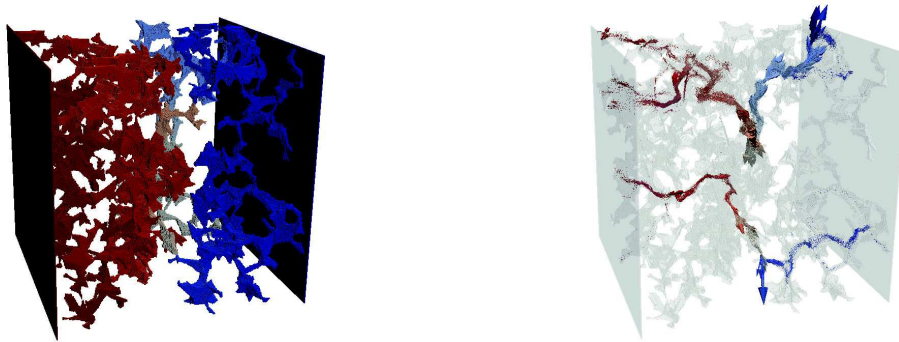
---

**Algorithm 7.1** Semi-Implicit Method for Pressure-Linked Equations (SIMPLE).
 

---

1. setting the boundary conditions
  2. solving the discretised equations to estimate intermediate velocity field
  3. computing mass fluxes at the cell faces
  4. solving the pressure equation and applying under-relaxation
  5. correcting fluxes at the cell faces
  6. correcting velocities by using updated pressure field
  7. updating boundary conditions
  8. repeating 1 - 7 till arriving to prescribed convergence criterion (which is discussed later)
- 

In our case simulations are pressure driven. It means that pressure is imposed on inlet and outlet of the system and flow is driven only by gradient of pressure. Example of flow field and pressure distribution in pore space is given in Figure 7.1.



(a) pressure distribution in a porous network      (b) velocity field (pressure distribution colours)

Figure 7.1: Visualisation of pressure distribution and velocity field.

Boundary conditions at the edges of computational domains are set to mimic experimental conditions. On the inlet and outlet of samples a gradient of pressure is imposed. No-flow conditions are specified on the external surfaces of the samples and no-slip conditions are imposed on the pore-solid surface [Fig. 7.2].

The convergence criterion of steady-state simulations is based on initial residual values. This value presents relative differences in flow field parameters (velocity components, pressure) between current and precedent iteration. Convergence, and stoppage of computations, occurs when the residuals for each of parameters are reduced to a value below a

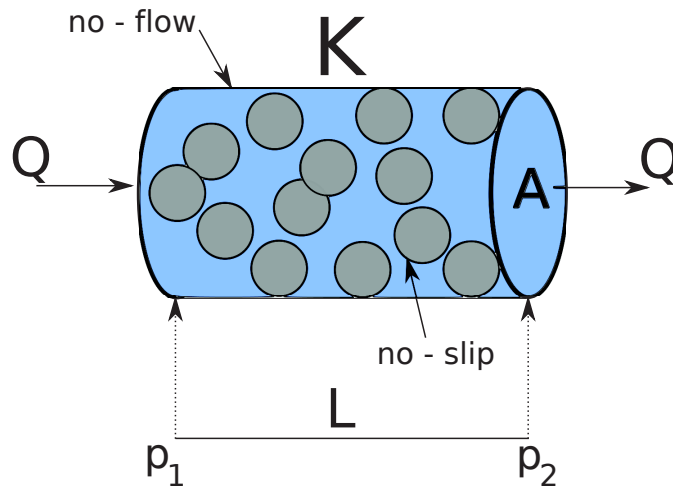


Figure 7.2: Simplified visualisation of boundary conditions.

tolerance. In order to estimate a convenient value we run simulations for initial and final dissolved state (percolated network dissolution) for geometry of sandstone using eight different initial residual values:  $10^{-1}, 10^{-2}, \dots, 10^{-8}$ . Computed fluxes were normalised by the flux obtained for initial residual value equal to  $10^{-8}$ . Figure 7.3 present evolution of normalised flux as a function of the logarithm of initial residual. Permeability is stabilised when initial residual level is equal to  $10^{-3}$  for the initial state of dissolution and  $10^{-5}$  for the last stage, for chosen geometry.

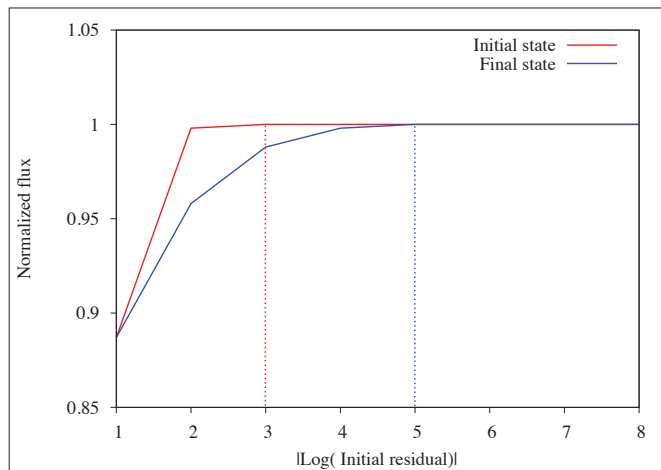


Figure 7.3: Convergence - normalised flux as function of initial residual.

### 7.1.3 Characteristic length and Reynolds number

When modelling a flow at the pore scale it is a common approach to solve Stokes equation, so the laminar regime is assumed. To justify the hypothesis we can estimate Reynolds number which is defined as follows:

$$Re = \frac{\rho \langle ||\vec{v}|| \rangle \lambda}{\tilde{\mu}}, \quad (7.1)$$

where  $\rho$  is fluid density,  $\langle ||\vec{v}|| \rangle$  is the mean velocity,  $\tilde{\mu}$  denotes dynamic viscosity and  $\lambda$  denotes the characteristic length.

Characteristic length is a property of porous media characterising its internal structure. In case of porous media it is usually mean grain diameter or mean pore diameter. For heterogeneous porous medium mean pore size or grain size can be estimated by covariance function or by morphological granulometry respectively. To ensure that the Reynolds number is much smaller than 1, the estimation is performed using the mean grain diameter and only for the final states where fluid velocities are expected to be maximal and by using mean grain sizes. Such estimation guarantee the following relation:

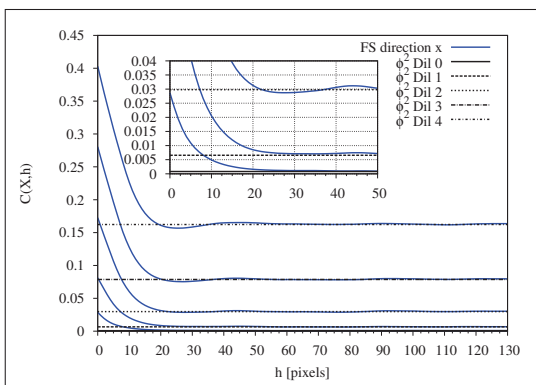
$$Re \ll 1. \quad (7.2)$$

In spite of small Reynolds number which implies occurrence of Stokes flow, comparison between built-in solvers in OpenFOAM shows that the solver for full Navier-Stokes equation, based on SIMPLE algorithm, is more efficient than the one for Stokes equation.

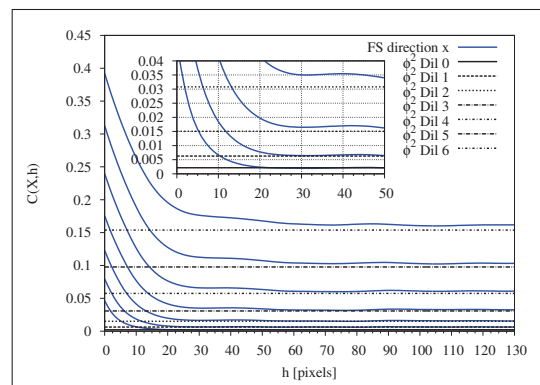
#### 7.1.4 RVE size estimation

To obtain a realistic velocity field of heterogeneous medium it is necessary to define RVE. Properties of a heterogeneous medium vary in space and therefore the volume on which simulations are performed should be large enough to capture sufficient amount of morphological properties of medium.

As we said before the maximal possible size of sample is considered as RVE. In order to verify a hypothesis that considered microstructure is sufficiently large we analyse evolution of covariance function, presented in Chapter 5. In term of covariance function, where the covariance range converges versus theoretical sill, the entire geometry can be considered as RVE. Due to the relation  $\lambda < L$ , where  $L$  denotes the size of the geometry and  $\lambda$  is a characteristic length. For both scenarii the entire geometry of sandstone and virtual samples ( $256 \times 256 \times 256$  px) are chosen to compute the flow.



(a) covariance function; isotropic dissolution



(b) covariance function; network dissolution

Figure 7.4: RVE's size estimation of sandstone.

## 7.2 Results

Permeability of investigated samples can be calculated according to Darcy's law which is given by following equation:

$$K = \frac{\mu QL}{\Delta p A}, \quad (7.3)$$

where  $\Delta p$  denotes macroscopic gradient of pressure in flow direction,  $Q$  is total flux,  $L$  denotes length of geometry in the flow direction,  $A$  is surface area of cross section perpendicular to the flow direction and  $\mu$  is dynamic viscosity [Fig. 7.2].

Aforementioned methodology was applied to estimate the diagonal permeability tensor components, what means that for each geometry 3 tests corresponding to three perpendicular directions of applied gradients of pressure ( $x$ ,  $y$  and  $z$ ), are performed. In order to obtain evolution of the components, for each geometry representing different dissolved state, numerical computations are performed. It means that for the scenario of isotropic dissolution, which is represented by 4 stages 132 velocity fields are obtained. In case of percolated network dissolution, represented by 6 stages, 198 computations are run and 33 calculations to obtain the initial permeability tensors.

### 7.2.1 Porosity - permeability relationships

In this subsection a porosity - permeability relationships for both scenarii of dissolution are presented. Figure 7.6 and Figure 7.7 present obtained results for isotropic and percolated network dissolution respectively.

Inhere, we start by analysing isotropic case. Evolution of each diagonal component of permeability tensor as a function of effective porosity is presented in Figure 7.6. For the sake of clarity, each component is presented separately. At first sight we can see that each components increase according to power law in the function of effective porosity. By using the least squares method the following relations, concerning sandstone, are obtained:

$$K_{xx} = 281797 \times \varphi_{eff}^{3.18}, \quad (7.4a)$$

$$K_{yy} = 244819 \times \varphi_{eff}^{3.07}, \quad (7.4b)$$

$$K_{zz} = 248655 \times \varphi_{eff}^{3.10}, \quad (7.4c)$$

and for averaged components of generated samples:

$$K_{xx} = 293665 \times \varphi_{eff}^{3.16}, \quad (7.5a)$$

$$K_{yy} = 327661 \times \varphi_{eff}^{3.25}, \quad (7.5b)$$

$$K_{zz} = 349107 \times \varphi_{eff}^{3.30}, \quad (7.5c)$$

Figure 7.7 shows evolution of each diagonal component of permeability tensor as a function of effective porosity in case of percolated network dissolution. Like in the previous case, for the sake of clarity, each component is presented separately. By using the same method,

the following relations for sandstone are obtained:

$$K_{xx} = 755820 \times \varphi_{eff}^{3.46}, \quad (7.6a)$$

$$K_{yy} = 1223793 \times \varphi_{eff}^{3.47}, \quad (7.6b)$$

$$K_{zz} = 1073691 \times \varphi_{eff}^{3.46}, \quad (7.6c)$$

and for averaged components of generated samples:

$$K_{xx} = 1015321 \times \varphi_{eff}^{3.48}, \quad (7.7a)$$

$$K_{yy} = 990757 \times \varphi_{eff}^{3.55}, \quad (7.7b)$$

$$K_{zz} = 982042 \times \varphi_{eff}^{3.57}, \quad (7.7c)$$

For each fit the correlation coefficient satisfies the inequality  $r^2 > 0.99$ . However, for each estimation the factor of proportionality is significantly different. To compare obtained results we evoke some commonly know models which deal with the permeability - porosity relationship.

Kozeny-Carman model [94] assumes that the porous media can be considered as a bundle of tubes of different radii and that the flow is laminar. The model is given by following equation:

$$K = \frac{\varphi_{eff}^3}{\omega \tau s^2}, \quad (7.8)$$

where,  $\omega$ ,  $\tau$  and  $s$  stands for shape factor, tortuosity and specific surface respectively. It is to notice that the power law is characterised by exponent equal to 3.

In the paper of Bourbie and Zinszner [95], where permeability was experimentally determined for 240 samples of Fontainebleau sandstone having different porosity values, it has been found that porosity-permeability relation can be described by two separate power laws: an exponent equal to 3.05 for porosities grater than 9 % and exponent equal to 7.33 for lower porosities. On the other hand Doyen [96] described this relation by an exponent equal to 3.8. Aforementioned models confirms consistency of obtained results of permeability - porosity relationships. However, in general, the relationship between porosity and the permeability can not be described by a simple power law over the whole range of porosity. Obtained results should be treated with a caution.

Analysing evolution for both scenarii we can say that permeability components increase much faster during percolated network dissolution. It may be explained by larger pore diameter due to bigger number of iterations corresponding to dissolution steps. Moreover, effective porosity is not a good descriptor for isotropic dissolution scenario due to the fact that during dissolution isolated pores (which are enlarging) get connected but their contribution to flow may be irrelevant since they can be treated as dead-ends pores [Fig. 7.5]. In case of percolated network dissolution, when the connections with isolated (non-dissolved) pores appears, we can assume that their influence to the permeability is negligible since their contribution to effective porosity is irrelevant [Fig. 7.5]. In general, reconstructed samples have similar behaviour satisfactorily imitates sandstone.

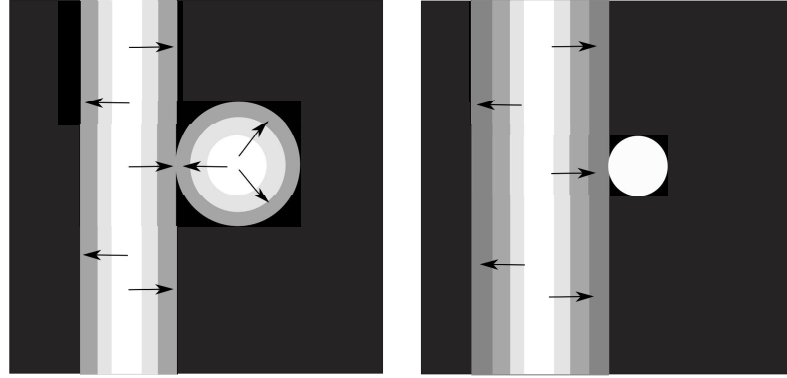


Figure 7.5: Visualisation of isolated pores connections during isotropic and percolated network dissolution respectively.

### 7.2.2 Tortuosity - permeability relationships

In general there exists a lot of different approaches to define tortuosity. Nevertheless, we present some basic estimations of tortuosity - permeability relationship based on the obtained results like in the previous subsection. Figures 7.6 and 7.7 present evolution of permeability components as a function of morphological tortuosity components for isotropic and percolated network scenario respectively. At first sight we can notice a general decreasing trend of permeability with increasing value of tortuosity. Obtained results for sandstone and reconstructed samples are in good convergence. Estimated sandstone's permeability is included in square determined by generated samples mean values and their standard deviations. By using the least squares method the following relations, concerning sandstone, are obtained:

$$K_{xx} = 61734 \times \tau_x^{-12.47}, \quad (7.9a)$$

$$K_{yy} = 127625 \times \tau_y^{-15.35}, \quad (7.9b)$$

$$K_{zz} = 52355 \times \tau_z^{-11.06}, \quad (7.9c)$$

and for averaged components of generated samples:

$$K_{xx} = 81613 \times \tau_x^{-12.64}, \quad (7.10a)$$

$$K_{yy} = 89350 \times \tau_y^{-12.95}, \quad (7.10b)$$

$$K_{zz} = 81064 \times \tau_z^{-12.11}, \quad (7.10c)$$

Figure 7.7 shows evolution of each diagonal component of permeability tensor as a function of effective porosity in case of percolated network dissolution. Like in the previous case, for the sake of clarity, each component is presented separately. By using the same method, the following relations for sandstone are obtained:

$$K_{xx} = 138171 \times \tau_x^{-12.77}, \quad (7.11a)$$

$$K_{yy} = 194089 \times \tau_y^{-16.54}, \quad (7.11b)$$

$$K_{zz} = 100456 \times \tau_z^{-11.95}, \quad (7.11c)$$



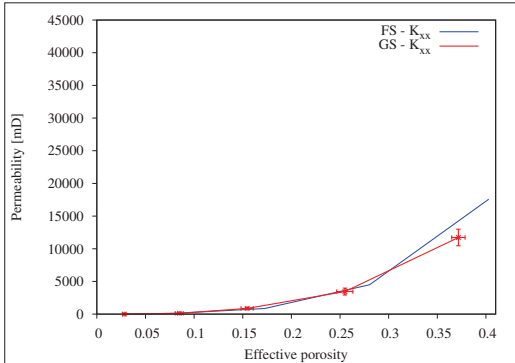
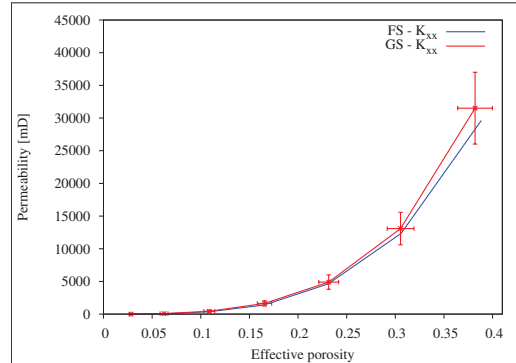
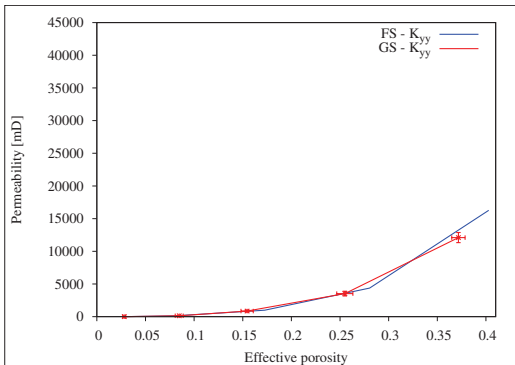
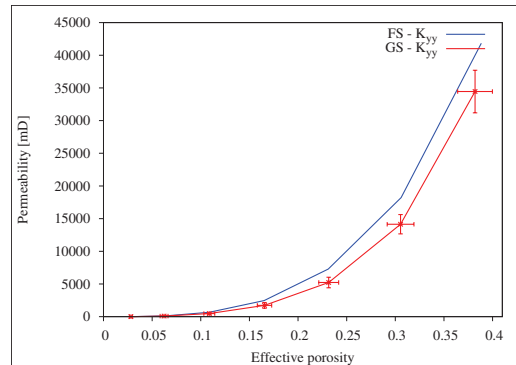
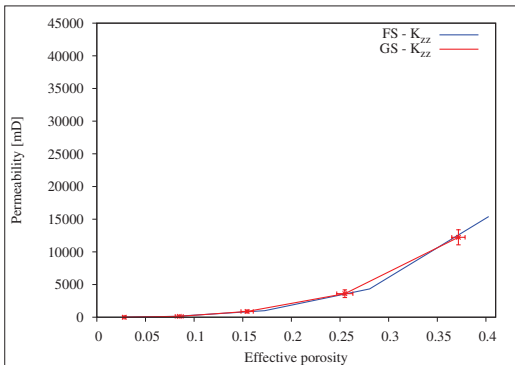
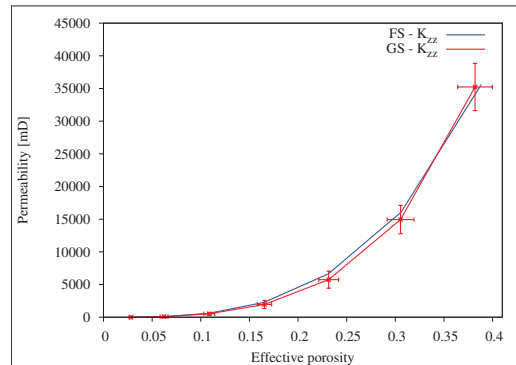
(a) component  $K_{xx}$ (a) component  $K_{xx}$ (b) component  $K_{yy}$ (b) component  $K_{yy}$ (c) component  $K_{zz}$ (c) component  $K_{zz}$ 

Figure 7.6: Diagonal components evolution during isotropic dissolution scenario of Fontainebleau sandstone (FS) and generated samples (GS) as a function of effective porosity.

Figure 7.7: Diagonal components evolution during percolated network dissolution of sandstone (FS) and generated samples (GS) as a function of effective porosity.

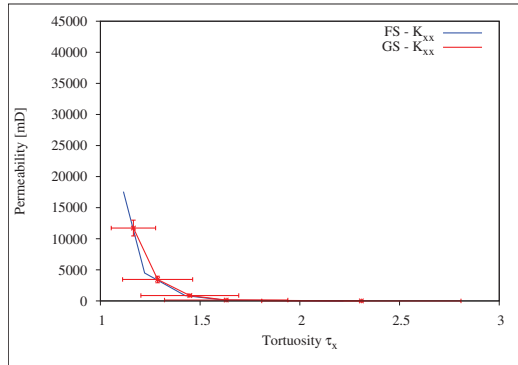
and for averaged components of generated samples:

$$K_{xx} = 155911 \times \tau_x^{-12.81}, \quad (7.12a)$$

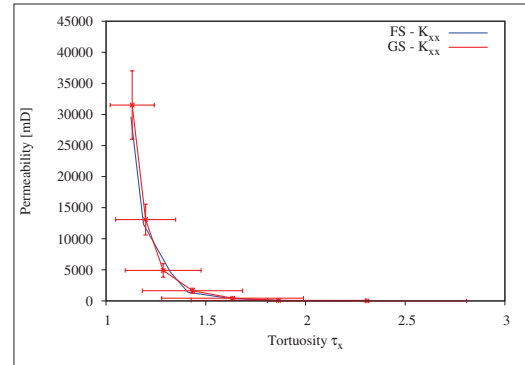
$$K_{yy} = 187083 \times \tau_y^{-13.49}, \quad (7.12b)$$

$$K_{zz} = 155978 \times \tau_z^{-12.46}, \quad (7.12c)$$

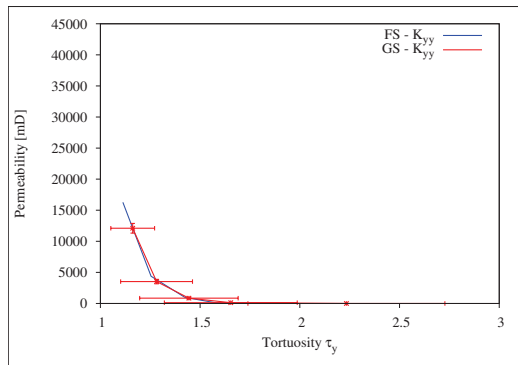
For each fit the correlation coefficient satisfies the inequality  $r^2 > 0.98$ .



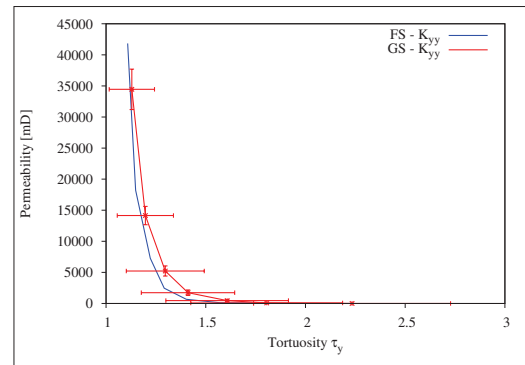
(a) component  $K_{xx}$



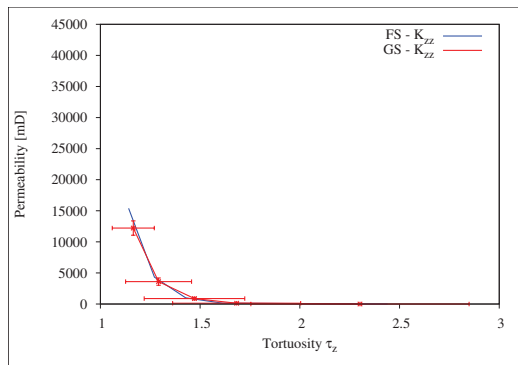
(a) component  $K_{xx}$



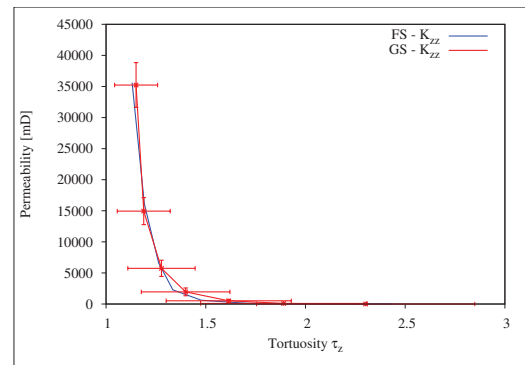
(b) component  $K_{yy}$



(b) component  $K_{yy}$



(c) component  $K_{zz}$



(c) component  $K_{zz}$

Figure 7.8: Diagonal components evolution during scenario of isotropic dissolution of sandstone (FS) and generated samples (GS) as a function of tortuosity.

Figure 7.9: Diagonal components evolution during percolated network dissolution of sandstone (FS) and generated samples (GS) as a function of tortuosity.

Estimation of anisotropy of permeability tensor has been proposed by Clavaud et al. [97] and can be evaluated using the anisotropy ratio  $R$  given by following formula:

$$R = \frac{K_{min}}{\sqrt{K_{int} K_{max}}}, \quad (7.13)$$

where  $K_{min}$ ,  $K_{max}$  and  $K_{int}$  denotes respectively minimal, maximal and intermediate value of diagonal permeability tensor components. We note that a perfectly isotropic tensor gives value equal to 1. Measurements of anisotropy of permeability tensor performed by Clavaud et al. (2008) give a large range of possible values of the factor  $R$ . It varies from 0.84 to 0.19 for the highest anisotropic sample. However, for the purpose of this thesis we use following anisotropy factor  $\zeta$ , given by equation:

$$\zeta(K) = 1 - \frac{\|K - Proj_{\mathbb{I}}(K)\|}{\|K\|}, \quad (7.14)$$

where  $\mathbb{I}$  is the identity matrix and  $Proj_{\mathbb{I}}(K)$  is given by:

$$Proj_{\mathbb{I}}(K) = \frac{1}{3}(K : \mathbb{I})\mathbb{I}. \quad (7.15)$$

Tables 7.1 and 7.2 present evolution of anisotropy factor calculated for sandstone's permeability tensors and for averaged permeability tensor obtained for generated samples. Due to errors related to refinement level and possible significant overestimations we skip the results obtained for the initial step. Therefore, we can say that during isotropic dissolution of sandstone no specific trend is observed, while for generated samples a quasi constant trend is observed. In case of virtual material we can say that anisotropy has constant value. In the other hand during dissolution of percolated porous network anisotropy factor of sandstone decreases systematically while for generated samples remains quasi constant.

Table 7.1: Evolution of anisotropy coefficient: definition proposed by Clavaud et al. [97] (grey) and according to equation 7.14. Isotropic dissolution scenario.

	Initial	Dil 1	Dil 2	Dil 3	Dil 4
FS	0.85	0.87	0.87	0.97	0.91
GS	0.75	0.98	0.98	0.97	0.96
FS	0.91	0.93	0.93	0.98	0.95
GS	0.83	0.99	0.99	0.98	0.98

Table 7.2: Evolution of anisotropy coefficient: definition proposed by Clavaud et al. [97] (grey) and according to equation 7.14. Percolated network dissolution.

	Initial	Dil 1	Dil 2	Dil 3	Dil 4	Dil 5	Dil 6
FS	0.85	0.58	0.57	0.59	0.67	0.72	0.77
GS	0.75	0.90	0.90	0.89	0.90	0.90	0.90
FS	0.91	0.77	0.76	0.78	0.82	0.85	0.86
GS	0.83	0.94	0.93	0.92	0.93	0.95	0.95

### 7.3 Mechanical properties versus permeability

Figures 7.10 and 7.11 present elastic moduli as a function of permeability, projected on isotropic basis, for isotropic and percolated network dissolution respectively. To the obtained results we fit function in the form:

$$P(K) = 1 - \frac{K^\beta}{\alpha} \quad \text{and} \quad \beta \in (0, 1), \quad (7.16)$$

where P stands for normalised elastic modulus and K is a permeability. For all obtained functions correlation factor satisfies inequality  $r^2 > 0.98$ .

In the first sight, a general decreasing trend is observed. For both scenarii shear modulus is more affected with increasing permeability. However, despite of significantly higher increase of permeability in case of percolated network dissolution, the corresponding elastic moduli show similar behaviour.

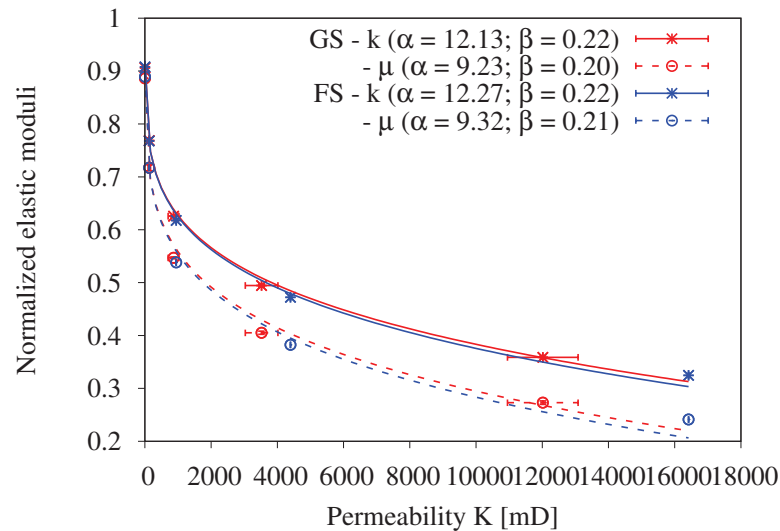


Figure 7.10: Elastic moduli as a function of permeability of sandstone (FS) and generated samples (GS). Isotropic dissolution scenario.

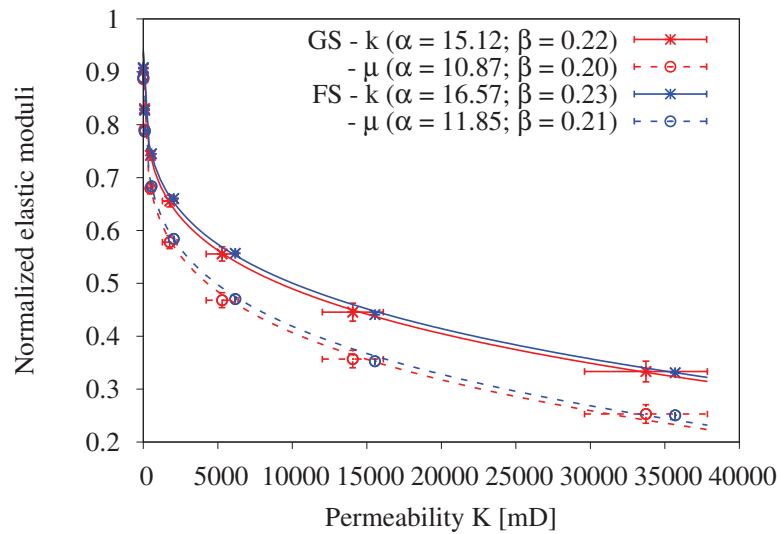


Figure 7.11: Elastic moduli as a function of permeability of sandstone (FS) and generated samples (GS). Percolated network dissolution.

## 7.4 Conclusions

In this chapter the common methodology used for solving flow from X-ray tomography images is presented. Starting from image analysis and segmentation, to the estimation of velocity field by using OpenFOAM and estimation of permeability according to Darcy's law are presented.

Similar to the other authors a significant increase in the permeability with the increase of porosity and progressive dissolution as well as with decreasing tortuosity are observed. It is noticed that in the case of percolated network dissolution permeability increases faster as a function of effective porosity and morphological tortuosity.

Numerical results show that the relationship permeability - morphological tortuosity is much complicated for 3D structure in considered media.

Moreover, a simple relation linking elastic moduli with permeability is proposed.

The reconstruction method based on the skeleton reconstruction is efficient in order to simulate behaviour of natural rock sample. What is confirmed by comparison of exponential power law describing porosity - permeability relation with some models existing in the literature.

*Everything has to come to an end, sometime.*

L. Frank Baum

# 8

## General conclusions & perspectives

### Conclusions

Studies presented in this thesis are set out to explore the evolution of mechanical and transport properties of saline aquifer, subjected to progressive chemical degradation triggered by acidification of saline water by injected CO<sub>2</sub>. For the purpose of the thesis chemical dissolution is taken into account in simplified way using morphological dilation of porous phase. In order to perform the modelling following main assumptions were applied:

- phenomena at micro-scale - considering microtomography image of investigated microstructure, numerical dissolution is performed directly on the image and governing equations of considered phenomena are solved at micro-scale
- uniform dissolution - this assumption led us to use isotropic structuring elements (cubic); due to the finite resolution of microtomography we investigate two different scenarii of numerical dissolution
- two-scale modelling and periodicity - obtained degraded microstructures are assumed to be representative, therefore upscaling methods of averaging techniques are used to obtain effective behaviour

Chapter 3 presents a first approach, linking the dissolution of rock at the microscopic scale and the effective behaviour of the saline aquifer. The point of this approach is to reconstruct periodic RVE using reflectional symmetry. Performed numerical computations for an orthotropic microstructure show progressive degradation of all components of the stiffness tensor that follow an exponential decay function. The relation between the mechanical parameters and the transfer properties (tortuosity and permeability tensors)

during the dissolution process is also studied. It is found that the high increase of conductivity (in the direction  $\vec{y}$ ) does not correspond (as could be expected) to the highest weakening of the Young modulus in this direction. Moreover, the highest decrease of Young modulus (in the direction  $\vec{x}$ ) is not associated with percolation in this direction. The results clearly show that the morphological information about the microstructure can be very useful in the qualitative explanation of the chemical degradation process.

Next chapter (Chapter 4), provides detailed characterisation of Fontainebleau sandstone microstructure and proposes a reconstruction method. Performed morphological characterisation is based on binary image analysis. In this analysis four main types of descriptors are used: global, sizing, spatial distribution and connectivity. An efficient method to generate equivalent microstructures, inspired by natural process and based on the extracted morphological characterization, is proposed. The reconstruction method consists in three steps: grain deposit, compaction and diagenesis process. Finally, morphological validation of the generated samples confirms that they can be treated as statistically equivalent realisations of investigated Fontainebleau sandstone microstructure.

Chapter 5 introduces two different scenarios of numerical dissolution that are imitating in simplified way chemical degradation of microstructure. Those scenarios are: isotropic scenario and dissolution of percolated porous network. Detailed analysis of micro-structural changes triggered by both scenarios is quantified using aforementioned morphological characterisation. Analysing covariance function, the most important facts state that:

1. during the isotropic dissolution scenario RVE size can remain constant
2. during the percolated network dissolution scenario RVE size increases significantly
3. entire geometry of sandstone and generated samples can be viewed as RVEs

Evolution of mechanical properties in the framework of linear elasticity is presented in Chapter 6. The point of the method is to find a solution in order to apply periodic boundary conditions on geometrically non-periodic RVE. This solution consists in spreading a layer over the considered RVE and to prescribe its properties (each component of stiffness matrix) by using fixed point method. The estimation of mechanical behaviour evolution is performed directly via binary images using a methodology proposed by Roberts, Day and Garboczi et al.. Due to the limitation of computer memory only the small resolutions were taken into account. Obtained results are in good agreement with this presented by Arns et al.. Analysis of evolution of effective properties of periodic geometry and the evolution of the same sample with using layer and fixed point method, shows that our method overestimate the result with relative error smaller than 1%. Averaged relationships of elastic behaviour - porosity of reconstructed samples are in very good agreement with evolution of the properties calculated for sandstone. It is shown that both scenarios give similar results of evolution of effective elastic moduli.

Chapter 7 presents the common methodology used for solving flow via binary images. Similar to the other authors a significant increase in the permeability with the increase of porosity and progressive dissolution as well as with decreasing tortuosity are observed. It is noticed that in the case of percolated network dissolution permeability increases faster as a function of effective porosity and morphological tortuosity. Numerical results show

that the relationship permeability - morphological tortuosity is much complicated for 3D structure in considered media. Moreover, a simple relation linking elastic moduli with permeability is proposed.

## Perspectives

In regarding to the modelling of chemical dissolution and its effects on effective properties of considered media few comments concerning used methodology are remarked.

Due to the implementation of numerical dissolution, in order to minimise some border effects, the used method should be performed on bigger image representing microstructures than the size of samples on which morphological analysis and numerical computations were performed. In order to confirm modelling of dissolution an analysis of microtomographic images representing real dissolved microstructures would be expected.

In regarding to the method of effective elastic properties estimation combined with using additional external layer requires more computation. In order to described properly the influence of the layer more detailed analysis is required.

In order to dispel any doubts concerning overestimation of mechanical properties evolution, in terms of the reason of overestimation - mechanism of dissolution or small resolution, computations should be performed using better resolution.

Analysis of evolution of homogenised stiffness tensors projected on orthotropic basis would be well viewed development in order to understand better impact of dissolution.

Methodology proposed in this thesis can be easily adapted, in order to perform similar analysis, on aforementioned limestone. This point of the perspectives is during the implementation.







# Algorithms and pseudocodes

For the purpose of the work, the 3D binary image was imported as a three-dimensional matrix. Where pixel which represents pore possess assigned value equal to 1 and a pixel denoting solid phase is valued by 0. Inhere we presented implementations of basic morphological operations: dilation and erosion.

## A.1 Morphological operations

According to the definition 2.2, dilation was implemented in following way, presented by Pseudocode A.2.

---

**Pseudocode A.2** Implementation of dilation

---

```
1: Input matrix[ N ][ N ][ N ];
2: Output matrix_dilated[ N ][ N ][ N ];
3: Initialization matrix_dilated[ N ][ N ][ N ] = matrix[ N ][ N ][ N ]
4: function dilation {
5:   for all elements : i, j, k in N do
6:     if matrix[ i ][ j ][ k ] == 1 then
7:       matrix_dilated[ i ][ j ][ k ] == 1;
8:       for all elements : i_next, j_next, k_next in neighbourhood do
9:         matrix_dilated[ i_next ][ j_next ][ k_next ] == 1;
10:      end for
11:    end if
12:  end for
13: return dilated matrix: matrix_dilated[ N ][ N ][ N ];
14: }
```

---

According to the definition 2.2, erosion was implemented like dilation of solid phase.

---

**Pseudocode A.3** Implementation of erosion
 

---

```

1: Input matrix[ N ][ N ][ N ];
2: Output matrix_eroded[ N ][ N ][ N ];
3: Initialization matrix_eroded[ N ][ N ][ N ] = matrix[ N ][ N ][ N ]
4: function erosion {
5:   for all elements : i, j, k in N do
6:     if matrix[ i ][ j ][ k ] == 0 then
7:       matrix_eroded[ i ][ j ][ k ] == 0;
8:       for all elements : i_next, j_next, k_next in neighbourhood do
9:         matrix_dilated[ i_next ][ j_next ][ k_next ] == 0;
10:      end for
11:    end if
12:  end for
13: return matrix_eroded[ N ][ N ][ N ];
14: }
```

---

## A.2 Morphological descriptors

Estimation of porosity consist of scanning pixel by pixel and increasing a counter  $p$  when scanned pixel represents porous phase

---

**Pseudocode A.4** Estimation of porosity – pseudocode
 

---

```

1: Input matrix[ N ][ N ][ N ]
2: Output porosity
3: function porosity {
4:   variable p = 0;
5:   for all elements : i j k in N do
6:     if matrix[ i ][ j ][ k ] == 1 then
7:       p = p+1;
8:     end if
9:   end for
10: return porosity: p/N3;
11: }
```

---

Specific surface is estimated directly by analysing binary image of the medium, pixel by pixel. For this purpose for each pixel of porous phase its neighbourhood is scanned by the structuring element. If any component of structuring element is located in opposite (solid) phase the value of specific surface counter increase by 1.

---

**Pseudocode A.5** representing estimation of specific surface

---

```

1: Input matrix[ N ][ N ][ N ]
2: Output specific surface
3: function specific surface {
4:   variable s = 0;
5:   for all elements : i, j, k in N do
6:     if matrix[ i ][ j ][ k ] == 1 then
7:       for all elements : i_next, j_next, k_next in 6-nearest neighbourhood do
8:         if matrix[ i_next ][ j_next ][ k_next ] == 0 then
9:           s = s+1;
10:        end if
11:       end for
12:     end if
13:   end for
14:   return specific surface: s/N3;
15: }
```

---

As presented in Section 2, morphological granulometry is estimated according to the method illustrated by Algorithm A.6.

---

**Algorithm A.6** Estimation of granulometry

---

1. import the initial image  $X_0$ .
  2. perform erosion on  $X_0$  by using  $B_r$ ,  $\rightarrow X_{eroded}(r)$ .
  3. perform dilation on  $X_{eroded}$  by using  $B_r$ ,  $\rightarrow X_{opened}(r)$ .
  4. compute porosity of the opened image  $\rightarrow \varphi(X_{opened}(r))$ .
  5. if  $\varphi(X_{opened}(r)) \neq 0$  increase  $r$ .
  6. repeat steps 1 – 5 until  $\varphi(X_{opened}(r)) = 0$ .
- 

Estimation of covariance function is summarised in Algorithm A.7. For the sake of clarity, Figure A.1 visualises the process.

---

<sup>1</sup>source: <http://ciks.cbt.nist.gov/garboocz/paper19/node2.html>.

---

**Algorithm A.7** Estimation of covariance function
 

---

1. import the image  $X$ .
  2. compute the power spectrum of DFT of the image  $X \rightarrow |F(X)|^2$ .
  3. compute the invert DFT  $\rightarrow \tilde{C}(X) = F^{-1}(|F(X)|^2)$ .
  4. estimate the maximum grey level value of the field  $\Omega_1 \rightarrow \omega_{max} = \max\{\tilde{C}(x \in \Omega_1)\}$ .
  5. find the mean grey level value of the field  $\Omega_2 \rightarrow \omega_{mean} = \langle \tilde{C}(x \in \Omega_2) \rangle$ .
  6. correlate linearly the map  $\tilde{C}(X)$  using relations:  $\omega_{max} = \varphi(X)$ ;  $\omega_{mean} = \varphi(X)^2$ .
  7. the result of the correlation is  $C(X)$ ; plot the covariance function for desired orientation.
- 

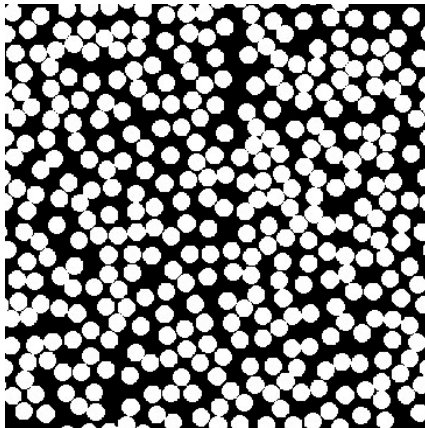
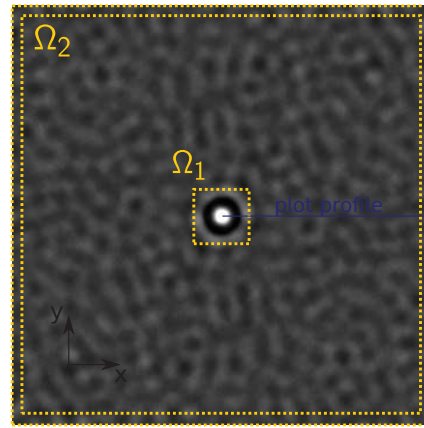
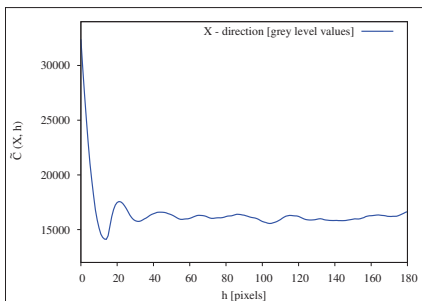
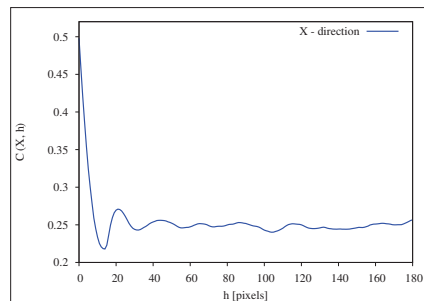
(a) binary image  $X^1$ (b)  $F^{-1}(|F(X)|^2)$ (c)  $\tilde{C}(X, \vec{h})$ (d) correlated  $\tilde{C}(X, \vec{h})$ 

Figure A.1: Microstructure and its covariance functions

# B

## Macroscopic problem

In the model, we assume that all upper layers apply constant stress  $\sigma_0$  on the aquifer and that the variations of stress caused by human or environment activities are negligible. We also consider the so called 'far field' and/or long term situation which means that the  $\text{CO}_2$  was completely dissolved in the saline aquifer. The presence of  $\text{CO}_2$  in water creates the acid environment, therefore, dissolution of rock material begins. The progressive dissolution causes changes of porosity, and variations of material properties, this process can take thousands of years. In the analysis we assume that the porous rock is homogeneous and periodic. The objective is to formulate an incremental model, in the framework of linear theory of elasticity, that will be able to capture the subsidence due to the chemical degradation of solid under a constant load.

Let us consider a macroscopic, one dimensional problem of settlement (creep) taking place in a rocks formation (saline aquifer). The medium is characterised by three dimensional microstructure presented in Figure B.1, where axis  $\vec{z}$  is parallel to the gravitational force and position of all axes remains unchanged during the process of settlement. We assume that saline water can flow out from the aquifer with no resistance (drained conditions) and that the external stress is constant in time. In order to derive an incremental law of elasticity, let us assume the validity of Hooke's law in which material properties (e.g. Young's modulus) and deformation depend on porosity  $\varphi$

$$\sigma_0 = E(\varphi)\epsilon(\varphi). \quad (\text{B.1})$$

By calculating the derivative with respect to porosity we obtain

$$0 = \frac{dE(\varphi)}{d\varphi}\epsilon(\varphi) + E(\varphi)\frac{d\epsilon(\varphi)}{d\varphi}. \quad (\text{B.2})$$

Equation B.2 can be presented in the following form

$$0 = \epsilon(\varphi)dE(\varphi) + E(\varphi)d\epsilon(\varphi), \quad (\text{B.3})$$

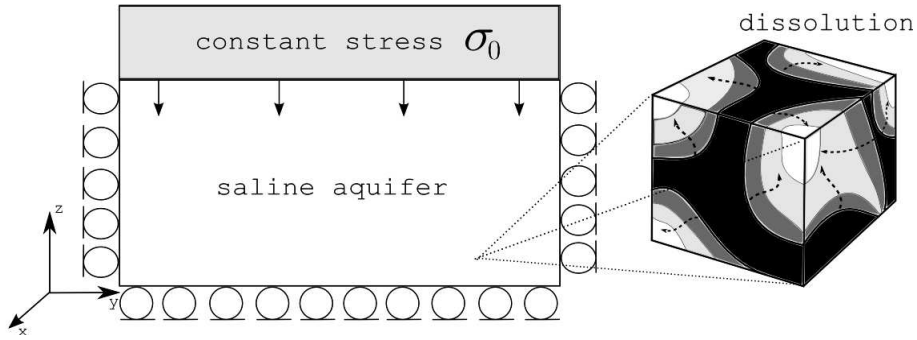


Figure B.1: Macroscopic problem with evolving microstructure.

which is equivalent to

$$0 = \epsilon(\varphi) [E(\varphi + d\varphi) - E(\varphi)] + E(\varphi) [\epsilon(\varphi + d\varphi) - \epsilon(\varphi)]. \tag{B.4}$$

After an algebraic transformation we can write

$$\epsilon(\varphi + d\varphi) = \epsilon(\varphi) \left[ 2 - \frac{E(\varphi + d\varphi)}{E(\varphi)} \right]. \tag{B.5}$$

By introduction the iterative notation we obtain

$$\epsilon_{i+1} = \epsilon_i \left[ 2 - \frac{E_{i+1}}{E_i} \right]. \tag{B.6}$$

We must notice that our problem is a feedback process. At each step, the change of porosity due to mass loss (dissolution) causes the decrease of Young’s modulus and increase of deformation. But on the other hand, each increment of deformation (settlement) leads to decrease of porosity and to associated increase of Young’s modulus value. For clarity the process is illustrated in Figure B.2, where  $\varphi_i$  is the current value of porosity

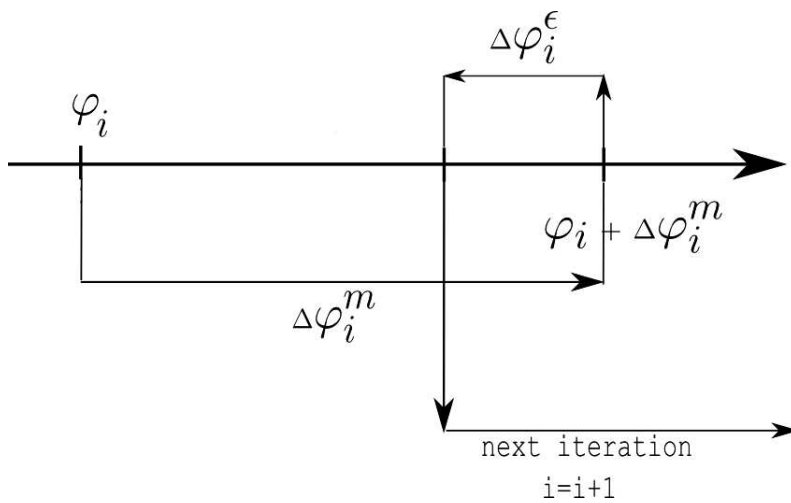


Figure B.2: Illustration of the algorithm.

of  $i$  step,  $\Delta\varphi_i^m$  is the change of porosity caused by loss of mass and  $\Delta\varphi_i^\epsilon$  is the variation

of porosity caused by deformation. The next step ( $i + 1$ ) starts from value of porosity  $\varphi_i + \Delta\varphi_i^m - \Delta\varphi_i^\epsilon$ . If we assume that the skeleton material is incompressible with respect to the porous material, than the macroscopic deformation can be considered as equal to the change of porosity. Finally, we write

$$\Delta\varphi_i^\epsilon = \frac{\sigma_0}{E(\varphi_i + \Delta\varphi_i^m)}, \quad (\text{B.7})$$

where  $E(\varphi_i + \Delta\varphi_i^m)$  means the value of Young modulus for porosity  $(\varphi_i + \Delta\varphi_i^m)$ , which is taken from the degradation function. Finally, to solve the problem we need to know the degradation functions of material parameters.

### B.0.1 Solution of the macroscopic boundary problem

The one-dimensional problem of subsidence defined in Annexe B was solved by using the degradation function of the Young modulus in the  $z$  direction (Figure 3.10), given by

$$E_z = A \exp(-\varphi/B) + C$$

where  $A = 16.78$  GPa,  $B = 0.16$ ,  $C = 10.02$  GPa and  $\varphi$  is a porosity. It is assumed that vertical stress is constant and equal  $\sigma_z = 20$  MPa. This stress corresponds to the weight of layer of 1 km of the unit volumetric weight  $20 \text{ kN/m}^3$ . In Figure B.3 the strain variation  $\epsilon_z = \Delta s/h$  (decreased by the value of initial deformation  $\epsilon_0 = \sigma_0/E_z(\varphi_0)$ ) as a function of porosity is shown. We observe the increase of strain to the value of  $-0.65 \times 10^{-3}$ , while the porosity varies from the 0.093 to 0.40 (initial and final values). The corresponding Young modulus varies from  $E_z = 20.19$  GPa to  $E_z = 12.19$  GPa, respectively. It can be said, that in the framework of the assumption of long term behaviour, drained condition and uniform dissolution the macroscopic effects of subsidence are very limited.

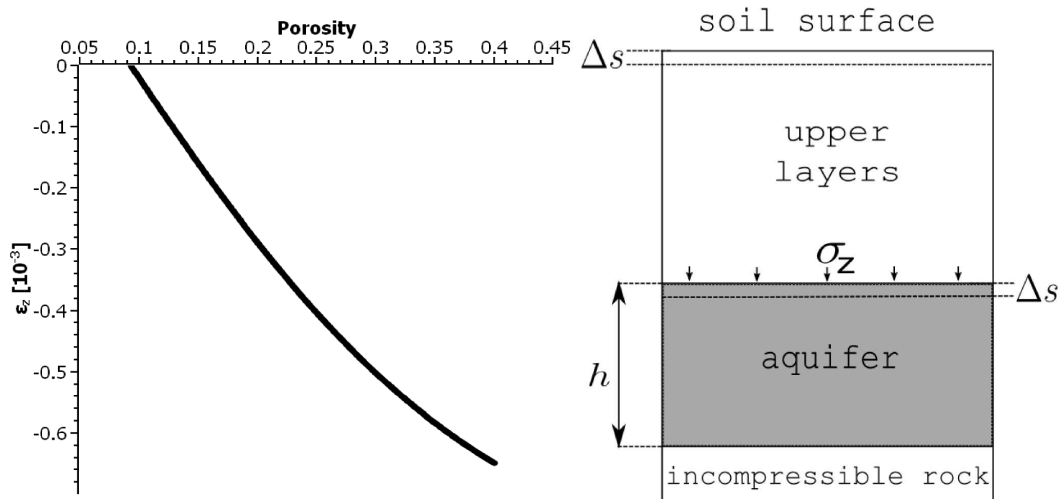


Figure B.3: Settlement problem;  $\epsilon_z$  denotes vertical macroscopic deformation and  $\Delta s$  is the change in height.







# Connected component labelling

Connected components labelling scans an image and groups its pixels into components based on pixel connectivity. For the purpose of this work we assume binary input images and 6-connectivity in 3D. The connected components labelling scans the image by moving along a row until it comes to a point  $p$  (where  $p$  denotes the pixel to be labeled) belonging to the foreground. When this is true, it examines the six neighbours of  $p$ . Labelling of scanned pixel  $p$  occurs as follows:

- if all four neighbours are 0 or 1 assign new label to  $p$
- if neighbourhood has a prescribed label, assign the maximal label to  $p$

After completing the scan, all the pixels representing porous phase possess assigned label. After this first step an iterative method is adapted to merge neighbouring labels sharing different values. This operation is repeated iteratively. Program stops when for each pixel of the foreground its neighbourhood (also belonging to the foreground) possess the same label value. Algorithm is illustrated in Figures C.2 and C.3

A pore, whose labels are located on opposite external faces of the geometry, is assumed to belong to percolated network. For the sake of clarity an example is illustrated in Figure C.1.

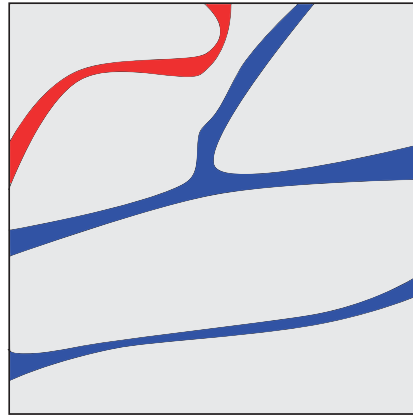


Figure C.1: Schema illustrating extracting of percolated network. Red colour stands for a pore which does not belong to percolated network.

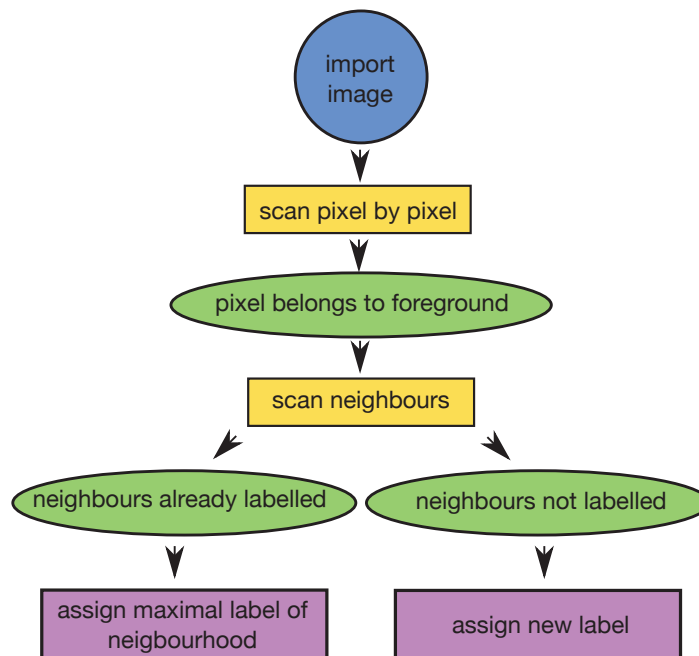


Figure C.2: Schema illustrating first step of the algorithm. All pixels have an assigned label.

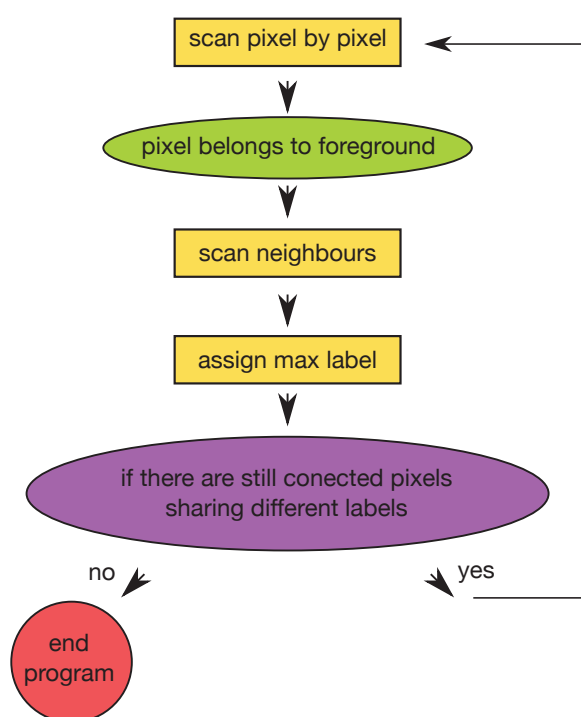


Figure C.3: Schema illustrating merging of labels.



# Bibliography

- [1] B. Metz, O. Davidson, H. de Coninck, M. Loos, and L. Meyer, editors. *IPCC Special Report on Carbon Dioxide Capture and Storage*. Cambridge University Press, Cambridge, United Kingdom and New York, USA, 2005.
- [2] J. Bemmer and J. M. Lombard. From injectivity to integrity studies of CO<sub>2</sub> geological storage. chemical alteration effects on carbonates petrophysical and geomechanical properties. *Oil & Gas Science and Technology*, 65:445–459, 2009.
- [3] Dominique Jeulin. Random texture models for material structures. *Statistics and Computing*, 10:121–132, 2000.
- [4] S. Bakke and P.-E. Øren. 3-d pore-scale modelling of sandstones and flow simulations in the pore networks. society of petroleum engineers. *Society of Petroleum Engineers*, 2:136 – 149, 1997.
- [5] P.-E. Øren and S. Bakke. Process based reconstruction of sandstones and prediction of transport properties. *Transport in Porous Media*, 46:311–343, 2002.
- [6] F. Dubois and M. Jean. Lmgc90 une plateforme de développement dédiée à la modélisation des problèmes d’interaction. *Actes du sixième colloque national en calcul des structures, CSMA-AFM-LMS*, 1:111–118, 2003.
- [7] F. Dubois and M. Jean. *The non smooth contact dynamic method: recent LMGC90 software developments and application*, volume 27 of *Lecture Notes in Applied and Computational Mechanics*. Springer Berlin Heidelberg, 2006.
- [8] P. Egermann, E. Bemmer, and B. Zisner. An experimental investigation of the rock properties evolution associated to different levels of CO<sub>2</sub> injection like alternation processes. *Paper SCA Presented at the Society of Core Analysts Symposium, Trondheim, Norway*, 12-16 September 2006.
- [9] M. Bornert, T. Bretheau, and P. Gilormini, editors. *Homogénéisation en mécanique des matériaux 1 : matériaux aléatoires élastiques et milieux périodiques*. Hermes Science Publications, Paris, France, 2001.
- [10] E. Sanchez-Palencia. *Non-Homogeneous Media and Vibration Theory*. Springer-Verlag, Berlin, Germany, 1980.
- [11] L. Francoise. *PhD thesis: Contribution a l’étude des matériaux composites et de leur endommagement*. Université Pierre et Marie Curie, Paris, France, 1984.

- [12] E. J. Garboczi and A. R. Day. An algorithm for computing the effective linear elastic properties of heterogeneous materials: Three-dimensional results for composites with equal phase poisson ratios. *Journal of the Mechanics and Physics of Solids*, 43:1349 – 1362, 1995.
- [13] A. P. Roberts and E. J. Garboczi. Elastic moduli of model random three-dimensional closed-cell cellular solids. *Acta Materialia*, 49:189 – 197, 2001.
- [14] A. P. Roberts and E. J. Garboczi. Elastic properties of model random three-dimensional open-cell solids. *Journal of the Mechanics and Physics of Solids*, 50:33 – 55, 2002.
- [15] C. H. Arns, M. A. Knackstedt, W. V. Pinczewski, and E. J. Garboczi. Computation of linear elastic properties from microtomographic images: Methodology and match to theory and experiment. *Journal of Geophysics*, 67:1396–1405, 2002.
- [16] European Commission. Directive 2009/31/EC of the European Parliament and of the Council of 23 April 2009 on the geological storage of carbon dioxide and amending Council Directive 85/337/EEC, European Parliament and Council Directives 2000/60/EC, 2001/80/EC, 2004/35/EC, 2006/12/EC, 2008/1/EC and Regulation (EC) No. 1013/2006. *Official Journal of the European Union*, 5:114–135, 2009.
- [17] D. Jeulin. Random texture models for material structures. *Statistics and Computing*, 10:121–132, 2000.
- [18] J. Bear. *Dynamics of fluids in porous media*. Dover Publications, New York, USA, 1972.
- [19] G. Matheron. *Random Set and Integral Geometry*. Wiley, New York, USA, 1975.
- [20] J. Serra. *Image Analysis and Mathematical Morphology Vol. 1*. Academic Press, New York, USA, 1982.
- [21] R. Harlick and L. Shapiro. *Computer and Robot Vision, Vol. 1*. Addison Wesley Publishing Company, USA, 1992.
- [22] P. Soille. *Morphological Image Analysis Principles and Applications*. Springer-Verlag, Berlin, Heidelberg, New York, 2004.
- [23] L. Najman and H. Talbot, editors. *Mathematical Morphology From Theory to Applications*. ISTE Ltd. and John Wiley & Sons Inc., United Kingdom, USA, 2010.
- [24] C. Lantuéjole. *Geostatistical Simulations Models and Algorithms*. Springer, Berlin, Gemany, 2002.
- [25] L. Shapiro and G. Stockman. *Computer Vision*. Prentice Hall PTR, Upper Saddle River, NJ, USA, 2002.
- [26] G. Birkhoff. *Lattice Theory*. AMS, Providence, USA, 1967.
- [27] G. Grätzer. *General Lattice Theory*. Birkhauser Verlag, Basel, Switzerland’, 1978.

- [28] K. Kuratowski and A. Mostowski. *Set Theory*. North Holland, Amsterdam, Holland, 1976.
- [29] F.A.L. Dullien. *Porous Media Fluid Transport and Pore Structure*. Academic Press, San Diego, USA, 1991.
- [30] S. Marchand-Maillet and Y. M. Sharaiha. *Binary Digital Image Processing*. Academic Press, London, 2000.
- [31] S. Matheron. *Éléments pour une théorie des milieux poreux*. Masson, Paris, 1967.
- [32] S. Torquato. *Random Heterogeneous Materials*. Springer, New York, USA, 1982.
- [33] C. Lantuejoul and S. Beucher. On the use of geodesic metric in image analysis. *Journal of Microscopy*, 121:39–49, 1981.
- [34] J. Serra. *Image Analysis and Mathematical Morphology Vol. 2: Theoretical Advances*. Academic Press, London, England, 1988.
- [35] L. Decker, D. Jeulin, and I. Tovená. 3d morphological analysis of the connectivity of a porous medium. *Acta Stereologica*, 17:107–112, 1998.
- [36] C. Peyrega and D. Jeulin. Estimation of tortuosity and reconstruction of geodesic paths in 3d. *Image Analysis and Stereology*, 32:27–43, 2013.
- [37] J. Sethian. *Level Set Methods and Fast Marching Methods Evolving Interfaces in Computational Geometry, Fluid Mechanics, Computer Vision, and Materials Science*. Cambridge University Press, Cambridge, England, 1996.
- [38] M. Ostojá-Starzewski. *Microstructural Randomness and Scaling in Mechanics of Materials*. Chapman & Hall/CRC, USA, 2007.
- [39] I.M. Gitman, H. Askes, and L.J. Sluys. Representative volume: Existence and size determination. *Engineering Fracture Mechanics*, 74:2518 – 2534, 2007.
- [40] H. Böhm. *Mechanics of Microstructured Materials*. Springer - Verlag, Wien, Austria, 2004.
- [41] L. Dormieux, D. Kondo, and F.-J. Ulm. *Mechanics of Microstructured Materials*. John Wiley and Sons Ltd., Chichester, England, 2004.
- [42] T. Kanit, S. Forest, I. Galliet, V. Mounoury, and D. Jeulin. Determination of the size of the representative volume element for random composites: statistical and numerical approach. *International Journal of Solids and Structures*, 40:3647 – 3679, 2003.
- [43] J.-M. Gatt, Y. Monerie, D. Laux, and D. Baron. Elastic behavior of porous ceramics: application to nuclear fuel materials. *Journal of Nuclear Materials*, 336:145 – 155, 2005.



- [44] V. H. Nguyen, H. Colina, C. Boulay, J. M. Torrenti, and B. Nedjar. Chemo-mechanical coupling behaviour of leached concrete part i: experimental results. *Nuclear Engineering and Design*, 237:2083–2089, 2007.
- [45] I. Yurtdas, S. Y. Xie, N. Burlion, J-F. Shao, J. Saint-Marc, and A. Garnier. Influence of chemical degradation on mechanical behavior of a petroleum cement paste. *Cement and Concrete Research*, 41:412–421, 2011.
- [46] B. Huang and C. Qian. Experiment study of chemo-mechanical coupling behavior of leached concrete. *Construction and Building Materials*, 25:2649–2654, 2011.
- [47] C. Le Bellégo, G. Pijaudier-Cabot, B. Gérard, J. Dubé, and L. Molez. Coupled mechanical and chemical damage in calcium leached cementitious structures. *Journal of Engineering Mechanics*, 129:333–341, 2003.
- [48] F. J. Ulm, E. Lemarchand, and F. H. Heukamp. Elements of chemomechanics of calcium leaching of cement-based materials at different scales. *Engineering Fracture Mechanics*, 70:871–889, 2003.
- [49] G. Chatzigeorgiou, V. Picandet, A. Khelidj, and G. Pijaudier-Cabot. Coupling between progressive damage and permeability of concrete: analysis with a discrete model. *International Journal for Numerical and Analytical Methods in Geomechanics*, 29:1005–1018, 2005.
- [50] V. H. Nguyen, H. Colina, C. Boulay, J. M. Torrenti, and B. Nedjar. Chemo-mechanical coupling behaviour of leached concrete part ii: modelling. *Nuclear Engineering and Design*, 237:2090–2097, 2007.
- [51] E. Stora, B. Bary, Q-C. He, E. Deville, and P. Montarnal. Modelling and simulations of the chemo-mechanical behaviour of leached cement-based materials: Leaching process and induced loss of stiffness. *Cement and Concrete Research*, 39:763–772, 2009.
- [52] L. Luquot and P. Gouze. Experimental determination of porosity and permeability changes induced by massive injection of  $CO_2$  into carbonate reservoirs. *Chemical Geology*, 265:148–159, 2009.
- [53] P. Gouze and L. Luquot. X-ray microtomography characterization of porosity, permeability and reactive surface changes during dissolution. *Journal of Contaminant Hydrology*, 120–121:45–55, 2011.
- [54] P. Egermann, S. Bekri, and O. Vizika. An integrated approach to assess the petrophysical properties of rocks altered by rock/fluid interactions ( $CO_2$  injection). *Paper SCA Presented at the Society of Core Analysts Symposium, Toronto, Canada*, 21-25 August 2005.
- [55] O. Izgec, B. Demiral, H. Bertin, and S. Akin.  $CO_2$  injection into saline carbonate aquifer formations i: laboratory investigations. *Transport in Porous Media*, 72:1–24, 2008.

- [56] S. Y. Xie, J. F. Shao, and W. Y. Xu. Influence of chemical degradation on mechanical behaviour of a limestone. *International Journal of Rock Mechanics & Mining Sciences*, 48:741–747, 2011.
- [57] J. Canal, J. Delgado, I. Falcón, Q. Yang, R. Juncosa, and V. Barrientos. Injection of CO<sub>2</sub>-saturated water through a siliceous sandstone plug from the hontomin test site (spain): experiment and modeling. *Environmental Science & Technology*, 47:159–167, 2013.
- [58] J. Qajar, N. Francois, and C. Arns. Micro-tomographic characterization of dissolution-induced local porosity changes including fines migration in carbonate rock. *Paper SPE Presented at the EOR Conference at Oil and Gas West Asia, Muscat, Oman*, 16-18 April 2011.
- [59] M. T. Nguyen, J. Bemmer, and L. Dormieux. Micromechanical modeling of carbonate geomechanical properties evolution during acid gas injection. *Paper ARMA Presented at the 45th U.S. Mechanics/Geomechanics Symposium, San Francisco, USA*, 26-29 June 2011.
- [60] G. Rimmelé, V. Barlet-Gouédard, and F. Renard. Evolution of the petrophysical and mineralogical properties of two reservoirs rocks under thermodynamic conditions relevant for CO<sub>2</sub> geological storage. *Oil & Gas Science and Technology*, 65:565–580, 2010.
- [61] P. Bachaud, P. Berne, F. Renard M. Sardin, and J. Leclerc. Use of tracers to characterize the effects of a CO<sub>2</sub>-saturated brine on petrophysical properties of a low permeability carbonate caprock. *Chemical Engineering Research and Design*, 89:1817–1826, 2011.
- [62] M. A. Peter. Homogenisation in domains with evolving microstructure. *Comptes Rendus Mécanique*, 335:357–362, 2007.
- [63] M. T. Nguyen. *PhD thesis: Caractérisation géomechanique de la dégradation des roches sous l'effet de l'injection de gaz acides*. Université Paris-Est, Paris, France, 2012.
- [64] M. A. Peter. Homogenisation of a chemical degradation mechanism inducing an evolving microstructure. *Comptes Rendus Mécanique*, 335:679–684, 2007.
- [65] M. A. Peter and M. Böhm. Multiscale modelling of chemical degradation mechanism in porous media with evolving microstructure. *Multiscale Modelling & Simulations*, 7:1643–1668, 2009.
- [66] J. Lewandowska. *Geomechanics in CO<sub>2</sub> storage facilities*. Wiley, 2008.
- [67] B. Coussy. *Poromechanics*. John Wiley and Sons Ltd., Chichester, England, 2004.
- [68] C. Doughty and K. Preuss. Modeling supercritical carbon dioxide injection in heterogeneous porous media. *Vadose Zone Journal*, 3:837–847, 2004.

- [69] A. Kumar, R. Ozah, M. Noh, and G. A. Pope. Reservoir simulations of CO<sub>2</sub> geological storage in deep saline aquifers. *SPE Journal*, 10:336–348, 2005.
- [70] S. D. Hovorka, S. M. Benson, and C. Doughty. Measuring permanence of CO<sub>2</sub> storage in saline formations: the frio experiment. *Environmental Geoscience*, 13:105–121, 2006.
- [71] P. Sarpialli and P. McGrail. Semi analytical approaches to modeling deep well injection of CO<sub>2</sub> for geological sequestration. *Conversion and Management*, 43:185–198, 2002.
- [72] M. J. Nordbotten, A. M. Celia, and S. Bachu. Injection and storage of CO<sub>2</sub> in deep saline aquifers: analytical solution for CO<sub>2</sub> plume evolution during injection. *Transport in Porous Media*, 58:339–360, 2005.
- [73] K. Wojtacki, J. Lewandowska, P. Gouze, and A. Lipkowski. Numerical computations of rock dissolution and geomechanical effects for CO<sub>2</sub> geological storage. *International Journal for Numerical and Analytical Methods in Geomechanics*, 39:482–506, 2015.
- [74] C. A. Schneider, W. Rasband, and K. W. Eliceiri. Nih image to imagej: 25 years of image analysis. *Nature Methods*, 9:671–675, 2012.
- [75] P. Gouze, Y. Melean, T. Le Borgne, M. Dentz, and J. Carrera. Non-fickian dispersion in porous media explained by heterogeneous microscale matrix diffusion. *Water Resources Research*, 44:W11416, 2008.
- [76] A. P. Boresi, R. J. Schmidt, and O. Sidebottom. *Advanced Mechanics of Materials*. Wiley, New York, USA, 1993.
- [77] J-L. Auriault. Homogenization analysis of diffusion and adsorption macrotransport in porous media: macrotransport in the absence of advection. *Géotechnique*, 43:457–469, 1993.
- [78] J-L. Auriault and J. Lewandowska. Effective diffusion coefficient: from homogenization to experiment. *Transport in Porous Media*, 27:205–223, 1997.
- [79] J-L. Auriault and J. Lewandowska. On the validity of diffusion/dispersion tests in soils. *Engineering Transactions*, 45(3-4):395 – 417, 1997.
- [80] J-L. Auriault and J. Lewandowska. Upscaling: cell symmetries and scale separation. *Transport in Porous Media*, 43:473–485, 2001.
- [81] J-L. Auriault. Heterogeneous medium. is an equivalent macroscopic description possible? *International Journal of Engineering Science*, 29:785–795, 1991.
- [82] A. G. Narsilio, O. Buzzi, S. Fityus, T. Sup Yun, and W. D. Smith. Upscaling of navier-stokes equations in porous media: Theoretical, numerical and experimental approach. *Computers and Geotechnics*, 36:1200–1206, 2009.
- [83] C. Voivret, F. Radjaï, J.-Y. Delenne, and M. S. El Youssoufi. Space-filling properties of polydisperse granular media. *Phys. Rev. E*, 76:021301, Aug 2007.

- [84] A. Taboada, K.-J. Chang, F. Radjaï, and F. Bouchette. Rheology, force transmission, and shear instabilities in frictional granular media from biaxial numerical tests using the contact dynamics method. *Journal of Geophysical Research: Solid Earth*, 110:n/a–n/a, 2005.
- [85] Stephen C. Cowin. A note on the microstructural dependence of the anisotropic elastic constants of textured materials. In Morteza Mehrabadi Ching S. Chang Hayley H. Shen, Masao Satake and Charles S. Campbell, editors, *Advances in Micromechanics of Granular Materials Proceedings of the Second US/Japan Seminar on Micromechanics of Granular Materials Potsdam, NY, USA, August 5–9, 1991*, volume 31 of *Studies in Applied Mechanics*, pages 61 – 70. Elsevier, 1992.
- [86] Christophe Geuzaine and Jean-François Remacle. Gmsh: A 3-d finite element mesh generator with built-in pre- and post-processing facilities. *International Journal for Numerical Methods in Engineering*, 79:1309–1331, 2009.
- [87] G. Mavko, T. Mukerji, and J. Dvorkin. *The Rock Physics Handbook*. Cambridge University Press, 2009.
- [88] R. Hill. A self-consistent mechanics of composite materials. *Journal of the Mechanics and Physics of Solids*, 13(4):213 – 222, 1965.
- [89] R. Guibert, M. Nazarova, P. Horgue, G. Hamon, P. Creux, and G. Debenest. Computational permeability determination from pore-scale imaging: Sample size, mesh and method sensitivities. *Transport in Porous Media*, 107:641–656, 2015.
- [90] H. G. Weller, G. Tabor, H. Jasak, and C. Fureby. A tensorial approach to computational continuum mechanics using object-oriented techniques. *Comput. Phys.*, 12:620–631, 1998.
- [91] S. Patankar. *Numerical heat transfer and fluid flow / Suhas V. Patankar*. Hemisphere Pub. Corp. ; McGraw-Hill Washington : New York, 1980.
- [92] S.V. Patankar and D.B. Spalding. A calculation procedure for heat, mass and momentum transfer in three-dimensional parabolic flows. *International Journal of Heat and Mass Transfer*, 15(10):1787 – 1806, 1972.
- [93] J. H. Ferziger and M. Peric. *Computational Methods for Fluid Dynamics*. Springer-Verlag Berlin Heidelberg, 2002.
- [94] P. C. Carman. *Flow of gases through porous media*. Butterworths, London, 1956.
- [95] T. Bourbie and B. Zinszner. Hydraulic and acoustic properties as a function of porosity in fontainebleau sandstone. *Journal of Geophysical Research: Solid Earth*, 90:11524–11532, 1985.
- [96] P. M. Doyen. Permeability, conductivity, and pore geometry of sandstone. *Journal of Geophysical Research: Solid Earth*, 93:7729–7740, 1988.

- [97] J-B. Clavaud, A. Maineult, M. Zamora, P. Rasolofosaon, and C. Schlitter. Permeability anisotropy and its relations with porous medium structure. *Journal of Geophysical Research: Solid Earth*, 113:n/a–n/a, 2008.



## Couplage entre transport, comportement mécanique et dégradation par dissolution de réservoirs de roche

**Résumé :** L'objectif de cette thèse est d'analyser l'évolution des propriétés mécaniques et de transport effectives de roches aquifères, qui sont soumises à une dégradation progressive par attaque chimique due à la dissolution par  $\text{CO}_2$ . L'étude proposée porte sur les conditions à long terme et en champ lointain, lorsque la dégradation de la matrice poreuse peut être supposée homogène à l'échelle de l'échantillon. La morphologie du réseau de pores et du squelette solide définissant les propriétés macroscopiques majeures de la roche (perméabilité, élasticité), la modélisation d'un tel matériau poreux doit être basée sur une caractérisation morphologique et statistique des roches étudiées. Tout d'abord, une méthode de reconstruction inspirée du processus naturel de formation des grès est développée afin d'obtenir des représentations statistiquement équivalentes à de véritables échantillons. Les échantillons générés sont sélectionnés afin de satisfaire les informations morphologiques extraites de l'analyse des images microtomographiques d'échantillons de roche naturelle. Une méthodologie afin d'estimer les propriétés mécaniques équivalentes des échantillons générés, fondées directement sur des maillages réguliers considérés comme images binaires, est présentée. Le comportement mécanique équivalent est obtenu dans le cadre de l'homogénéisation périodique. Mais en raison du manque de périodicité géométrique des échantillons considérés, deux approches différentes sont développées : la reconstruction de VER par symétrie de réflexion ou l'addition d'une couche homogène associée à une méthode de point fixe. L'évolution de la perméabilité est estimée de manière classique en utilisant la méthode de mise à l'échelle dans la forme de la loi de Darcy. Enfin, la dissolution chimique du matériau est abordée par dilatation morphologique de la phase poreuse. De plus, une analyse détaillée de l'évolution des descripteurs morphologiques liée aux modifications de la microstructure lors des étapes de dissolution est présentée. La relation entre les propriétés morphologiques - perméabilité - modules d'élasticité est également fournie. La méthodologie développée dans ce travail pourra être facilement appliquée à d'autres classes de matériaux hétérogènes.

**Mots-clés :** milieux poreux, modélisation multi-échelles, couplage chemo-mécanique, homogénéisation, morphologie mathématique, numérique.

## Coupling between transport, mechanical properties and degradation by dissolution of rock reservoir

**Abstract:** The aim of this thesis is to analyse evolution of effective mechanical and transport properties of rock aquifer, which is subjected to progressive chemical degradation due to  $\text{CO}_2$  dissolution. The proposed study focuses on long-term and far field conditions, when degradation of porous matrix can be assumed to be homogeneous at sample scale. It is very well known that morphology of pore network and solid skeleton defines important macroscopic properties of the rock (permeability, stiffness). Therefore, modelling of such porous material should be based on morphological and statistical characterisation of investigated rocks. First of all, in order to obtain statistically equivalent representations of real specimen a reconstruction method inspired by natural process of sandstone formation is adapted. Then the selected generated samples satisfy morphological informations which are extracted by analysing microtomography of the natural rock sample. Secondly, a methodology to estimate effective mechanical properties of investigated material, based directly on pixel-like regular meshes, is featured. Effective mechanical behaviour is obtain within the framework of periodic homogenization. However due to lack of geometrical periodicity two different approaches are used (reflectional symmetry of considered RVE and a fixed point method, using additional layer spread over the considered geometry). Evolution of permeability is estimated in classical way using upscaling method in the form of Darcy's law. Finally, chemical dissolution of material is tackled in a simplified way by performing morphological dilation of porous phase. Detailed analysis of chosen morphological descriptors evolution, triggered by modifications of microstructures is provided. The relation between morphological properties - permeability - elastic moduli is also provided. The methodology developed in this work could be easily applied to other heterogeneous materials.

**Key words:** porous media, multi-scale modeling, chemo-mechanical coupling, homogenization, mathematical morphology, numerical computation.